Journal of Heat Transfer

Published Monthly by ASME

VOLUME 128 • NUMBER 11 • NOVEMBER 2006

RESEARCH PAPERS

Micro/Nanoscale Heat Transfer

Natural and Mixed Convection

Heat and Mass Transfer

Evaporation, Boiling, and Condensation

Forced Convection

Porous Media

TECHNICAL BRIEFS

(Contents continued)

The ASME Journal of Heat Transfer is abstracted and indexed in the following:

Applied Science and Technology Index, Chemical Abstracts, Chemical Engineering and Biotechnology Abstracts (Electronic equivalent of Process and Chemical Engineering), Civil Engineering Abstracts, Compendex (The electronic equivalent of Engineering Index), Corrosion Abstracts, Current Contents, E & P Health, Safety, and Environment, Ei EncompassLit, Engineered Materials Abstracts, Engineering Index, Enviroline (The electronic equivalent of Environment Abstracts), Environment Abstracts, Environmental Engineering Abstracts, Environmental Science and Pollution Management, Fluidex, Fuel and Energy Abstracts, Index to Scientific Reviews, INSPEC, International Building Services Abstracts, Mechanical & Transportation Engineering Abstracts, Mechanical Engineering Abstracts, METADEX (The electronic equivalent of Metals Abstracts and Alloys Index), Petroleum Abstracts, Process and Chemical Engineering, Referativnyi Zhurnal, Science Citation Index, SciSearch (The electronic equivalent of Science Citation Index), Theoretical Chemical Engineering

X. Jack Hu[1]
e-mail: jack.hu@intel.com

Antonio A. Padilla

Mechanical Engineering Department,
Stanford Univeristy,
440 Escondido Mall,
Stanford, CA 94305

Jun Xu

Timothy S. Fisher

School of Mechanical Engineering and Birck
Nanotechnology Center,
Purdue University,
585 Purdue Mall,
West Lafayette, IN 47907

Kenneth E. Goodson
Mechanical Engineering Department,
Stanford University,
440 Escondido Mall,
Stanford, CA 94305

3-Omega Measurements of Vertically Oriented Carbon Nanotubes on Silicon

An exploratory thermal interface structure, made of vertically oriented carbon nanotubes directly grown on a silicon substrate, has been thermally characterized using a 3-omega method. The effective thermal conductivities of the carbon nanotubes (CNT) sample, including the effects of voids, are found to be 74 W/m K to 83 W/m K in the temperature range of 295 K to 323 K, one order higher than that of the best thermal greases or phase change materials. This result suggests that the vertically oriented CNTs potentially can be a promising next-generation thermal interface solution. However, fairly large thermal resistances were observed at the interfaces between the CNT samples and the experimental contact. Minimizing these contact resistances is critical for the application of these materials. [DOI: 10.1115/1.2352778]

Keywords: thermal conductivity, contact thermal resistance, carbon nanotube, thermal interface material, 3-omega method, thermal management

Introduction

Excessive chip heating is becoming a major cause of failures in electronic components and a critical obstacle in developing more advanced electronic devices. Related to this problem is the fact that the thermal interface materials (TIMs), used for attaching an electronic chip to its heat spreader or heat sink, have very low thermal conductivity, which causes large thermal resistances at packaging interfaces. These interface resistances are in series with the resistance of any heat sink and cannot be removed or reduced by using advanced cooling techniques on the heat sink side. Because chip sizes are remaining the same and power dissipation continues to increase, without improvements in TIM thermal conductivity, the temperature rise at package interfaces will increase proportionally and occupy an increasing fraction of the total allowable junction-to-ambient temperature rise. According to the projection of the International Technology Roadmap for Semiconductors [1], by the year of 2010, if TIM thermal conductivity remains the same, the overall thermal resistance budget will be completely occupied by the TIM resistance, and performance improvements in electronic chips may no longer be sustained. To meet the increasing power dissipation requirements, large improvements in TIM thermal conductivity are needed in next few years.

Carbon nanotubes (CNTs), a man-made material first reported by Iijima in 1991 [2], are promising candidates for improving TIM thermal conductivity. Many reports suggest CNTs to be the best heat conductor among all the materials. Hone et al. [3] found that the thermal conductivity of aligned single-wall nanotube

(SWNT) ropes is about 250 W/m K at 300 K and estimated that the thermal conductivity of a single SWNT in the longitude direction ranges from 1750 W/m K to 5800 W/m K. The thermal conductivity of individual CNTs (multiwall nanotube (MWNT) [4] or SWNT [5]) has been measured to be at least 3000 W/m K at room temperature, which is about eight times higher than that of copper and 20 times higher than that of silicon. Theoretical studies predict even higher thermal conductivity values, such as 6600 W/m K at room temperature by Berber et al. [6].

Owing to their high thermal conductivity, CNTs have received much attention for thermal management in recent years. Early attempts used CNTs as fillers to form high thermal conductivity fluids or TIM composites. Choi et al. [7] measured the effective thermal conductivity of nanotube-in-oil suspensions and found that with only 1 vol % of nanotubes, the effective thermal conductivity can be 2.5 times the value of the base fluid. Such an increase in thermal conductivity has never been found previously with any other particles. Biercuk et al. [8] also found that epoxy filled with 1 wt % of CNTs exhibited a 70% increase in thermal conductivity at 40 K and 125% at room temperature. Hu et al. [9] proposed the combined use of CNTs and traditional heat conductive fillers for TIMs. They achieved a thermal conductivity value seven times that of the base material, almost double the thermal conductivity of the corresponding TIM composite with only traditional fillers. However, this thermal conductivity value is still one thousandth that of an individual CNT. The potential heat conduction capability of CNTs is far from optimal.

Two problems can lead to the low efficiency. One problem is that CNTs are randomly dispersed, and only a few portions of CNTs are effectively contributing to heat conduction. The other problem is that heat is not directly conducted from one side to the other through CNTs. CNTs are discontinued by other fillers or the base fluid. The low thermal conductivity of the interstitial media, as well as the contact resistance between those and CNTs, degrades the thermal performance of the CNT composites.

A more advanced approach is to grow CNTs directly on a sili-
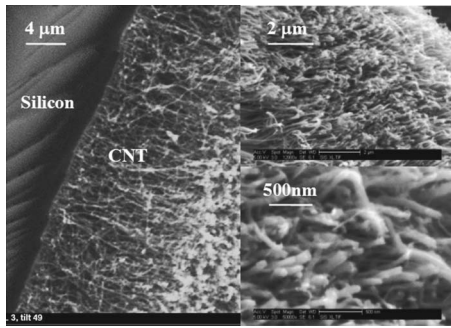
Fig. 1 SEM images of the CNT sample

Fig. 2 Schematic of the experimental structure

con wafer and oriented CNTs in the direction of heat conduction (i.e., perpendicular to the silicon wafer). These CNTs can be attached to a copper heat spreader and serve as a thermal interface structure [10]. Xu and Fisher [11] first tested such a structure using a 1D steady-state method. This test, however, can only yield a total thermal resistance, summed over the depth of the CNT layer including interfaces, and suffered from relatively large uncertainties. In this paper, we develop an MEMS-based frequency-domain measurement to precisely characterize the thermal properties of the aligned CNT sample and contact resistances. Various challenges in using the aligned CNTs as an interfacial structure and possible solutions are also discussed.

Experimental Measurements

Sample Preparation. The CNT samples are grown on 7 mm $\times$ 7 mm double-side-polished silicon chips using direct synthesis with a trilayer (Ti-Al-Ni) catalyst configuration and microwave plasma enhanced chemical vapor deposition (PECVD) (the same process as [11]). The thicknesses of the titanium, aluminum, and nickel layers are 30, 10, and 6 nm respectively, and the thickness of the silicon substrate is about 420 μm. The H_2/CH_4 plasma is excited at a chamber pressure of 10 Torr and a microwave power of 150 W. The synthesis temperature is maintained at 800°C.

Figure 1 shows scanning electron microscope (SEM) images of the synthesized CNTs on a silicon substrate. Vertically oriented, multiwalled CNTs evenly cover all over the silicon substrate. The length of the CNT layer is about 13 μm, and the diameters range from 10 nm to 80 nm. The two images on the right side are taken after the measurements, suggesting that the CNT sample can withstand an attachment pressure up to 100 kPa without noticeable degrading in quality.

Measurement Method. A schematic of the experimental structure is given in Fig. 2. The CNT sample, with the CNT-side facing downward, is attached to a test device under a controlled attachment pressure. The test device is fabricated on a glass wafer to reduce heat loss from the substrate and contains a microscale patterned metal bridge operated in the kilohertz regime using the 3ω technique (for reviews of the 3ω technique see [12,13]). The metal bridge is a platinum line, 7 mm long, 50 μm wide, and 200 nm thick, with four-wire electrical connects. Beneath the metal bridge, a 0.5 nm titanium layer is used to ensure good adhesion to the substrate; and on top of the metal bridge, 20 nm silicon nitride is deposited to insulate the electrical conductive bridge from the CNT sample.

The experimental structure, attached with a chip carrier, is placed in a Lakeshore MTD-135 cryostat chamber and connected in an electrical circuit as shown in Fig. 3. The metal bridge serves both as a heater and a thermometer. Driven by the sine out of a SR830 lock-in amplifier at an angular frequency of ω, the metal bridge generates joule heat and produces a temperature oscillation ΔT at 2ω. It is noted that the electrical resistance of the metal bridge is proportional to its temperature, and thus the electrical
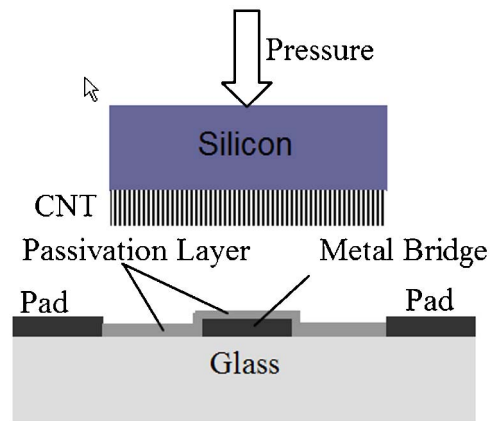
resistance is also modulated at 2ω. With the applied current at ω, the voltage drop along the metal bridge thus contains a modulated component at 3ω. This 3ω voltage component, $V_{3\omega}$ is related to the temperature oscillation ΔT as [12]

$$\Delta T = 2\frac{dT}{dR}\frac{R_0}{V}V_{3\omega} \tag{1}$$

where V is the applied voltage and R_0 is the electrical resistance along the metal bridge, respectively, and dT/dR depicts the temperature dependence of R_0, which is calibrated at chamber temperatures ranging from 295 K to 324 K. After subtracting the ω voltage component using a Wheatstone bridge, as shown in Fig. 3, $V_{3\omega}$ is determined by measuring the nonequilibrium voltage $v_{3\omega}$, using the SR830 lock-in amplifier. The conversion from $v_{3\omega}$ to $V_{3\omega}$ is given by [14]

$$V_{3w} = \frac{(R_0 + R_1) \cdot (R_2 + R_3)}{R_1 \cdot (R_2 + R_3)}v_{3w} \tag{2}$$

Thermal Model and Data Analysis. We model the transient heat conduction problem using a one-dimensional (1D) model. 1D heat conduction is a good approximation because the width of the heater is several times larger than the thickness of the CNT layer (50 μm versus 13 μm), and more importantly, because the thermal coupling between CNTs is weak and the in-plane heat conduction in the CNT layer is negligible. If not specially noted, the thermal conductivity of the CNT layer in this paper is always considered in the longitude direction.

For 1D heat conduction in a homogeneous medium, if only the
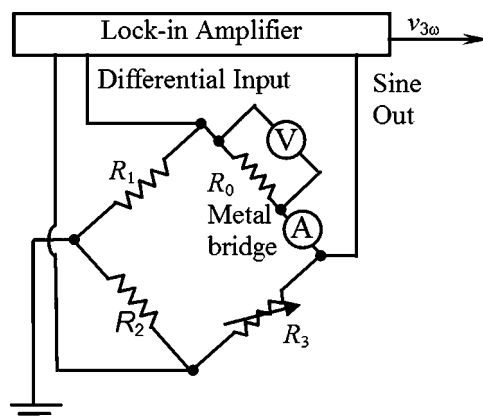
Fig. 3 Electronic circuit of the experimental system [14]

temperature difference relative to its substrate is considered, the periodic steady-state heat conduction equation in the frequency domain can be written as

$$\frac{d^2\Delta T(x,\omega)}{dx^2} = a^2\Delta T(x,\omega) \tag{3}$$

with boundary conditions

$$-k\frac{d\Delta T(x,\omega)}{dx}\bigg|_{x=0} = P'' \tag{4}$$

$$\Delta T(l,\omega) = 0 \tag{5}$$

where $a=\sqrt{j\omega\rho c/k}$, j is imaginary unit, ρ, c, k, l are the density, specific heat, thermal conductivity, and thickness of the media, P'' is the applied power density, and ω is the angular frequency of the heat flux. The solution of this differential equation at $x=0$ and a given frequency ω is

$$\Delta T(\omega) = \frac{P''\tanh(al)}{ak} \tag{6}$$

If we define a thermal impedance as $Z(\omega)=\Delta T(\omega)/P''$, then

$$Z(\omega) = \frac{\tanh(al)}{ak} \tag{7}$$

For small al, $\tanh(al)\approx 2al/(2+a^2l^2)$ by neglecting $O(a^3L^3)$ terms, resulting in

$$Z^{-1}(\omega) = R^{-1} + j\omega C \tag{8}$$

with thermal resistance

$$R = l/k \tag{9}$$

and thermal capacitance

$$C = \rho cl/2 \tag{10}$$

As $al\to\infty$, $\tanh(al)\to 1$, and

$$Z^{-1}(\omega) = \sqrt{j\omega\rho ck} = \sqrt{\omega\rho ck/2} + j\omega\sqrt{\rho ck/(2\omega)} \tag{11}$$

The thermal resistance and thermal capacitance for a semi-infinite medium thus can be expressed as

$$R = \sqrt{2/(\omega\rho ck)} \tag{12}$$

and

$$C = \sqrt{\rho ck/(2\omega)} \tag{13}$$

The layer of CNT can be modeled as a thin film by introducing an effective thermal conductivity

$$k_{e,CNT} = \phi k_{CNT} + (1-\phi)k_{air} \approx \phi k_{e,CNT} \tag{14}$$

and effective volume-based specific heat

$$C_{e,CNT} = \phi(\rho c)_{CNT} + (1-\phi)(\rho c)_{air} \tag{15}$$

The two substrates (silicon and glass) are modeled as semi-infinite media, and the corresponding thermal resistance and thermal capacitance are given by Eqs. (12) and (13). Between the CNT sample and the heater, a contact thermal resistance R_c exists, which can be caused by the impacts of imperfect contact, boundary scattering as well as passivation and catalyst. No capacitance term exists at the contacts because the passivation and catalyst layers are extremely thin (<0.07 μm in total), without contribution to heat storage.

Thus the transient heat conduction problem can be modeled using the equivalent thermal circuit given in Fig. 4. It should be noted that the CNT capacitor should be grounded directly to the ambient since the amount of heat storage in the CNT layer is calculated based on the temperature rise above the ambient temperature. A detailed solution for multilayered structures can be found in [15,16]. As can be seen from Fig. 4, heat generated from the heater diffuses to the ambient through two paths in parallel:
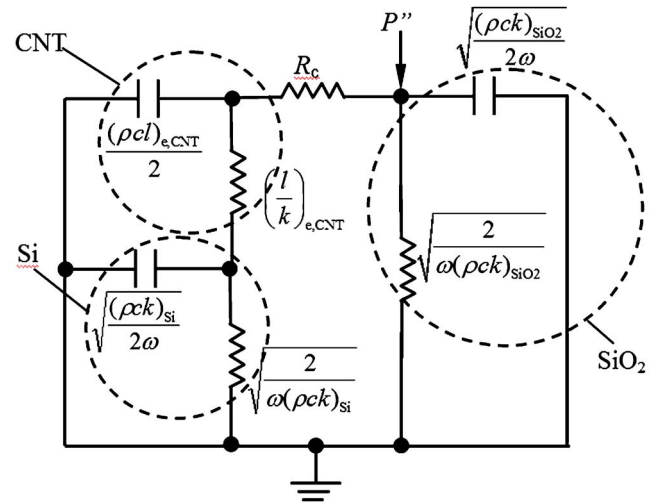
Fig. 4 Equivalent thermal circuit for 1D heat conduction approximation

one through the CNT layer to the silicon substrate and the ambient; the other to the glass substrate and the ambient. The total equivalent thermal impedance $Z_t(\omega)$ can be calculated as

$$\frac{1}{Z_t(\omega)} = \frac{1}{R_C + 1/[(R_{CNT} + Z_{Si}(\omega))^{-1} + j\omega C_{CNT}]} + \frac{1}{Z_{SiO2}(\omega)} \tag{16}$$

The temperature oscillation ΔT then can be predicted as

$$\Delta T = P'' \cdot Z_t(\omega) \tag{17}$$

The thermal properties of the CNT sample $k_{e,CNT}$ and $c_{e,CNT}$, as well as the contact thermal resistance R_c are obtained by fitting the temperature oscillation data with the prediction of Eq. (17). The summed square of residues, minimized during the data fitting process, is given by

$$S(k_{e,CNT}, c_{e,CNT}, R_c(P_1), R_c(P_2)) = \sum_{\omega} [\Delta T_{exp}(\omega) - \Delta T_{mdl}(2\omega)]^2 \tag{18}$$

where $P_1=40$ kPa and $P_2=100$ kPa are attachment pressures, and ΔT_{exp} and ΔT_{mdl} are temperature oscillations obtained from the experiment and modeling, respectively.

It should be noted that the contribution of the CNT layer to the temperature oscillation is different than that of the contact resistance. For variable modulated frequencies, the contact resistance R_c contributes a fixed offset, but the contribution of the CNT layer Z_{CNT} is frequency dependent. For variable attachment pressures, the contact resistance R_c varies with pressure, but, for moderate pressures (such as the pressures of 40 kPa and 100 kPa used herein), the thermal properties of the CNTs should remain the same. Therefore, both the effective thermal properties of the CNT sample and the contact resistance can be subtracted by fitting the experimental data at variable frequencies. Figure 5 shows an example of data fitting at 300 K. The 1D model is clearly sufficient for frequencies higher than 10 Hz. At lower frequencies, heat can diffuse deep into the bulk substrates, and the assumption of 1D heat conduction fails. Therefore, data points at frequencies lower than 10 Hz are excluded from data fitting.

Results and Discussion

Measured results are given in Figs. 6 and 7 for thermal properties and contact thermal resistance, respectively. The hollow points represent measured data and the solid lines shows the slope of temperature dependence. The measurement uncertainty mainly
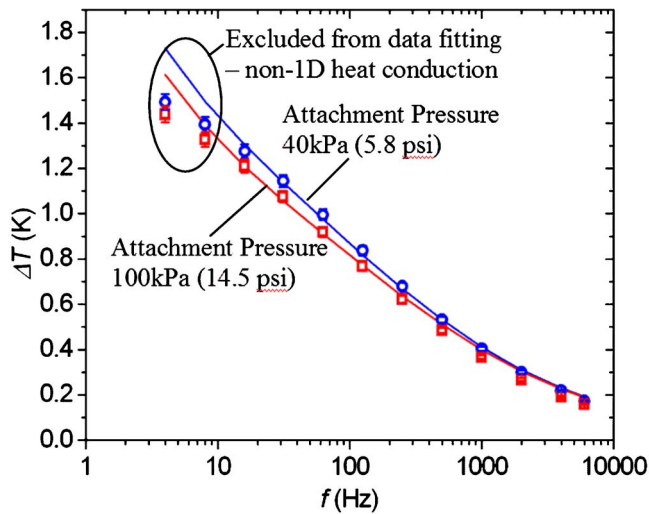
Fig. 5 Observed temperature oscillation amplitudes versus theoretic predictions at 300 K (empty circles and squares are experimental data; solid lines are theoretic predictions)

comes from the uncertainty of the 3-omega signal V_{3w} (about 2%) and the measurements of dT/dR, R_0, and V are found to be very accurate ($<0.1\%$). According to Eq. (1), the uncertainty of the temperature oscillation ΔT_{exp} is also about 2%. The uncertainty of any fitted quantity y ($y=k_{e,CNT}$, $c_{e,CNT}$, $R_c(P_1)$ or $R_c(P_2)$) is then estimated by

$$\left(\frac{\delta y}{y} \right) = \left(\frac{\partial y}{\partial \Delta T} \right) \left(\frac{\delta \Delta T_{exp}}{\Delta T_{exp}} \right) \qquad (19)$$

The partial deviation of y with respect to ΔT can be estimated by examining the difference of data fitting after applying an offset of the temperature oscillations. The estimated uncertainties do not include the approximations made to the analytical model.

The measured effective thermal conductivity of the CNT sample is 74 W/m K at 295 K and increases to 83 W/m K at 323 K, an increase of 12%. The specific heat, from the slope of the fitted curve, increases by more than 20% over the same temperature range. Because the thermal conductivity of a CNT is proportional to the product of its volume-based specific heat and its phonon mean free path, the measured results can be explained as follows. At higher temperatures, more phonons occupy higher energy levels and carrying more heat (i.e., higher specific heat), conversely, the phonon mean free path decreases with increasing temperature due to increased phonon-phonon scattering at higher temperatures. The first factor is dominant in the measure temperature range, which increases the thermal conductivity of the CNT sample, but at a smaller percentage than the increase of volume-based specific heat due to the second factor. Another possible reason is the increase of the thermal conductivity of the surrounding air with increasing ambient temperate since the samples are exposed to the air during testing.

The actual thermal conductivity of a CNT itself, considering the volume fraction of the CNT sample, can be hundreds of W/mK. This value is still lower than the theoretical predictions [6] and the measured results for an individual CNT [4]. However, with improvements in CNT quality, the effective thermal conductivity of the aligned CNT layer can potentially increase further. These high thermal conductivity values suggest that the aligned CNT can be a promising candidate for future TIM solutions.

We also note that the contact resistance between the CNT and the heater is rather large, even with increased attachment pressures. This contact resistance includes the resistances summed over the passivation and catalyst layers and the interfaces in between. But this portion should be small because the passivation
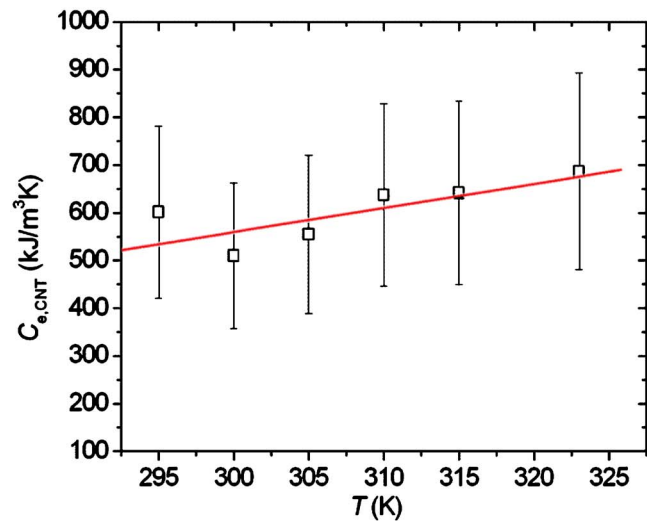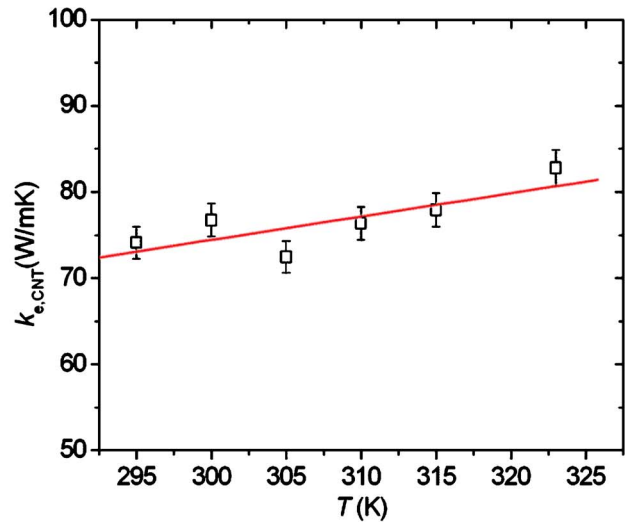
Fig. 6 Measured effective thermal properties (solid lines are linear curve fits)

and catalyst layers are extremely thin and the interfaces are well prepared. The contact resistance is probably dominated by other factors. One problem is that the tubes are not exactly the same length; some of them may not form good mechanical contacts. Better mechanical contacts can be obtained by increasing attachment pressure. However, there exist other fundamental problems that may not be solved with increased pressure, such as constriction effects and acoustic mismatch at the contact points. More experimental and modeling work is needed to understand the fundamental mechanism of the heat transport at the contact points of CNTs.

In practice, a few possible solutions exist to reduce the impact of the contact thermal resistance without an overall increase in attachment pressure. The first method is the combined use of other TIM materials, including thermal greases [9] and phase change materials [17]. The second possible solution is to grow vertically orientated CNTs on both of the contact surfaces to form a CNT cross-talk interface [18].

Conclusions

In summary, vertically oriented CNTs on a silicon substrate have been thermally characterized using a 3ω method. The results indicate that the aligned-CNT layer has much higher thermal conductivity than that of common commercial TIMs, and therefore
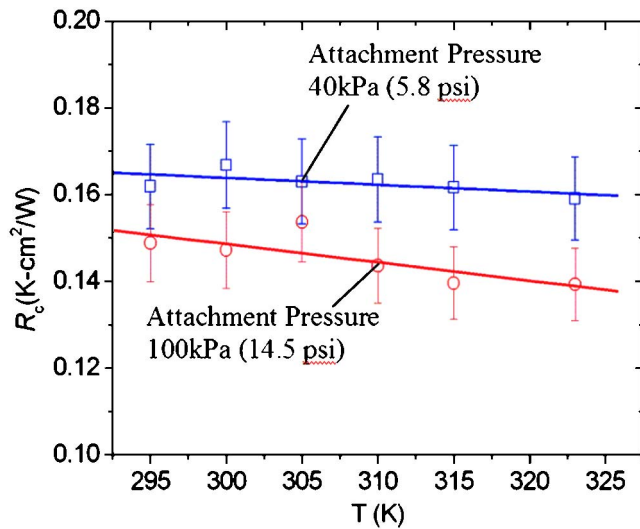
Fig. 7 Measured contact thermal resistance between the CNT sample and the experimental contact (solid lines are linear curve fits)

these materials may be a promising TIM candidate for next-generation electronic packaging. The contact resistance at the tips of the aligned CNTs, however, is still a challenge.

Acknowledgment

Nomenclature

a = $\sqrt{j\omega\rho c}/k$, m^{-1}
C = thermal capacitance, $\mathrm{J/m^3\,K}$
c = specific heat, $\mathrm{J/kg\,K}$
f = frequency, Hz
j = imaginary unit
k = thermal conductivity, $\mathrm{W/m\,K}$
l = thickness, $\mu\mathrm{m}$
P'' = power density, $\mathrm{W/m^2}$
R = thermal resistance, $\mathrm{K\,m^2/W}$
R_0 = electrical resistance of the metal bridge, Ω
R_i = electrical resistance of the resistors in the Wheatstone bridge, $i=1,2,3$
S = summed squares of residues, K^2
T = temperature, K
V = electrical voltage along the metal bridge, mV
$V_{3\omega}$ = 3ω voltage component along the metal bridge, mV
$v_{3\omega}$ = Nonequilibrium voltage of the Wheatstone bridge, mV
y = $k_{e,CNT}$, $c_{e,CNT}$, $R_c(P_1)$ or $R_c(P_2)$
Z = thermal impedance, $\mathrm{K\,m^2/W}$

Greek symbols

ΔT = Temperature oscillation along the metal bridge, K
δ = experimental uncertainty
ϕ = volume fraction
ρ = density, $\mathrm{kg/m^3}$
ω = angular frequency, rad/s

Subscripts

CNT = carbon nanotube
c = contact
e = effective value
exp = experimental measurement
mdl = model prediction
Si = silicon substrate
SiO2 = glass substrate
t = total

References

[1] International Technology Roadmap for Semiconductors, 2003 edition and 2004 update, http://public.itrs.net/
[2] Iijima, S., 1991, "Helical Microtubules of Graphitic Carbon," Nature (London), **354**, pp. 56–58.
[3] Hone, J., Whitney, M., Piskoti, C., and Zettl, A., 1999, "Thermal Conductivity of Single-Walled Nanotubes," Phys. Rev. B, **59**(4), pp. R2514–R2516.
[4] Kim, P., Shi, L., Majumdar, A., and McEuen, P. L., 2001, "Thermal Transport Measurements of Individual Multiwalled Nanotubes," Phys. Rev. Lett., **87**, pp. 215502 (1–4).
[5] Yu, C., Shi, L., Yao, Z., Li, D., and Majumdar, A., 2005, "Thermal Conductance and Thermopower of an Individual Single-Walled Carbon Nanotube," Nano Lett., **5**(9), pp. 1842–1846.
[6] Berber, S., Kwon, Y. K., and Tomanek, D., 2000, "Unusually High Thermal Conductivity of Carbon Nanotubes," Phys. Rev. Lett., **84**(20), pp. 4613–4617.
[7] Choi, S. U. S., Zhang, Z. G., Yu, W., Lockwood, F. E., and Grulke, E. A., 2001, "Anomalous Thermal Conductivity Enhancement in Nanotube Suspensions," Appl. Phys. Lett., **79**(14), pp. 2252–2254.
[8] Biercuk, M. J., Llaguno, M. C., Radosavljevic, M., Hyun, J. K., Johnsond, A. T., and Fischer, J. E., 2002, "Carbon Nanotube Composites for Thermal Management," Appl. Phys. Lett., **80**(15), pp. 2667–2769.
[9] Hu, X., Jiang, L., and Goodson, K. E., 2004, "Thermal Conductance Enhancement of Particle-filled Thermal Interface Materials Using Carbon Nanotube Inclusions," *Proc. 9th Intersociety Conference on Thermal and Thermo-Mechanical Phenomena in Electronic System* (ITHERM), Las Vegas, NV, June 1–4, Vol. 1, pp. 63–69.
[10] Montgometry, S. W., and Holalkere, V. R., 2003, "Carbon Nanotube Thermal Interface Structures," US Patent Application No. 20030117770.
[11] Xu, J., and Fisher, T. S., 2006, "Enhanced Thermal Contact Conductance Using Carbon Nanotube Arrays," IEEE Trans. Compon. Packag. Technol., **29**(2), pp. 261–267.
[12] Cahill, D. G., 1990, "Thermal Conductivity Measurement From 30 to 750 K: The 3ω Method," Rev. Sci. Instrum., **61**(2), pp. 802–808.
[13] Cahill, D. G., Goodson, K. E., and Majumdar, A., 2002, "Thermometry and Thermal Transport in Micro/Nanoscale Solid-State Devices and Structures," J. Heat Transfer, **124**(2), pp. 223–241.
[14] Yamane, T., Nagai, N., Katayama, S., and Todoki, M., 2002, "Measurement of Thermal Conductivity of Silicon Dioxide Thin Films Using a 3ω Method," J. Appl. Phys., **91**(12), pp. 9772–9776.
[15] Touzelbaev, M., 2001, "Thermal Properties of Novel Electronic Materials," Ph.D. dissertation, Stanford Univeristy.
[16] Borca-Tasciuc, T., Kumar, A. R., and Chen, G., 2001, "Data Reduction in 3ω Method for Thin-Film Thermal Conductivity Determination," Rev. Sci. Instrum., **72**(4), pp. 2139–2147.
[17] Xu, J., and Fisher, T. S., 2006, "Enhancement of Thermal Interface Materials With Carbon Nanotube Arrays," Int. J. Heat Mass Transfer, **49**, pp. 1658–1666.
[18] Tong, T., Zhao, Y., Delzeit, L., Kashani, A., and Majumdar, A., 2004, "Multiwalled Carbon Nanotube/Nanofiber Arrays as Conductive and Dry Adhesive Interface Materials," *Proceedings Integrated Nanosystems: Design, Synthesis and Applications Conference*, ASME Conference NANO2004-46013, Pasadena, CA, Sept. 22–24.

Carlos J. Gomes
Graduate Student
Department of Mechanical Engineering and
Institute for Complex Engineered Systems,
Carnegie Mellon University,
Pittsburgh, PA 15213-3890

Marcela Madrid
Senior Scientific Specialist
Pittsburgh Supercomputing Center and Institute
for Complex Engineered Systems,
Carnegie Mellon University,
Pittsburgh, PA 15213-3890

Javier V. Goicochea
Graduate Student
Department of Mechanical Engineering and
Institute for Complex Engineered Systems,
Carnegie Mellon University,
Pittsburgh, PA 15213-3890

Cristina H. Amon[1]
ASME Life Fellow
Raymond Lane Distinguished Professor,
Department of Mechanical Engineering and
Institute for Complex Engineered Systems,
Carnegie Mellon University,
Pittsburgh, PA 15213-3890
e-mail: camon@cmu.edu

In-Plane and Out-Of-Plane Thermal Conductivity of Silicon Thin Films Predicted by Molecular Dynamics

The thermal conductivity of silicon thin films is predicted in the directions parallel and perpendicular to the film surfaces (in-plane and out-of-plane, respectively) using equilibrium molecular dynamics, the Green-Kubo relation, and the Stillinger-Weber interatomic potential. Three different boundary conditions are considered along the film surfaces: frozen atoms, surface potential, and free boundaries. Film thicknesses range from 2 to 217 nm and temperatures from 300 to 1000 K. The relation between the bulk phonon mean free path (Λ) and the film thickness (d_s) spans from the ballistic regime ($\Lambda \gg d_s$) at 300 K to the diffusive, bulk-like regime ($\Lambda \ll d_s$) at 1000 K. When the film is thin enough, the in-plane and out-of-plane thermal conductivity differ from each other and decrease with decreasing film thickness, as a consequence of the scattering of phonons with the film boundaries. The in-plane thermal conductivity follows the trend observed experimentally at 300 K. In the ballistic limit, in accordance with the kinetic and phonon radiative transfer theories, the predicted out-of-plane thermal conductivity varies linearly with the film thickness, and is temperature-independent for temperatures near or above the Debye's temperature. [DOI: 10.1115/1.2352781]

Keywords: equilibrium molecular dynamics, silicon thin films, in-plane, out-of-plane thermal conductivity, ballistic phonon transport

Introduction

[1]The trend towards miniaturization of electronic devices has led to device features in the nanometer range. In fact, silicon-on-insulator (SOI) transistors are predicted to reach a gate length of 28 nm by the year 2009 [1]. Understanding and predicting thermal transport at these length scales is essential to further the advance of the nanoelectronics industry. Phonons (quantized lattice vibrations) are the main carriers of thermal energy in semiconductors. When the dimensions of the material are comparable to the phonon mean free path, boundary, or interface scattering can limit the mean free path and affect the thermal conductivity [2–4]. At this scale, the phonon group velocity and density of states may also be modified [5]. These special phonon properties have led to theoretical and experimental investigations of thermal transport in nanotubes [6–8], nanowires [9–11], silicon thin films [12–14], and multilayers [15–17].

Silicon films with thicknesses in the nanometers are used in silicon-on-insulator (SOI) and strained silicon transistors. The thickness of the silicon film is comparable to or smaller than the phonon's mean free path (estimated as 300 nm at 300 K [12]). The film is deposited on top of poor thermally conducting materials, and the thermal energy generated by the Joule effect is dissipated along the silicon film plane. Measurements of the thermal conductivities of silicon thin films found a large reduction with respect to the thermal conductivity of bulk silicon [12–14]. This reduction depends on the temperature and the thickness of the film [12,18]. Comparisons of the experimental thermal conductivity to predictions from the Boltzmann transport equation show that the

decrease in thermal conductivity with film thickness can be explained by assuming that the boundaries of the film provide an additional scattering mechanism [13,19]. This phonon-boundary scattering reduces the phonon mean free path with respect to its bulk value [13,19].

Several theoretical methods have been proposed to study the thermal conductivity of semiconductors in different geometric configurations. These approaches include solving the Boltzmann transport equation [20–30], Monte Carlo [31–34], and molecular dynamics [16,35–40]. Molecular dynamics allows the study of phonon thermal transport without the need of prior assumptions about the physics of the phonons. Given an interatomic potential and the initial positions and velocities of the atoms, Newton's second law is used to obtain the atomic trajectories. The method is entirely classical and, therefore, it does not account for quantum effects. Recent studies have shown that molecular dynamics can predict the thermal conductivity of crystalline materials [35–38,41–43], superlattices [15–17], nanotubes [44], amorphous materials [40,45,46], thin films [36,47], and multilayers [16]. Recently, the out-of-plane thermal conductivity of silicon thin films has been predicted at 500 K by means of nonequilibrium molecular dynamics [47]. It was found that, for film thicknesses less than approximately 32 nm, the out-of-plane thermal conductivity decreases linearly as the film thickness is reduced [47]. However, comparisons of these predictions to experimental results are not possible because, to date, the thermal conductivity of silicon thin films has been experimentally measured only in the in-plane direction.

In the present study, we apply equilibrium molecular dynamics to the study of the thermal conductivities of silicon thin films. Equilibrium molecular dynamics allows the prediction, from each simulation, of both the in-plane and out-of-plane thermal conductivities. The predicted in-plane thermal conductivity is compared to existing in-plane experimental data. Thermal conductivities are obtained as a function of temperature, film thickness, and different

---

Copyright © 2006 by ASME

boundary conditions. The film thicknesses studied are d_s =2–217 nm, and the temperature of the simulations ranges between 300 and 1000 K. The phonon mean free path (Λ) in silicon has been estimated from experimental thermal conductivity data as 300 nm at 300 K [12], and from kinetic theory as 30 nm at 1000 K. This range of phonon mean free paths and film thicknesses correspond to Knudsen numbers (Kn=Λ/d_s) between Kn =0.14 at 1000 K and Kn=150 at 300 K. Thus, our simulations span the ballistic and diffusive regimes. In the diffusive regime, (Kn≪1), the thermal conductivity is limited by the scattering among phonons. In the ballistic regime, (Kn≫1), the probability of scattering among phonons is negligible compared to that of the scattering of phonons with the boundaries of the film, which becomes the dominant thermal resistance mechanism.

Molecular dynamics of single-crystal thin films can be performed on a simulation domain consisting of a finite number of lattice constants. Periodic boundary conditions are applied in the directions parallel to the film surfaces (in-plane directions) in order to simulate an infinite slab (Fig. 1). Strategies to treat the surfaces of the film include free boundary conditions [36,47–49], or constraining the atoms on the surface. The surface atoms can be constrained by keeping a few layers of atoms frozen at their equilibrium positions [36,47,50], subjecting them to a harmonic potential [50], or to a one-dimensional force perpendicular to the surface [39]. Free surface boundary conditions have been used to predict the thermal conductivity of argon [36,50], the longitudinal thermal conductivity of silicon nanowires [9], and the atomic reconstruction of silicon surfaces [48,49]. Recently, we have shown that the addition of a one-dimensional force acting perpendicular to the film surface and inwards towards the film can be used to predict silicon thin films thermal conductivities using equilibrium molecular dynamics [39].

In this study, periodic boundary conditions are applied in the directions parallel to the film surfaces. Atoms near the surfaces of the film are subjected to the one-dimensional perpendicular force

[39] in addition to the Stillinger-Weber potential [51]. For comparison purposes, simulations are also performed adding to each surface four layers of atoms kept frozen during the simulation, and using free boundary conditions. Next, this paper presents the numerical simulation methodology based on the molecular dynamics (MD) approach, and then reports the predicted in-plane and out-of-plane thermal conductivities for the ballistic and diffusive regimes. The MD predicted in-plane thermal conductivities are next compared to reported experimental values for silicon thin films at 300 K [12,13].

Numerical Simulation Methodology

We focus on the numerical methodology in this section and discuss its application to determining thermal properties of thin films in the next section.

Molecular Dynamics Approach with Stillinger-Weber Potential. Molecular dynamics refers to the solution of classical equations of motion (Newton's second law) for a set of atoms. In the context of phonon transport in solids, this corresponds to solving the dynamics of atoms in a crystal lattice. The approach is classical in origin and involves the use of statistical mechanics to compute transport coefficients. The inputs to the molecular dynamics simulation are the interatomic potential and the initial positions of the atoms. Among the interatomic potentials available for silicon, the Stillinger-Weber (SW) potential [51] accurately predicts temperature related properties such as the melting point [52] and the thermal expansion of silicon [53], as well as the elastic properties [54] and the yield strength [55]. Equations (1) and (2) represent the two and three-body terms of the SW potential, respectively

$$\phi_2(r_{ij}) = \begin{cases} \varepsilon \cdot A \left[B \left(\dfrac{\sigma}{r_{ij}} \right)^p - \left(\dfrac{\sigma}{r_{ij}} \right)^q \right] \cdot e^{\sigma/r_{ij}-\sigma r_c} & r_{ij} < \sigma r_c \\ 0 & r_{ij} \geqslant \sigma r_c \end{cases} \qquad (1)$$

$$\phi_3(r_{ij}, r_{ik}) = \begin{cases} \varepsilon \lambda e^{\left[\gamma \sigma/(r_{ij}-\sigma r_c) + \gamma \sigma/(r_{ik}-\sigma r_c) \right]} \cdot \left(\cos(\theta_{jik}) + \dfrac{1}{3} \right)^2 & r_{ij}, r_{ik} < \sigma r_c \\ 0 & r_{ij}, r_{ik} \geqslant \sigma r_c \end{cases} \qquad (2)$$
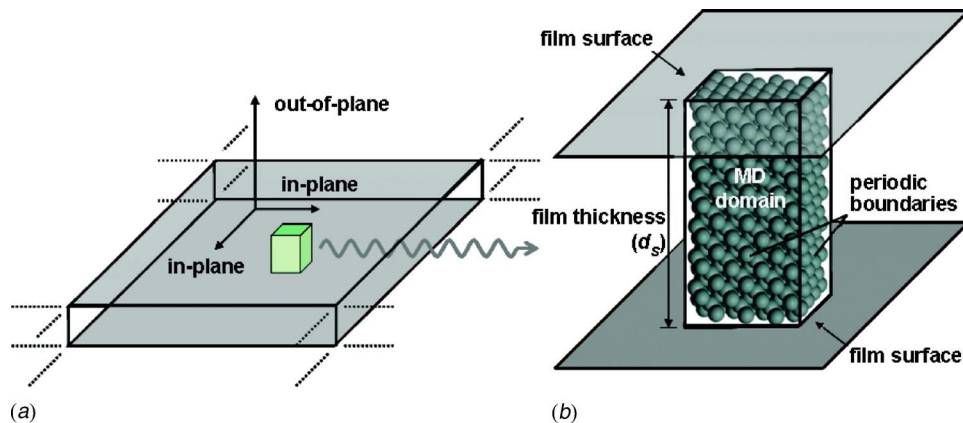

Fig. 1 (*a*) Sketch of a thin film defining the in-plane and out-of-plane directions. (*b*) Simulation domain consisting of 4×4×8 silicon lattice constants and film thickness d_s.

where the values of the potentials' constants used in this work are those reported in [51].

A surface potential is added to the Stillinger-Weber potential of atoms that are near the surfaces [39]

$$\phi_w(d_w) = \begin{cases} \varepsilon_w \cdot \left(\dfrac{\sigma}{d_w}\right)^p \cdot e^{\sigma/(d_w - \sigma r_{cw})} & d_w < \sigma r_{cw} \\ 0 & d_w \geq \sigma r_{cw} \end{cases} \tag{3}$$

where $\varepsilon_w = 1.474 \times 10^{-18}$ J, $\sigma = 0.20951$ nm, and the dimensionless cutoff radius is $r_{cw} = 1.26$. While the mathematical expression of Eq. (3) is similar to the first term in Eq. (1), d_w in Eq. (3) is not an interatomic distance, it represents the distance between an atom and a plane parallel to the nearest surface of the film. The distance between this plane and the surface atoms is initially set at $d_w = 0.264$ nm [39]. The force on atom i due to the surface potential is given by

$$\mathbf{F}_w = \phi_w \cdot \left(\frac{p}{d_w} + \frac{\sigma}{(d_w - \sigma r_{cw})^2}\right) \cdot n \tag{4}$$

where n is the unit vector perpendicular to the reference plane. The scalar quantities in Eq. (4) are always positive and, therefore, the unit vector determines the direction of the force. In order to result in an inward pressure that simulates the effect of a surrounding gas, the unit vector always points into the film.

Green-Kubo Relation for Determining Thermal Conductivity. To determine the thermal conductivity, equilibrium molecular dynamics uses the Green-Kubo relation between the thermal conductivity and the heat current autocorrelation function $J(\tau) \cdot J(0)$ [56–58]

$$k_{MD} = \frac{1}{nVk_BT_{MD}^2} \int_0^\infty \langle J(\tau) \cdot J(0) \rangle d\tau \tag{5}$$

where k_{MD} is the thermal conductivity; V is the ensemble volume; T_{MD} is the ensemble average temperature; k_B is Boltzmann's constant; n is the dimensionality (3 for bulk, 2 for the in-plane directions and 1 for the out-of-plane direction); J is the heat current; and the integrant is the ensemble average of the heat current autocorrelation function. The in-plane thermal conductivity is given by the average of the two in-plane components of the heat current, while the orthogonal component gives the out-of-plane thermal conductivity. The heat current is given by [56,58,59]

$$J = \frac{\partial}{\partial t}\left(\sum_i r_i . E_i\right) \tag{6}$$

where the total energy E_i is the sum of the kinetic and potential energies of atom i.

Replacing the integral in Eq. (6) by a sum over equal-size time steps Δt, the thermal conductivity becomes

$$k_{MD}(\tau_{MD}) = \frac{\Delta t}{nVk_BT_{MD}^2} \sum_{m=1}^M \frac{1}{N_s - m} \sum_{n=1}^{N_s - m} J(m+n) \cdot J(n) \tag{7}$$

where N_s is the number of heat current autocorrelation function averages; M is the number of time steps required for the heat current autocorrelation function to decay to zero; and τ_{MD} is the integration time [38,43]. The simulations are stabilized for 100,000 molecular dynamics steps, during which the temperature is scaled every ten time steps. The neighbor list [43] is updated every 25 time steps.

Computational Domain. The thermal conductivities of silicon thin films are predicted for film thicknesses ranging from 2.2 to 217.2 nm (corresponding to 4 to 400 silicon lattice constants in the out-of-plane direction). The simulation domain cross-section consists of 2×2 lattice constants in the in-plane directions, with periodic boundary conditions. The choice of this small cross-

section is justified by the observation that the predicted thermal conductivity is independent of the number of lattice constants used in the simulation domain cross-section, for simulation cross sections between 2×2 and 10×10 lattice constants, at 300 and 1000 K. For example, simulations of a 4.3 nm film at 300 K yielded in-plane thermal conductivities of 32 and 38 ± 4 W/mK for cross-sections of 2×2 and 10×10 lattice constants, respectively.

Quantum Corrections. The temperature of the molecular dynamics simulation (T_{MD}) is set at the beginning of the simulation by scaling the atomic velocities according to the classical statistical mechanics equipartition theorem [60]

$$\frac{3}{2}Nk_BT_{MD} = \frac{1}{2}\sum_{i=1}^N m_i v_i \cdot v_i \tag{8}$$

where N is the number of atoms in the ensemble and v_i is the velocity of atom i.

Since molecular dynamics is a classical method, quantum corrections must be applied to the MD predicted thermal conductivity and to the temperature given by Eq. (8) at temperatures below the Debye temperature (θ_D), where, for a solid, quantum effects start to become important. Quantum corrections can be estimated by equating the ensemble's total energy to the phonons' total energy [15,42,45] as

$$3Nk_BT_{MD} = \sum_i \left(f_{\omega_i}^0 + \frac{1}{2}\right)\hbar\omega_i \tag{9}$$

where ω is the phonon's frequency and $f_{\omega_i}^0$ is the equilibrium phonon distribution function, given by the Bose-Einstein distribution function. The summation is over the phonons' frequencies and branches. The quantum energy of a system includes the zero-point energy, the factor $\frac{1}{2}\hbar\omega$ in Eq. (9). In this study, we have included this factor, because our objective is to correct the classical energy (left hand side of Eq. (9)), and obtain the quantum one (right hand side of Eq. (9)). Quantum-correction factors can be estimated as [15]

$$\frac{k}{k_{MD}} = \frac{\partial T_{MD}}{\partial T} \tag{10}$$

where k_{MD}, T_{MD}, k, and T are the MD predicted thermal conductivity, the temperature of the simulation, and the quantum-corrected thermal conductivity and temperature, respectively. Since the derivative with respect to the temperature of the energy is the specific heat C, Eqs. (9) and (10) become

$$\frac{k}{k_{MD}} = \frac{\partial T_{MD}}{\partial T} = \frac{C}{3Nk_B} \tag{11}$$

and the correction factors can be taken from the reported experimental specific heat for silicon [61,62]. The correction factors for the temperature are obtained by integrating Eq. (11).

Equation (9) can also be solved analytically, assuming that the medium is isotropic, the first Brillouin zone is approximated by a sphere, and the number of atoms is large enough so that the dispersion relation can be treated as a continuum curve. The dispersion relation for silicon is calculated from the Stillinger Weber potential [63]. Table 1 lists the temperature of the molecular dynamics simulation (T_{MD}), the corrected temperatures (T_c and T_a) and thermal conductivity correction factors (k_c/k_{MD} and k_a/k_{MD}), determined from the experimental silicon specific heat [61,62], and analytically, respectively. Table 1 shows that, for $T < \theta_D$ (with $\theta_D \sim 625$ K for silicon [64]), T and k depend on the quantum correction scheme selected; while for $T > \theta_D$, where the system behaves classically, these corrections are negligible.

All MD predicted thermal conductivities reported in this paper

Table 1 Temperature of the molecular dynamics simulation (T_{MD}), and quantum correction factors determined from the experimental specific heat (T_c and k_c) and analytically (T_a and k_a)

T_{MD}	T_c	T_a	k_c/k_{MD}	k_a/k_{MD}
300	248	140	0.72	0.40
400	375	305	0.85	0.75
500	480	430	0.91	0.85
700	700	650	0.94	0.93
1000	1000	970	0.99	0.97

Fig. 2 (*a*) Starting configuration of the atoms located on the surface of a film consisting of 10×10 lattice constants in the cross-section, and eight lattice constants (4.34 nm) thickness. (*b*) Surface reconstruction after 100,000 steps of molecular dynamics, showing the individual dimes oriented in the [110] crystallographic direction and the group of dimes aligned in the [1 1̄ 0] direction.

are corrected according to the experimental specific heat, thus avoiding the mathematical approximations of the analytical method.

Results and Discussion

Our molecular dynamics simulations show that the atomic positions near the surfaces depend on the applied boundary conditions: The addition of a surface potential to the Stillinger Weber potential of the atoms near the surface, addition of a layer of frozen atoms, or free boundaries. It has been experimentally observed that when a free surface is formed, the atoms on the surface rearrange themselves in order to minimize the number of dangling bonds. MD simulations using either the surface potential or free boundaries allow this reconfiguration of the atoms on the surfaces. However, when the film is limited by four layers of frozen atoms, no surface reconstruction can take place. Figure 2(*a*) shows the starting configuration of the silicon atoms on the surface layer, with the atoms in the crystallographic face centered cube locations. Figure 2(*b*) shows the same layer after several steps of molecular dynamics, performed using either the surface potential or free boundaries. The silicon atoms have spontaneously rearranged to form dimes aligned in the [110] crystallographic direction. The distance between the atoms in a dime is 2.4 Å, in close agreement with experimental observations [65] and previous theoretical studies of Si surfaces [48,49,66].

The different boundary conditions also affect the atomic vibrations of several atomic layers below the surfaces. These vibrations are analyzed by means of the two-dimensional radial distribution function $g(r)$, which depends on the relative atomic distances as

$$g(r) = \frac{1}{N \cdot N_{atoms} \cdot N_s} \sum_{s=1}^{N_s} \sum_{j=1}^{N_{atoms}-1} \sum_{k=j+1}^{N_{atoms}}$$
$$\times \left\{ \begin{array}{ll} 2 & \text{if } |\sqrt{(x_j^{(s)} - x_k^{(s)})^2 + (y_j^{(s)} - y_k^{(s)})^2} - r| < \text{binwidth} \\ 0 & \text{otherwise} \end{array} \right\}$$

(12)

where N_s is the number of samples from the molecular dynamics simulation, N_{atoms} is the number of atoms in a layer, N is the number of atoms in the crystal structure occupying the same bin area, and binwidth is the width of the bin at the radial distance r. The distribution function is computed using 2000 bins of width 0.0027 nm. Figure 3 shows the two-dimensional radial distribution function of the first four layers of a film consisting of 7×7×8 lattice constants (d_s=4.3 nm), simulated at 1000 K using periodic boundary conditions in the in-plane direction and different boundary conditions in the out-of-plane direction (i.e., surface potential, atoms kept frozen or free boundaries). The first layer in the case of frozen atoms refers to the first atomic layer of atoms not kept frozen, and to the film surface in the case of the other two boundary conditions studied. Large differences are observed in the atomic distribution of the atoms on the first atomic layer (Fig. 3(*a*)). When the film is limited by a layer of frozen atoms, the in-plane mobility of the first layer of nonfrozen atoms is strongly altered, and the atoms remain, in average, at their crystallographic equilibrium positions. Very similar amplitudes of vibrations (as

seen by the width of the peaks in Fig. 3(*a*)) and atomic positions are observed on the surface layers for both the surface potential and the free boundaries. These two boundary conditions result in a peak at 0.24 nm, corresponding to the interatomic distance between the dimes on the reconstructed surface. This peak is absent for the frozen atoms boundary conditions, because no surface reconstruction takes place, and the first atomic position occurs at 0.38 nm, corresponding to the atoms centered on the cube face. Free boundaries and surface potential predict identical radial distributions for the second, third, and fourth layers, while differences in the amplitudes of vibration are observed with the frozen boundary conditions even for the second and third atomic layers. On the fourth atomic layer, (Fig. 3(*d*)), the amplitude of vibrations and atomic positions become independent of the boundary conditions investigated.

The MD predicted in-plane thermal conductivities are shown in Fig. 4 for T_{MD}=400 K, for the three surface boundary conditions studied. It is seen that similar thermal conductivities are predicted with the three boundary conditions, except for very small film thicknesses. When the film thickness is smaller than approximately 10 nm (shown as an inset in Fig. 4), the thermal conductivities predicted using the surface potential or free boundaries follow the experimentally observed trend of decreasing thermal conductivity with decreasing film thickness, while those calculated with frozen atoms do not. Adding a few layers of atoms kept frozen decreases the amplitude of vibrations of the atoms located near the frozen atoms (as shown in Fig. 3), suggesting a stronger harmonic component of the potential, which would result in an increase of the thermal conductivity. Similar results are obtained at 1000 K. No differences between the three surface treatments are observed for the out-of-plane thermal conductivity.

Since the molecular dynamics simulations using the surface potential or free boundaries predict similar thermal conductivities, we next report only the results obtained using the surface potential. The MD predicted thermal conductivities are shown for T_{MD}=400 and 1000 K (Fig. 5), as a function of film thickness. The experimental bulk thermal conductivities [67] corresponding to the quantum-corrected temperatures T_c=375 and 1000 K are shown as dashed lines. It is seen that both the in-plane and out-of-plane thermal conductivities are affected by the thickness of the film. For thicknesses smaller than the phonon mean free path (approximately 300 and 30 nm at 300 and 1000 K, respectively), both the in-plane and out-of-plane thermal conductivities decrease with decreasing thickness, an effect attributed to the scattering of phonons with the boundaries of the thin film. This effect is more pronounced in the out-of-plane direction, where the dimensions of
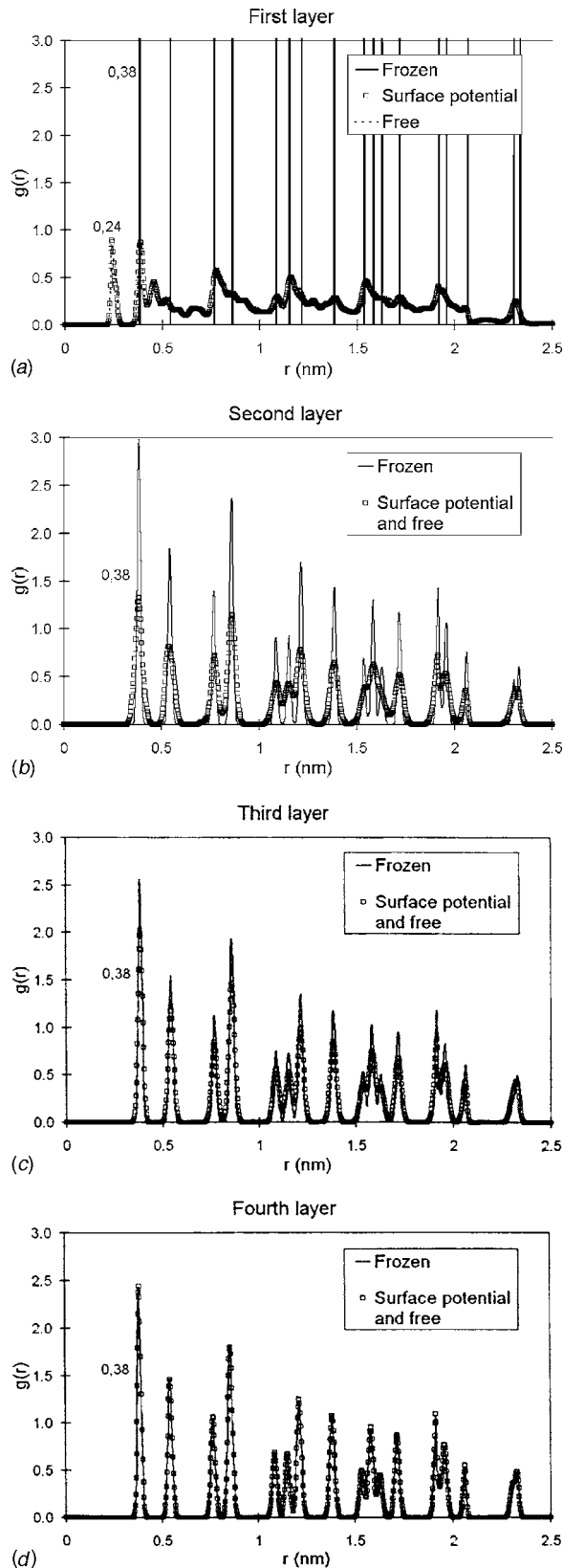
Fig. 3 Radial distribution functions of the atoms located on the first four layers of a film consisting of $7 \times 7 \times 8$ lattice constants, for the different boundary conditions used

Fig. 4 MD predicted in-plane thermal conductivity at T_{MD} =400 K as a function of film thickness, for the three boundary conditions simulated: Addition of a surface potential (□), frozen atoms (○), and free boundaries (△)

the bulk value. The bulk thermal conductivity value is reached at smaller thicknesses at 1000 K, due to the smaller phonon mean free path at this temperature.

Figure 6 shows the MD predicted in-plane thermal conductivities at T_{MD}=400 K, as a function of film thickness. We performed three different MD simulations for each thickness, starting with different initial atomic velocities, from which the average thermal conductivity and the statistical deviations, shown in Fig. 6, are calculated. The temperature of the simulations is 400 K, which, quantum corrected according to Table 1, corresponds to T_c =375 K or T_a=305 K. The MD predicted thermal conductivities are corrected according to the experimental specific heat reported in Table 1; however, the exact value of T and k will depend on the quantum correction scheme used. The MD results are compared to the available experimental data at 300 K [12–14]. It is seen that the MD predictions, while reproducing the observed experimental trend of decreasing thermal conductivity with decreasing film thickness, are higher than the experimental results. The discrepancy increases for film thicknesses smaller than approximately 75 nm. This discrepancy might be a consequence of quantum effects, not captured by classical MD, and not appropriately corrected by the quantum correction factors used in this study. These

the thin film make the phonon transport ballistic. At large thicknesses $(d_s > \Lambda)$, corresponding to diffusive regimes, the in-plane and out-of-plane thermal conductivities asymptotically approach

Fig. 5 MD predicted thermal conductivities: In-plane (■) and out-of-plane (□) at T_{MD}=400 K, and in-plane (●) and out-of-plane (○) at T_{MD}=1000 K, as a function of film thickness d_s. Experimental bulk silicon thermal conductivities at 375 and 1000 K are shown as dashed lines [67].
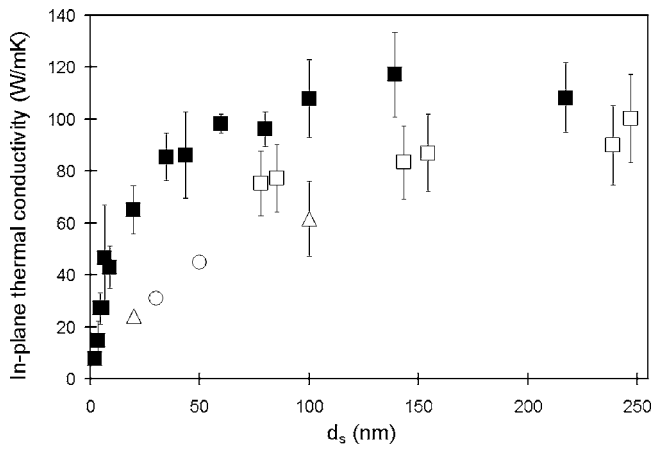
Fig. 6 In-plane silicon thermal conductivity predicted by molecular dynamics at T_{MD}=400 K (■), and experimental data at 300 K: (□) [12], (△) [13], and (○) [14]

effects are expected to be higher at temperatures below the Debye's temperature, and for small film thicknesses. Other sources of discrepancy may include the interatomic potential used in the MD simulations.

The predicted out-of-plane thermal conductivities are shown in Fig. 7 for temperatures ranging from T_{MD}=300 to 1000 K, for film thicknesses up to 217 nm, and as an inset, up to 14 nm. It is seen that for small thicknesses (smaller than the smallest mean free path, approximately 30 nm at 1000 K) the out-of-plane thermal conductivity varies linearly with the thickness of the film, and is almost independent of the temperature. These results are consistent with the expression for the thermal conductivity deduced from kinetic theory [60]

$$k = \frac{1}{3}Cv\Lambda \tag{13}$$

where k is the thermal conductivity, C is the specific heat, v is the phonon group velocity, and Λ is the phonon mean free path. In the ballistic limit, the predominant collision mechanism is the scattering of phonons with the boundaries of the film, and the phonon mean free path becomes of the order of the film thickness, d_s. At the temperatures studied, the silicon specific heat varies only slightly with temperature, decreasing a maximum of 30% for T_{MD}=300 K. Therefore, the out-of-plane thermal conductivity is almost independent of the temperature until the film is thick enough for scattering among phonons to become relevant. This
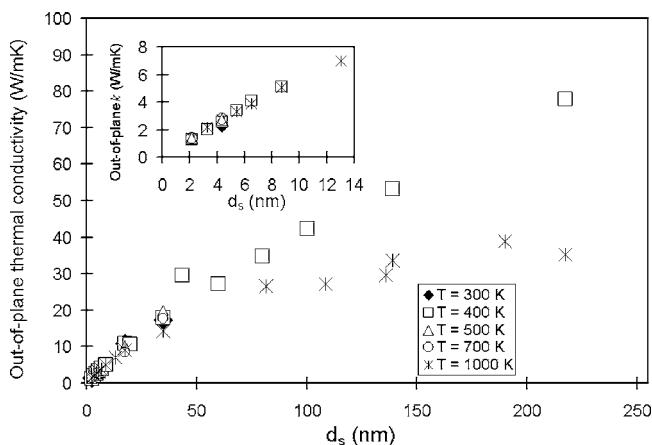
Fig. 7 Out-of-plane thermal conductivity versus film thickness at different temperatures T_{MD}, for film thicknesses up to 217 nm, and in the insert, for film thicknesses up to 14 nm

limit is reached faster at 1000 K, because of the shorter phonon mean free path (30 nm at 1000 K). Even though the transport in the thin film limit is ballistic, the predicted out-of-plane thermal conductivities are consistent with the predictions from kinetic theory, Eq. (13), which assumes local equilibrium. Indeed, it has been recently shown that, in the ballistic regime at $T \ll \theta_D$, the thermal conductivity developed from the phonon radiative transfer equations reduces to that given by the kinetic theory (Eq. (13)), if Λ is replaced by an effective phonon mean free path Λ_{eff} given by [68]
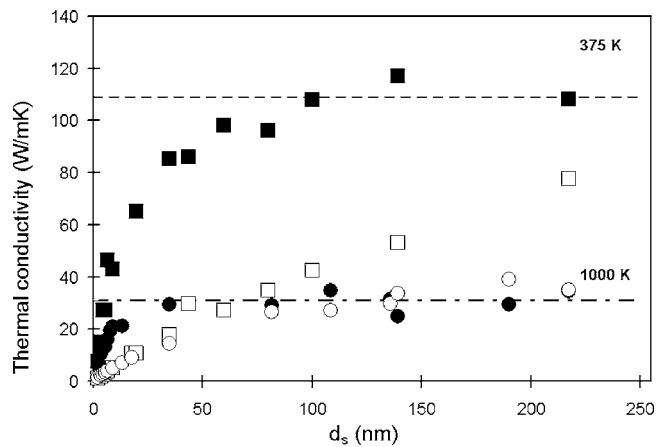
$$\Lambda_{eff} = \frac{\Lambda}{1 + \dfrac{4\Lambda}{3d_s}} \tag{14}$$

Our results indicate that Eqs. (13) and (14) are also valid in the limit $\Lambda \gg d_s$ at $T \geq \theta_D$.

Conclusions

Using equilibrium molecular dynamics, we have studied the thermal conductivity of silicon thin films in a broad range of film thicknesses (2 nm < d_s < 217 nm) and temperatures (300 K < T < 1000 K), spanning from the ballistic to the diffusive phonon transport regimes. Three different boundary conditions are used to treat the atoms on the surfaces of the thin films: The addition of four layers of atoms kept frozen at their crystallographic positions, the addition of a surface potential to the atoms located near the surfaces, and free boundary conditions. Differences in the thermal conductivity between the three boundary conditions are predicted only for the in-plane thermal conductivity of very thin films (d_s < 10 nm).

For film thicknesses much larger than the phonon mean free path, the molecular dynamics predicted in-plane and out-of-plane thermal conductivities asymptotically approach the experimentally determined bulk value. This limit is reached faster at the highest temperature investigated (1000 K), because of the smaller phonon mean free path at this temperature. As the film thickness becomes comparable to the phonon mean free path, the in-plane and out-of-plane thermal conductivities differ from each other. Molecular dynamics simulations performed with the addition of a surface potential or with free boundaries both predict similar thermal conductivities. Comparisons of the in-plane thermal conductivity with the available experimental data at 300 K show that these predictions follow the experimentally observed trend of decreasing thermal conductivity with decreasing film thickness. Simulations performed adding four layers of frozen atoms do not reproduce the observed experimental trend for thicknesses d_s < 10 nm, because the presence of frozen atoms alters the vibrations of the neighboring atoms.

The reduction of the thermal conductivity with film thickness is more pronounced in the out-of-plane direction and at low temperature (T_{MD}=400 K). In the ballistic limit ($\Lambda \gg d_s$) the probability of scattering among phonons becomes negligible compared to the probability of collisions of the phonons with the boundaries of the film. In this limit, the out-of-plane thermal conductivity depends linearly on the film's thickness and is independent of temperature, for temperatures T_{MD} between 400 and 1000 K. These results are in agreement with predictions from the kinetic theory [60] and the equation for phonon radiative transfer [68]. According to these theories, when the phonon mean free path is limited by the scattering with the boundaries of the film, the thermal conductivity becomes proportional to an effective mean free path, which is of the order of the film thickness. The temperature dependence of the thermal conductivity is given mainly by the specific heat, which is almost constant for T=400–1000 K (the temperature of Debye for silicon is $\theta_D \sim 625$ K). Our results for the out-of-plane thermal conductivity show the broad application of

the kinetic theory (which is derived for diffusion and assumes local equilibrium) and the phonon radiative theory (derived for $T \ll \theta_D$) in the range $\Lambda \ll d_s$ and $T \geq \theta_D$.

Our results show that equilibrium molecular dynamics and the Green-Kubo formalism allow the prediction of the in-plane and out-of-plane thermal conductivities of silicon thin films in a wide range of film thicknesses and temperatures. These results are relevant for predictions of the thermal performance of devices with nano-sized thin films, such as silicon-on-insulator and strained silicon transistors.

Acknowledgment

Nomenclature

d_w = distance between an atom and the surface potential reference plane, nm
d_s = thin film thickness, nm
E_i = total energy of atom i, J
F_w = force on an atom due to the surface potential, N
f_ω^0 = equilibrium phonon distribution function
$g(r)$ = radial distribution function
J = heat current, J/m^2
k = thermal conductivity, W/(mK)
k_B = Boltzmann's constant, 1.3807×10^{-23} J/K
k_{MD} = MD predicted thermal conductivity, W/(mK)
n = unit vector perpendicular to the reference plane
r_{ij} = relative distance between atoms i and j, nm
r_c, r_{cw} = cutoff radius for the Stillinger Weber potential and the surface potential, respectively.
T_{MD} = temperature of the MD simulation, K
V = volume, m^3
v = phonon group velocity, m/s
v_i = velocity of atom i, m/s

Greek symbols

ε_w = surface potential scaling factor, J
ϕ_2 = two-body term of the SW potential, J
ϕ_3 = three-body term of the SW potential, J
ϕ_w = surface potential, J
Λ = phonon mean free path, nm
θ_D = Debye's temperature, K

References

[1] *International Technology Roadmap for Semiconductors*, 2005, http://public.itrs.net.
[2] Cahill, D. G., Ford, W. K., Goodson, K. E., Mahan, G. D., Majumdar, A., Maris, H. J., Merlin, R., and Phillpot, S. R., 2003, "Nanoscale Thermal Transport," J. Appl. Phys., **93**(2), pp. 793–818.
[3] Li, D., Huxtable, S. T., Abramson, A. R., and Majumdar, A., 2005, "Thermal Transport in Nanostructured Solid-State Cooling Devices," ASME J. Heat Transfer, **127**, pp. 108–114.
[4] Yang, R., Chen, G., Laroche, M., and Taur, Y., 2005, "Simulation of Nanoscale Multidimensional Transient Heat Conduction Problems Using Ballistic-Diffusive Equations and Phonon Boltzmann Equation," ASME J. Heat Transfer, **127**, pp. 298–306.
[5] Srivastava, G. P., 1990, *The Physics of Phonons*, A. Hilger, New York, pp. 175–178.
[6] Hone, J., Llaguno, M. C., Biercuk, M. J., Johnson, A. T., Batlogg, B., Benes, Z., and Fischer, J. E., 2002, "Thermal Properties of Carbon Nanotubes and Nanotube-Based Materials," Appl. Phys. A, **A74**(3), pp. 339–343.
[7] Dresselhaus, M. S., Dresselhaus, G., Charlier, J. C., and Hernandez, E., 2004, "Electronic, Thermal and Mechanical Properties of Carbon Nanotubes," Philos. Trans. R. Soc. London, Ser. A, **362**(1823), pp. 2065–2098.
[8] Zhong, H., and Lukes, J. R., "Thermal Conductivity of Single-Wall Carbon Nanotubes," *Proc. ASME International Mechanical Engineering Congress and Exposition*, Anaheim, CA., IMECE2004-61665.
[9] Volz, S. G., and Chen, G., 1999, "Molecular Dynamics Simulation of Thermal Conductivity of Silicon Nanowires," Appl. Phys. Lett., **75**(14), pp. 2056–2058.
[10] Li, D., Wu, Y., Kim, P., Shi, L., Yang, P., and Majumdar, A., 2003, "Thermal Conductivity of Individual Silicon Nanowires," Appl. Phys. Lett., **83**(14), pp. 2934–2936.
[11] Li, D., Wu, Y., Fan, R., Yang, P., and Majumdar, A., 2003, "Thermal Conductivity of Si/SiGe Superlattice Nanowires," Appl. Phys. Lett., **83**(15), pp. 3186–3188.
[12] Ju, Y. S., and Goodson, K. E., 1999, "Phonon Scattering in Silicon Thin Films with Thickness of Order 100 nm," Appl. Phys. Lett., **74**(20), pp. 3005–3007.
[13] Liu, W., and Asheghi, M., 2004, "Phonon-Boundary Scattering in Ultrathin Single-Crystal Silicon Layers," Appl. Phys. Lett., **84**(19), pp. 3819–3821.
[14] Liu, W., and Asheghi, M., "Thermal Conductivity in Ultra-Thin Pure and Doped Single Crystal Silicon Layers at High Temperatures," *Proc. ASME Summer Heat Transfer Conference*, San Francisco, CA., HT2005-72540.
[15] Volz, S., Saulnier, J. B., Chen, G., and Beauchamp, P., 2000, "Computation of Thermal Conductivity of Si/Ge Superlattice by Molecular Dynamics Technique," Microelectron. J., **31**(9–10), pp. 815–819.
[16] Abramson, A. R., Tien, C.-L., and Majumdar, A., 2002, "Interface and Strain Effects on the Thermal Conductivity of Heterostructures: A Molecular Dynamics Study," ASME J. Heat Transfer, **124**(5), pp. 963–970.
[17] Daly, B. C., and Maris, H. J., 2002, "Calculation of the Thermal Conductivity of Superlattices by Molecular Dynamics Simulation," Physica B, **316–317**, pp. 247–249.
[18] Asheghi, M., Touzelbaev, M. N., Goodson, K. E., Leung, Y. K., and Wong, S. S., 1998, "Temperature-Dependent Thermal Conductivity of Single-Crystal Silicon Layers in SOI Substrates," ASME J. Heat Transfer, **120**, pp. 30–36.
[19] Liu, W., and Asheghi, M., "Thermal Conductivity of Ultra Thin Single Crystal Silicon Layers, Part 1—Experimental Measurements at Room and Cryogenic Temperatures," *Proc. ASME International Mechanical Engineering Congress and Exposition*, Anaheim, CA., IMECE2004-62105.
[20] Majumdar, A., Fushinobu, K., and Hijikata, K., 1995, "Effect of Gate Voltage on Hot-Electron and Hot-Phonon Interaction and Transport in a Submicrometer Transistor," J. Appl. Phys., **77**(12), pp. 6686–6694.
[21] Fushinobu, K., Majumdar, A., and Hijikata, K., 1995, "Heat Generation and Transport in Submicron Semiconductor Devices," ASME J. Heat Transfer, **117**, pp. 25–31.
[22] Lai, J., and Majumdar, A., 1996, "Concurrent Thermal and Electrical Modeling of Sub-Micrometer Silicon Devices," J. Appl. Phys., **79**(9), pp. 7353–7361.
[23] Narumanchi, S. V. J., Murthy, J. Y., and Amon, C. H., 2003, "Simulation of Unsteady Small Heat Source Effects in Sub-Micron Heat Conduction," ASME J. Heat Transfer, **125**(5), pp. 896–903.
[24] Narumanchi, S. V. J., Murthy, J. Y., and Amon, C. H., 2004, "Submicron Heat Transport Model in Silicon Accounting for Phonon Dispersion and Polarization," ASME J. Heat Transfer, **126**, pp. 946–955.
[25] Amon, C. H., Ghai, S. S., Kim, W. T., and Jhon, M. S., 2006, "Modeling of Nanoscale Transport Phenomena: Application to Information Technology," Physica A, **362**, pp. 36–41.
[26] Escobar, R. A., Smith, B., and Amon, C. H., 2006, "Lattice Boltzmann Modeling of Subcontinuum Energy Transport in Crystalline and Amorphous Microelectronic Devices," ASME J. Electron. Packag., **128**(2), pp. 115–124.
[27] Escobar, R. A., Ghai, S. S., Jhon, M. S., and Amon, C. H., 2006, "Multi-Length and Time Scale Thermal Transport Using the Lattice Boltzmann Method With Applications to Electronics Cooling," Int. J. Heat Mass Transfer, **49**, pp. 97–107.
[28] Ghai, S. S., Kim, W. T., Escobar, R., Amon, C. H., and Jhon, M. S., 2005, "A Novel Heat Transfer Model and Its Application to Information Storage Systems," J. Appl. Phys., **97**, pp. 10P703-1–3.
[29] Narumanchi, S. V. J., Murthy, J. Y., and Amon, C. H., 2005, "Comparison of Different Phonon Transport Models for Predicting Heat Conduction in Silicon-on-Insulator Transistors," ASME J. Heat Transfer, **127**(7), pp. 713–723.
[30] Narumanchi, S. V. J., Murthy, J. Y., and Amon, C. H., 2006, "Boltzmann Transport Equation-Based Thermal Modeling Approaches for Hotspots in Microelectronics," Heat Mass Transfer, **42**(6), pp. 478–491.
[31] Klitsner, T., VanCleve, J. E., Fischer, H. E., and Pohl, R. O., 1988, "Phonon Radiative Heat Transfer and Surface Scattering," Phys. Rev. B, **38**, pp. 7576–7594.
[32] Peterson, R. B., 1994, "Direct Simulation of Phonon-Mediated Heat Transfer in a Debye Crystal," ASME J. Heat Transfer, **116**, pp. 815–822.
[33] Mazumder, S., and Majumdar, A., 2001, "Monte Carlo Study of Phonon Transport in Solid Thin Films Including Dispersion and Polarization," ASME J. Heat Transfer, **123**, pp. 749–759.
[34] Chen, Y., Li, D., Lukes, J., and Majumdar, A., 2005, "Monte Carlo Simulation of Silicon Nanowire Thermal Conductivity," ASME J. Heat Transfer, **127**, pp. 1129–1137.
[35] Li, J., Porter, L. J., and Yip, S., 1998, "Atomistic Modeling of Finite-Temperature Properties of Crystalline β-SiC. II. Thermal Conductivity and Effects of Point Defects," J. Nucl. Mater., **255**, pp. 139–152.
[36] Lukes, J. R., Li, D. Y., Liang, X.-G., and Tien, C.-L., 2000, "Molecular Dy-

namics Study of Solid Thin-Film Thermal Conductivity," ASME J. Heat Transfer, **122**, pp. 536–543.

[37] Volz, S. G., and Chen, G., 2000, "Molecular-Dynamics Simulation of Thermal Conductivity of Silicon Crystals," Phys. Rev. B, **61**(4), pp. 2651–2656.

[38] Schelling, P. K., Phillpot, S. R., and Keblinski, P., 2002, "Comparison of Atomic-Level Simulation Methods for Computing Thermal Conductivity," Phys. Rev. B, **65**, pp. 144306.

[39] Gomes, C. J., Madrid, M., and Amon, C. H., "Thin Film In-Plane Thermal Conductivity Dependence on Molecular Dynamics Surface Boundary Conditions," *Proc. ASME International Mechanical Engineering Congress and Exposition*, Anaheim, CA, IMECE2004-62264.

[40] McGaughey, A. J. H., and Kaviany, M., 2004, "Thermal Conductivity Decomposition and Analysis Using Molecular Dynamics Simulations. Part II. Complex Silica Structures," Int. J. Heat Mass Transfer, **47**, pp. 1799–1816.

[41] Che, J., Cagin, T., Deng, W., and Goddard, W. A., 2000, "Thermal Conductivity of Diamond and Related Materials From Molecular Dynamics Simulations," J. Chem. Phys., **113**(16), pp. 6888–6900.

[42] Volz, S. G., and Chen, G., 1999, "Lattice Dynamic Simulation of Silicon Thermal Conductivity," Physica B, **263–264**, pp. 709–712.

[43] Gomes, C. J., Madrid, M., and Amon, C. H., "Parallel Molecular Dynamics Code Validation Through Bulk Silicon Thermal Conductivity Calculations," *Proc. ASME International Mechanical Engineering Congress and Exposition*, Washington, DC., IMECE2003-42352.

[44] Che, J., Cagin, T., and Goddard, W. A., III, 2000, "Thermal Conductivity of Carbon Nanotubes," Nanotechnology, **11**, pp. 65–69.

[45] Lee, Y. H., Biswas, R., Soukoulis, C. M., Wang, C. Z., Chan, C. T., and Ho, K. M., 1991, "Molecular-Dynamics Simulation of Thermal Conductivity in Amorphous Silicon," Phys. Rev. B, **43**(8), pp. 6573–6580.

[46] Ding, K., and Andersen, H. C., 1986, "Molecular-Dynamics Simulation of Amorphous Germanium," Phys. Rev. B, **34**(10), pp. 6987–6991.

[47] Feng, X.-L., Li, D., and Guo, Z.-Y., 2003, "Molecular Dynamics Simulation of Thermal Conductivity of Nanoscale Thin Silicon Films," Microscale Thermophys. Eng., **7**, pp. 153–161.

[48] Weakliem, P. C., and Carter, E. A., 1992, "Constant Temperature Molecular Dynamics Simulations of Si(100) and Ge(100): Equilibrium Structure and Short-Time Behavior," J. Chem. Phys., **96**(4), pp. 3240–3250.

[49] Yu, Q., and Clancy, P., 1994, "Molecular Dynamics Simulation of the Surface Reconstruction and Strain Relief in $Si_{1-x}Ge_x$/Si(100) Heterostructures," Modell. Simul. Mater. Sci. Eng., **2**, pp. 829–844.

[50] Chantrenne, P., and Barrat, J.-L., 2004, "Finite Size Effects in Determination of Thermal Conductivities: Comparing Molecular Dynamics Results With Simple Models," ASME J. Heat Transfer, **126**, pp. 577–585.

[51] Stillinger, F. H., and Weber, T. A., 1985, "Computer Simulation of Local Order in Condensed Phases of Silicon," Phys. Rev. B, **31**(8), pp. 5262–5271.

[52] Broughton, J. Q., and Li, X. P., 1987, "Phase Diagram of Silicon by Molecular Dynamics," Phys. Rev. B, **35**(17), pp. 9120–9127.

[53] Cook, S. J., and Clancy, P., 1993, "Comparison of Semi-Empirical Potential Functions for Silicon and Germanium," Phys. Rev. B, **47**(13), pp. 7686–7699.

[54] Karimi, M., Yates, H., Ray, J. R., Kaplan, T., and Mostoller, M., 1998, "Elastic Constants of Silicon Using Monte Carlo Simulations," Phys. Rev. B, **58**(10), pp. 6019–6025.

[55] Kallman, J. S., Hoover, W. G., Hoover, C. G., Groot, A. J. D., Lee, S. M., and Wooten, F., 1993, "Molecular Dynamics of Silicon Indentation," Phys. Rev. B, **47**(13), pp. 7705–7709.

[56] Allen, M. P., and Tildesley, D. J., 1987, *Computer Simulation of Liquids*, Clarendon Press, Oxford, UK, pp. 61–62.

[57] Frenkel, D., and Smit, B., 2001, *Understanding Molecular Simulation: From Algorithms to Applications*, Academic, San Diego, CA., p. 90.

[58] McQuarrie, D. A., 1976, *Statistical Mechanics*, University Science Books, Sausalito, CA., p. 521.

[59] Hardy, R. J., 1963, "Energy-Flux Operator for a Lattice," Phys. Rev., **132**(1), pp. 168–177.

[60] Reif, F., *Fundamentals of Statistical and Thermal Physics*, McGraw-Hill, New York, pp. 480–483.

[61] Flubacher, P., Leadbetter, A. J., and Morrison, J. A., 1959, "Heat Capacity of Pure Silicon and Germanium and Properties of Their Vibrational Frequency Spectra," Philos. Mag., **4**(39), pp. 273–294.

[62] Desai, P. D., 1986, "Thermodynamic Properties of Iron and Silicon," J. Phys. Chem. Ref. Data, **15**(3), pp. 967–983.

[63] Porter, L. J., Justo, J. F., and Yip, S., 1997, "The Importance of Gruneisen Parameters in Developing Interatomic Potentials," J. Appl. Phys., **82**, pp. 5378–5381.

[64] Ashcroft, N. W., and Mermin, N. D., 1976, *Solid State Physics*, Holt, Rinehart and Winston, New York, p. 461.

[65] Aono, M., Hou, Y., Oshima, C., and Ishizawa, Y., 1982, "Low-Energy Ion Scattering From the Si(001) Surface," Phys. Rev. Lett., **49**, pp. 567–570.

[66] Yang, W. S. F., Jona, F., and Marcus, P. M., 1983, "Atomic Structure of Si{001}2×1," Phys. Rev. B, **28**(4), pp. 2049–2059.

[67] Ho, C. Y., Powell, R. W., and Liley, P. E., 1972, "Thermal Conductivity of the Elements," J. Phys. Chem. Ref. Data, **1**(2), pp. 279–421.

[68] Majumdar, A., 1993, "Microscale Heat Conduction in Dielectric Thin Films," ASME J. Heat Transfer, **115**, pp. 7–16.

Turbulent Heat Transfer in an Enclosure With a Horizontal Permeable Plate in the Middle

Edimilson J. Braga

Marcelo J. S. de Lemos[1]
Mem. ASME
e-mail: delemos@ita.br

Departamento de Energia—IEME,
Instituto Tecnológico de Aeronáutica—ITA,
12228-900, São José dos Campos, SP,
Brazil

Turbulent natural convection in a vertical two-dimensional square cavity, isothermally heated from below and cooled at the upper surface, is numerically analyzed using the finite volume method. The enclosure has a thin horizontal porous obstruction, made of a highly porous material and extremely permeable, located at the cavity midheight. Governing equations are written in terms of primitive variables and are recast into a general form. For empty cavities, no discrepancies result for the Nusselt number when laminar and turbulent model solutions are compared for Rayleigh numbers up to 10^7. Also, in general the porous obstruction decreases the heat transfer across the heated walls showing overall lower Nusselt numbers when compared with those without the porous obstruction. However, the presence of a porous plate in the cavity seems to force an earlier separation from laminar to turbulence model solutions due to higher generation rates of turbulent kinetic energy into the porous matrix. [DOI: 10.1115/1.2352779]

Keywords: turbulence, porous media, heat transfer, natural convection

1 Introduction

The analysis of buoyancy-driven flows in an enclosed cavity provides useful comparisons for evaluating the robustness and performance of numerical methods dealing with viscous flow calculations. The importance of the enclosure natural-convection phenomena can best be appreciated by noting several of their application areas. Nuclear reactor safety, heat exchangers, underground spread of pollutants, environmental control, grain storage, food processing, material processing, geothermal systems, oil extraction, store of nuclear waste material, solar power collectors, optimal design of furnaces, crystal growth in liquids, and packed-bed catalytic reactors are some examples of applications of heat removal or addition by free convection mechanism.

The study of natural convection in enclosures still attracts the attention of researchers and a significant number of experimental and theoretical works have been carried out mainly from the 1970s. During the conference on Numerical Methods in Thermal Problems, which took place in Swansea, Jones [1] proposed that buoyancy-driven flow in a square cavity would be a suitable vehicle for testing and validating computer codes. Following discussions at Swansea, contributions for the solution of the problem were invited. The compilation and discussion of the main contributions yielded the classical benchmark of Refs. [2,3].

The first to introduce a turbulence model in their calculations were Markatos and Pericleous [4]. They performed steady 2D simulations for Ra up to 10^{16} and presented a complete set of results. The work of Henkes, van der Vlugt, and Hoogendoorn [5] used the same turbulence model adopted by Markatos and Pericleous [4] for 2D calculations up to $Ra = 10^{11}$. In Ref. [5] 2D calculations using various versions of the k-ε turbulence model was performed. These versions included the standard as well as the low-Reynolds number k-ε models. A comparison with experimental results for Nu showed the superiority of the low-Reynolds number k-ε closures. In Ref. [6], 3D calculations for laminar flow

for Ra up to 10^{10} were presented. Their graphs revealed the 3D character of the flow. Comparisons were made with 2D simulations and differences were reported for the heat transfer correlation between Nu and Ra. A recent paper by Barakos, Mitsoulis, and Assimacopoulos [7] reworked the problem for laminar and turbulent flows for a wide range of Ra. Turbulence was modeled with the standard k-ε closure and the effect of wall functions on heat transfer was investigated.

Studies concerning natural convection in porous media can be found in the monographs of Refs. [8,9]. The case of free convection in a rectangular cavity heated on a side and cooled at the opposing side is also an important problem in thermal convection in porous media. The works of Walker and Homsy [10], Bejan [11], Prasad and Kulacki [12], Beckermann, Viskanta, and Ramadhyani [13], Gross, Bear, and Hickox [14], and Manole and Lage [15] have contributed with some important results to this problem. The recent work of Baytas and Pop [16] was concerned with a numerical study of the steady free convection flow in rectangular and oblique cavities filled with homogeneous porous media using a nonlinear axis transformation. The Darcy momentum and energy equations are solved numerically using the (ADI) method.

Studies on macroscopic transport modeling of incompressible flows in porous media have been based on the volume-average methodology for either heat [17] or mass transfer [18–20]. In turbulent flows, when time fluctuations of the flow properties are also considered in addition to spatial deviations, there are two possible methodologies to follow in order to obtain macroscopic equations: (*a*) application of time-average operator followed by volume averaging [21–24], or (*b*) use of volume-averaging before time-averaging is applied [25–27]. However, both sets of macroscopic mass transport equations are equivalent when examined under the recently established *double decomposition concept* [28–31]. This theoretical work has been extended to heat transfer in porous media where both time fluctuations and spatial deviations were considered for temperature and velocity [32,33]. Further, a consistent program of systematic analyzes based on the *double-decomposition theory* for treating turbulent buoyant flows [34,35], nonequilibrium heat transfer [36,37], mass transfer [38], and double diffusion [39], has been applied to investigate flow trough porous inserts [40], heat transfer in permeable baffles [41], and flow over a finite porous substrate considering a diffusion-
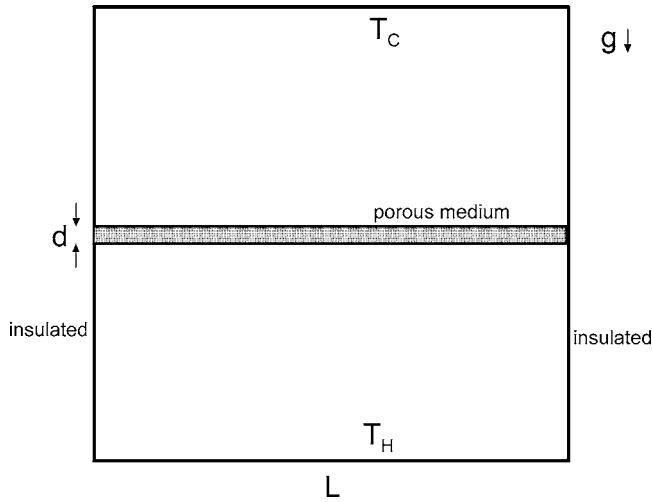

Transactions of the ASME

Fig. 1 Geometry under consideration

jump condition at the interface for the mean [42,43] and turbulence fields [44,45]. All those studies were based on the concepts first proposed by [28–31], which were compared to other views the literature in [46]. Recently, a book has been published on the subject of turbulence modeling in porous media [47].

Motivated by the foregoing work, this work presents turbulent natural convection in a vertical two-dimensional square cavity, isothermally heated from below and cooled at the upper surface. The enclosure has a thin horizontal porous obstruction located at the cavity mid height. As the overall heat flux across the enclosure is from bottom to top, this geometry is here considered a vertical. The turbulence model here adopted is the standard k-ε with wall function.

2 The Problem Considered

The problem considered is shown schematically in Fig. 1 and refers to the two-dimensional flow of a Boussinesq fluid of Prandtl number 1 in a square cavity of side $L=1$ m. The cavity is assumed to be of infinite depth along the z-axis and is isothermally heated from the bottom and cooled from the ceiling. The vertical square cavity has a porous obstruction of thickness $d=0.05$ m positioned at cavity midheight.

The no-slip condition is applied for velocity and the resulting flow is treated as steady. The controlling parameter is the Rayleigh number, $Ra=g\beta H^3\Delta T/\nu\alpha$, which was varied up to 10^7 only to ensure that for unobstructed cavities the flow is practically laminar. Further, a relationship for the permeability was proposed in Refs. [46,48] for circular rods, which are in good accord with the empirical expression proposed by Ref. [49], as:

$$K = \frac{D_p^2\phi^3}{144(1-\phi)^2} \qquad (1)$$

3 Governing Equations

The equations used herein are derived in details in the work of Refs. [29,32,33,35]. Basically, for porous media analysis, a macroscopic form of the governing equations is obtained by taking the volumetric average of the entire equation set. In that development, the porous medium is considered to be rigid and saturated by an incompressible fluid.

The macroscopic continuity equation is given by,

$$\boldsymbol{\nabla}\cdot\bar{\mathbf{u}}_D = 0 \qquad (2)$$

The Dupuit–Forchheimer relationship, $\bar{\mathbf{u}}_D=\phi\langle\bar{\mathbf{u}}\rangle^i$, has been used and $\langle\bar{\mathbf{u}}\rangle^i$ identifies the intrinsic (liquid) average of the local

velocity vector $\bar{\mathbf{u}}$. The macroscopic time-mean Navier–Stokes (NS) equation for an incompressible fluid with constant properties is given as

$$\rho\left[\frac{\partial\bar{\mathbf{u}}_D}{\partial t} + \boldsymbol{\nabla}\cdot\left(\frac{\bar{\mathbf{u}}_D\bar{\mathbf{u}}_D}{\phi}\right)\right] = -\boldsymbol{\nabla}(\phi\langle\bar{p}\rangle^i) + \mu\boldsymbol{\nabla}^2\bar{\mathbf{u}}_D + \boldsymbol{\nabla}\cdot(-\rho\phi\langle\overline{\mathbf{u}'\mathbf{u}'}\rangle^i)$$
$$-\rho\beta_\phi\mathbf{g}\phi(\langle\bar{T}\rangle^i - T_{\text{ref}})$$
$$-\left[\frac{\mu\phi}{K}\bar{\mathbf{u}}_D + \frac{c_F\phi\rho|\bar{\mathbf{u}}_D|\bar{\mathbf{u}}_D}{\sqrt{K}}\right] \qquad (3)$$

The use of Eq. (3) is largely employed in the literature when "numerical" solutions are sought for a "macroscopic" view of the flow. As such, Eq. (3) is used when one seeks modeling the "overall" effect of the porous substrate on the flow. The interested reader is referred to Refs. [28–31] for extensive discussions on this important point.

Further, when treating turbulence with statistical tools, the correlation $-\rho\mathbf{u}'\mathbf{u}'$ appears after application of the time-average operator to the local instantaneous NS equation. Applying further the volume-average procedure to this correlation results in the term $-\rho\phi\langle\overline{\mathbf{u}'\mathbf{u}'}\rangle^i$. This term is here recalled the macroscopic Reynolds stress tensor (MRST). Further, a model for the MRST in analogy with the Boussinesq concept for clear fluid can be written as

$$-\rho\phi\langle\overline{\mathbf{u}'\mathbf{u}'}\rangle^i = \mu_{t_\phi}2\langle\bar{\mathbf{D}}\rangle^v - \tfrac{2}{3}\phi\rho\langle k\rangle^i\mathbf{I} \qquad (4)$$

where

$$\langle\bar{\mathbf{D}}\rangle^v = \tfrac{1}{2}[\boldsymbol{\nabla}(\phi\langle\bar{\mathbf{u}}\rangle^i) + [\boldsymbol{\nabla}(\phi\langle\bar{\mathbf{u}}\rangle^i)]^T] \qquad (5)$$

is the macroscopic deformation rate tensor, $\langle k\rangle^i$ is the intrinsic average for k and μ_{t_ϕ} is the macroscopic turbulent viscosity. The macroscopic turbulent viscosity, μ_{t_ϕ}, is modeled similarly to the case of clear fluid flow and a proposal for it was presented in Ref. [29] as

$$\mu_{t_\phi} = \rho c_\mu \frac{\langle k\rangle^{i^2}}{\langle\varepsilon\rangle^i} \qquad (6)$$

In a similar way, applying both time and volumetric average to the microscopic energy equation, for either the fluid or the porous matrix, two equations arise. Assuming further the local thermal equilibrium hypothesis, which considers $\langle\overline{T_f}\rangle^i=\langle\overline{T_s}\rangle^i=\langle\bar{T}\rangle^i$, and adding up these two equations, one has

$$(\rho c_p)_f\boldsymbol{\nabla}\cdot(\phi\langle\overline{\mathbf{u}T_f}\rangle^i)$$
$$= (\rho c_p)_f\boldsymbol{\nabla}\cdot\left\{\phi(\langle\bar{\mathbf{u}}\rangle^i\langle\overline{T_f}\rangle^i + \underset{\uparrow}{\overline{\langle\mathbf{u}'\rangle^i\langle T_f'\rangle^i}} + \underset{\uparrow}{\langle{}^i\bar{\mathbf{u}}{}^i\overline{T_f}\rangle^i} + \underset{\uparrow}{\overline{\langle{}^i\mathbf{u}'{}^iT_f'\rangle^i}})\right\}$$
$$\qquad\qquad\qquad\qquad \text{I}\qquad\qquad \text{II}\qquad\qquad \text{III}\qquad\qquad \text{IV} \qquad (7)$$

where to each term on the right hand side of Eq. (7), the following significance can be attributed: I convection—due to macroscopic time-averaged velocity and temperature, II turbulent heat flux—due to the macroscopic time fluctuations of local velocity and temperature, III thermal dispersion—associated with spatial deviations of the time averaged velocity and temperature. Note that this term is also present in laminar flows in porous media. IV turbulent thermal dispersion—due to both time fluctuations and spatial deviations of local velocity and temperature.

A modeled form of Eq. (7) has been given in detail in the work of Rocamora, Jr. and de Lemos [32,33], as

$$\{(\rho c_p)_f\phi + (\rho c_p)_s(1-\phi)\}\frac{\partial\langle\bar{T}\rangle^i}{\partial t} + (\rho c_p)_f\boldsymbol{\nabla}\cdot(\mathbf{u}_D\langle\bar{T}\rangle^i)$$
$$= \boldsymbol{\nabla}\cdot\{\mathbf{K}_{\text{eff}}\cdot\boldsymbol{\nabla}\langle\bar{T}\rangle^i\} \qquad (8)$$

where, $\mathbf{K}_{\text{eff}}$, given by

$$\text{Nu} = hH/k \therefore \text{Nu} = \left(\frac{\partial \langle T \rangle^v}{\partial y}\right)_{y=0} \frac{H}{T_H - T_C} \tag{12}$$

and the average Nusselt number is given by

$$\bar{\text{Nu}} = \frac{1}{L}\int_0^L \text{Nu}\,dx \tag{13}$$

4 Turbulence Model

Transport equations for $\langle k \rangle^i = \overline{\langle \mathbf{u}' \cdot \mathbf{u}' \rangle}^i/2$ and $\langle \epsilon \rangle^i = \mu \overline{\langle \nabla \mathbf{u}' : (\nabla \mathbf{u}')^T \rangle}^i/\rho$ in their so-called high Reynolds number form are proposed in Ref. [29] and extended in Ref. [35] to incorporate the buoyant effects as

$$\rho\left[\frac{\partial}{\partial t}(\phi\langle k \rangle^i) + \nabla \cdot (\bar{\mathbf{u}}_D\langle k \rangle^i)\right] = \nabla \cdot \left[\left(\mu + \frac{\mu_{t_\phi}}{\sigma_k}\right)\nabla\,(\phi\langle k \rangle^i)\right]$$
$$+ P^i + G^i + G^i_\beta - \rho\phi\langle \epsilon \rangle^i \tag{14}$$

$$\rho\left[\frac{\partial}{\partial t}(\phi\langle \epsilon \rangle^i) + \nabla \cdot (\bar{\mathbf{u}}_D\langle \epsilon \rangle^i)\right] = \nabla \cdot \left[\left(\mu + \frac{\mu_{t_\phi}}{\sigma_\varepsilon}\right)\nabla\,(\phi\langle \epsilon \rangle^i)\right]$$
$$+ c_1 P^i \frac{\langle \epsilon \rangle^i}{\langle k \rangle^i} + c_2 \frac{\langle \epsilon \rangle^i}{\langle k \rangle^i}G^i + c_1 c_3 G^i_\beta \frac{\langle \epsilon \rangle^i}{\langle k \rangle^i}$$
$$- c_2\rho\phi\frac{\langle \epsilon \rangle^{i^2}}{\langle k \rangle^i} \tag{15}$$

where c_1, c_2, c_3, and c_k are constants, $P^i = (-\rho\langle \overline{\mathbf{u}'\mathbf{u}'} \rangle^i : \nabla\bar{\mathbf{u}}_D)$ is the production rate of $\langle k \rangle^i$ due to gradients of $\bar{\mathbf{u}}_D$, G^i $[=c_k\rho(\phi\langle k \rangle^i |\bar{\mathbf{u}}_D|/\sqrt{K})]$ is the generation rate of the intrinsic average of $\mathbf{k}$ due to the action of the porous matrix and G^i_β $[=\phi(\mu_{t_\phi}/\sigma_t)\mathbf{g}\beta_\phi\nabla\langle \bar{T} \rangle^i]$ is the generation rate of $\langle k \rangle^i$ due to the buoyant effects.

Before proceeding, a word about the class of problems under consideration herein seems timely. Cases here investigated are akin to having a forced flow through a grid. The grid, or any "highly permeable" structure, will perturb the flow rather the "suppress" it, inducing instabilities leading eventually to turbulent regime. Evidently, if the flow restriction is intense, then a substantial reduction on the mass flow rate across the porous material is resultant for the same ΔT across the cavity. This, however, is not the situation here. The class of problems treated in this paper deals only with highly permeable, highly porous structure so that no substantial head loss is added to the flow. The source term G^i in Eq. (14) reflects this notion and physically represents an additional generation rate of k due to the flow perturbation caused by the highly permeable obstruction. Comprehensive discussions on this matter are available in Refs. [29–31,46], which are suggested for further reading.

The interface conditions between the clear medium and the porous medium follows the work of Ochoa-Tapia and Whitaker [50] using the "shear stress jump" concept. At the interface one has (see Fig. 1),

$$\bar{\mathbf{u}}_D|_{\phi<1} = \bar{\mathbf{u}}_D|_{\phi=1} \tag{16}$$

$$\langle \bar{p} \rangle^i|_{\phi<1} = \langle \bar{p} \rangle^i|_{\phi=1} \tag{17}$$

$$\phi^{-1}\left.\frac{\partial \bar{u}_{D_1}}{\partial x_2}\right|_{\phi<1} - \left.\frac{\partial \bar{u}_{D_1}}{\partial x_2}\right|_{\phi=1} = \frac{\beta_i}{\sqrt{K}}\bar{u}_{D_1}|_{\text{interface}} \tag{18}$$

$$\langle k \rangle^v|_{\phi<1} = \langle k \rangle^v|_{\phi=1} \tag{19}$$

$$\left.\left(\mu + \frac{\mu_{t_\phi}}{\sigma_k}\right)\frac{\partial \langle k \rangle^v}{\partial x_2}\right|_{\phi<1} = \left.\left(\mu + \frac{\mu_t}{\sigma_k}\right)\frac{\partial \langle k \rangle^v}{\partial x_2}\right|_{\phi=1} \tag{20}$$
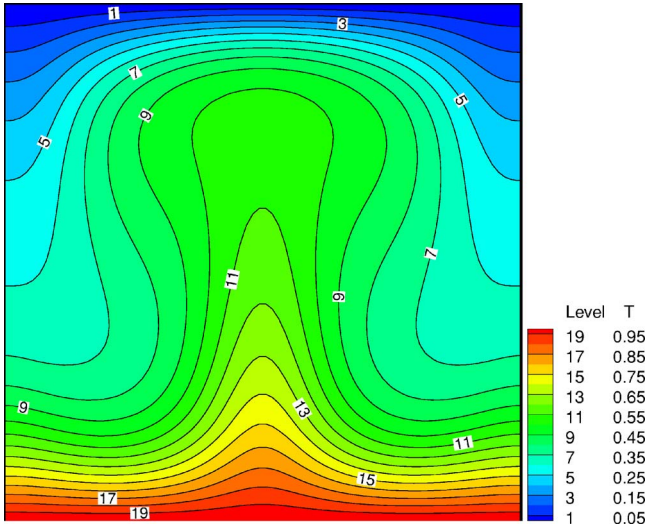

Fig. 2 Isotherms for laminar solution for a square cavity heated from below and cooled from the ceiling for Ra=4×10^4

Level	T
19	0.95
17	0.85
15	0.75
13	0.65
11	0.55
9	0.45
7	0.35
5	0.25
3	0.15
1	0.05

$$\mathbf{K}_{\text{eff}} = [\phi k_f + (1-\phi)k_s]\mathbf{I} + \mathbf{K}_{\text{tor}} + \mathbf{K}_t + \mathbf{K}_{\text{disp}} + \mathbf{K}_{\text{disp},t} \tag{9}$$

is the effective conductivity tensor. In order to be able to apply (8), it is necessary to determine the conductivity tensors in (9), i.e., $\mathbf{K}_{\text{tor}}$, $\mathbf{K}_t$, $\mathbf{K}_{\text{disp}}$, and $\mathbf{K}_{\text{disp},t}$. Following Ref. [23], this can be accomplished for the tortuosity and thermal dispersion conductivity tensors, $\mathbf{K}_{\text{tor}}$ and $\mathbf{K}_{\text{disp}}$, by making use of a unit cell subjected to periodic boundary conditions for the flow and a linear temperature gradient imposed over the domain. The conductivity tensors are then obtained directly from the microscopic results for the unit cell (see Ref. [23] for details on the expressions here used).

The turbulent heat flux and turbulent thermal dispersion terms, $\mathbf{K}_t$ and $\mathbf{K}_{\text{disp},t}$, which cannot be determined from such a microscopic calculation, are modeled here through the Eddy diffusivity concept, similarly to Ref. [24]. It should be noticed that these terms arise only if the flow is turbulent, whereas the tortuosity and the thermal dispersion terms exist for both laminar and turbulent flow regimes.

Starting out from the time averaged energy equation coupled with the microscopic modeling for the "turbulent heat flux" through the eddy diffusivity concept, one can write, after volume averaging

$$-(\rho c_p)_f\langle \overline{\mathbf{u}'T'_f} \rangle^i = (\rho c_p)_f\frac{\nu_{t_\phi}}{\sigma_T}\nabla\,\langle \bar{T}_f \rangle^i \tag{10}$$

where the symbol ν_{t_ϕ} expresses the macroscopic eddy viscosity, $\mu_{t_\phi} = \rho_f\nu_{t_\phi}$, given by (6) and σ_T is a constant. According to (10), the macroscopic heat flux due to turbulence is taken as the sum of the turbulent heat flux and the turbulent thermal dispersion found by Ref. [33]. In view of the arguments given above, the turbulent heat flux and turbulent thermal dispersion components of the conductivity tensor, $\mathbf{K}_t$ and $\mathbf{K}_{\text{disp},t}$, respectively, are expressed as

$$\mathbf{K}_t + \mathbf{K}_{\text{disp},t} = \phi(\rho c_p)_f\frac{\nu_{t_\phi}}{\sigma_T}\mathbf{I} \tag{11}$$

In the equation set shown above, when the variable $\phi=1$, the domain is considered as a clear medium. For any other value of ϕ, the domain is treated as a porous medium.

3.1 Nusselt tumber. The local Nusselt number on the hot wall for the square cavity at $x=0$ is defined as

$$\langle\varepsilon\rangle^v\big|_{\phi<1} = \langle\varepsilon\rangle^v\big|_{\phi=1} \tag{21}$$

$$\left(\mu + \frac{\mu_{t_\phi}}{\sigma_\varepsilon}\right) \frac{\partial\langle\varepsilon\rangle^v}{\partial x_2}\bigg|_{\phi<1} = \left(\mu + \frac{\mu_t}{\sigma_\varepsilon}\right)\frac{\partial\langle\varepsilon\rangle^v}{\partial x_2}\bigg|_{\phi=1} \tag{22}$$

$$\langle\bar{T}\rangle^i\big|_{\phi<1} = \langle\bar{T}\rangle^i\big|_{\phi=1} \tag{23}$$

$$\mathbf{e}_2 \cdot \left(\underline{K}_{\text{eff}} \cdot \boldsymbol{\nabla}\langle\bar{T}\rangle^i\right)\big|_{\phi<1} = k_f \frac{\partial\langle\bar{T}\rangle^i}{\partial x_2}\bigg|_{\phi=1} \tag{24}$$

where β_i in Eq. (18) is a nondimensional coefficient that expresses a "jump" condition in the shear stress at the interface. Such discontinuity might be due to interface roughness or be a way to comply with irregular interfaces. In addition, it can also be seen as an accommodation of the fact that close to the interface the permeability K attains higher values than those used within the porous substrate. The interface conditions for k and ε, Eqs. (19)–(22) were proposed by Ref. [51] and used in Refs. [42–45]. They assume continuity of k and ε at the interface. On should point out, however, that the use of Eq. (18) has very little influence on flows mostly normal to the interface, as in the case here analyzed (see Ref. [40] for flow computations normal to a porous insert). Here, Eq. (18) is considered for the sake of completeness only.

5 Numerical Method and Solution Procedure

The numerical method employed for discretizing the governing equations is the control-volume approach with a generalized collocated grid. The flux blended deferred correction which combines linearly the upwind differencing scheme and central differencing scheme, was used for interpolating the convective fluxes, see Ref. [52]. The well-established SIMPLE algorithm [53] is followed for handling the pressure-velocity coupling. Individual algebraic equation sets were solved by the SIP procedure of (see Refs. [54,55] for details). Further, concentration of nodal points to walls reduces eventual errors due to numerical diffusion which, in turn, are further annihilated due to the hybrid scheme here adopted.

6 Results and Discussion

Calculations for turbulent flow were performed for all cases using an 80×120 grid with concentration of nodes near the horizontal walls. Runs were performed with high porosity, $\phi=0.95$, $k_s/k_f=2$, Pr=1, and an equivalent particle diameter, $D_p=1$ mm (see Eq. (1)), which gives a Da$=K/L^2=0.2382\times10^{-5}$ in order to permit a high mass flux through the porous obstruction and to avoid suppression of convective currents.

It is important to emphasize that the main objective of this work is not to simulate the transition mechanism from laminar regime to fully turbulent flow, which involves modeling of complex physical processes and hydrodynamic instabilities. Here, the aim of this work is to establish when both turbulent and laminar models do not differ substantially as far as predictions of overall Nu are of concern. Therefore, a strategy for determining the range of validity of a laminar flow solution was to simulate the *laminarization* of turbulent flow when the Raleigh number is reduced. Or say, we start with a low value of Ra and the "laminar" model, compute Nu and repeat the calculations for increasing Raleigh numbers. Also, we turn on the k-ε model for Ra$=10^7$, calculate Nu, and repeat the procedure for smaller Ra's, remembering that such a two-equation model was first proposed with the aim of predicting the laminarization process. We perform calculations with and without the porous obstruction and compare the behavior of Nu in both cases.

According to Ref. [5], the separation of the averaged wall-heat transfer between laminar and turbulent fields depends on the turbulence model used. When Ra is varied, the literature often refers to laminar and turbulent "branches" of solutions as Ra passes a critical value. When a turbulence model is included, the solution can depart from the laminar branch for Ra$>$Ra$_c$ and follows the turbulent branch: Ra$_c$ in this analysis is called separation point of the governing equations.

The Rayleigh number is calculated as in the clear fluid case. It is important to emphasize that the present results were started with the solution for the cavity without the porous obstruction and Ra$=4\times10^4$, Fig. 2, which has a remarkable plume impinging at the center of the cavity. It is known that the solutions for vertical cavities are not unique, but, the bifurcation of the solution is out of the concern of this work.

Figures 3–5 show the streamlines, isotherms, and isolines of turbulent kinetic energy for turbulent flow in a vertical square cavity with a porous obstruction at its midheight for Ra ranging from 4×10^4 to 10^7. For lower values of Ra, not shown here, the isotherms are stratified and the main mechanism of heat transfer is conduction and the generation of turbulent kinetic energy is null due to the low velocity gradients.

For Ra$=4\times10^4$, a plume arise from the bottom of the heated wall impinging through the porous obstruction, Fig. 4(a). The flow is divided in two vortices of each side of the porous obstruction, Fig. 3(a). The generation of turbulent kinetic energy remains small and it is almost null everywhere, Fig. 5(a).

Increasing Ra to 10^6, the plume becomes stronger, impinging through the porous obstruction more intensively, Fig. 4(b). The vortices move a little faster than before, Fig. 3(b), and the generation of turbulent kinetic energy is now evident, mainly inside and around the vicinity of the porous obstruction (Fig. 5(b)). As proposed by Ref. [29], the porous matrix contributes with the generation of turbulent kinetic energy such that a new term G^i in the $\langle k\rangle^i$ transport equation (14) was introduced. For a fixed value of the Darcy velocity through a porous bed, the amount of mechanical energy converted into turbulence should depend on the medium properties. For the limiting case of high porosity and permeability media ($\phi\to1\Rightarrow K\to\infty$) no fraction of this available mechanical energy is expected to generate turbulence. The flow, in this situation, behaves like clear fluid flow. As the flow resistance increases, by increasing $\phi/\sqrt{K}$, gradients of local u within the pore will contribute to increasing $\langle k\rangle^i$. This porous obstruction, as will be shown later, forces an earlier departure of Nu calculated for both regimes, namely, laminar and turbulent.

For Ra$=10^7$, two plumes arise from the porous obstruction of each side of the square cavity. Both plumes point to opposing directions and move toward to the heated walls, Fig. 4(c). This feature makes the streamlines, Fig. 3(c), change its directions, probably to minimize the shear stresses between the vortices. Therefore, the isolines of turbulent kinetic energy are very pronounced in the porous matrix and present symmetry with respect to the center of the cavity, Fig. 5(c).

Table 1 shows the Nusselt numbers for a vertical square cavity with two possibilities: (a) vertical square cavity with a porous obstruction and (b) vertical square cavity without a porous obstruction. It is interesting to note that for clear cavities (unobstructed flow) the values of Nu calculated with and without the turbulence model shows nearly the same values (cases (b) in Table 1). As mentioned above, this is an indication that within the selected range for Ra, namely $10^2<$Ra$<10^7$, turbulence seems to be not yet fully established in an "empty" cavity. An increase in k within the flow has to be "promoted" by some sort of agent, similarly to what happens when an orderly laminar flow is forced through a "grid," generating turbulence by disturbing the flow past the solid wires.

Further, Table 1 clearly shows that the overall values of the Nusselt number for a vertical square cavity without a porous obstruction are higher than those with porous obstruction (cases (a) and (b) in Table 1). The porous plate damps the heat transfer across the heated walls, showing an overall lower Nusselt numbers, for each Ra, when compared with those without porous obstruction.

Also, when the two solutions are compared for the cases with
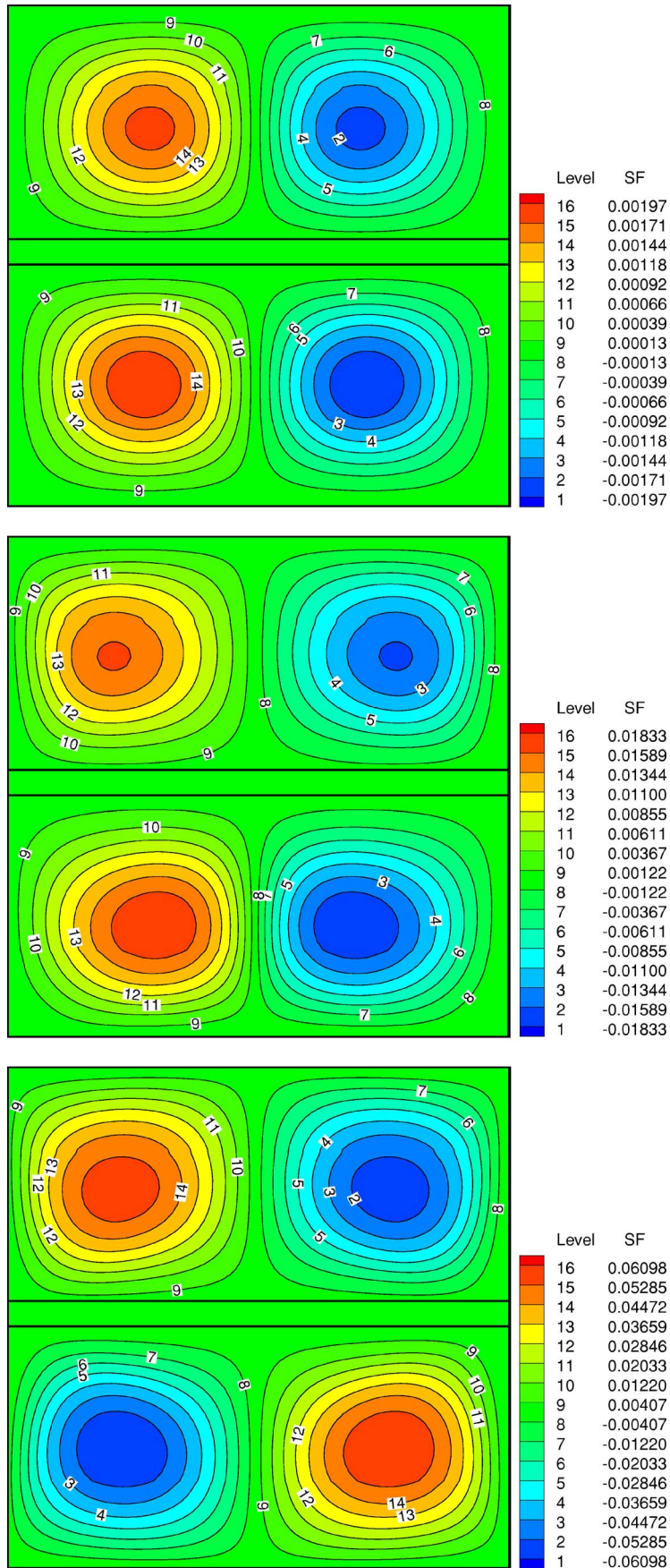
Fig. 3   Streamlines of turbulent solution of a vertical square cavity with a porous obstruction for Ra=4×10^4, 10^6, and 10^7 with ϕ=0.95 and D_p =1 mm

(a)

(b)

(c)

Fig. 4 Isotherms of turbulent solution of a vertical square cavity with a porous obstruction for (a) Ra=4×10⁴, (b) 10⁶, and (c) 10⁷ with ϕ=0.95 and D_p=1 mm

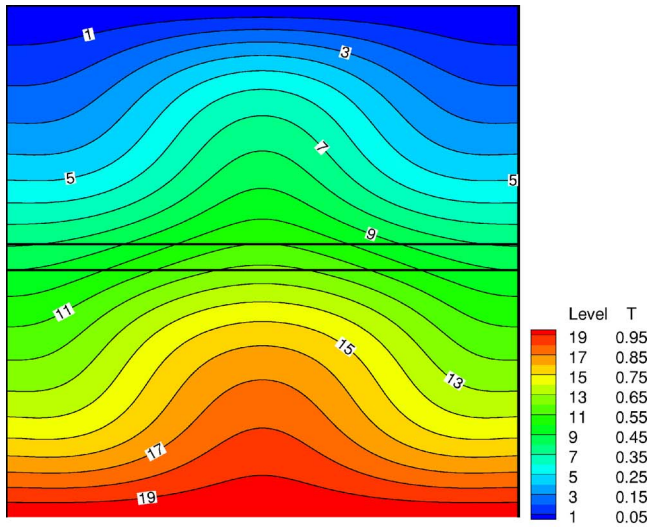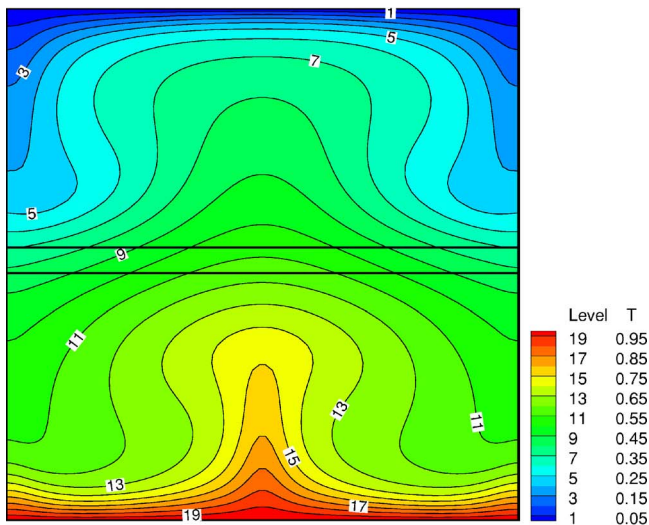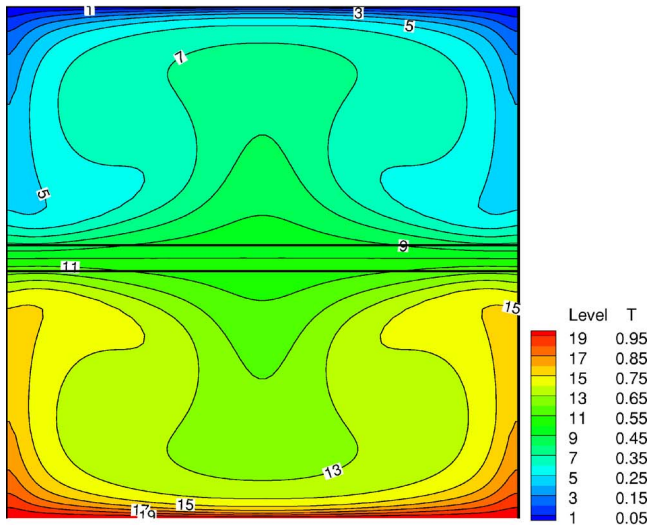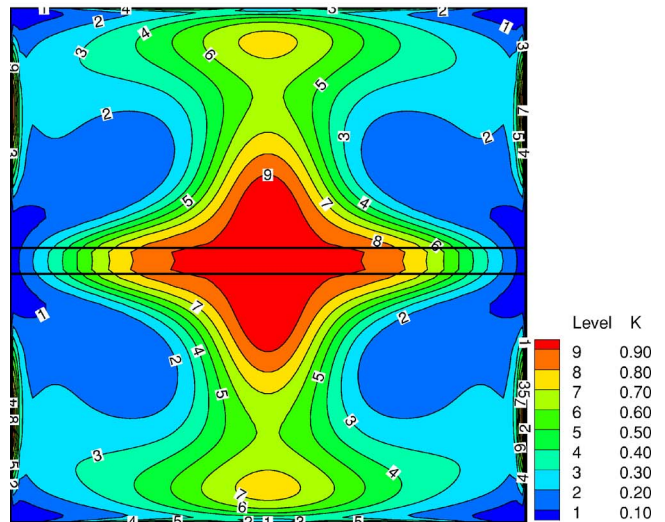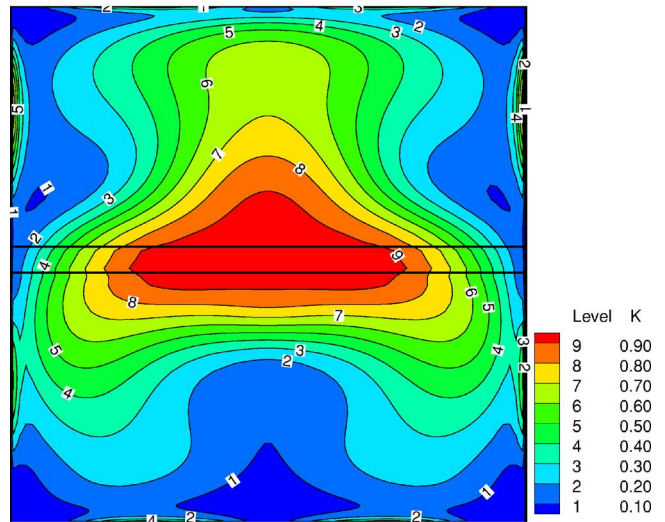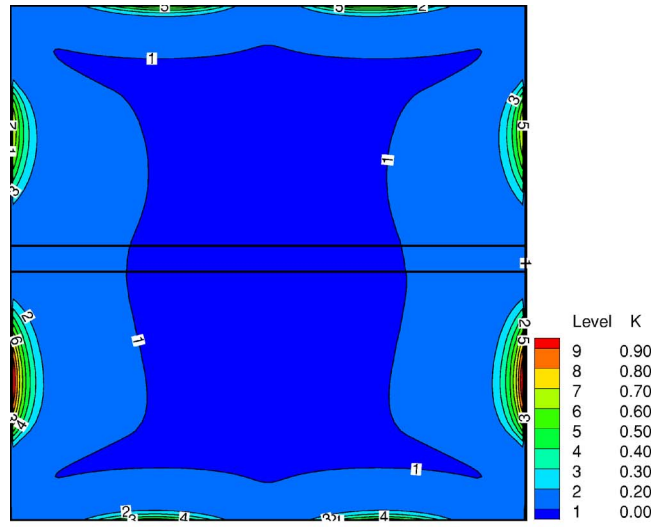**Fig. 5 Isolines of k for turbulent solution for a vertical square cavity with a porous obstruction for Ra=4×10⁴, 10⁶, and 10⁷ with ϕ=0.95 and D_p=1 mm**

the porous plate (cases (a) in Table 1), even for a relatively low Ra number, $\mathrm{Ra} < 10^7$, the turbulent model solution differs by a considerable amount from the laminar one. For example, for Ra

Table 1 Average Nusselt numbers for $10^2 < Ra < 10^7$ with ϕ =0.95 and D_p=1 mm: (a) with porous obstruction and (b) without porous obstruction

Ra		10^2	4×10^4	10^6	10^7
Laminar solution	a	1.00	1.32	3.79	7.05
	b	1.00	2.87	6.58	11.74
Turbulent solution	a	1.00	1.32	5.44	10.83
	b	1.00	2.88	6.65	12.32

$=10^6$ Nu is $100 \times (5.44 - 3.79)/3.79 = 43.53\%$ higher if the turbulent model is compared with the laminar result, whereas for the clear cavity case the laminar and turbulent solutions gives similar values. For Ra$=10^7$, the inclusion of the porous plate yield an increase in Nu by $100 \times (10.83 - 7.05)/7.05 = 53.62\%$ when turbulent and laminar models are compared. As such, the presence of a porous obstruction in the square cavity seems to force an earlier increase in Nu, and that can be interpreted as an earlier separation of the laminar branch to the turbulent branch of the solution.

7 Conclusion

This paper presented computations for laminar and turbulent flows with the standard k-ε model with a wall function for natural convection in a square cavity with a porous obstruction in the middle. Nusselt numbers for a vertical square cavity without a porous obstruction are higher than those with porous obstruction. The porous obstruction damps the heat transfer across the heated walls, showing an overall lower Nusselt numbers when compared with those with porous obstruction. However, the presence of a porous obstruction in the square cavity seems to force an earlier separation of the laminar branch to the turbulent branch due to the higher generation of turbulent kinetic energy in the porous matrix. Analyses of important environmental and engineering flows can benefit from the derivations herein and, ultimately, it is expected that additional research on this new subject be stimulated by the work here presented.

Acknowledgment

Nomenclature

Latin Characters

c_F = Forchheimer coefficient
$c_{1,2,3,k,\mu}$ = model constants
c_p = fluid specific heat, J/kg°C
Da = Darcy number, Da$=K/L^2$
$\mathbf{g}$ = gravity acceleration vector, m/s^2
H = square height, m
K = permeability, $K=D_p^2 \phi^3/144(1-\phi)^2$, m^2
k = turbulent kinetic energy, J/kg
k_f = fluid thermal conductivity, W/m°C
k_s = solid thermal conductivity, W/m°C
L = square width
Nu = Nu$=hH/k$, Nusselt number
Ra = Ra$=g\beta H^3 \Delta T/\nu\alpha$, fluid Rayleigh number
T = Temperature, °C
$\mathbf{u}$ = microscopic velocity, m/s
$\mathbf{u}_D$ = Darcy or superficial velocity (volume average of $\mathbf{u}$)

Greek Characters

α = fluid thermal diffusivity, m^2/s
β = fluid thermal expansion coefficient, 1/°K
ΔV = representative elementary volume, m^2
ΔV_f = fluid volume inside ΔV
ε = dissipation rate ok k, W/kg
μ = fluid dynamic viscosity, N s/m^2
μ_{t_ϕ} = macroscopic turbulent viscosity, N s/m^2
ν = fluid kinematic viscosity, m^2/s
ρ = fluid density, kg/m^3
$\sigma_{k,\varepsilon,T}$ = turbulence model constants
ϕ = $\phi=\Delta V_f/\Delta V$, prosity

Special Characters

φ = general variable
$\bar{\varphi}$ = temporal average
φ' = temporal fluctuation
$\langle\varphi\rangle^i$ = intrinsic average
$\langle\varphi\rangle^v$ = volume average
$^i\varphi$ = spatial deviation
$\boldsymbol{\varphi}$ = vectorial general variable
$\varphi_{s,f}$ = solid/fluid
$\phi_{H,C}$ = hot/cold
$( )^T$ = transpose

References

[1] Jones, I. P., 1979, *A Comparison Problem for Numerical Methods in Fluid Dynamics: The Double-Glazing Problem, Numerical Methods in Thermal Problems*, R. W. Lewis and K. Morgan, eds., Pineridge Press, Swansea, pp. 338–348.
[2] de Vahl Davis, G., 1983, "Natural Convection in a Square Cavity: A Benchmark Numerical Solution," Int. J. Numer. Methods Fluids, **3**, pp. 249–264.
[3] de Vahl Davis, G., and Jones, I. P., 1983, "Natural Convection in a Square Cavity—A Comparison Exercise," Int. J. Numer. Methods Fluids, **3**, pp. 227–248.
[4] Markatos, N. C., and Pericleous, K. A., 1984, "Laminar and Turbulent Natural Convection in an Enclosed Cavity," Int. J. Heat Mass Transfer, **27**, pp. 755–772.
[5] Henkes, R. A. W. M., van der Vlugt, F. F., and Hoogendoorn, C. J., 1991, "Natural-Convection Flow in a Square Cavity Calculated With Low-Reynolds-Number Turbulence Models," Int. J. Heat Mass Transfer, **34**(2), pp. 377–388.
[6] Fusegi, T., Hyun, J. M., and Kuwahara, K., 1991, "Three-Dimensional Simulations of Natural Convection in a Sidewall-Heated Cube," Int. J. Numer. Methods Fluids, **3**, pp. 857–867.
[7] Barakos, G., Mitsoulis, E., and Assimacopoulos, D., 1994, "Natural Convection Flow in a Square Cavity Revised: Laminar and Turbulent Models With Wall Function," Int. J. Numer. Methods Fluids, **18**, pp. 695–719.
[8] Nield, D. A., and Bejan, A., 1992, *Convection in Porous Media*, Springer, New York.
[9] Ingham, D. B., and Pop, I., 1998, *Transport Phenomena in Porous Media*, Elsevier, Amsterdam.
[10] Walker, K. L., and Homsy, G. M., 1978, "Convection in Porous Cavity," J. Fluid Mech., **87**, pp. 449–474.
[11] Bejan, A., 1979, "On the Boundary Layer Regime in a Vertical Enclosure Filled With a Porous Medium," Lett. Heat Mass Transfer, **6**, pp. 93–102.
[12] Prasad, V., and Kulacki, F. A., 1984, "Convective Heat Transfer in a Rectangular Porous Cavity-Effect of Aspect Ratio on Flow Structure and Heat Transfer," ASME J. Heat Transfer, **106**, pp. 158–165.
[13] Beckermann, C., Viskanta, R., and Ramadhyani, S., 1986, "A Numerical Study of Non-Darcian Natural Convection in a Vertical Enclosure Filled With a Porous Medium," Numer. Heat Transfer, **10**, pp. 557–570.
[14] Gross, R. J., Bear, M. R., and Hickox, C. E., 1986, "The Application of Flux-Corrected Transport (Fct) to High Rayleigh Number Natural Convection in a Porous Medium," *Proc. 8th Int. Heat Transfer Conf.*, San Francisco, CA.
[15] Manole, D. M., and Lage, J. L., 1992, "Numerical Benchmark Results for Natural Convection in a Porous Medium Cavity, Heat and Mass Transfer in Porous Media," Asme Conference, Htd, **216**, pp. 55–60.
[16] Baytas, A. C., and Pop, I., 1999, "Free Convection in Oblique Enclosures Filled With a Porous Medium," Int. J. Heat Mass Transfer, **42**, pp. 1047–1057.
[17] Hsu, C. T., and Cheng, P., 1990, "Thermal Dispersion in a Porous Medium," Int. J. Heat Mass Transfer, **33**, pp. 1587–1597.
[18] Bear, J., 1972, *Dynamics of Fluids in Porous Media*, American Elsevier, New York.
[19] Whitaker, S., 1966, "Equations of Motion in Porous Media," Chem. Eng. Sci., **21**, pp. 291–300.
[20] Whitaker, S., 1967, "Diffusion and Dispersion in Porous Media," Am. Inst. Chem. Eng. Symp. Ser., **13**(3), pp. 420–427.
[21] Masuoka, T., and Takatsu, Y., 1996, "Turbulence Model for Flow Through Porous Media," Int. J. Heat Mass Transfer, **39**(13), pp. 2803–2809.
[22] Kuwahara, F., Nakayama, A., and Koyama, H., 1996, "A Numerical Study of Thermal Dispersion in Porous Media," ASME J. Heat Transfer, **118**, pp. 756–761.

[23] Kuwahara, F., and Nakayama, A., 1998, "Numerical Modeling of Non-Darcy Convective Flow in a Porous Medium," *Heat Transfer 1998: Proceedings. 11th Int. Heat Transf. Conf., Kyongyu, Korea*, Taylor & Francis, Washington, D. C., Vol. 4, pp. 411–416.

[24] Nakayama, A., and Kuwahara, F., 1999, "A Macroscopic Turbulence Model for Flow in a Porous Medium," ASME J. Fluids Eng., **121**, pp. 427–433.

[25] Lee, K., and Howell, J. R., 1987, "Forced Convective and Radiative Transfer Within a Highly Porous Layer Exposed to a Turbulent External Flow Field," *Proceedings of the 1987 ASME-JSME Thermal Engineering Joint Conf., Honolulu, Hawaii*, ASME, New York, Vol. 2, pp. 377–386.

[26] Antohe, B. V., and Lage, J. L., 1997, "A General Two-Equation Macroscopic Turbulence Model for Incompressible Flow in Porous Media," Int. J. Heat Mass Transfer, **40**(13), pp. 3013–3024.

[27] Getachewa, D., Minkowycz, W. J., and Lage, J. L., 2000, "A Modified Form of the k-ε Model for Turbulent Flow of an Incompressible Fluid in Porous Media," Int. J. Heat Mass Transfer, **43**, pp. 2909–2915.

[28] Pedras, M. H. J., and de Lemos, M. J. S., 2000, "On the Definition of Turbulent Kinetic Energy for Flow in Porous Media," Int. Commun. Heat Mass Transfer, **27**(2), pp. 211–220.

[29] Pedras, M. H. J., and de Lemos, M. J. S., 2001, "Macroscopic Turbulence Modeling for Incompressible Flow Through Undeformable Porous Media," Int. J. Heat Mass Transfer, **44**(6), pp. 1081–1093.

[30] Pedras, M. H. J., and de Lemos, M. J. S., 2001, "Simulation of Turbulent Flow in Porous Media Using a Spatially Periodic Array and a Low-Re Two-Equation Closure," Numer. Heat Transfer, Part A, **39**(1), pp. 35–59.

[31] Pedras, M. H. J., and de Lemos, M. J. S., 2001, "On the Mathematical Description and Simulation of Turbulent Flow in a Porous Medium Formed by an Array of Elliptic Rods," ASME J. Fluids Eng., **123**(4), pp. 941–947.

[32] Rocamora, F. D., Jr., and de Lemos, M. J. S., 2000, "Analisys of Convective Heat Transfer of Turbulent Flow in Saturated Porous Media," Int. Commun. Heat Mass Transfer, **27**(6), pp. 825–834.

[33] de Lemos, M. J. S., and Rocamora, F. D., 2002, "Turbulent Transport Modeling for Heated Flow in Rigid Porous Media," *Proceedings of the Twelfth International Heat Transfer Conference*, Grenoble, France, August 18–23, pp. 791–795.

[34] de Lemos, M. J. S., and Braga, E. J., 2003, "Modeling of Turbulent Natural Convection in Saturated Rigid Porous Media," Int. Commun. Heat Mass Transfer, **30**(5), pp. 615–624.

[35] Braga, E. J., and de Lemos, M. J. S., 2004, "Turbulent Natural Convection in a Porous Square Cavity Computed With a Macroscopic k-ε Model," Int. J. Heat Mass Transfer, **47**, pp. 5639–5650.

[36] Saito, M., and de Lemos, M. J. S., 2005, "Interfacial Heat Transfer Coefficient for Non-Equilibrium Convective Transport in Porous Media," Int. Commun. Heat Mass Transfer, **32**(5), pp. 667–677.

[37] Saito, M., and de Lemos, M. J. S., 2006, "A Correlation for Interfacial Heat Transfer Coefficient for Turbulent Flow Over an Array of Square Rods," ASME J. Heat Transfer, **128**(5), pp. 444–452.

[38] de Lemos, M. J. S., and Mesquita, M. S., 2003, "Turbulent Mass Transport in Saturated Rigid Porous Media," Int. Commun. Heat Mass Transfer, **30**(1), pp. 105–113.

[39] de Lemos, M. J. S., and Tofaneli, L. A., 2004, "Modeling of Double-Diffusive Turbulent Natural Convection in Porous Media," Int. J. Heat Mass Transfer, **47**(19–20), pp. 4221–4231.

[40] Assato, M., Pedras, M. H. J., and de Lemos, M. J. S., 2005, "Numerical Solution of Turbulent Channel Flow Past a Backward-Facing Step With a Porous Insert Using Linear and Nonlinear k-ε Models," J. Porous Media, **8**(1), pp. 13–29.

[41] Santos, N. B., and de Lemos, M. J. S., 2006, "Flow and Heat Transfer in a Parallel Plate Channel With Porous and Solid Baffles," Numer. Heat Transfer, Part A, **49**(5), pp. 471–494.

[42] Silva, R. A., and de Lemos, M. J. S., 2003, "Numerical Analysis of the Stress Jump Interface Condition for Laminar Flow Over a Porous Layer," Numer. Heat Transfer, Part A, **43**(6), pp. 603–617.

[43] Silva, R. A., and de Lemos, M. J. S., 2003, "Turbulent Flow in a Channel Occupied by a Porous Layer Considering the Stress Jump at the Interface," Int. J. Heat Mass Transfer, **46**, pp. 5113–5121.

[44] de Lemos, M. J. S., 2005, "Turbulent Kinetic Energy Distribution Across the Interface Between a Porous Medium and a Clear Region," Int. Commun. Heat Mass Transfer, **32**(1–2), pp. 107–115.

[45] de Lemos, M. J. S., and Silva, R. A., 2006, "Turbulent Flow Over a Layer of a Highly Permeable Medium Simulated With a Diffusion-Jump Model for the Interface," Int. J. Heat Mass Transfer, **49**(3–4), pp. 546–556.

[46] de Lemos, M. J. S., and Pedras, M. H. J., 2001, "Recent Mathematical Models for Turbulent Flow for Saturated Rigid Porous Media," ASME J. Fluids Eng., **123**(4), pp. 935–940.

[47] de Lemos, M. J. S., 2006, *Turbulence in Porous Media: Modeling and Applications*, Elsevier, New York.

[48] Kuwahara, F., Kameyama, Y., Yamashita, S., and Nakayama, A., 1998, "Numerical Modeling of Turbulent Flow in Porous Media Using a Spatially Periodic Array," J. Porous Media, **1**(1), pp. 47–55.

[49] Ergun, S., 1952, "Fluid Flow Through Packed Columns," Chem. Eng. Process., **48**, pp. 89–94.

[50] Ochoa-Tapia, J. A., and Whitaker, S., 1995, "Momentum Transfer at the Boundary Between a Porous Medium and a Homogeneous Fluid—I. Theoretical Development," Int. J. Heat Mass Transfer, **38**, pp. 2635–2646.

[51] Lee, K., and Howell, J. R., 1987, "Forced Convective and Radiative Transfer Within a Highly Porous Layer Exposed to a Turbulent External Flow Field," *Proceedings Of The 1987 ASME-JSME Thermal Engineering Joint Conf.*, Vol. 2, pp. 377–386.

[52] Khosla, P. K., and Rubin, S. G., 1974, "A Diagonally Dominant Second-Order Accurate Implicit Scheme," Comput. Fluids, **2**, pp. 207–209.

[53] Patankar, S. V., and Spalding, D. B., 1972, "A Calculation Procedure for Heat, Mass and Momentum Transfer in Three Dimensional Parabolic Flows," Int. J. Heat Mass Transfer, **15**, pp. 1787–1806.

[54] Stone, H. L., 1968, "Iterative Solution of Implicit Approximations of Multi-Dimensional Partial Differential Equations," SIAM (Soc. Ind. Appl. Math.) J. Numer. Anal., **5**, pp. 530–558.

[55] Ozoe, H., Mouri, A., Ohmuro, M., Churchill, S. W., and Lior, N., 1985, "Numerical Calculations of Laminar and Turbulent Natural Convection in Water in Rectangular Channels Heated and Cooled Isothermally on the Opposing Vertical Walls," Int. J. Heat Mass Transfer, **28**, pp. 125–138.

Rotational Buoyancy Effects on Heat Transfer in Five Different Aspect-Ratio Rectangular Channels With Smooth Walls and 45 Degree Ribbed Walls

Wen-Lung Fu

Lesley M. Wright[1]

Je-Chin Han
Distinguished Professor
and Marcus Easterling Endowed Chair
e-mail: jc-han@tamu.edu

Turbine Heat Transfer Laboratory,
Department of Mechanical Engineering,
Texas A&M University,
College Station, TX 77843-3123

This paper experimentally studies the effects of the buoyancy force and channel aspect ratio ($W:H$) on heat transfer in two-pass rotating rectangular channels with smooth walls and 45 deg ribbed walls. The channel aspect ratios include 4:1, 2:1, 1:1, 1:2, and 1:4. Four Reynolds numbers are studied: 5000, 10,000, 25,000, and 40,000. The rotation speed is fixed at 550 rpm for all tests, and for each channel, two channel orientations are studied: 90 deg and 45 or 135 deg, with respect to the plane of rotation. The maximum inlet coolant-to-wall density ratio $(\Delta\rho/\rho)_{inlet}$ is maintained around 0.12. Rib turbulators are placed on the leading and trailing walls of the channels at an angle of 45 deg to the flow direction. The ribs have a 1.59 by 1.59 mm square cross section, and the rib pitch-to-height ratio (P/e) is 10 for all tests. Under the fixed rotation speed (550 rpm) and fixed inlet coolant-to-wall density ratio (0.12), the local buoyancy parameter is varied with different Reynolds numbers, local rotating radius, local coolant-to-wall density ratio, and channel hydraulic diameter. The effects of the local buoyancy parameter and channel aspect ratio on the regional Nusselt number ratio are presented. The results show that increasing the local buoyancy parameter increases the Nusselt number ratio on the trailing surface and decreases the Nusselt number ratio on the leading surface in the first pass for all channels. However, the trend of the Nusselt number ratio in the second pass is more complicated due to the strong effect of the 180 deg turn. Results are also presented for this critical turn region of the two-pass channels. In addition to these regions, the channel averaged heat transfer, friction factor, and thermal performance are determined for each channel. With the channels having comparable Nusselt number ratios, the 1:4 channel has the superior thermal performance because it incurs the least pressure penalty. [DOI: 10.1115/1.2352782]

Introduction

Gas turbines are playing an increasingly important role throughout the industrialized world. While these engines are most notably used for aircraft propulsion and land based power generation, they are also used for marine propulsion, and a variety of other industrial applications. As the demand for power, in the form electricity or thrust, continues to increase, engineers must develop engines to meet this demand. The power output can be increased by raising the temperature of the gas entering the turbine. However, increasing the gas temperature must be done cautiously. The temperature of this hot mainstream gas is limited by the turbine components, namely the turbine blades and vanes. The extremely hot gases create excessive thermal stresses and result in premature failure of a blade or vane which is detrimental to the operation of the engine.

Various cooling techniques have been implemented in the engine design to increase the life of the turbine components. Air is extracted from the compressor and injected into the blades and vanes of the turbine. This cooling air passes internally through the components. This coolant air removes heat from the blade before it is expelled out of the blade through film cooling holes. This relatively cool air forms a protective film on the surface of the blade protecting the blade from the hot mainstream gas.

A number of methods are commonly used in various combinations to remove heat from the blade internally. Internally, jet impingement is a common technique used for the leading edge. One cooling technique for the trailing edge is pin-fin cooling. With the pins attached to both the pressure and suction sides of the cooling channel, they provide additional structural support while enhancing the heat transfer in this narrow cooling passage.

With the leading and trailing edges of the blades being cooled, only the midchord region remains. A number of serpentine passages can be used as channels for the coolant air. The cooling channels are commonly lined with rib turbulators, or trip strips. These ribs enhance the heat transfer in the cooling channels by tripping the boundary layer and creating additional mixing of the warmer fluid near the channel wall with the relatively cooler air near the center of the channel. The cross section of the channels varies depending on where the channel is located in the blade. In other words, channels closer to the leading edge may have a relatively large distance between the leading and trailing surfaces (in the cooling channel, the leading surface of the channel is on the suction side of the blade, and the trailing surface is on the pressure side). Near the trailing edge of the blade, the opposite may be true for the cooling channels; the channels have a very small distance between the leading and trailing surfaces. The channels near the

---

Copyright © 2006 by ASME

center of the blade vary from the two extremes of the leading and trailing edges, and these channels may have cross sections which are nearly square.

Although cooling the turbine components with air taken from the compressor effectively increases the life of the components, it also reduces the overall efficiency of the engine. The coolant air reduces the amount of the working fluid used to generate power. Therefore, a balance must be maintained between increasing the gas temperature and extracting gas for cooling. Understanding flow through the coolant channels can lead to effective cooling designs which minimize the amount of coolant. These optimized cooling schemes lead to engines which operate more efficiently with increased power output.

Researchers have spent many years trying to optimize the coolant flow through these internal channels. Han et al. [1] chronicle many studies that began with flow through nonrotating channels with and without rib turbulators. The size, shape, and placement of the turbulators have been varied to determine the optimal design for given flow conditions. Early cooling designs used transverse ribs, or ribs placed 90 deg to the coolant flow. These ribs created more heat transfer enhancement than a smooth channel, but this configuration was soon replaced with angled, or skewed, ribs. The angled ribs induce secondary flow along the ribs that further increase the heat transfer from the channel wall to the coolant. Although multiple rib configurations have been shown to increase the heat transfer beyond that of angled ribs, this geometry is commonly used in the engine due to the simplicity of the design.

Additional consideration must be given to the fact that many blades use serpentine passages. These cooling passages wind through the blade, and are not limited to a simple straight channel. Coolant flow in the 180 deg turns is very complex, and the heat transfer is dependent on both the channel and turn geometry. Due to the complexity of the turn, studies have concentrated on the heat transfer in only the turn areas [2–4]. It has been determined that the heat transfer coefficients in the turn and downstream of the turn are greater than those upstream of the turn. However, the overall level of heat transfer enhancement is dependent on the cross section of the channel.

Understanding the flow through the coolant passages is not limited to understanding the flow through turbulated, serpentine passages. With the turbine blades rotating, the coolant flow does not behave as typical channel flow. Wagner et al. [5,6] first recorded a difference in the heat transfer coefficients on the leading and trailing surfaces of a rotating channel. From their studies they showed in a square channel (AR=1:1) with radially outward flow, the heat transfer coefficients from the trailing surface increase with rotation, while they decrease from the leading surface. Due to the reversal of the Coriolis force, in channels with radially inward flow, the heat transfer coefficients on the leading surface increase, and they decrease on the trailing surface. Johnson et al. [7] extended this work to show that when the channel is oriented so it is not orthogonal to the direction of rotation, the effect of rotation decreases; in other words, the difference between the heat transfer coefficients on the leading and trailing surfaces decreases. Dutta and Han [8] confirmed this result, and they noted the effect of rotation is greatest in the first pass, and the effect decreases in the subsequent passes.

As stated previously, the geometry of the cooling channels varies depending on the location of the channel in the blade. Many studies have been conducted to study the effect of rotation on rectangular channels. High aspect ratio channels located near the trailing edge have been thoroughly investigated. Azad et al. [9] used a 2:1 (*W:H*) two-pass channel, a more narrow 4:1 channel was used in multiple studies [10–12], and a very narrow 10:1 channel was investigated by Willett and Bergles [13]. In these narrow channels, the heat transfer coefficients on the leading and trailing surfaces are not equal. If the orientation of the 2:1 channel

is varied, the trends are similar to the 1:1 channel; however, when the orientation of the 4:1 channel is varied, all surfaces experience heat transfer enhancement with rotation.

Because the secondary flow patterns in rotating channels are strongly influenced by the cross section of the channel, it is imperative to investigate the effect of rotation in low aspect ratio channels (*W/H*<1) located near the leading edge of a turbine blade. Cho et al. [14] used a mass transfer method to study the effect of rotation in a rotating two-pass rectangular channel (AR =1:2). Their results showed that the rotation effect diminished in the second pass due the 180 deg turn effect. An experimental result for a 1:4 rotating two-pass channel was reported by Agarwal et al. [15] using the mass transfer method. For a smooth surface, they found that the 1:4 channel has lower heat/mass transfer compared to square channel. Fu et al. [16] studied the effect of rotation in both 1:2 and 1:4 channels. They confirmed the reduced effect of rotation in the second pass.

As it was noted earlier, in gas turbine blades, rib turbulators are used in the cooling channels to enhance the heat transfer from the channel walls. Although it is beneficial to study coolant flows in channels with smooth walls, an understanding of flow in channels with ribs is needed by the engine designers. Johnson et al. [7,17] used their square channel to measure the heat transfer coefficients in channels with 45 deg angled ribs. Similar to their smooth channels, the leading and trailing surfaces of the channel experience different levels of heat transfer enhancement. However, because the rib turbulators increase the heat transfer from the channel walls, the difference between the leading and trailing ribbed walls is less than the difference between the smooth walls. Similar results have been observed in square channels with angled ribs by Dutta et al. [18].

Similar to the progression of smooth channels, studies of rotating channels with ribs have evolved to include a wide range of channel cross sections. Al-Hadhrami et al. [19] and Fu et al. [20] investigated the heat transfer enhancement in 2:1 channels with rib turbulators. The more narrow 4:1 channels with rib turbulators have been the focus of several studies [10,21]. With these channels having relatively wide leading and trailing surfaces, both studies recorded significant spanwise variation in the heat transfer coefficients on both the leading and trailing surfaces. The effect of rotation on the heat transfer coefficients in channels located near the leading edge of the blade has also been reported. Similar to the smooth channels, the effect of rotation reduces in these 1:2 [14,22] and 1:4 [15,22] channels.

Many studies have investigated the effect of rotation on the heat transfer in a wide range of cooling channels. However, designers are still left with many holes when applying the published results to their cooling designs. The majority of data available for designers focuses only on the leading and trailing surfaces of the channel; however, it would be beneficial for them to know the heat transfer coefficients on the inner and outer walls of the channels. In addition, the turn regions remain an area of concern. Many factors affect the level of heat transfer enhancement in the 180 deg turns, but these data are rarely reported. Not only are there gaps in the heat transfer data provided to designers, in most cases the overall thermal performance of a cooling scheme is not reported. In other words, the heat transfer enhancement comes at the sacrifice of pressure losses in the channel. Therefore, designers need more information than heat transfer coefficients; they need to know how the rib geometry, turn geometry, and rotation affect the friction factor in the channel.

With these areas needing more attention, the current study is an attempt to fill many of these gaps. With that in mind, the objectives of the current study are the following:

1. Provide designers with heat transfer results at specific locations in channels with smooth walls or walls with angled ribs. Results will be obtained on both the leading and trailing surfaces, as well as the inner and outer walls in selected regions of the
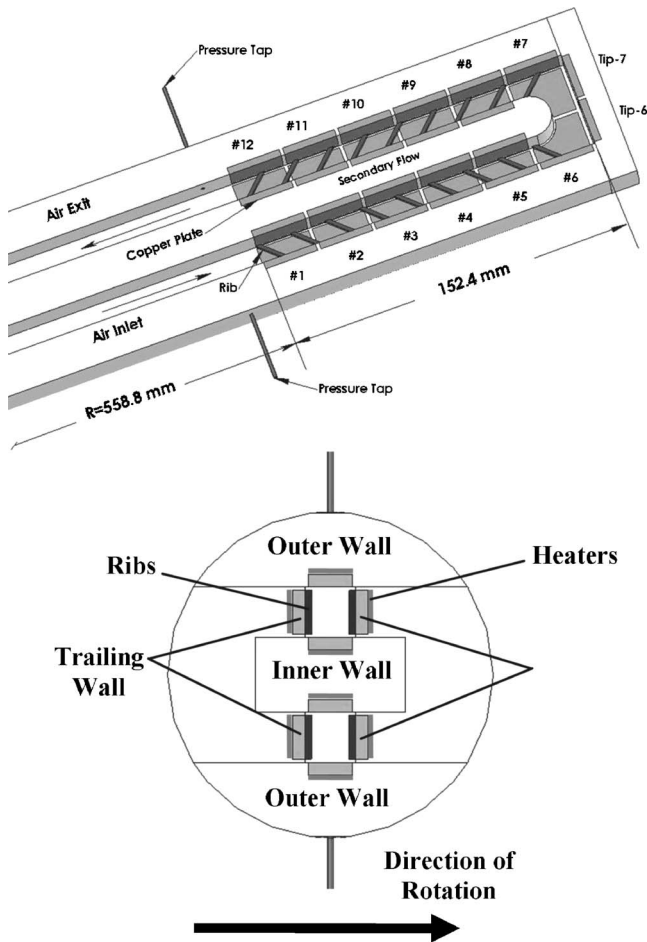
Fig. 1 Three-dimensional view of the square (AR=1:1) test section

Table 1 Dimension of various aspect ratio channels (unit: mm)

$W{:}H$	1:4	1:2	1:1	2:1	4:1[a]
W	12.7	12.7	12.7	25.4	50.8
H	50.8	25.4	12.7	12.7	12.7
e	1.59	1.59	1.59	1.59	1.59
D_h	20.32	16.93	12.7	16.93	20.32
e/D_h	0.078	0.094	0.125	0.094	0.078
e/H	0.031	0.063	0.125	0.125	0.125
P/e	10	10	10	10	10

[a]One-pass channel.

fully developed flow condition. Each pass has a 152.4 mm long heating section. The clearance of the 180 deg sharp turn is 12.7 mm from tip to end wall. The divider wall has a thickness of 19.1 mm with a 9.53 mm radius at the tip.

As shown in Fig. 1, each pass is divided into six segments. Each segment contains four copper plates: one for the leading, one for the trailing, one for the outer, and one for the inner wall. The inner wall has only five segments in the flow direction because of the 180 deg turn. The copper plates are mounted in a nylon substrate, which comprises the bulk of the test section. Prefabricated flexible heaters are installed beneath the copper plates. The round tip of the divider wall is unheated. A total of nine heaters are used for this test section. As shown in Fig. 1(b), each pass has four heaters, and the ninth heater is placed at the tip. All heaters supply steady, uniform heat flux to the copper plates. Sufficient power is supplied in order to maintain a maximum wall temperature of nearly 65°C for the corresponding section. Thermal conducting paste is applied between the heater and copper plates to promote heat transfer from the heater to the plates. Each 3.18 mm thick copper plate has a 1.59 mm deep blind hole drilled in the backside in which a copper-constantan thermocouple is installed 1.59 mm from the plate surface with thermal conducting glue. Thin nylon strips (1.59 mm) between the copper plates reduce the conduction effect between the plates.

Static pressure taps are used to measure the pressure of the coolant at the inlet and outlet of the test section. The inlet pressure tap is located on the outer wall near the inlet of the first pass, and likewise, the outlet tap is placed on the outer wall of the channel downstream of the copper plates. Each pressure tap is connected to a separate channel of the Scani-valve pressure transducer. From the calibration of the transducer with a standard U-tube manometer, the voltage signals obtained from the Scani-valve give the gauge pressure at both the inlet and outlet of the test section. From these measurements, the total pressure drop incurred in the test section can be determined.

The ribs made of brass with a 1.59×1.59 mm cross section are glued on the leading and trailing walls at an angle of 45 deg to the flow direction. There is a 0.79 mm gap between the ribs and the sidewalls to prevent the conduction from ribs to the sidewalls. A thin layer of conductive glue is used so the thermal resistance between the brass ribs and the copper plates is negligible. The ratio of rib pitch-to-rib height is 10. This rib configuration was chosen due to its wide acceptability as a good design. In addition, with this angle and spacing, it is possible to make comparisons with previous studies. The entire test duct is surrounded by insulating nylon material and fits in a hollow cylindrical aluminum alloy arm for structural rigidity.

In addition to the square (AR=1:1) test section described in detail, the thermal performance of four other test sections is considered ($W{:}H$=1:4, 1:2, 2:1, and 4:1). For comparison all cooling channels have an unheated entrance with a constant cross section matching the respective channel. Therefore, in each channel the flow is hydrodynamically developed at the entrance of the heated section. Table 1 shows the dimensions for each test section and

channels. Data for the outer wall of the turn will also be obtained. These measurements are taken in cooling channels with aspect ratios of 1:4, 1:2, 1:1, and 2:1.

2. Compare the overall heat transfer enhancement in rotating channels in various aspect ratio channels. These channel averaged results will give designers an overall picture of the heat transfer trends in various size cooling channels.

3. Provide friction factor for each cooling channel. The overall friction factor will include pressure losses due to channel flow, the 180 deg turn, and, in ribbed channels, the 45 deg angled ribs.

4. Calculate the overall thermal performance (ratio of heat transfer enhancement to friction losses) for each channel and present for comparison of the various channels.

Experimental Facility

To meet the objectives stated above, the rotating test rig previously used by Fu et al. [22] is used here, but the rig underwent minor modification following the previous study. In addition to the components described in the previous study, a 48 channel Scani-valve pressure transducer was fixed to the rotating rig above the slip ring, on the axis of rotation. The signals to and from the transducer were transmitted through the slip ring, as with the thermocouples and heaters (as described in detail by Fu et al. [22]).

Although this study involves the comparison of results from four test sections with various cross sections, the test section comprising the square channel is described here. A schematic of the test section is shown in Fig. 1. The 1:1 ($W{:}H$) test section is 12.7×12.7 mm in cross section. The test section contains a 222.25 mm unheated entrance length to provide a hydrodynamic

the rib parameters. With a constant rib height, the rib height-to-hydraulic diameter ratio varies with the changing hydraulic diameter. In addition, the rib spacing remains constant for each channel ($P/e=10$). Further details for each test section are given by Fu [23]. For all test sections, the experiments were conducted for Reynolds numbers of 5000, 10,000, 25,000, and 40,000, and the test sections rotate at a speed of 550 rpm.

Data Reduction

Heat Transfer Enhancement. This study investigates the regionally averaged heat transfer coefficient at various locations within the rotating ducts. The heat transfer coefficient is determined by the net heat transferred from the heated plate, the surface area of the plate, the regionally averaged temperature of the plate, and the local bulk mean temperature in the channel. Therefore, the heat transfer coefficient is given as

$$h = (Q_{net}/A)/(T_w - T_{b,x}) \tag{1}$$

The net heat transfer is calculated using the measured voltage and current supplied to each heater from the variac transformers multiplied by the area fraction of the heater exposed to the respective plate minus the external heat losses escaping from the test section. The heat losses are predetermined by performing a heat loss calibration for both the rotational and stationary experiments for each test section. The heat loss calibration is performed under no-flow condition by inserting insulation material (fiberglass) into the channel. Therefore the natural convection inside the channel was eliminated. During the calibration, the heat transfer (in the form of power from the variac transformers) and wall temperature of each plate are measured; therefore, from the conservation of energy principle it is possible to know how much heat is being lost to the environment.

The surface area used in this study is the projected surface area of the channel; in other words the surface area of a smooth channel (the 24% area increase due to the ribs is neglected). The regionally averaged wall temperature ($T_{w,x}$) is directly measured using the thermocouple installed in the blind hole on the backside of each copper plate. Because the plates are made of copper, which has a high thermal conductivity, the temperature of each plate is assumed uniform. One thermocouple at the inlet and one thermocouple at the outlet of the test section measure the inlet and outlet bulk temperatures, respectively. Therefore, the bulk temperature at any location in the test section can be calculated using linear interpolation. The results presented from this study are based on the linear interpolation method. Figure 2 shows typical heat flux and temperature distributions for the square channel. The temperature distributions for other Reynolds numbers or channels will be similar to this square channel with Re=10,000. However, the level of power supplied by the heaters will vary, but the trend in the streamwise direction will be similar to the square channel. The data were collected for both rotating and nonrotating ribbed channels, and the Reynolds number of the flow is 10,000. Although linear interpolation is the method of choice for determining the coolant temperature at various locations in the channel, the coolant temperature can also be calculated using the conservation of energy principle. For the present study, both methods compare very well.

The Dittus-Boelter/McAdams [24] correlation for heating ($T_{w,x} > T_{b,x}$) is used in this study to provide a basis of comparison. The Dittus-Boelter/McAdams correlation is used to calculate the Nusselt number for fully developed turbulent flow through a smooth stationary circular tube. Therefore, the Nusselt number ratio is given as

$$Nu/Nu_0 = (hD_h/k)/(0.023Re^{0.8}Pr^{0.4}) \tag{2}$$

All air properties are taken based on the bulk air temperature with a Prandtl number (Pr) for air of 0.71.
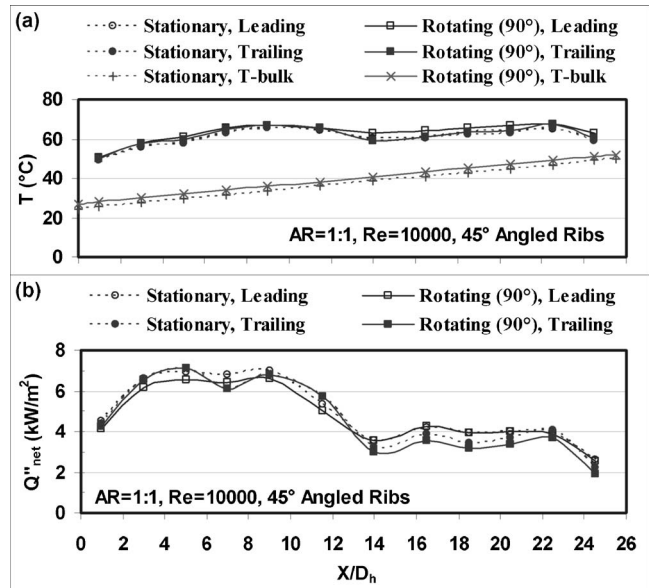
Fig. 2 Sample temperature and heat flux distributions in the square channel

Frictional Losses. The frictional losses in the cooling channel are determined by measuring the pressure drop from the inlet to the outlet of the heated test section. The friction factor is calculated using the measured inlet and outlet pressures as shown in Eq. (3)

$$f = (P_i - P_o)/[4(L/D_h)(0.5\rho V^2)] \tag{3}$$

The friction factor ratio can then be calculated by dividing the fiction factor by the turbulent friction factor in a smooth tube as given by the Blasius equation [25]. This ratio is shown in Eq. (4)

$$f/f_0 = f/(0.079Re^{-0.25}) \tag{4}$$

Thermal Performance. Based on the heat transfer enhancement (Nu/Nu_0) and the pressure loss penalty (f/f_0), the thermal performance, η, of each rib configuration can be calculated. Equation (5) shows the thermal performance based on the constant pumping power condition as used by Han et al. [26]

$$\eta = (Nu/Nu_0)/(f/f_0)^{1/3} \tag{5}$$

An uncertainty analysis was performed based on the method described by Kline and McClintock [27]. Air properties were taken based on the mean bulk air temperature. The estimated uncertainty for the temperature measurements is $0.5\,^\circ C$. The uncertainty of the Nusselt number ratio is approximately 5–8% for the highest Reynolds number. For the lowest Reynolds number (Re=5000), the maximum uncertainty is approximately 20% on the low heat flux wall under the rotating condition. The maximum uncertainty of the friction factor ratio is 7% at Re=10,000. The uncertainty of the friction factor ratio decreases to approximately 3% at the highest Reynolds number.

Results and Discussion

Secondary Flow Behavior. As briefly described earlier, the flow through a serpentine, rotating passage is influenced by many factors, each increasing the complexity of the flow. Only a brief discussion of these factors is given here, as several previous experimental [1,22] and numerical [28,29] studies describe the secondary flow in more detail.

When the coolant travels through the 180 deg turn of a serpentine passage, areas of impingement, separation, and recirculation are created, as shown in Fig. 3. On the outer walls, where the flow
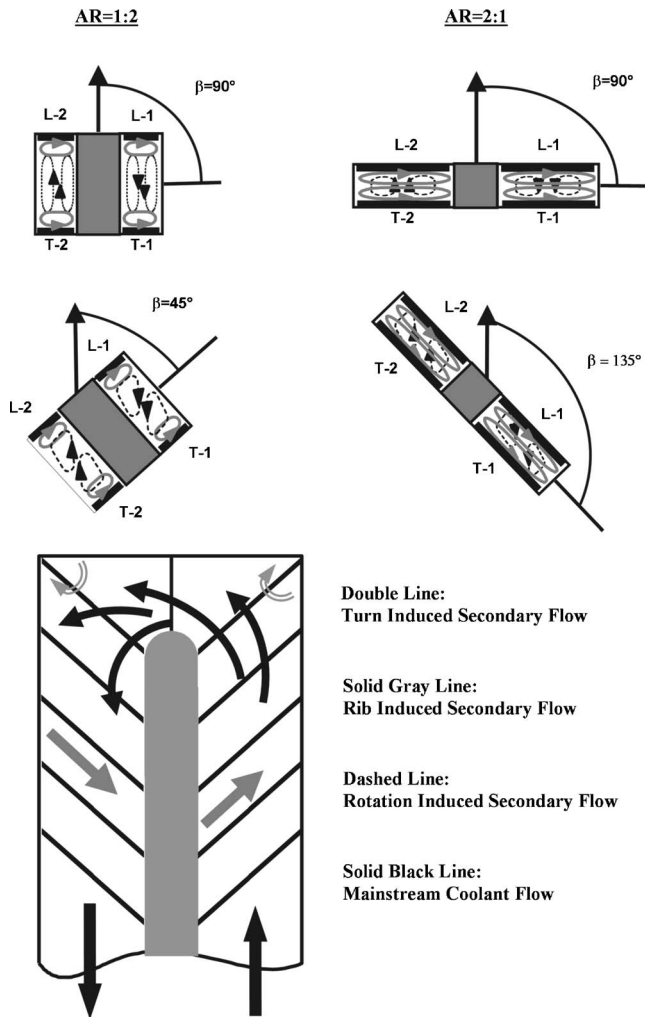
Fig. 3 Conceptual secondary flow patterns

impinges, the heat transfer coefficients are typically elevated. However, near the inner wall, were flow separation occurs, the heat transfer coefficients typically decrease. Depending on the turn geometry, pockets of recirculation may also appear in the corners of the turn.

Angled rib turbulators induce secondary flow patterns that have been shown to increase the heat transfer in the cooling channel. Not only do the angled ribs effectively trip the boundary layer of the coolant, they also induce secondary flow vortices (also shown in Fig. 3) which further enhance the heat transfer. The rib induced vortices impinge on the outer wall in the first pass and on the inner wall in the second pass as a result of the rib orientation. In addition to the leading and trailing walls, heat transfer enhancement is expected on the outer wall in the first pass and on the inner wall in the second pass due to the rib induced secondary flow.

The coolant flow through a rotating channel is altered by both Coriolis forces and buoyancy. The Coriolis force alters both the velocity and temperature profiles of the coolant through the channel. In a channel with radial outward flow (first pass), the coolant is forced toward the trailing surface of the channel, and in channels with radial inward flow (second pass), the core of the coolant is forced toward the leading surface. A secondary effect of the Coriolis force is the formation of a pair of counter-rotating vortices, conceptually drawn in Fig. 3. These vortices significantly increase the heat transfer on the trailing wall in the first pass and the leading wall of the second pass, while the heat transfer de-

creases on the leading wall of the first pass and the trailing wall of the second pass. The strength of the Coriolis force is dependent upon the velocity of the coolant, the channel geometry, and the rotational speed of the channel. These factors can be combined to define the rotation number, Ro, and are shown in Eq. (6)

$$\mathrm{Ro} = \Omega D_h / V \tag{6}$$

In aircraft engines, the rotation number may vary up to 0.25.

The buoyancy parameter due to the centrifugal force and temperature difference is important because of the high rotating speed and large temperature difference in the actual engine. For the radial outward flow, the rotation-induced buoyancy force aids the inertia force. This force opposes the inertia force in the second pass because the flow direction is reversed. A local buoyancy parameter is used to present the combined effects of the Coriolis and buoyancy forces, and in aircraft engines this parameter typically varies from 0-1

$$\mathrm{Bo}_x = (\Delta\rho/\rho)_x(\Omega R_x/V)(\Omega D_h/V) = (\Delta\rho/\rho)_x(\mathrm{Ro}^2)(R_x/D_h) \tag{7}$$

This local buoyancy parameter can be rewritten by incorporating the measured wall and coolant temperatures. Also, as a more direct derivation from the Grashof number of natural convection, the coefficient of volume expansion is defined using the local film temperature. Therefore, the local buoyancy parameter can be defined as shown in Eq. (8)

$$\mathrm{Bo}_x = [(T_{w,x} - T_{b,x})/T_{f,x}](\mathrm{Ro}^2)(R_x/D_h) \tag{8}$$

The local film temperature is the average of the local wall and the local coolant temperatures

$$T_{f,x} = (T_{w,x} + T_{b,x})/2 \tag{9}$$

Square Channel Results. Before meaningful comparisons can be made, it is important to establish a baseline data set. Figure 4 shows the regionally averaged Nusselt number ratio for a square channel (W:H=1:1); the heat transfer enhancement is shown for both smooth and ribbed channels. As expected, the Nusselt number ratios in the smooth non-rotating channels approach a value of unity when the flow becomes fully developed. Through the turn, the values are elevated, and as the flow redevelops in the second pass the Nusselt number ratios gradually decrease. The effect of rotation is most clearly shown for the Reynolds number of 5000. Because the experiments were performed at a constant rotational speed of 550 rpm, the rotation number varies inversely with the Reynolds number of the coolant. Therefore, as the Reynolds number increases, the effect of rotation decreases. At Re=5000, the heat transfer from the trailing surface of the first pass is clearly enhanced above the nonrotating channel, while the first pass leading surface decreases. In the second pass, the trends are reversed, with rotation enhancing the heat transfer from the leading surface. As previous studies have shown (Johnson et al. [7], Dutta and Han [18], and Fu et al. [22]), the effect of rotation is greater in a channel oriented normal to the direction of rotation, than the channel oriented at 135 deg to the direction of rotation. The effect of rotation diminishes as the Reynolds number increases to 40,000 (rotation number decreases).

Figures 4(c) and 4(d) show typical trends for the square channel with angled ribs. Immediately, one can see the angled ribs enhance the heat transfer 2–4 times greater than flow through a smooth channel. In addition the effect of rotation is clearly seen at the Reynolds number of 5000 (Ro=0.118). However, the effect of rotation is less in the ribbed channel than the smooth channel.

Aspect Ratio Comparisons—Channel Average. With a basic understanding of flow through a square channel, these results can be extended and compared with other aspect ratio channels. Because the cooling channels of the blades vary as the cross section of the blade changes, designers need measurements for a wide range of channels. Figure 5 shows a comparison of the aspect ratios that were used to obtain data. Four aspect ratios are consid-
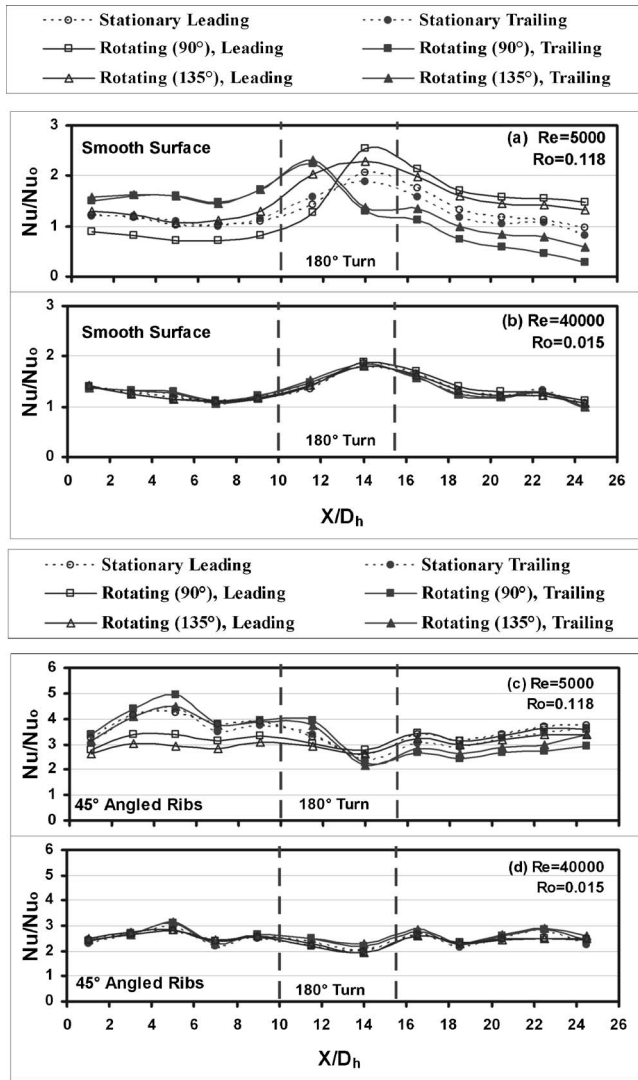
Fig. 4 Regionally averaged Nusselt number distributions for the square channel with smooth and ribbed walls

Fig. 5 Channel cross sections considered in the current study

vided by the rib turbulators is clearly seen in Fig. 6. The trends of the Nusselt number ratios in the ribbed channels are similar to those in the smooth channels with the level of enhancement ranging from 3.7 to 2.5.

Although the levels of heat transfer enhancement for the various aspect ratios are comparable, more information is needed for a complete comparison. Figure 7 shows the friction factor ratio for each of the channels. The pressure penalty for the smooth channels ranges from approximately 2 to 4. These friction ratios are elevated above unity due to the pressure loss incurred in the 180 deg turn. As shown in Fig. 7(a), the friction factor ratio for the 1:4 ribbed channels are only 1.5–2 times greater than the 1:4 smooth channels. This is a stark contrast to the 2:1 channels shown in Fig. 7(d). The pressure penalty for the 2:1 ribbed channels is four times greater than the smooth channels. The size of the rib turbulators is the same for every channel. Therefore, the ribs placed on the leading and trailing walls of the 1:4 channel only affect a very small portion on the coolant flow. However, in the 2:1 channels, these ribs block a significant part of the flow area; therefore, the flow is obstructed, and a significant pressure drop is

ered: W:H=1:4, 1:2, 1:1, and 2:1. Measurements were taken in channels with both smooth walls and ribbed walls. In addition, both nonrotating and rotating channels are considered, and the orientation of the rotating channels is varied. The 1:4 and 1:2 channels are rotated at β=90 and 45 deg, and the 1:1 and 2:1 channels are rotated at β=90 and 135 deg. The orientation angles are comparable to the actual alignment of the various cooling passages in the turbine blades. The data were taken under a fixed maximum inlet coolant-to-wall density ratio (0.12) for both nonrotating and rotating channels. The rotational speed was fixed at 550 rpm for rotating channels.

The first comparisons are done for the overall, or channel averaged, heat transfer. Figure 6 presents the channel averaged Nusselt number ratios for smooth and ribbed channels, and the figure is separated by the channel aspect ratio. The channel averaged Nusselt number ratio is obtained by averaging the leading and trailing surfaces of every point (including the turn). In Fig. 6(a), the Nusselt number ratios in the smooth, rotating channels are greater than the nonrotating channels. The ratios never reach the expected value of unity due to the elevated values at the entrance and in the turn. As the Reynolds number increases, the difference between the rotating and nonrotating results decreases. Similar trends are seen for the 1:2, 1:1, and 2:1 channels in Figs. 6(b), 6(c), and 6(d), respectively. The heat transfer enhancement pro-

Fig. 6 Channel averaged Nusselt number ratios for nonrotating and rotating channels
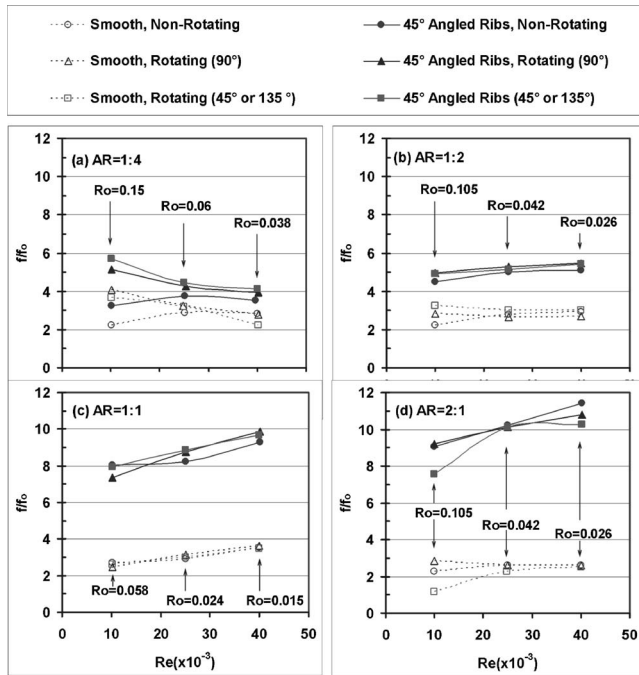
Fig. 7 Overall friction factor ratios for nonrotating and rotating channels

Fig. 8 Overall thermal performance for nonrotating and rotating channels

incurred. This blockage effect is clearly seen by comparing the rib height-to-channel height ratio for each channel (e/H). As shown in Table 1, this blockage ratio is 0.031 for the 1:4 channel, 0.094 for the 1:2 channel, and 0.125 for the 1:1 and 2:1 channels. The effective blockage in the 1:1 and 2:1 channels is four times greater than in the 1:4 channel, and this clearly affects the pressure drop in these channels. The difference between the ribbed and smooth surfaces increases from the 1:4 to the 1:2 channels, and similarly to the 1:1 channel.

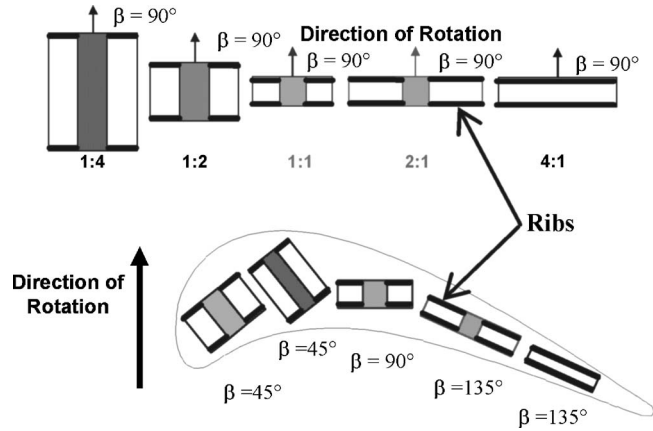Finally, with the channel averaged Nusselt number and friction factor ratios, the thermal performance for each channel can be calculated. As shown in Fig. 8, the trends for the thermal performance are similar to those for the Nusselt number ratios. This should be expected as no significant variations are present with the Nusselt number ratios and the friction factor ratio has a small impact on performance (one-third power on friction factor ratio). The performance for all the smooth channels is approximately 1. Both the Nusselt number ratios and the friction factor ratios are elevated above unity, and when they are combined with the constant pumping power expression, the performance of the smooth channels is approximately one. As shown in Fig. 8, the thermal performance in a channel decreases as the aspect ratio increases. Therefore, the 1:4 channel has the superior thermal performance. This is directly related to the increasing friction factor ratio with the increasing aspect ratio.

Aspect Ratio Comparison—Regional Comparisons. Not only is it desirable to compare the overall performance of the channels, it is also interesting to compare the heat transfer enhancement at specific locations in the channels. All of the two-pass channels contain six copper plates in the first pass and six plates in the second pass. A $W:H=4:1$ single pass test section is also compared to the first pass of the other test sections, and this single pass test section consists of six copper plates in the streamwise direction. Because the test sections have similar construction, the Nusselt number ratios are compared at specific copper plates, rather than at a given x/D_h location. The regions chosen for comparison are 4, 11, 6, and 7; the locations of these regions can be seen in Fig. 1. Regions 4 and 11 should represent fully developed flow in the first and second passes, respectively. Regions 6 and 7
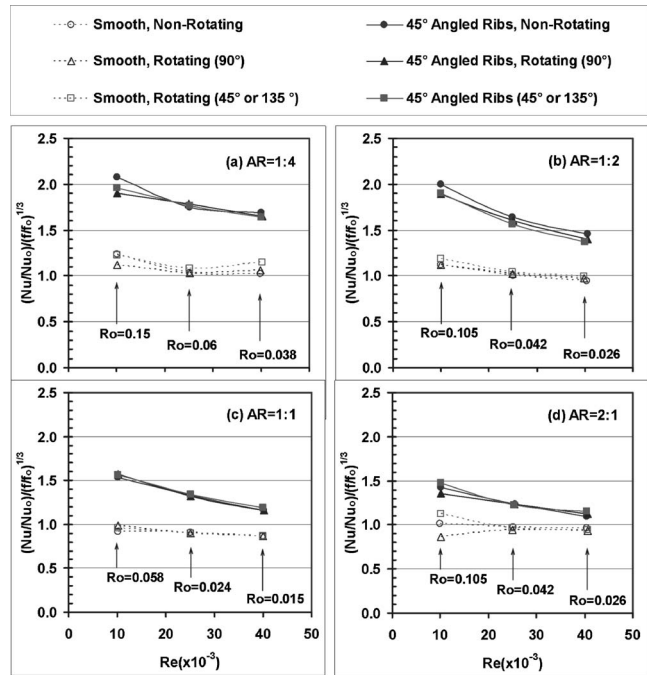
are interesting, as they give more insight to the complexities of the 180 deg turn. For regions 4 and 11, the Nusselt number ratios are presented on the leading, trailing, inner, and outer walls. At regions 6 and 7, similar results are shown including the leading, trailing, outer, and tip surfaces. These local comparisons are completed to show how the heat transfer enhancement varies with the increasing buoyancy parameter, and the comparisons are made for both smooth and ribbed channels positioned normal and skewed to the direction of rotation. Reference points for a nonrotating channel ($Bo_x=0$, $Re=40,000$) are included on each figure. In the nonrotating channels, the difference between the leading and trailing surfaces is negligible, so the points shown are the average of the Nusselt number ratios on the leading and trailing surfaces at the given region. However, the reference points for the inner, outer, and tip surfaces are all included.

Figure 9 shows the effect of the buoyancy parameter on the
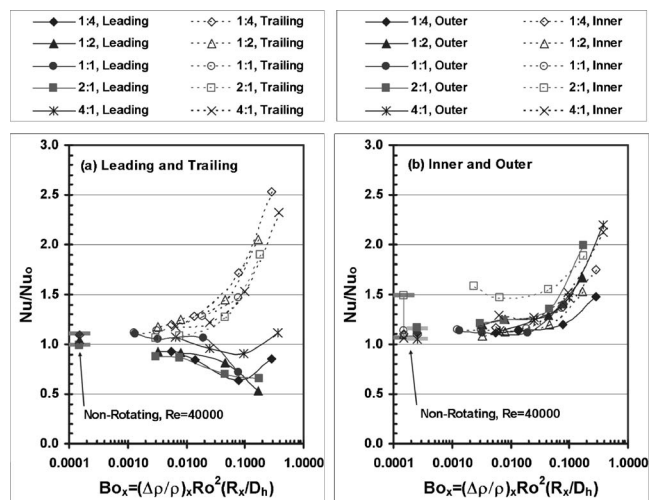
Fig. 9 Nusselt number ratio comparison at region 4 in the smooth channels ($\beta=90$ deg)
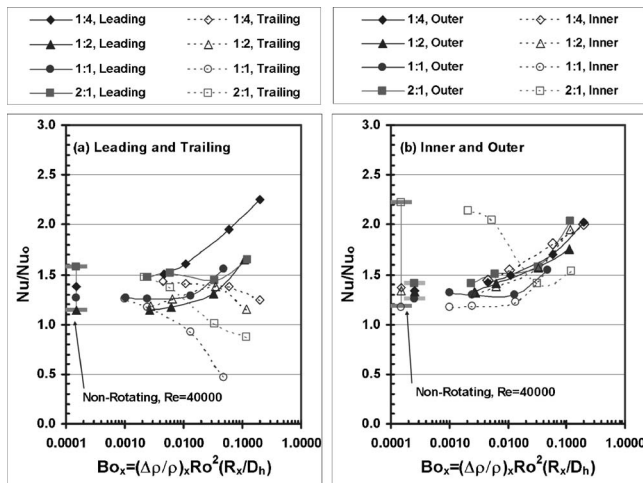
Fig. 10 Nusselt number ratio comparison at region 11 in the smooth channels (β=90 deg)

Fig. 11 Nusselt number ratio comparison at region 6 in the smooth channels (β=90 deg)

Nusselt number ratios at region 4, in the smooth channels oriented at β=90 deg. The separation of the leading and trailing surfaces is clearly seen in Fig. 9(*a*). For the 2:1, 1:1, and 1:2 channels, the Nusselt number ratios on the trailing surface continue to increase with the increasing buoyancy parameter, while the leading surfaces experience a gradual decrease in the heat transfer coefficients. However, in the 1:4 channel, the trailing surface behaves as expected, while the leading surface decreases to a minimum at Bo_x=0.08, and then the Nusselt number ratios increase with the increasing effect of rotation. The 4:1 channel behaves similarly, with less degradation on the leading surface. The trends for the outer and inner walls are less decisive than the leading and trailing surfaces. As Fig. 9(*b*) shows, the heat transfer on both the outer and inner walls increases with rotation for all channels. The level of enhancement for the inner and outer walls of a given aspect ratio is comparable, with the largest separation of the two surfaces occurring in the 1:4 channel.

As expected, the trends for the heat transfer enhancement in the second pass are opposite of those in the first pass. Figure 10 shows the Nusselt number ratios at region 11 in the second pass. As the effect of rotation increases, the heat transfer on the leading surfaces increases and decreases on the trailing surfaces. The level of enhancement and declination is reduced as the effect of rotation is reduced in the second pass. In general, the heat transfer from both the inner and outer surfaces increases with the buoyancy parameter. Figure 10(*b*) shows the exception is with the inner wall of the 2:1 channel. It is conjectured that the elevated Nusselt number ratios, at the lower buoyancy parameters, are the result of flow reattachment after the turn. This 2:1 channel has the largest turn gap; therefore, flow reattachment may occur further downstream than the other channels in the present study. However, it appears as the buoyancy parameter continues to increase, the Nusselt number ratios will continue to rise, after the initial decline, as the effect of rotation overcomes the effect of the turn.

Figures 11 and 12 show the Nusselt number ratios in the 180 deg turns. In region 6 (Fig. 11), both the leading and trailing surfaces experience heat transfer enhancement with rotation, with the trailing surfaces enhanced more than the leading surfaces. In Fig. 11(*b*) it can be seen that the Nusselt numbers on the tip also increase as the rotation number increases. The enhancement on the tip is greater than the leading and trailing surfaces, and this is expected as the coolant flow impinges on the tip. Results for the outer wall are also shown for the 1:1 and 2:1 channels; data were not recorded for this location in the 1:4 and 1:2 channels. It is clear the level of enhancement on this outer wall is much less than
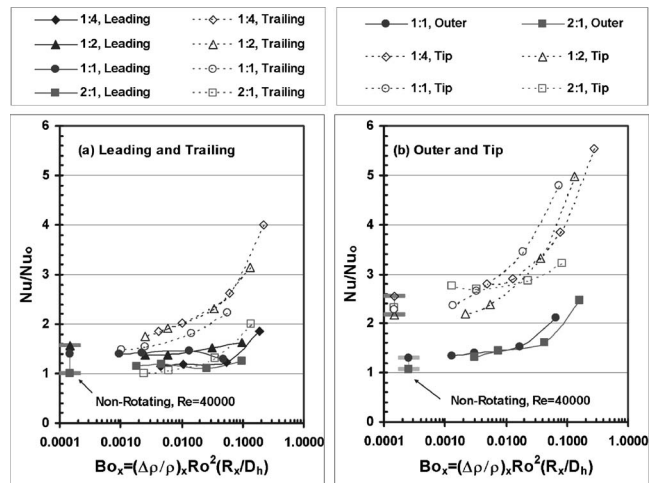
on the tip. In the corner of the turn an area of recirculation exists which hurts the heat transfer performance, and the impingement that occurs on the tip is absent on the outer walls.

Figure 12 shows the Nusselt number ratios for the second half of the turn. As with region 11, the heat transfer on the leading surfaces is enhanced. It is more difficult to make a blanket statement for trailing surface, as both enhancement and declination are shown depending on the channel aspect ratio. An important observation is the comparison of the heat transfer coefficients in region 7 with those in region 6. The level of enhancement in region 7 is significantly greater than in region 6. Figure 12(*b*) shows the tip and outer wall results. The Nusselt number ratios on the outer wall are much higher than those on the outer wall of region 6. As the flow travels through the turn, it now impinges on this outer wall. In general, the level of enhancement on the tip is the same at both locations in the turn.

Local comparisons were also made for the smooth channel with varied orientations. To model the location of the cooling channels in the blade, Figs. 13–16 show the Nusselt number ratios for the 1:4 and 1:2 channels oriented at 45 deg, the 1:1 channel maintaining its orientation of 90 deg, and the 2:1 and 4:1 channels oriented at 135 deg, with respect to the direction of rotation. Immediately seen in Fig. 13(*a*) is that the effect of rotation decreases in the skewed channels. The heat transfer on the trailing surfaces in-

Fig. 12 Nusselt number ratio comparison at region 7 in the smooth channels (β=90 deg)
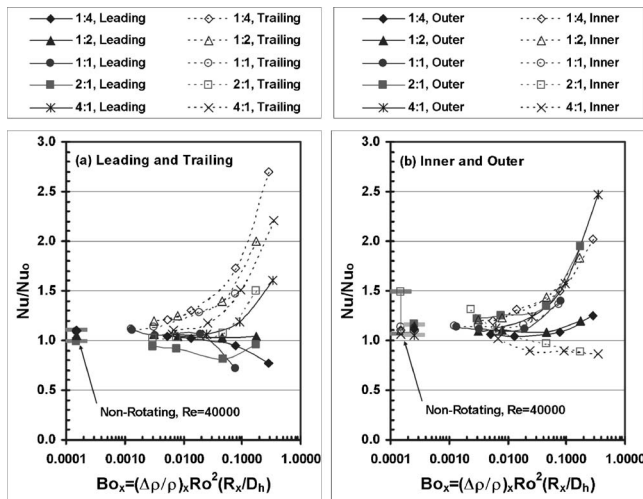
Fig. 13 Nusselt number ratio comparison at region 4 in the smooth channels (β=45 or 135 deg)

Fig. 15 Nusselt number ratio comparison at region 6 in the smooth channels (β=45 or 135 deg)

creases at region 4 in every channel. While on the leading surface, the Nusselt number ratios increase for the 4:1 and 2:1 channels, and see a slight declination in the 1:4 and 1:2 channels.

The general increase that was seen for the inner and outer surfaces in the normal channel is not seen for the skewed channels. The rotation induced vortices are altered, as shown in Fig. 3, and they do not impinge directly on the trailing surface of the first pass (as they do when the orientation angle is 90 deg). In the 1:4 and 1:2 channels, with β=45 deg the rotation induced vortices travel from the leading-outer corner to the trailing-inner corner. Therefore, the secondary flow impinges on the inner wall of these channels; thus increasing the heat transfer coefficients on the inner surface. However, the 2:1 and 4:1 channels are oriented at 135 deg, so the secondary induced vortices travel from the leading-inner wall to the trailing-outer all. For this orientation, the coolant impinges on the outer surface, rather than the inner, and the heat transfer coefficients increase on the outer wall.

For region 11, the heat transfer coefficients on the leading surface are greater than the trailing surface for all channels, as shown in Fig. 14. With the skewed channel (β=45 deg), both the leading and trailing surfaces of the 1:4 and 1:2 channels experience heat transfer enhancement with rotation. The trends for the inner and outer wall are similar to those of region 4. Again, due to the
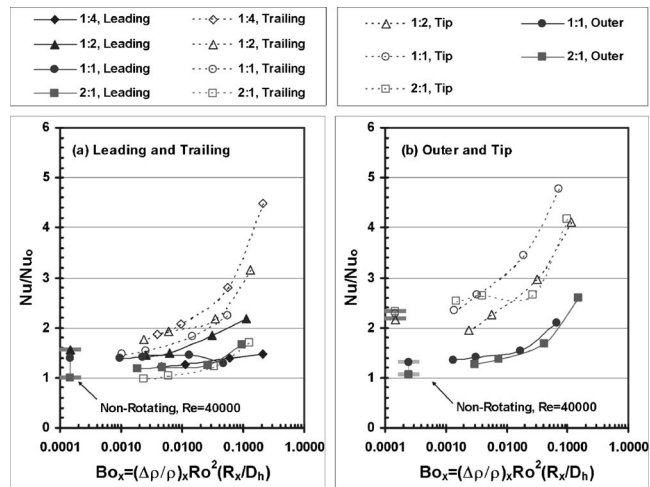
shifting of the rotation induced vortices, the inner walls of the 1:2 and 1:4 are the recipients of impingement of the coolant, and therefore, the enhancement is greater for the inner walls than the outer walls. The opposite is true for the 2:1 channel (β =135 deg) where the rotation induced secondary flow impinges on the outer wall.

The turn results are shown in Figs. 15 and 16 for regions 6 and 7, respectively. The trends for region 6 are similar to those of region 4; the difference lies with the level of enhancement. The heat transfer enhancement of region 6 is much greater than of region 4. The same can be said for the trends of regions 7 and 11. The orientation angle does not have a significant effect on the Nusselt number ratios on the tip and outer walls of the points in the turn (Figs. 15(b) and 16(b)). The level of the trends for the heat transfer enhancement on both the outer and tip walls is very similar to the results for the channels oriented normal (β =90 deg) to the direction of rotation (Figs. 11(b) and 12(b)).

The sequence of Figs. 17–24 is the same as Figs. 9–16. Whereas the previous figures compared the Nusselt number ratios in smooth channels, the following figures compare the heat transfer enhancement in rotating channels with angled ribs. Figure 17 shows the Nusselt number ratios at region 4 in the ribbed channel with β=90 deg. For all aspect ratios, heat transfer from the trail-

Fig. 14 Nusselt number ratio comparison at region 11 in the smooth channels (β=45 or 135 deg)

Fig. 16 Nusselt number ratio comparison at region 7 in the smooth channels (β=45 or 135 deg)

Fig. 17 Nusselt number ratio comparison at region 4 in the ribbed channels ($\beta=90$ deg)
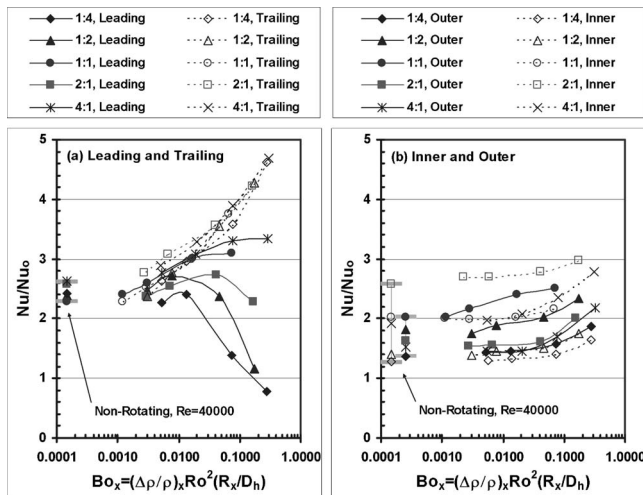
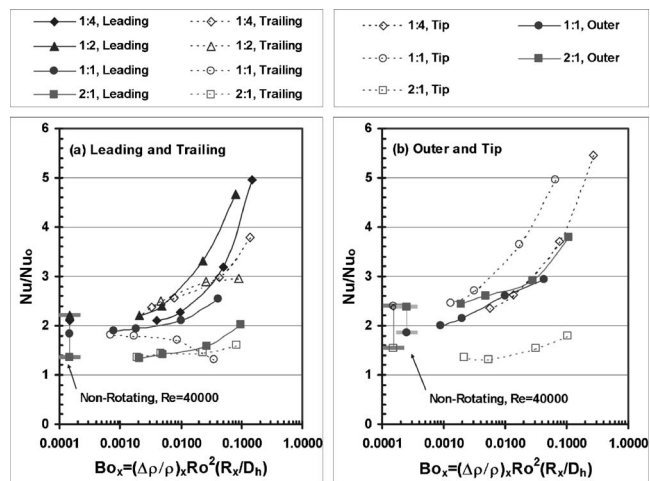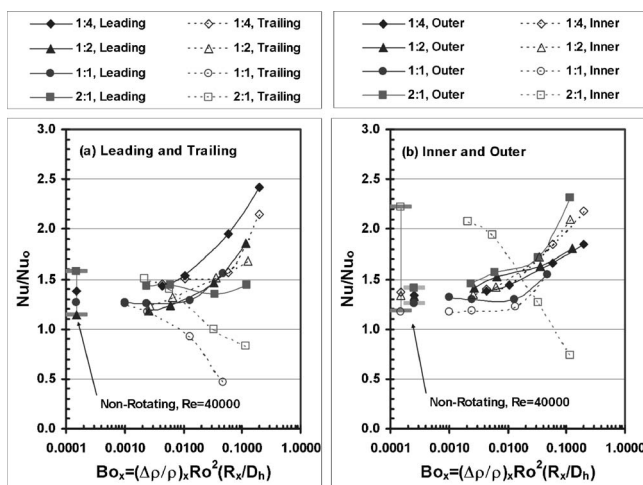**Fig. 19 Nusselt number ratio comparison at region 6 in the ribbed channels ($\beta=90$ deg)**

ing surfaces is enhanced with rotation. However, the trends on the leading surfaces vary significantly depending on the aspect ratio. The heat transfer coefficients on the leading surface decrease in the 2:1, 1:2, and 1:4 channels. The most severe declination clearly occurs in the 1:4 channel. The predictions of Su et al. [29] showed two vortices are formed from the interaction of the rotation and rib induced secondary flow. One vortex encompasses the majority of the channel, while the second, much smaller vortex, is limited to a small area near the leading surface of the channel. With limited interaction of the coolant core with the leading wall, this would explain why the Nusselt number ratios on the leading surface are very low.

The heat transfer on all of the inner and outer walls in region 4 is enhanced with rotation. The ribs are placed so the coolant near the wall travels from the inner wall to the outer wall. With the varying aspect ratios, the actual length of the ribs varies. In other words, the ribs in the 1:2 and 1:4 channels are much shorter than those in the 2:1 and 4:1 channels. In the 1:2 and 1:4 channels, the heat transfer on the outer walls is greater than the inner walls. The coolant travels along the rib from the inner wall and impinges on the outer surface; thus, increasing the heat transfer. Although the secondary flow pattern in the 2:1 and 4:1 channels is the same as for the 1:2 and 1:4 channels, the heat transfer coefficients on the

inner surface are greater than those on the outer surface. In this case the ribs are much longer, and as the coolant travels along the rib, the boundary becomes thicker, and the heat transfer decreases as the coolant temperature increases. Therefore, the impingement of the relatively warmer fluid on the outer wall is less effective than in the 1:2 and 1:4 channels.

Figure 18 shows the results for region 11 in the ribbed channels. In the second pass, the heat transfer on both the leading and trailing surfaces increases with rotation. In the second pass, the ribs are placed so the secondary flow travels from the outer to the inner wall. However, the clear distinction between the outer and inner walls is not seen in the second pass as it is in the first pass. The extreme drop in the Nusselt number ratios on the inner wall of the 2:1 channel is unusual, and this result must be further investigated to establish the validity of the trend.

The data collected in the 180 deg turns of the ribbed channels are shown in Figs. 19 and 20. As shown in Fig. 1, the ribs do not extend all the way to the tip of the turn. The trends for the leading and trailing surfaces of region 6 (Fig. 19(a)) are similar to those of region 4. In this location the Nusselt numbers are much greater than those at region 4. The tip and outer wall of region 6 are shown in Fig. 19(b), the increase with rotation is less than for the smooth channel, but this is expected as the effect of rotation de-

Fig. 18 Nusselt number ratio comparison at region 11 in the ribbed channels ($\beta=90$ deg)

Fig. 20 Nusselt number ratio comparison at region 7 in the ribbed channels ($\beta=90$ deg)

Fig. 21 Nusselt number ratio comparison at region 4 in the ribbed channels ($\beta = 45$ or 135 deg)
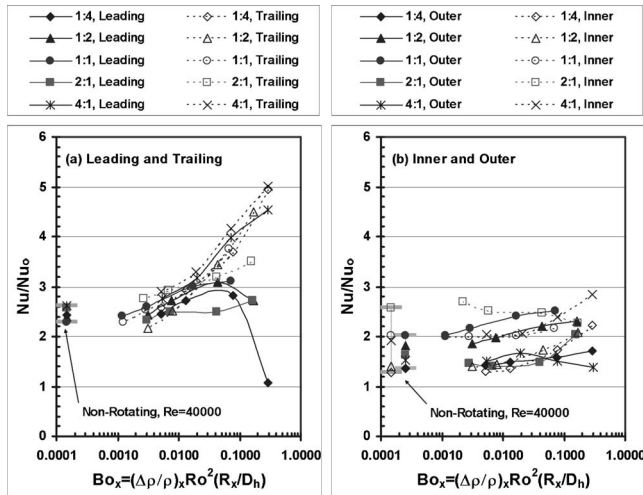
Fig. 23 Nusselt number ratio comparison at region 6 in the ribbed channels ($\beta = 45$ or 135 deg)

creases with the use of rib turbulators. All surfaces at region 7 are increasing with rotation (Fig. 20). As with the smooth channel, the Nusselt number ratios are greater after the turn than before the turn.

The final group of plots (Figs. 21–24) shows the Nusselt number ratios in ribbed channels with varying orientations. Combinations of the various trends shown previously are shown in these plots. The effect of rotation is reduced with the varied orientation. The difference between the leading surface and the trailing surface is smaller compared to the channel oriented normal to the flow direction. With only a couple of exceptions, the heat transfer from all surfaces at all locations is enhanced with rotation. This offers positive information for the engine designers. The most glaring exception occurs in the 1:4 channel. The low heat transfer from the leading surface is the result of the interaction of the rotation and rib induced secondary flow. The combined effect traps the warm air near the surface, resulting in decreased heat transfer on the leading surface in the first pass.

Conclusions

This study presents a variety of heat transfer results in a wide range of turbine blade cooling channels. The data were taken with a fixed, maximum inlet coolant-to-wall density ratio (0.12) for both nonrotating and rotating channels and a fixed rotational speed (550 rpm) for rotating channels. In addition to the W:H = 1:1 channel results, both smooth and angled ribs, overall channel averaged and regional results are shown for aspect ratios ranging from 1:4 to 4:1. This range of cross sections covers the majority of channels that could be seen in actual engines. From this experimental study, the following conclusions can be drawn:
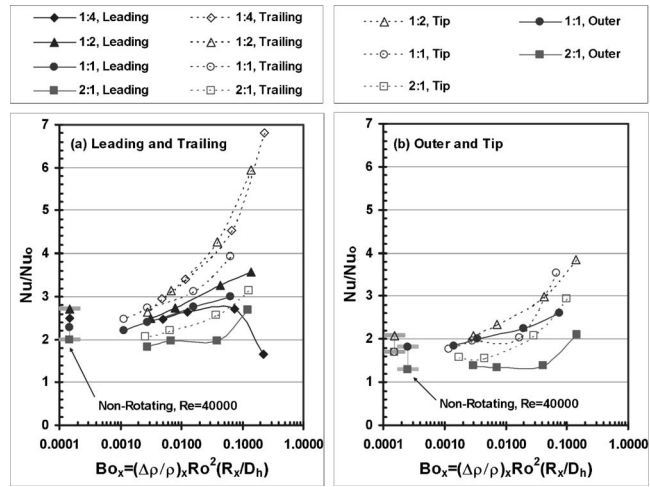
1. The overall levels of heat transfer enhancement for all the ribbed channels are comparable. However, significant differences arise with the pressure losses incurred in the channel. The 1:4 channel incurred the lowest pressure penalty; therefore, the thermal performance of the 1:4 channel is superior to 1:2, 1:1, and 2:1 channels, respectively.

2. The trends of the Nusselt number ratios on the leading and trailing surfaces of the smooth channel depend on the location within the channel. In the first pass, the heat transfer on the trailing surfaces increases, while it decreases on the leading surfaces. However, at the inlet of the 180 deg turn, the heat transfer increases on both the leading and trailing surfaces for all aspect ratios. In the second passes of the smooth channels, the effect of rotation is reduced.

3. In general, the heat transfer coefficients on the inner and outer walls of the smooth channel increase with rotation. The elevation of the inner above the outer, or vice versa, depends on
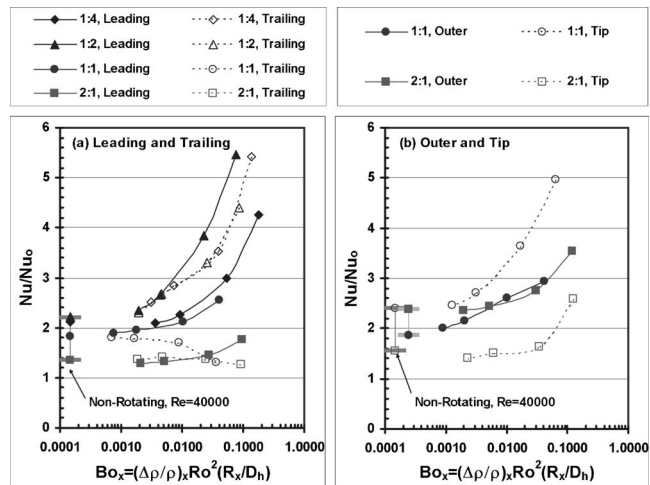

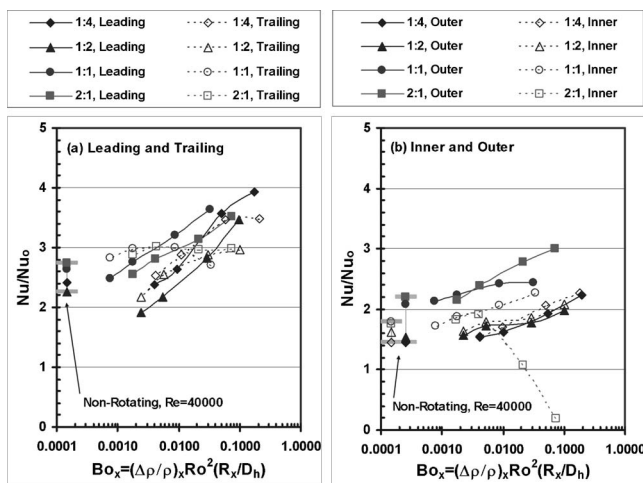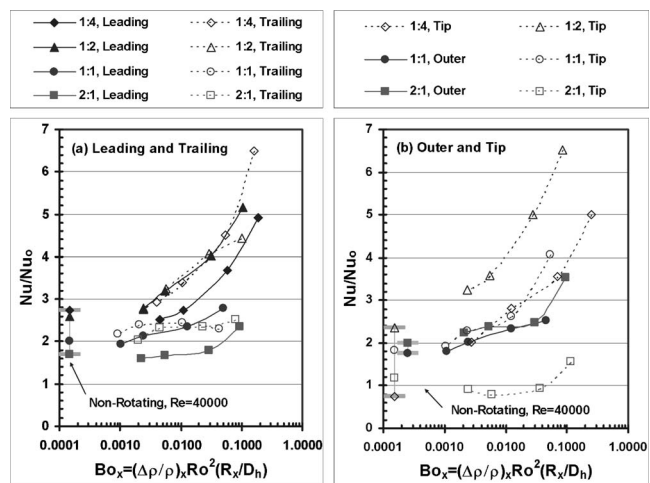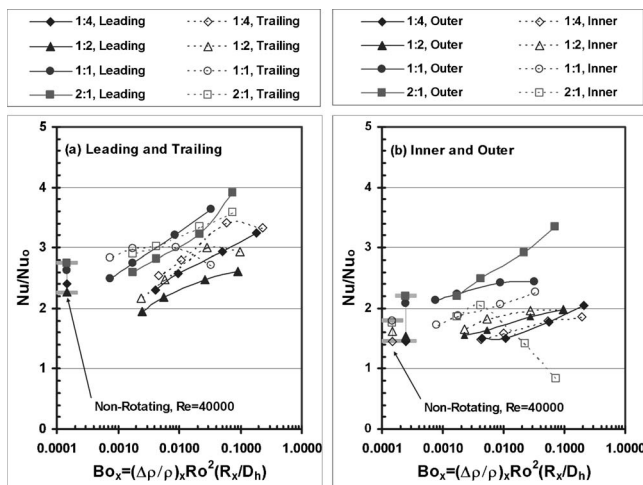**Fig. 22 Nusselt number ratio comparison at region 11 in the ribbed channels ($\beta = 45$ or 135 deg)**

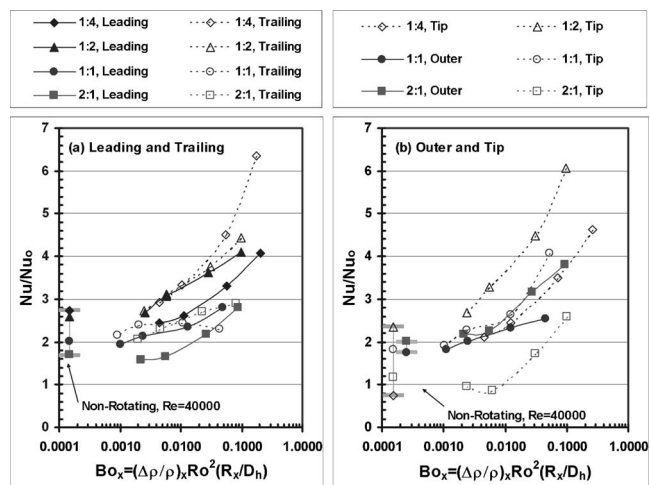**Fig. 24 Nusselt number ratio comparison at region 7 in the ribbed channels ($\beta = 45$ or 135 deg)**

1140 / Vol. 128, NOVEMBER 2006

which location of which channel is being considered. For channels with $\beta=90$ deg, the inner and outer wall are enhanced equally. However, when the orientation is altered, separation occurs between the inner and outer surfaces depending on the direction of the rotation induced vortices.

4. The general trends of the leading and trailing surfaces in ribbed channels follow those of the smooth channel. For the chosen angled rib geometry, the first pass, leading surface is adversely affected by the interaction of the rotation and rib induced vortices.

5. Positive information for designers is the heat transfer enhancement on both the inner and outer walls in the ribbed channels. With the increasing buoyancy parameter, the Nusselt number ratios increase at each point on both the inner and outer walls.

To further understand the heat transfer in rotating channels with smooth walls and ribbed walls, future studies should include the following parameters: rotational speed, Reynolds number (including high Reynolds numbers), coolant-to-wall density ratio, rib spacing, and rib height-to-channel hydraulic diameter ratio.

Nomenclature

A = area of smooth wall
AR = aspect ratio, W:H
Bo_x = local buoyancy parameter, $(\Delta\rho/\rho)_x(\mathrm{Ro}^2)(R_x/D_h)$
D_h = channel hydraulic diameter
e = rib height
f = friction factor
f_0 = fully developed friction factor in nonrotating smooth tube
h = heat transfer coefficient
H = channel height
k = thermal conductivity of coolant
L = heated length of the test section
Nu = local Nusselt number, hD_h/k
Nu_0 = Nusselt number for fully developed turbulent flow in smooth pipe
P = rib pitch
P_i = pressure at the inlet of the test section
P_o = pressure at the outlet of the test section
Pr = Prandtl number
Q = heat transfer rate at wall
Q_{net} = net heat transfer rate at wall
Q_{loss} = heat loss
R = rotating radius
R_x = local rotating radius
Re = Reynolds number, $\rho V D_h/\mu$
Ro = rotation number, $\Omega D_h/V$
$T_{b,i}$ = inlet coolant temperature
$T_{b,x}$ = local coolant temperature
$T_{f,x}$ = local film temperature, $T_{f,x}=(T_{b,x}+T_{w,x})/2$
$T_{w,x}$ = regionally averaged wall temperature
V = bulk velocity in streamwise direction
W = channel width
x = streamwise location
β = angle of channel orientation with respect to the axis of rotation
μ = dynamic viscosity of coolant
ρ = density of coolant
$(\Delta\rho/\rho)_{\mathrm{inlet}}$ = maximum inlet coolant-to-wall density ratio, $(\Delta\rho/\rho)_{\mathrm{inlet}}=(T_w-T_{b,i})/T_w$
$(\Delta\rho/\rho)_x$ = local coolant-to-wall density ratio, $(\Delta\rho/\rho)_x=(T_{w,x}-T_{b,x})/T_{f,x}$
Ω = rotational speed

References

[1] Han, J. C., Dutta, S., and Ekkad, S. V., 2000, *Gas Turbine Heat Transfer and Cooling Technology*, Taylor And Francis, New York.
[2] Metzger, D. E., and Sahm, M. K., 1986, "Heat Transfer Around Sharp 180° Turns in Smooth Rectangular Channels," ASME J. Heat Transfer, **108**, pp. 500–506.
[3] Fan, C. S., and Metzger, D. E., 1987, "Effects of Channel Aspect Ratio on Heat Transfer in Rectangular Passage Sharp 180° Turn," ASME Paper No. 87-GT-113.
[4] Han, J. C., Chandra, P. R., and Lau, S. C., 1988, "Local Heat/Mass Transfer in Distributions Around Sharp 180 Deg. Turns in Two-Pass Smooth and Rib-Roughened Channels," ASME J. Heat Transfer, **110**, pp. 91–98.
[5] Wagner, J. H., Johnson, B. V., and Hajek, T. J., 1991, "Heat Transfer in Rotating Passage With Smooth Walls and Radial Outward Flow," ASME J. Turbomach., **113**, pp. 42–51.
[6] Wagner, J. H., Johnson, B. V., and Kooper, F. C., 1991, "Heat Transfer in Rotating Passage With Smooth Walls," ASME J. Turbomach., **113**, pp. 321–330.
[7] Johnson, B. V., Wagner, J. H., Steuber, G. D., and Yeh, F. C., 1994, "Heat Transfer in Rotating Serpentine Passage With Selected Model Orientations for Smooth or Skewed Trip Walls," ASME J. Turbomach., **116**, pp. 738–744.
[8] Dutta, S., and Han, J. C., 1996, "Local Heat Transfer in Rotating Smooth and Ribbed Two-Pass Square Channels With Three Channel Orientations," ASME J. Heat Transfer, **118**, pp. 578–584.
[9] Azad, G. S., Uddin, M. J., Han, J. C., Moon, H. K., and Glezer, B., 2002, "Heat Transfer in a Two-Pass Rectangular Rotating Channel With 45-Deg Angled Rib Turbulators," ASME J. Turbomach., **124**, pp. 251–259.
[10] Griffith, T. S., Al-Hadhrami, L., and Han, J. C., 2002, "Heat Transfer in Rotating Rectangular Cooling Channels (AR=4) With Angled Ribs," ASME J. Heat Transfer, **124**, pp. 617–625.
[11] Acharya, S., Agarwal, P., and Nikitopoulos, D. E., 2004, "Heat/Mass Transfer in a 4:1 AR Smooth and Ribbed Coolant Passage With Rotation in 90-Degree and 45-Degree Orientations," ASME Paper No. GT2004–53928.
[12] Zhou, F., Lagrone, J., and Acharya, S., 2004, "Internal Cooling in 4:1 AR Passages at High Rotation Numbers," ASME Paper No. GT2004–53501.
[13] Willett, F. T., and Bergles, A. E., 2001, "Heat Transfer in Rotating Narrow Rectangular Ducts With Heated Sides Orientated at 60° to the *R-Z* Plane," ASME J. Turbomach., **123**, pp. 288–295.
[14] Cho, H. H., Kim, Y. Y., Kim, K. M., and Rhee, D. H., 2003, "Effects of Rib Arrangements and Rotation Speed on Heat Transfer in a Two-Pass Duct," ASME Paper No. 2003-GT-38609.
[15] Agarwal, P., Acharya, S., and Nikitopoulos, D. E., 2003, "Heat Transfer in 1:4 Rectangular Passages With Rotation," ASME J. Turbomach., **125**, pp. 726–733.
[16] Fu, W. L., Wright, L. M., and Han, J. C., 2005, "Heat Transfer in Two-Pass Rotating Rectangular Channels (A=1:2 and AR=1:4) With Smooth Walls," ASME J. Turbomach., **127**, pp. 265–277.
[17] Johnson, B. V., Wagner, J. H., Steuber, G. D., and Yeh, F. C., 1994, "Heat Transfer in Rotating Serpentine Passage With Trips Skewed to the Flow," ASME J. Turbomach., **116**, pp. 113–123.
[18] Dutta, S., and Han, J. C., 1996, "Local Heat Transfer in Rotating Smooth and Ribbed Two-Pass Square Channels With Three Channel Orientations," ASME J. Turbomach., **118**, pp. 578–584.
[19] Al-Hadhrami, L., and Han, J. C., 2003, "Effect of Rotation on Heat Transfer in Two-Pass Square Channels With Five Different Orientations of 45° Angled Rib Turbulators," Int. J. Heat Mass Transfer, **46**, pp. 653–669.
[20] Fu, W. L., Wright, L. M., and Han, J. C., 2004, "Heat Transfer in Two-Pass Rotating Rectangular Channels (AR=2:1) With Discrete V-Shaped and Discrete Angled Rib Turbulators," ASME Paper No. IMECE2004–50563.
[21] Wright, L. M., Fu, W. L., and Han, J. C., 2005, "Thermal Performance of Angled, V-Shaped, and W-Shaped Rib Turbulators in Rotating Rectangular Cooling Channels (AR=4:1)," ASME J. Turbomach., **126**, pp. 604–614.
[22] Fu, W. L., Wright, L. M., and Han, J. C., 2005, "Heat Transfer in Two-Pass Rotating Rectangular Channels (A=1:2 and AR=1:4) With 45 Deg Angled Rib Turbulators," ASME J. Turbomach., **127**, pp. 164–174.
[23] Fu, W. L., 2005, "Aspect Ratio Effect on Heat Transfer in Rotating Two-Pass Rectangular Channels With Smooth Walls and Ribbed Walls," Ph.D., thesis, Texas A&M University, College Station, TX.
[24] Rohsenow, W. M., and Choi, H., 1961, *Heat, Mass, and Momentum Transfer*, Prentice-Hall, Englewood Cliffs, NJ, pp. 192–193.
[25] Kays, W. M., and Crawford, M. E., 1993, *Convective Heat and Mass Transfer*, 3rd ed., McGraw-Hill, New York, p. 249.
[26] Han, J. C., Park, J. S., and Lei, C. K., 1985, "Heat Transfer Enhancement in Channels With Turbulence Promoters," ASME J. Eng. Gas Turbines Power, **107**, pp. 628–635.
[27] Kline, S. J., and McClintock, F. A., 1953, "Describing Uncertainty in Single-Sample Experiments," Mech. Eng. (Am. Soc. Mech. Eng.), **75**, pp. 3–8.
[28] Al-Qahtani, M., Jang, Y. J., Chen, H. C., and Han, J. C., 2002, "Prediction of Flow and Heat Transfer in Rotating Two-Pass Rectangular Channels With 45-deg Rib Turbulators," ASME J. Turbomach., **124**, pp. 242–250.
[29] Su, G., Chen, H. C., Han, J. C., and Heidmann, D., 2004, "Computation of Flow and Heat Transfer in Two-Pass Rotating Rectangular Channels (AR=1:1, AR=1:2, AR=1:4) with 45-Deg Angled Ribs by a Reynolds Stress Turbulence Model," ASME Paper No. GT2004–53662.

An Analytical Approach to the Heat and Mass Transfer Processes in Counterflow Cooling Towers

Chengqin Ren

College of Mechanical and Automotive Engineering,
Hunan University,
Changsha, 410082, China
e-mail: renchengqin@163.com

Quick and accurate analysis of cooling tower performance, outlet conditions of moist air, and parameter profiles along the tower height is very important in rating and design calculations. This paper developed an analytical model for the coupled heat and mass transfer processes in counterflow cooling towers based on operating conditions more realistic than most conventionally adopted Merkel approximations. In modeling, values of the Lewis factor were not necessarily specified as unity. Effects of water loss by evaporation and water film heat transfer resistance were also considered in the model equations. Within a relatively narrow range of operating conditions, the humidity ratio of air in equilibrium with the water surface was assumed to be a linear function of the surface temperature. The differential equations were rearranged and an analytical solution was developed for newly defined parameters. The analytical model predicts the tower performances, outlet conditions, and parameter profiles quickly and accurately when comparing with the numerical integration of the original differential equations.
[DOI: 10.1115/1.2352780]

Keywords: cooling towers, performances, parameter profiles, modeling

1 Introduction

Cooling towers are widely used in most industrial power generation units, refrigeration and air conditioning plants, chemical, petrochemical, and petroleum industries to reject waste heat to the environment. Quick and accurate analysis of tower performance, outlet conditions of moist air, as well as parameter profiles along the tower height is very important in rating and design calculations. This paper aims at developing an analytical model for counterflow cooling tower operation.

Systems of differential equations for simultaneous heat and mass transfer processes in counterflow cooling towers were developed with different assumptions in history. The Merkel method [1], developed in the 1920s, relies on several critical assumptions to reduce the solution to a simple manual iteration. These assumptions are: (1) the resistance for heat transfer in the water film is negligible, (2) the effect of water loss by evaporation on energy balance or air process state is neglected, (3) the specific heat of air-stream mixture at constant pressure is same as that of the dry air, and (4) the Lewis factor for humid air is unity. Merkel combined equations for heat and water vapor transfer into a single equation similar as

$$\dot{m}_w c_w dt_w = h_D a dV (h_I - h_a) = \dot{m}_a dh_a \qquad (1)$$

Further, when the outlet conditions of air are to be calculated, air is assumed to be saturated at the exit position [2,3]. Baker and Shryock [4] reviewed Merkel's work and examined the effects of the first two approximations listed above. An offset ratio, which was defined as the reciprocal of the slope of tie line E [5] as follows, was introduced to improve the model accuracy

$$\frac{t_I - t_w}{h_I - h_a} = -\frac{h_D}{h_{c,w}} = -\frac{1}{E} \qquad (2)$$

Exactly to say, the E value which is equal to $h_{c,w}/h_D$ represents the slope of tie line only when the Lewis factor is equal to unity. Otherwise, Eq. (2) may not be true and E only represents the ratio of the water film heat transfer coefficient to the air film mass transfer coefficient. Baker and Shryock found that taking into consideration the effect of water film heat transfer resistance with a value of -0.09 lb F/Btu offset ratio (i.e., $E = 11.1$ Btu/lb F $= 46.5$ kJ/kg K) and the effect of water loss by evaporation on energy balance yields the best results. However, when dealing with the effect of water film heat transfer resistance, Dessouky et al. [5] used the values of $E = 15 - \infty$ J/(kg K) and Khan and Zubair [6] used the values of $E = 11.1 - \infty$ kJ/(kg K) while Webb [7] assumed that t_w is nearly equal to $(t_i + 0.5)$°C. A comparative study showed that the error caused by the Merkel approximation increases as the E value decreases. Sutherland [8] compared a simulation analysis of mechanical draught cooling towers, including the effect of water loss by evaporation and setting the Lewis factor to 0.9, with the approximate Merkel method analysis. The results showed that substantial underestimates of tower volume of from 5% to 15% with the average value being as good as 8% were obtained when the approximate Merkel method was used. Osterle [9] developed a wet-cooling tower model that corrected the Merkel assumption so that the effect of water loss by evaporation was accounted for. However, he still assumed that the Lewis factor was equal to unity. Khan and Zubair [6] performed simulation studies with the Lewis factor ranges from 0.8 to 1.2. Kloppers and Kröger [2] argued by citation from published literatures that the Lewis factor may deviate significantly from unity in different operating conditions and different Lewis factors were specified for their investigations. The minimum Lewis factor specified was 0.5 and the maximum 1.5. It was found that the higher the Lewis factor, the more heat is rejected from the tower, with a corresponding increase in outlet air temperature and a decrease in outlet water temperature. The Poppe method [10], developed in

the 1970s, does not make most of the simplifying assumptions of the Merkel method but still neglects the liquid film heat transfer resistance. The Poppe method allows the moist air to be supersaturated during the heat and mass transfer processes. A comparative study of the Merkel, Poppe, and effectiveness-number of transfer units (e-NTU) methods was performed by Kloppers and Kröger [3]. The Merkel number (or transfer characteristic) was found to be underestimated by the Merkel method due to the neglecting of the effect of water loss by evaporation on energy balance. It was also found that the degree of supersaturation does not have a great influence on the relative difference between the outlet air temperatures predicted by the Merkel and Poppe analyses. In the unsaturated region, however, a large discrepancy in the air temperatures predicted by the Poppe and Merkel methods was found.

Hardly can an analytical solution be developed without assorting to at least some of the Merkel approximations discussed above. Maclaine-Cross and Banks [11] developed an analytical solution for wet surface heat exchangers where the Lewis factor was assumed to be unity. When the flowing fluid is water and the wall is removed, the model represents a cooling tower. In modeling, the moisture content of air in equilibrium with the water surface was assumed as a linear function of the water surface temperature. The differential equations were rearranged, enabling solutions for wet bulb depression and wet bulb temperature to be obtained independently, by analogy from conventional solutions for dry surface heat exchangers. Jaber and Webb [12] presented an effectiveness-number of transfer units (ε-NTU) approach. The model assumed Lewis factor to be unity and a linear variation of moist air saturation enthalpy versus temperature. The model did not consider the effect of water film heat transfer resistance and the effect of water loss by evaporation on the air process states along the vertical length of the tower. Braun et al. [13] also presented an effectiveness model for cooling towers. They also did not consider the effect of water film heat transfer resistance. They did consider the effect of water evaporation on the air process states along the vertical length of the tower. The results were also only presented for the Lewis factor equal to unity. Dessouky [5] presented a modified version of Jaber and Webb's model with the inclusion of the Lewis factor, which appeared only as a multiplication factor to the enthalpy driving potential. Comparison of the results from Dessouky's model with numerical results of a more realistic model performed by Khan and Zubair [6] showed that an appreciable difference occurred with the nonunity Lewis factors. Halasz [14,15] presented a general nondimensional mathematical model for the description of all types of evaporative cooling devices. The model was composed of a system of four ordinary differential equations. However, no general analytical solution was given in his works for this set of equations. When applied to counterflow cooling towers, the general model was reduced to a system of three ordinary differential equations that did not consider the water film heat transfer resistance either. The analytical solution of parameter profiles was obtained for the cases with the Lewis factor being equal to unity. A cooling tower performance was obtained simply by further rearranging the reduced differential equations and by solving the resultant equations similar to those for the counterflow recuperative heat exchangers. This is in effect similar to the Maclaine-Cross and Banks' method except for the differences between the linear approximations to the real air saturation humidity data and between the evaluations of the thermodynamic properties such as latent heat of evaporation and moist air specific heat capacity. Makkinejad [16] presented a mathematical solution for cooling towers and industrial absorbers based on a model that also neglected the water film heat transfer resistance and assumed a unity Lewis factor. The moisture content of air at the water surface was still linearized with respect to the surface temperature within their boundary values but with no difference between the real and linearized distribution at the boundaries themselves. In order to make the differential equation for the
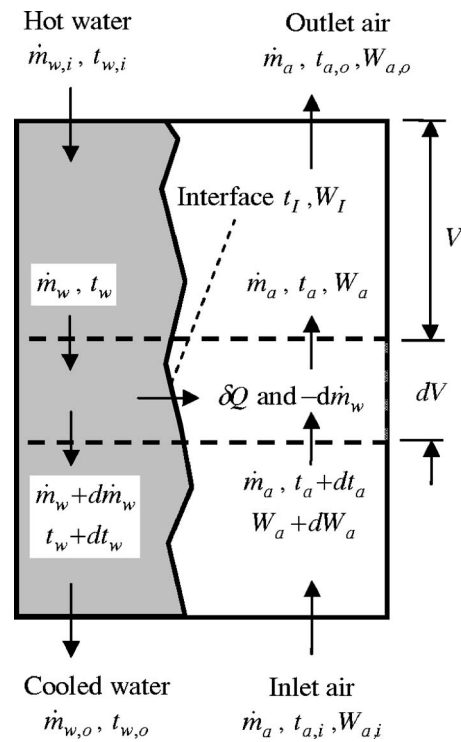
Fig. 1 A schematic diagram of a counterflow cooling tower

moisture content of bulk air simply integrable, a critical and somewhat arbitrary assumption was made without theoretical foundation that the water surface temperature and, in consequence, the moisture content of air at the water surface would be linearized with respect to the moisture content of bulk air.

In conclusion, to develop an analytical model with contemplation of all the critical Merkel approximations is still worthy to be investigated. This paper aims at developing an analytical model for the coupled heat and mass transfer processes in counterflow cooling towers based on operating conditions more realistic than most conventionally adopted Merkel approximations. A comparison of analytical and numerical results will be given in this paper and good agreements will be shown for the typical cases studied. Compared with the numerical integration of the original differential equations, the model also accommodates direct and quick calculation of gas, liquid and interface temperature profiles, and moisture content of air along the vertical length of the tower.

2 Mathematical Formulation

A schematic of a counterflow cooling tower is given in Fig. 1. The major assumptions that were used to derive the basic modeling equations are summarized as follows:

(1) heat and mass transfer in a direction normal to the flows only
(2) no heat transfer to the surroundings occurs
(3) negligible heat transfer from the tower fans to air or water streams
(4) water lost by drift is negligible
(5) constant specific heats of water, water vapor and dry air
(6) constant heat and mass transfer coefficients along the heat exchanger surface
(7) humidity ratio of air in equilibrium with the water surface is assumed to be a linear function of the water surface temperature and the relation is given by

$$W_I = d + e t_I \qquad (3)$$

The errors introduced by condition (7) can be minimized by choosing appropriate values of constants d and e in Eq. (3) to give an approximate least squares fit to the true or actual saturation line over the range of water surface temperatures [11].

From steady state energy and mass balances on an incremental volume (refer to Fig. 1), a set of differential equations can be obtained as follows:

Energy balance equation for air

$$\dot{m}_a dh_a = -[h_c a(t_I - t_a) + h_D a(W_I - W_a)h_{g,I}]dV \qquad (4)$$

Mass balance equation for air and water

$$\dot{m}_a dW_a = -h_D a(W_I - W_a)dV = d\dot{m}_w \qquad (5)$$

Energy balance equation for the incremental volume

$$d(\dot{m}_w c_{pw} t_w) - \dot{m}_a dh_a = 0 \qquad (6)$$

Energy balance equation for interface

$$h_{c,w}a(t_w - t_I) = h_c a(t_I - t_a) + h_{fg,I}h_D a(W_I - W_a) \qquad (7)$$

For specific enthalpy of moist air, the following equation applies

$$h_a = c_{pa}t_a + W_a h_{fg,0} \qquad (8)$$

Detailed simulation can be obtained by numerical integration of Eqs. (4)–(8). However, an analytical solution will be more valuable in application because it gives the tower performance and parameter profiles more directly and quickly. In addition, it reduces the round-off errors in numerical simulation.

3 Linearized Differential Equations

After rearrangement of Eqs. (4)–(8), we can get the following set of equations:

$$dt_a = -\frac{Le_f}{B_1}(t_I - t_a)dNTU \qquad (9)$$

$$dW_a = -(W_I - W_a)dNTU \qquad (10)$$

$$dt_w = -(t_w - t_I)\frac{\widetilde{E}}{C_w^*}B_2 dNTU \qquad (11)$$

Using Eq. (3) to eliminate W_I in Eq. (7) and solving the resultant equation for t_I give the following equation:

$$t_I = \left[\frac{\widetilde{E}}{Le_f}t_w + t_a + B_3\bar{h}_{fg,0}\frac{1}{Le_f}(W_a - d)\right] \bigg/ \left(\frac{\widetilde{E}}{Le_f} + B_4\right) \qquad (12)$$

In the above equations, the dimensionless B coefficients can be expressed as $B_1 = (1+W_aR_{cv})/[1+(R_{cv}/Le_f)(W_I-W_a)]$, $B_2 = 1 + (R_{cw}/\widetilde{E})(W_I-W_a)$, $B_3 = 1 + t_I(R_{cv}-R_{cw})/\bar{h}_{fg,0}$ and $B_4 = 1 + B_3 e\bar{h}_{fg,0}/Le_f$. Here, B_1, B_2, and B_3 are all approximately equal to unity. The definition of the other grouped parameters appeared in above equations are given as follows:

NTU $= h_D aV/\dot{m}_a$—the number of transfer units;

$\widetilde{E} = h_{c,w}/h_D c_{p,da}$—dimensionless E value;

$C_w^* = \dot{m}_w c_w/\dot{m}_a c_{p,da}$—water to dry air heat capacity rate ratio;

$\bar{h}_{fg,0} = h_{fg,0}/c_{p,da}$—a normalized heat of evaporation at reference temperature ($0°C$);

$R_{cv} = c_{pv}/c_{p,da}$ and $R_{cw} = c_{pw}/c_{p,da}$—water vapor and liquid water to dry air specific heat capacity ratios, respectively;

$Le_f = h_c a/(h_D a c_{p,da})$—Lewis factor for air water mixture (for simplicity and consistency, the definition of Le_f is slightly different from that in conventional practice, where Le is defined as $h_c/h_D c_{pa}$. The relation between these two different definitions is $Le_f = Le(1 + W_a R_{cv})$ if $h_c a/(h_D a) = h_c/h_D$).

A dimensionless temperature variable is defined as follows:

$$\vartheta = t/\bar{h}_{fg,0} \qquad (13)$$

Using Eqs. (3) and (12) to eliminate W_I and t_I in Eqs. (9)–(11) and rewriting the resultant equations in dimensionless form will give a set of differential equations as follows:

$$\frac{d}{dNTU}\mathbf{Y} = \mathbf{AY} \qquad (14)$$

where the variable vector $\mathbf{Y}$ is defined as

$$\mathbf{Y} = (\vartheta_w, \vartheta_a, W_a - d)^T \qquad (15)$$

and the coefficients matrix $\mathbf{A}$ is as follows:

$$\mathbf{A} = (a_{ij})_{3\times3}$$

$$= \frac{Le_f}{\widetilde{E}+B_4 Le_f}\begin{bmatrix} -\dfrac{\widetilde{E}}{C_w^*}B_2 B_4 & \dfrac{\widetilde{E}}{C_w^*}B_2 & \dfrac{\widetilde{E}}{C_w^* Le_f}B_2 B_3 \\[3mm] -\dfrac{\widetilde{E}}{B_1} & -\dfrac{Le_f(1-B_4)-\widetilde{E}}{B_1} & -\dfrac{B_3}{B_1} \\[3mm] -e\bar{h}_{fg,0}\dfrac{\widetilde{E}}{Le_f} & -e\bar{h}_{fg,0} & \left(\dfrac{\widetilde{E}}{Le_f}+1\right) \end{bmatrix}$$
$$(16)$$

Mathematical details with regard to the differential equations (14)–(16) are given in the Appendix. All the elements in the coefficients matrix are approximately equal to constants. For simplification of analysis, these elements will be represented with the averaged values along the vertical length of the tower. By this approximation, Eq. (14) represents a set of linear and homogeneous ordinary equations and can be solved analytically.

4 Analytical Approach

For Eq. (14), the characteristic equation is as follows:

$$|\lambda \mathbf{E} - \mathbf{A}| = 0 \qquad (17)$$

Within the practical range of operating conditions, numerical calculation shows that the solution of this characteristic equation will give three different real roots. Thus, the analytical solution of Eq. (14) can be expressed as follows:

$$\mathbf{Y} = \mathbf{K}(C_1 e^{\lambda_1 NTU_x}, C_2 e^{\lambda_2 NTU_x}, C_3 e^{\lambda_3 NTU_x})^T \qquad (18)$$

The elements of coefficients matrix $\mathbf{K} = (k_{ij})_{3\times3}$ can be determined by the following equation:

$$(\lambda_i \mathbf{E} - \mathbf{A})(k_{1i}, k_{2i}, k_{3i})^T = \mathbf{0} \qquad (19)$$

By satisfying Eq. (18) to the top boundary condition, i.e., for $NTU_x = 0$, $\mathbf{Y} = \mathbf{Y}_T$, we can get

$$(C_1, C_2, C_3)^T = \mathbf{K}^{-1}\mathbf{Y}_T \qquad (20)$$

Here $\mathbf{Y}_T = (\vartheta_{w,T}, \vartheta_{a,T}, W_{a,T} - d)^T$. By substituting Eq. (20) into Eq. (18), we get

$$\mathbf{Y} = \mathbf{K}\mathbf{e}(NTU_x)\mathbf{K}^{-1}\mathbf{Y}_T \qquad (21)$$

where

$$\mathbf{e}(NTU_x) = \begin{pmatrix} e^{\lambda_1 NTU_x} & & \mathbf{0} \\ & e^{\lambda_2 NTU_x} & \\ \mathbf{0} & & e^{\lambda_3 NTU_x} \end{pmatrix} \qquad (22)$$

Setting $NTU_x = NTU$ in Eq. (21), we can get the function vector at the heat exchanger's bottom position as:

$$\mathbf{Y}_B = \mathbf{B}\mathbf{Y}_T \qquad (23)$$

where the coefficients matrix $\mathbf{B}$ is defined as

$$\mathbf{B} = (b_{ij})_{3\times3} = \mathbf{K}e(\text{NTU})\mathbf{K}^{-1} \tag{24}$$

Equation (23) correlates three unknown variables $\vartheta_{w,o}$, $\vartheta_{a,o}$, and $W_{a,o}$ in three linear algebraic equations and can be rearranged to give the following equation

$$\mathbf{P}(\vartheta_{w,o}, \vartheta_{a,o}, W_{a,o} - d)^T = \mathbf{q} \tag{25}$$

where the expressions for coefficients matrix $\mathbf{P}$ and vector $\mathbf{q}$ are given as follows:

$$\mathbf{P} = \begin{pmatrix} 1 & -b_{12} & -b_{13} \\ 0 & -b_{22} & -b_{23} \\ 0 & -b_{32} & -b_{33} \end{pmatrix} \text{ and } \mathbf{q} = \begin{bmatrix} b_{11}\vartheta_{w,i} \\ b_{21}\vartheta_{w,i} - \vartheta_{a,i} \\ b_{31}\vartheta_{w,i} - (W_{a,i} - d) \end{bmatrix} \tag{26}$$

Solving Eq. (25) will give the three unknown outlet variables $\vartheta_{w,o}$, $\vartheta_{a,o}$, and $W_{a,o}$ (or in consequence $t_{w,o}$, $t_{a,o}$, and $W_{a,o}$). With these calculated outlet parameters, parameter profiles along the vertical length of the tower can be calculated directly and quickly using Eqs. (21) and (12).

5 Solution Procedures

For a given set of control parameters (for example, with known values of $t_{w,i}$, $t_{a,i}$, $W_{a,i}$, $C_{w,i}^*$, $\widetilde{E}$, Le_c, and NTU), it will still be necessary to evaluate the averaged values of constants and coefficients d, e, B_1, B_2, B_3, and B_4 involved in the analytical model. These constants and coefficients will also depend on the analytical results of outlet parameters and thus 2–4 steps in iteration will be needed for the analytical solution. In evaluating constants d and e, Maclaine-Cross and Banks' suggestion [11] was utilized to give an approximate least squares fit to actual saturation line over the range of water surface temperatures. That is

$$e = (W_{I,\max} - W_{I,\min})/(t_{I,\max} - t_{I,\min}) \tag{27}$$

$$d = [2(W_{I,\min} + W_{I,\mathrm{mean}}) - W_{I,\max}]/3 - et_{I,\min} \tag{28}$$

Here, $t_{I,\max} = t_{I,T}$ and $t_{I,\min} = t_{I,B}$ and $W_{I,\mathrm{mean}}$ is saturation humidity at temperature of $t_{I,\mathrm{mean}} = (t_{I,\max} + t_{I,\min})/2$. Both $t_{I,T}$ and $t_{I,B}$ can be obtained by solving Eq. (12) with given values of parameters t_w, t_a, and W_a at the top and bottom positions, respectively. In the above calculations, outlet temperatures $t_{w,o}$, $t_{a,o}$ and humidities $W_{a,o}$ can be obtained by analytical solutions. For preliminary evaluation, however, analytical results of outlet temperatures $t_{w,o}$, $t_{a,o}$ and humidities $W_{a,o}$ are not available and the two temperatures $t_{I,\max}$ and $t_{I,\min}$ have to be evaluated in another way. In this occasion, these two temperatures can be given by letting $t_{I,\min} = (t_{w,i} + t_{a,i})/2$ and $t_{I,\max} = t_{I,\min} + 1$. Though this is rather arbitrarily an evaluation of the two temperatures, it will not affect the final results of the iteration solution. In evaluating the averaged values of B_1, B_2, B_3, and B_4, the arithmetic mean values of temperatures and humidities at end positions of the tower were used in their expressions.

Based on the given conditions and the evaluated constants and coefficients, procedures for the analytical solution are as follows:

(1) Calculate values of the elements of coefficients matrix $\mathbf{A}$ according to Eq. (16);
(2) Solve Eq. (17) for the roots of the characteristic equation ($\lambda_1 - \lambda_3$);
(3) Solve Eq. (19) for the values of the elements of coefficients matrix $\mathbf{K}$;
(4) Calculate values of the elements of coefficients matrix $\mathbf{B}$ according to Eq. (24);
(5) Calculate values of the elements of coefficients matrix $\mathbf{P}$ and vector $\mathbf{q}$ according to Eq. (26);
(6) Solve Eq. (25) to get the dimensionless outlet parameters ($\vartheta_{w,o}$, $\vartheta_{a,o}$, and $W_{a,o}$) and using the definition of these dimensionless parameters to get the values of the original variables ($t_{w,o}$, $t_{a,o}$, and $W_{a,o}$);
(7) If parameter profiles needs to be determined, Eq. (21)

should only be solved explicitly using dimensionless parameters vector $\mathbf{Y}_T$ and NTU_x as input parameters. Here $\mathbf{Y}_T$ can be determined from given values or analytical results of parameters at top position. This solution gives the dimensionless parameters vector defined in Eq. (15) at any local positions. Use the definition of these dimensionless parameters to get the values of the original variables and use Eq. (12) to calculate the interface temperatures.

For evaluating, cooling tower performance were usually defined as

$$\varepsilon = \frac{t_{w,i} - t_{w,o}}{t_{w,i} - t_{\mathrm{wb},i}} \tag{29}$$

This definition was also adopted in this study. With the given values of the inlet parameters and the analytical results of the outlet parameters, the performance defined in the above equation can be easily calculated.

6 Comparison and Discussion

In the analytical model, the assumption of the linear relation of saturation humidity with water surface temperature as described by Eq. (3) and the assumptions of constant coefficients d, e, B_1, B_2, B_3, and B_4 were adopted. These are the only differences between the analytical model and the model described by the original differential equations (4)–(8) where the saturation humidity can be calculated from an accurately fitted equation of the published data [17]. In order to demonstrate the validity of the analytical model, the results of the analytical model were compared with those from the numerical integration of the original differential equations. For numerical integration, the tower was divided into 160 intervals with equal $\Delta\text{NTU} = h_D a\Delta V/\dot{m}_a$ across each interval. Above this number of intervals, the numerical results were found to be unaffected by the increased intervals. Finite difference equations derived from Eqs. (4)–(6) were used to determine the values of h_a, W_a, and t_w at each node between intervals or at the top or bottom position. Equations (7) and (8) were utilized to calculate the values of temperatures t_I and t_a. Numerical integration was implemented starting from the air inlet side of the tower. The guess value of the water temperature at the position of the air inlet must be assumed. Iteration proceeded until the calculated water inlet temperature matched the actual temperature value.

For supersaturated air, Eqs. (4), (5), (7), and (8) should be replaced with the following equations (according to the discussions in Ref. [3])

$$\dot{m}_a dh_a = -[h_c a(t_I - t_a) + h_D a(W_I - W_{sa})h_{g,I}]dV \tag{30}$$

$$\dot{m}_a dW_a = -h_D a(W_I - W_{sa})dV = d\dot{m}_w \tag{31}$$

$$h_{c,w}a(t_w - t_I) = h_c a(t_I - t_a) + h_{fg,I}h_D a(W_I - W_{sa}) \tag{32}$$

and

$$h_a = c_{p,da}t_a + W_{sa}(c_{pv}t_a + h_{fg,0}) + (W - W_{sa})c_{pw}t_a \tag{33}$$

Numerical integration should be performed over Eqs. (6) and (30)–(33) for supersaturated air. In order to make the analytical model be also applicable for supersaturated air, the following equations were utilized to get the supersaturated air humidity W_a and temperature t_a from the analytical results (W_a', t_a') by Eq. (25) or Eq. (21)

$$W_a = W_a' \tag{34}$$

$$c_{pa}t_a + W_{sa}h_{fg} = c_{pa}t_a' + W_a h_{fg} \tag{35}$$

Here h_{fg} and W_{sa} are enthalpy of evaporation and saturation humidity at temperature t_a, respectively.

The comparison was made under typical operating conditions determined to be within the range of the conditions investigated

Table 1 Comparison of calculation results with different methods

Case No.	$t_{w,i}$ (°C)	$t_{a,i}$ (°C)	$W_{a,i}$ (kg$_w$/kg$_a$)	$t_{wb,i}$ (°C)	$C^*_{w,i}$/$\dfrac{\dot m_{w,i}}{\dot m_a}$	$\tilde E$	Le_f	NTU	Anal. $t_{w,o}$ (°C)	Anal. $t_{a,o}$ (°C)	Anal. $W_{a,o}$ (kg$_w$/kg$_a$)	Anal. ε	Num. $t_{w,o}$ (°C)	Num. $t_{a,o}$ (°C)	Num. $W_{a,o}$ (kg$_w$/kg$_a$)	Num. ε	Merkel $t_{w,o}$ (°C)	Merkel $t_{a,o}$ (°C)	Merkel $W_{a,o}$ (kg$_w$/kg$_a$)	Anal. e_{t_w} (%)	Anal. e_{t_a} (%)	Anal. e_W (%)	Anal. e_ε (%)	Merkel e_{t_w} (%)	Merkel e_{t_a} (%)	Merkel e_W (%)
1	60	35	0.0085	20	4.161/1.0	11	1	3	29.68	42.38	0.05674[a]	0.758	29.02	42.86	0.0583[a]	0.775	25.38	43.79	0.06109	−2.16	−2.08	−3.13	−2.16	11.73	4.05	5.60
2	30	35	0.0085	20	4.161/1.0	11	1	3	23.50	27.72	0.02260	0.650	23.5	27.71	0.02263	0.650	22.65	27.53	0.02355	0.04	0.21	−0.18	0.04	13.09	−2.54	6.56
3	40	7	0.0005	−0.68	4.161/1.0	11	1	3	18.07	30.25	0.02810[a]	0.539	18.14	30.32	0.02854[a]	0.537	15.61	31.87	0.03055	0.33	−0.22	−1.57	0.33	11.55	4.94	7.17
4	40	35	0.0252	30	4.161/1.0	11	1	3	32.05	35.86	0.03841	0.795	32.04	35.88	0.03846	0.796	31.03	36.14	0.0393	−0.14	−0.28	−0.39	−0.14	12.70	4.61	6.28
5	40	25	0.0127	20	4.161/1.0	11	1	3	26.03	33.14	0.03303[a]	0.699	26.03	33.19	0.03316[a]	0.699	24.25	34.03	0.03472	−0.02	−0.37	−0.63	−0.02	12.71	6.34	7.62
6	40	35	0.0085	20	2.081/0.5	11	1	3	21.94	29.51	0.02602	0.903	21.43	29.76	0.02643	0.929	20.56	29.55	0.02661	−2.73	−2.64	−2.27	−2.73	4.68	−2.27	0.98
7	40	35	0.0085	20	8.323/2.0	11	1	3	31.35	35.93	0.03763	0.432	31.39	35.86	0.03771	0.430	29.68	37	0.0413	0.45	0.45	−0.25	0.45	19.83	7.32	12.31
8	40	35	0.0085	20	4.161/1.0	11	1	3	26.03	33.51	0.03283	0.699	26.02	33.52	0.03294	0.699	24.19	34.01	0.03469	−0.05	−0.10	−0.46	−0.05	13.09	3.72	7.14
9	40	35	0.0085	20	4.161/1.0	60	1	3	24.88	34.21	0.03455	0.756	24.78	34.26	0.03468	0.761	24.19	34.01	0.03469	−0.62	−0.33	−0.48	−0.62	3.88	−1.74	0.03
10	40	35	0.0085	20	4.161/1.0	11	0.5	3	25.83	33.29	0.03337[a]	0.708	25.85	33.33	0.03346[a]	0.708	24.19	34.01	0.03469	0.11	−0.30	−0.36	0.11	11.72	5.12	4.92
11	40	35	0.0085	20	4.161/1.0	11	1.5	3	26.11	34.17	0.03242	0.694	26.08	34.18	0.03257	0.696	24.19	34.01	0.03469	−0.24	−0.08	−0.62	−0.24	13.56	−1.23	8.82
12	40	35	0.0085	20	4.161/1.0	11	1	0.5	34.46	34.3	0.01825	0.277	34.52	34.31	0.01827	0.274	32.3	27.84	0.024	1.17	−0.13	−0.25	1.17	40.58	−104.38	58.68
13	40	35	0.0085	20	4.161/1.0	11	1	6	23.59	34.81	0.03644	0.820	23.48	34.9	0.03673	0.826	22.28	35.24	0.03729	−0.71	−0.57	−1.05	−0.71	7.21	2.26	1.96

[a] For supersaturated air conditions.

[b] Definitions for relative errors: $e_{t_w}=(t^m_{w,o}-t^n_{w,o})/(t^n_{w,o}-t^n_{w,i})$, $e_{t_a}=(t^m_{a,o}-t^n_{a,o})/(t^n_{wb,o}-t^n_{wb,i})$, $e_W=(W^m_{a,o}-W^n_{a,o})/(W^n_{a,o}-W^n_{a,i})$, $e_\varepsilon=(\varepsilon^m-\varepsilon^n)/\varepsilon^n$, here superscript "$m$" represents results by the analytical or the Merkel model and superscript "n" represents the numerical results of differential equations (4)–(8).

by many researchers [2–8,11,12]. The base case condition was chosen as $t_{w,i}=40\,°\text{C}$, $t_{a,i}=35\,°\text{C}$, $W_{a,i}=0.00852\ \text{kg}_w/\text{kg}_a$, $C^*_{w,i}=4.161$, $\tilde E=11$, $Le_f=1$, and $\text{NTU}=3$. Other conditions were basically obtained by changing one or a few independent input parameters from their base case values each test. The performances and outlet parameters of the cooling towers were predicted by the analytical method and numerical integrations. Results were presented in Table 1, where relative errors for the outlet water temperature and air humidity were defined as the ratios of the errors (the differences between the analytical and numerical results) to the overall changes of the corresponding variables (the differences between the outlet and inlet values of those variables) by numerical integration and relative errors for the effectiveness value were defined as the ratios of the errors to the numerical results. These relative errors also reflect the relative errors in the calculation of the cooling power and the amount of evaporated water from the cooling tower, respectively, and can thus be considered as physically meaningful. Due to the possible big curvature of air dry bulb temperature distributions along the tower, the overall changes of that temperature may be very small and cannot reflect the order of the maximum changes of that temperature in the tower and, thus, the "physically meaningful" definition cannot reflect exactly the relative error. For dry bulb temperatures, relative errors were defined as the ratios of the errors to the overall changes of the wet bulb temperatures (the differences between the outlet and inlet values of wet bulb temperatures). Though this definition is not physically meaningful, it can be utilized in evaluating the relative errors by different methods fairly and with ease of implementation. From Table 1, it is easy to find that the relative errors for the outlet water temperature are always equal to those for the effectiveness value. This is because both these relative errors reflect the errors in the calculation of the cooling power. From Table 1, it can also be found that the relative errors by the analytical method are generally less than 2% except for cases 1 and 6. In case 1, the inlet water temperature is very high and the error in the linearization of air saturation humidity at the water surface is great. This leads to increased relative errors by the analytical model. In case 6, the great relative errors by the analytical method are due to the fact that the water flow rate is small and the tower water temperature is quickly approaching its theoretical limit, i.e., the inlet wet bulb temperature of air in the cooling tower, where the linearized air saturation humidity is significantly different from the actual value. In case 12, a relatively great error (approximately 1%) in the predicted effectiveness value results from a small denominator in its definition though the absolute error is actually small. By comparing cases 3 and 4, it can also be found that a larger cooling range of water $(t_{w,i}-t_{w,o})$ would increase the linearization error and thus the relative errors by the analytical method.

In order to show the improvement in accuracy when the analytical procedure presented by this paper is implemented, results calculated by the Merkel method were also presented in Table 1 and the corresponding errors were defined similarly as above. The results show that, for all the given operating conditions and tower volume (characterized by NTU), the Merkel method always gives lower water outlet temperatures and higher effectiveness values than those from numerical integration. This is due to the fact that the Merkel method neglected water film heat transfer resistance and the effect of water loss by evaporation on energy balance. This phenomenon is also consistent with the observation that, as is reviewed in Sec. 1, the tower volumes or Merkel numbers would be underestimated by the Merkel approximate analysis with given inlet conditions and specified tower performances [3,8]. By comparing cases 8 and 12, large relative errors in the outlet air parameters by the Merkel method can be observed for small tower volume due to the assumption of the saturated outlet air conditions. By comparing cases 8 and 10 and 11, it can be observed that the Merkel method predicts the outlet parameters with different relative errors in accordance with different values of the Lewis factor. With smaller values of the Lewis factor, the numerical method
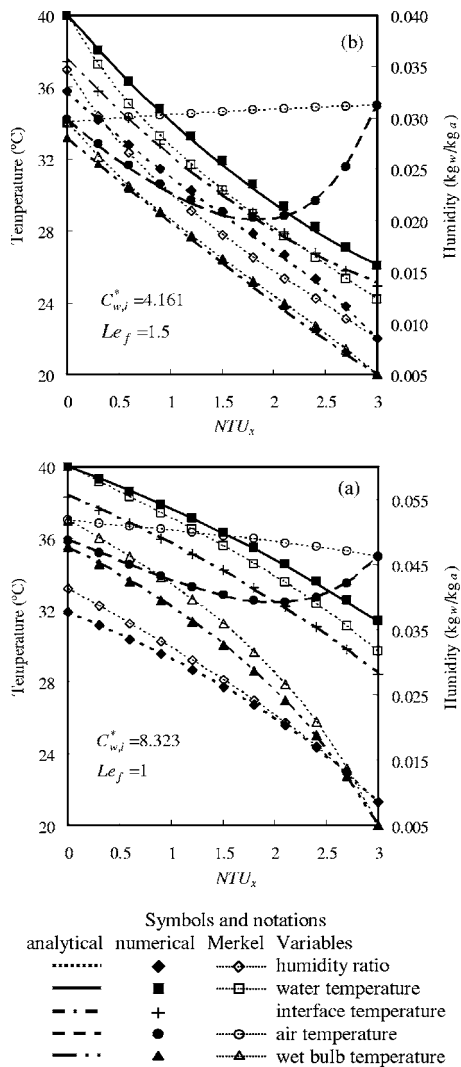
Fig. 2 Parameter profiles along the vertical length of the tower for the conditions with $t_{w,i}=40\,^\circ\text{C}$, $t_{a,i}=35\,^\circ\text{C}$, $t_{wb,i}=20\,^\circ\text{C}$, $W_{a,i}=0.00852\ \text{kg}_w/\text{kg}_a$, NTU=3, and $\tilde{E}=11$

predicts lower outlet air and water temperatures and higher outlet humidity ratios while the Merkel method gives no differences in these cases. Averagely, the analytical method predicts the outlet conditions with a relative error of 0.67% for outlet water temperatures, 0.6% for outlet air temperatures, and 0.9% for outlet air humidity ratios for the set of the operating conditions presented in Table 1. In contrast, the Merkel approximate analysis predicts the outlet conditions with an averaged relative error of 13.56% for outlet water temperatures, 11.58% for outlet air temperatures, and 9.85% for outlet air humidity ratios under the same set of operating conditions. Thus, for the cases discussed, the analytical method gives rather accurate predictions of the outlet conditions, with 12.89–8.95% reduction in the averaged relative errors from those by the Merkel method.

Parameter profiles determined by different methods were also compared. Figure 2 shows as examples such profiles for two different cases listed in Table 1. Figure 2(a) shows the parameter profiles for case 7. In that case, the water to dry air heat capacity rate ratio is large ($C_{w,i}^*=8.323$) and the cooling range of water is less than the air wet bulb temperature change over the length of the tower. Thus, the water to air wet bulb temperature difference increases as NTU increases from the tower top to bottom. This increasing heat transfer driving potential makes the curves of the water temperature and the air wet bulb temperature to bend down

toward the lower right corner of the figure. Figure 2(b) shows the parameter profiles for case 11. In that case, the Lewis factor is equal to 1.5 that is much greater than unity, and as a result, the curve for the dry bulb temperature of air bends away from its wet bulb temperature. In both cases, the dry bulb temperature of air drops first and then rises again along its flow direction. The numerical integration shows that the temperature difference between the bulk water and the water surface, and thus the water film heat transfer resistance, is not negligible. This is in contrast with the Merkel approximation. In addition, the bulk air humidity ratio cannot always be correlated with the water surface temperature in a linear relation (see for example Fig. 2(b)), i.e., the linear approximation of Eq. (13) by Makkinejad [16] may not necessarily be satisfied. Nevertheless, the analytical method predicts these trends and variations quite accurately. This is shown by the coincidence of data from the analytical method and the numerical integration of the original differential equations plotted in Figs. 2(a) and 2(b). The maximum relative error is only 2.36% for the interface temperature occurred at NTU=1.5 in Fig. 2(b). For all other predicted values in both cases, the relative errors by the analytical method are uniformly less than this value. However, the predicted values by the Merkel method deviate significantly from that by numerical integration of the original differential equations and the relative errors are very high. This can be obviously observed from both Figs. 2(a) and 2(b). The maximum errors amount to 13.6% for water temperature, 12.9% for interface temperature, 42.3% for air temperature, 9.96% for air saturation humidity, and 7.49% for wet bulb temperature. For the two cases discussed, the analytical method gives rather accurate predictions of the parameter profiles, with about 6.1–41.3% reduction in the maximum relative errors and about 2.6–17.9% reduction in the averaged relative errors along the vertical length of the tower from those by the Merkel method.

On the above comparison and discussion, it can be concluded that good agreements are observed between analytical predictions and numerical integrations for both the outlet parameters and the parameter profiles, with both the averaged and maximum relative errors being much less than those by Merkel method for the typical cases discussed. Because the analytical model requires only a few steps of iteration to calculate the related constants and coefficients to obtain accurate analytical results, the model thus also accommodates a direct and quick calculation of gas, liquid, and interface temperature profiles and moisture content of air along the vertical length of the tower in comparison with accurate numerical integration. The validity and usefulness of the analytical model are thus demonstrated.

7 Conclusion

Quick and accurate analysis of tower performance, exit conditions of moist air as well as profiles of temperatures and moisture content along the tower height is very important in rating and design calculations. This paper developed an analytical model for the counterflow cooling towers based on more realistic conditions as discussed by many recent studies [2,3,6,8] than the most conventionally adopted Merkel approximations. The analytical model predicts the tower performances and outlet conditions accurately when comparing with the numerical integration of the one-dimensional differential equations. The analytical model also accommodates the direct and quick calculation of gas, liquid, and interface temperature profiles and moisture content of air along the vertical length of the tower. However, this model does not use the assumption of correlating the absolute humidity of bulk air with the interface temperature in a linear relation as adopted by Makkinejad [16] and will thus be expected to be more accurate.

Nomenclature

$\mathbf{A}$ = coefficients matrix defined in Eq. (16)
B_1–B_4 = constants in Eqs. (9), (11), and (12), etc.
$\mathbf{B}$ = coefficients matrix defined in Eq. (24)

c_p = specific heat capacity, kJ/kg°C

$c_{p,da}$ = specific heat capacity of dry air, kJ/kg$_a$°C

c_{pa} = specific heat capacity of moist air ($c_{pa} = c_{p,da} + w_a c_{pv}$), kJ/kg$_a$°C

d, e = constants in Eq. (3)

E = ratio of water film heat transfer coefficient to air film mass transfer coefficient, kJ/kg$_a$ K

$\widetilde{E}$ = dimensionless E value defined as $h_{c,w}/h_D c_{p,da}$

$\mathbf{e}(\text{NTU}_x)$ = independent variable matrix defined in Eq. (22)

C_w^* = water to air heat capacity rate ratio $\dot{m}_w c_{pw}/\dot{m}_a c_{p,da}$

$C_1 - C_3$ = coefficients in Eq. (18)

h = specific enthalpy of moist air, kJ/kg$_a$

$h_{c,w}$ = water film heat transfer coefficient, kW/m^2°C

$h_c a$ = volumetric convective heat transfer coefficient, kW/m^3°C

h_D = air film mass transfer coefficient, kg$_w$/m^2 s (kg$_w$/kg$_a$)

$h_D a$ = volumetric convective mass transfer coefficient, kg$_w$/m^3 s (kg$_w$/kg$_a$)

h_{fg} = enthalpy of evaporation of water, kJ/kg$_w$

$h_{fg,0}$ = enthalpy of evaporation of water at reference temperature condition (0°C), kJ/kg$_w$

$\bar{h}_{fg,0}$ = normalized enthalpy of evaporation of water at reference temperature condition, °C

h_g = specific enthalpy of saturated water vapor, kJ/kg$_w$

$\mathbf{K}$ = coefficients matrix in Eq. (18)

Le_f = Lewis factor ($\text{Le}_f = h_c a/h_D a c_a$)

$\dot{m}$ = mass flow rate, kg/s

NTU = number of transfer units ($h_D a V/\dot{m}_a$)

NTU_x = number of transfer units measured from tower top to any local position

$\mathbf{P}$ = coefficients matrix in Eq. (25)

$\mathbf{q}$ = constants vector in Eq. (25)

R_{cv}, R_{cw} = water vapor and liquid water to dry air specific heat capacity ratios, respectively

t = temperature, °C

V = tower volume for heat and mass transfer, m^3

W = humidity ratio of moist air, kg$_w$/kg$_a$

$\mathbf{Y}$ = function variable vector defined in Eq. (15)

Greek Letters

ε = effectiveness

ϑ = dimensionless temperature defined in Eq. (13)

$\lambda_1 - \lambda_3$ = roots of the characteristic equation

Subscript

a = bulk air

B = bottom position

i = inlet

I = for interface or at interface temperature condition

max = maximum value

min = minimum value

mean = mean value

o = outlet

sa = for saturated moist air at temperature t_a

sw = for saturated moist air at temperature t_w

T = top position

v = water vapor

w = for bulk water

wb = wet bulb

Appendix: Mathematical Details With Regard to the Differential Equations (14)–(16)

Substituting Eqs. (12) and (13) into Eq. (11) gives

$$d\vartheta_w = \frac{\text{Le}_f}{\widetilde{E} + B_4 \text{Le}_f} \left\{ -\frac{\widetilde{E}}{C_w^*} B_2 B_4 \vartheta_w + \frac{\widetilde{E}}{C_w^*} B_2 \vartheta_a + \frac{\widetilde{E}}{C_w^* \text{Le}_f} B_2 B_3 (W_a - d) \right\} d\text{NTU} \quad (A1)$$

Substituting Eqs. (12) and (13) into Eq. (9) gives

$$d\vartheta_a = \frac{\text{Le}_f}{\widetilde{E} + B_4 \text{Le}_f} \left\{ -\frac{\widetilde{E}}{B_1} \vartheta_w - \frac{\text{Le}_f(1 - B_4) - \widetilde{E}}{B_1} \vartheta_a - \frac{B_3}{B_1}(W_a - d) \right\} d\text{NTU} \quad (A2)$$

Substituting Eqs. (3) and (12) into Eq. (10) gives

$$d(W_a - d) = \frac{\text{Le}_f}{\widetilde{E} + B_4 \text{Le}_f} \left\{ -e\bar{h}_{fg,0} \frac{\widetilde{E}}{\text{Le}_f} \vartheta_w - e\bar{h}_{fg,0} \vartheta_a + \left(\frac{\widetilde{E}}{\text{Le}_f} + 1 \right) \times (W_a - d) \right\} d\text{NTU} \quad (A3)$$

Simply writing Eqs. (A1)–(A3) in matrix form gives the differential equations (14)–(16).

References

[1] Merkel, F., 1925, "VerdunstungsküHlung," Zeitschrift des Vereines Deutscher Ingenieure (V. D. I.), **70**, pp. 123–128.

[2] Kloppers, J. C., and Kröger, D. G., 2005, "Cooling Tower Performance Evaluation-Merkel, Poppe and E-NTU Methods of Analysis," ASME J. Eng. Gas Turbines Power, **127**, pp. 1–7.

[3] Kloppers, J. C., and Kröger, D. G., 2005, "A Critical Investigation Into the Heat and Mass Transfer Analysis of Counterflow Wet-Cooling Towers," Int. J. Heat Mass Transfer, **48**(3–4), pp. 765–777.

[4] Baker, D. R., and Shryock, H. A., 1961, "A Comprehensive Approach to the Analysis of Cooling Tower Performance," ASME J. Heat Transfer, **83**, pp. 339–349.

[5] El-Dessouky, H. T. A., Al-Haddad, A., and Al-Juwayhel, F., 1997, "A Modified Analysis of Counter Flow Cooling Towers," ASME J. Heat Transfer, **119**(3), pp. 617–626.

[6] Khan, J. R., and Zubair, S. M., 2001, "An Improved Design and Rating Analyses of Counter Flow Wet Cooling Towers," ASME J. Heat Transfer, **123**(4), pp. 770–778.

[7] Webb, R. L., 1984, "A Unified Theoretical Treatment for Thermal Analysis of Cooling Towers, Evaporative Condensers, and Fluid Coolers," ASHRAE Trans., **90**(2), pp. 398–415.

[8] Sutherland, J. W., 1983, "Analysis of Mechanical-Draught Counterflow Air/Water Cooling Towers," ASME J. Heat Transfer, **105**, pp. 576–583.

[9] Osterle, F., 1991, "On the Analysis of Counter-Flow Cooling Towers," Int. J. Heat Mass Transfer, **34**(4–5), pp. 1313–1316.

[10] Poppe, M., and Rögener, H., 1991, "Berechnung Von RüCkküHlwerken," VDI-Wärmeatlas Mi 1-Mi 15.

[11] Maclaine-Cross, I. L., and Banks, P. J., 1981, "A General Theory of Wet Surface Heat Exchangers and Its Application to Regenerative Cooling," ASME J. Heat Transfer, **103**, pp. 578–585.

[12] Jaber, H., and Webb, R. L., 1989, "Design of Cooling Towers by the Effectiveness-NTU Method," ASME J. Heat Transfer, **111**(4), pp. 837–843.

[13] Braun, J. E., Klein, S. A., and Mitchell, J. W., 1989, "Effectiveness Models for Cooling Towers and Cooling Coils," ASHRAE Trans., **95**(2), pp. 164–174.

[14] Halasz, B., 1998, "A General Mathematical Model of Evaporative Cooling Devices," Rev. Gen. Therm., **37**(4), pp. 245–255.

[15] Halasz, B., 1999, "Application of a General Non-Dimensional Mathematical Model to Cooling Towers," Int. J. Therm. Sci., **38**(1), pp. 75–88.

[16] Makkinejad, N., 2001, "Temperature Profile in Countercurrent/Cocurrent Spray Towers," Int. J. Heat Mass Transfer, **44**(2), pp. 429–442.

[17] ASHRAE, 2001, *ASHRAE Handbook of Fundamentals*, American Society of Heating, Refrigerating and Air Conditioning Engineers, Atlanta, pp. 6.1–6.21.

A Three-Dimensional Numerical Modeling of Atmospheric Pool Boiling by the Coupled Map Lattice Method

A. Gupta

P. S. Ghoshdastidar
Mem. ASME
e-mail: psg@iitk.ac.in

Department of Mechanical Engineering,
Indian Institute of Technology Kanpur,
Kanpur, U.P. 208016 India

In the present paper, the characteristic atmospheric pool boiling curve is qualitatively reproduced for water on a temperature controlled thin copper strip having comparable length and breadth by the coupled map lattice (CML) method using a three-dimensional boiling field model. The basic objective of the work is to improve the prediction of the critical heat flux (CHF) with respect to the 2D CML model of Ghoshdastidar et al. (Ghoshdastidar, P. S., Kabelac, S., and Mohanty, A., 2004, "Numerical Modelling of Atmospheric Pool Boiling by the Coupled Map Lattice Method," J. Mech. Eng. Sci., IMechE Part C, 218, pp. 195–205). The work models saturated pool boiling of water at 1 bar on a large (much larger than the minimum wavelength of 2D Taylor waves) and thin horizontal copper strip. The pool height is 0.7 mm, indicating thin film boiling. In the present model, it is assumed that boiling is governed by (a) nucleation from cavities on a heated surface, (b) thermal diffusion, (c) bubble rising motion and associated convection, (d) phase change and (e) Taylor instability. The changes with respect to the 2D model are primarily with respect to 3D modeling of thermal diffusion and 2D distribution of nucleating cavity sizes. The predicted CHF is 1.57 MW/m^2 as compared to the actual value of 1.3 and 0.36 MW/m^2 predicted by the 2D CML model of Ghoshdastidar et al. (see above). It can be said that for the first time a coupled map lattice method which is essentially qualitative in nature has been able to predict the CHF of saturated pool boiling of water at 1 bar very close to the actual value. Furthermore, a sensitivity analysis shows that the model gives physically realistic and stable results.
[DOI: 10.1115/1.2352785]

Keywords: pool boiling, coupled map lattice, CML, 3D numerical modeling, nonlinear dynamics

1 Introduction

1.1 Introduction and Literature Review. Nukiyama [1] was the first to identify different regimes of saturated pool boiling of water at 1 bar on a horizontal nichrome wire which was heated by passing electric current through it. The experiment was heat flux $(q_w^{\parallel})$ controlled. Nukiyama observed that boiling did not begin until $\Delta T_w \approx 5\,°C$. As the imposed heat flux increased slightly above the critical value $q_{max}^{\parallel}$, the wire temperature jumped to the melting point and burnout occurred. However, repeating the experiment with a platinum wire having a higher melting point (2045 versus 1500 K), he was able to maintain heat fluxes above the maximum value $q_{max}^{\parallel}$ without burnout. When he ran the experiment in reverse, that is, by decreasing the heat flux, he found that below $q_{min}^{\parallel}$, the vapor film collapsed, isolated bubbles formed and the wire temperature dropped to the low level associated with the nucleate boiling regime. In short, during heat flux controlled boiling the transition boiling regime was inaccessible. The missing transitional boiling regime of the curve was obtained by Drew and Mueller [2] in temperature (T_w) controlled experiments on pool boiling of low boiling point organic fluids.

Since the pioneering work of Nukiyama [1] many researchers conducted experiments on pool boiling to understand the basic physics and obtain various experimental correlations. Jakob [3] was the first to report the relationship between wall heat flux and the density of active nucleation sites. Wang and Dhir [4] in a significant work quantified experimentally how surface wettability affects the active nucleation site density and the distribution of the active nucleation sites.

For the past several decades, numerous researchers have made efforts to model nucleate boiling. Recently, Sakashita and Kumada [5] proposed a nucleate boiling correlation based on the model in which heat transfer occurs primarily by heat conduction through conduction layers formed under primary bubbles. The correlation results in a good agreement with the data of heat flux, wall superheat, and nucleation site density from the isolated to coalesced bubble region. He et al. [6] reported a numerical simulation model of boiling heat transfer. In this model, the boiling curve is reproduced numerically by determining the macrolayer thickness. Based on the physical model of Maruyama et al. [7] they used a simple numerical method and fewer empirical relations to determine the wall superheat from the heat flux. In addition, the formation of nucleation site density was included to investigate the effect of surface cavities. Furthermore, the model is applied in the transient boiling process. From the aforementioned literature review it is clear that there is no complete numerical model which can predict the entire pool boiling curve.

Ideally speaking, a computational fluid dynamics study of pool boiling would be possible if the Navier-Stokes equations could be solved together with continuity and energy equations along with phase change and appropriate boundary conditions. However, there are several problems with simulating the boiling phenomena

based on the Navier-Stokes equations. First, numerical instability will occur because the boundary of the two phases is complex and varies in time. Second, the amount of CPU time needed for the integration of the equation will be very large since the calculations need to be carried out with high accuracy to avoid such numerical instabilities. Therefore, the models based on Navier-Stokes equations cannot be used for the simulation of boiling phenomena in a practical sense. With the numerical techniques available at present only a few bubbles at most can be dealt with.

Coupled map lattice (CML) has been recognized as a powerful tool of analysis to grasp the qualitative and fundamental nature of complex boiling phenomena and has been applied to many physical systems [8,9]. The CML method is based on a dynamic system with continuous field variables but discrete space and time, in which local dynamics propagates in space by diffusion or flow and time is advanced by repeated mapping.

From the study of non-linear chaos dynamics it is known that a complex physical system is not always governed by a complex system of equations. Earlier studies of boiling based on non-linear dynamics, though few and recent, suggest that boiling is a kind of spatio-temporal chaotic phenomenon. The relevant papers in this regard are by Sadasivan et al. [10], Shoji and Tajima [11], Shoji [12], Ellepola and Kenning [13], and Nelson et al. [14,15]. However, applications to CML are not restricted to the problems in spatio-temporal chaos, but include pattern formations, some solid-state problems, biological information processing, and engineering problems [8].

Using the CML method, Yanagita [16] simulated the pool boiling phenomenon and succeeded in explaining the mode of transition from nucleate to film boiling. He assumed that fundamental dynamic processes of boiling are thermal convection, bubble rising motion, and phase change. Although Yanagita's model is very attractive and path breaking, it deviates from the actual boiling process at some points. First, his model permits liquid to evaporate in the bulk, a phenomenon known as homogeneous nucleation, which is different from boiling in the usual sense. Second, in Yanagita's model, pool boiling takes place even when the heater surface temperature is less than the saturation temperature of the liquid. This never happens in the actual boiling systems. Finally, the strict mode of film boiling is not realized by Yanagita's model.

Shoji [12] corrected the deficiencies of the model of Yanagita by including nucleation sites on the heater surface and the Taylor instability. The model was applied to saturated and transient pool boiling of water on a small heated surface at 1 bar. The effects of liquid subcooling and surface roughness were also investigated. Although Shoji's model is basically sound, it has the following limitations. First, the calculation of nucleation superheat distribution is sketchy and cannot be easily reproduced by other researchers. Second, no effect due to stirring action of bubbles is incorporated into his model. Finally, rather than using actual heat flux he used an apparent heat flux (without a unit) to plot the pool boiling curve and hence no information about the predicted CHF could be obtained.

Ghoshdastidar et al. [17] modified the basic theoretical model proposed by Shoji [12] in terms of nucleation superheat distribution and mixing. The stirring action of the bubbles was modeled by increasing the fluid thermal diffusivity by an enhancement factor. The effectiveness of the enhancement factor approach in the model of Ghoshdastidar et al. [17] is clearly seen in its capability of reproducing the atmospheric saturated pool boiling curve for water well and predicting the critical heat flux in the same order of magnitude of the actual value.

1.2 Objectives. The basic objective of this work is to improve the prediction of the critical heat flux (CHF) with respect to the 2D CML model of Ghoshdastidar et al. [17].

2 Problem Formulation

A CML is a dynamical system with discrete time, discrete space, and continuous states. It usually consists of dynamical el-
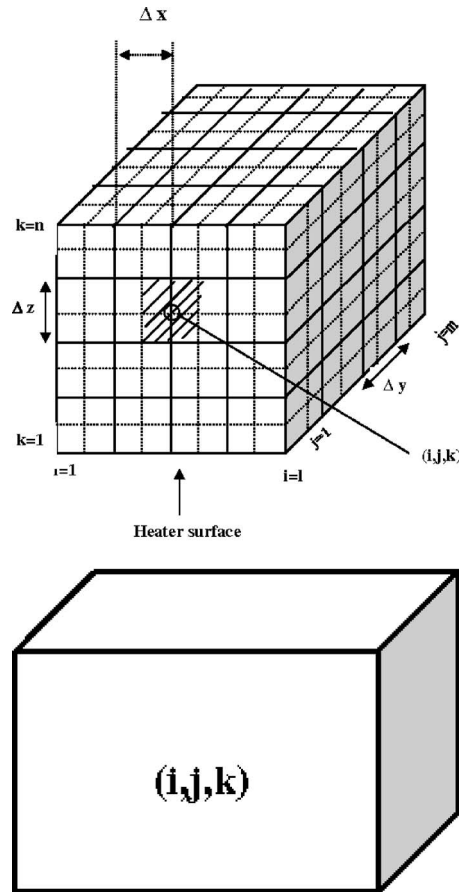
Fig. 1 (*a*) **Computational domain and lattices;** (*b*) **expanded view of an interior cubic lattice**

ements on a lattice which interact (are "coupled") with suitably chosen sets of other elements. Basically in this method a (set of) macroscopic variable(s) is chosen on a lattice. The basic physical processes underlying the phenomena are then decomposed into independent components. Each component is then replaced by a simple parallel dynamics on a lattice. Finally each unit dynamics (or procedure) is carried out successively (Kaneko [8]).

In the present problem it is assumed that boiling is governed by (a) nucleation from cavities on a heated surface, (b) thermal diffusion, (c) bubble rising motion and associated convection, (d) phase change, and (e) Taylor instability.

2.1 Modeling. Saturated boiling of water at one atmospheric pressure on a large (much larger than the minimum wavelength of 2D Taylor waves) and thin horizontal strip is considered, but boiling only on a 3.5 mm × 3.5 mm section is investigated in this work. It is assumed that the boiling scenario is identical in every 3.5 mm × 3.5 mm section of the plate. The heater material is copper. The temperature distribution in the copper strip is ignored as it has a very high thermal conductivity and very small thickness. The three-dimensional boiling field is approximated and modeling is based on CML method as followed by Shoji [12]. The height of the pool of water on the strip is 0.7 mm, indicating thin-film boiling (Kenning [18]). No prior assumption regarding the chaotic nature of the boiling phenomena needs to be made.

2.2 Computational Domain and Lattices. The computational domain is divided into $30 \times 30 \times 30$ lattices as shown in Fig. 1. The volume of each lattice in the pool can contain either liquid or vapor. There are 30 grid points in the horizontal direction, 30 in the vertical direction, and 30 grid points in the direction perpendicular to the plane of paper. The intersection of solid lines

in Fig. 1(a) represents location of grid points. The broken lines in the same figure indicate the faces of lattices. Each lattice contains one grid point at its center. A typical lattice is shown by the shaded region in Fig. 1(a) and an expanded view of an interior lattice is shown in Fig. 1(b). Grid points at the boundaries or at the interface between the heater and the liquid are surrounded by half lattices while those at the corners are surrounded by quarter-lattices, as shown in Fig. 1(a). A grid point is designated by (i,j,k) with "i" increasing in the x direction, "j" in the y direction, and "k" in the "z" direction. A cubic lattice that encloses a grid point (i,j,k) is also referred to as (i,j,k) as shown in Fig. 1(b).

2.3 Field Variable. For simplicity, temperature is employed as the only one field variable. In addition, a flag function, $F_{i,j,k}$ is used for the convenience of calculations to show the phase of each lattice. $F_{i,j,k}$="0" and "1" represent the lattice (i,j,k) in liquid and vapor phases, respectively.

2.4 Formulation of Dynamic Processes. In the CML method, dynamic processes are usually formulated in mappings. In the present model, it is assumed that boiling is governed by the following physics and dynamics.

2.4.1 Nucleation on the Heated Surface. According to Wang and Dhir [4], nucleation cavities are distributed at random on the heated surface. Many cavities are distributed on each surface lattice but if it is assumed that every cavity has a conical shape, a larger cavity yields lower nucleation superheat. Therefore, only the cavity of maximum size (in this case, D_c as calculated from Eq. (2)) is employed, since the active cavity of each surface lattice which determines the local nucleation superheat, ΔT_{act} (Eq. (1)), is required for bubble nucleation. The term $\beta R(i,j)$ is added to D_m to create a randomness among the size of the large cavities. The nucleation superheat is given by

$$\Delta T_{\text{act}} = T_{\text{act}} - T_{\text{sat}} = \frac{4\sigma T_{\text{sat}}}{\rho_v h_{fg} D_c} \qquad (1)$$

where D_c is the diameter of the largest nucleating cavity on a surface lattice. To calculate D_c, the following formula is used:

$$D_c(i,j,1) = D_m + \beta R(i,j) \qquad (2)$$

where $D_c(i,j,1)$ represents the diameter of the largest nucleating cavity on the lattice $(i,j,1)$, D_m is the minimum diameter of nucleating cavities on a heater surface lattice, β, which is assigned a value of 0.99, and indicates the maximum deviation from D_m and has the same unit as D_c and D_m, i.e., micrometer, and $R(i,j)$ is a random number between 0 and 1 assigned at the ith surface lattice, with i and j varying from 1 to 30. Although the number of grid points in the x and y directions is taken as 30×30 in the present study, it may be varied. A total of 302×302 random numbers is generated in x and y directions, that is, from $i=1$ to l and $j=1$ to m using a numerical algorithm group library random number generator subroutine. Every tenth random number of the set is employed at each (i,j) surface lattice starting from the first, that is, for each j starting from 1, i is varying from 1 to l.

The minimum cavity diameter is arbitrarily taken as 1.77 μm. It is assumed that sites smaller than 1.77 μm do not exist on this particular heater surface. Thus, the maximum diameter of the nucleating cavities on a heater surface lattice becomes 2.76 μm as calculated from Eq. (2) when the random number takes on a value of 1.

Thus, using Eqs. (1) and (2), the nucleation superheat distribution on the horizontal surface is calculated. Figures 2(a) and 2(b) show the distribution of nucleation superheat at $j=10$ and $j=15$ in the present case. It can be seen that with an increase of wall superheat more and more nucleation sites are activated. The bubble nucleation is formulated as follows:

$$\text{If } F_{i,j,k}=0 \quad \text{and} \quad T_{i,j,1} > T_{\text{act}} \text{ then } F_{i,j,k}=1 \qquad (3)$$
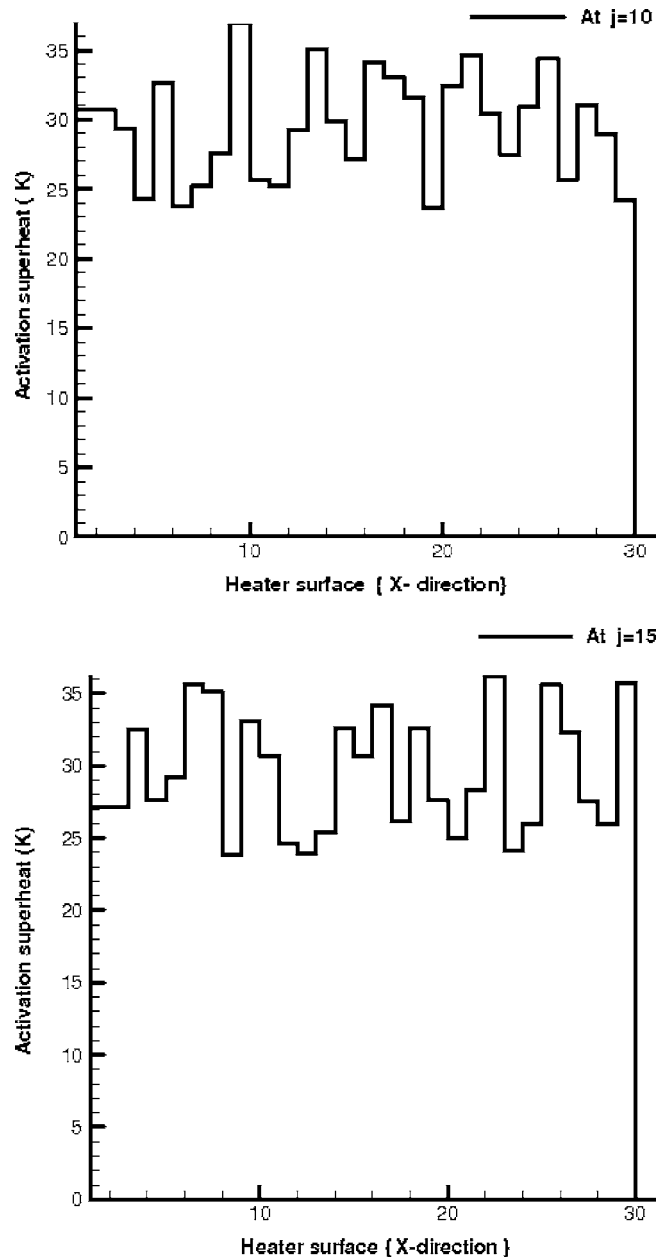
Fig. 2 (a) Nucleation superheat distribution in the *x-z* plane at *j*=10 of the pool; (b) nucleation superheat distribution in the *x-z* plane at *j*=15 of the pool

Thus one nucleation event suddenly fills a complete column of lattices with vapor. Although this is unlikely to occur in an actual case, in the present model this happens only once (i.e., only when the pool is completely liquid) in the iterative cycle leading to the steady state for each wall temperature. This is required for creating the transitional boiling regime at a later stage. It may be noted that there is a fundamental assumption that the nucleate-to-film boiling transition is determined by events in the vapor-liquid space and not by surface chemistry.

Thus to sum up the procedure of obtaining the nucleation superheat distribution, the following points should be kept in mind. The most important point in the calculation of nucleation superheat distribution is the minimum cavity diameter, D_m, on a surface lattice. It may be noted that the minimum cavity diameter is assumed to be the same for all surface lattices in the present problem. If for a given surface D_m is provided then the nucleation superheat distribution can be calculated by the combined applica-

tion of Eqs. (1) and (2).

The following needs to be said about the physical (and mathematical) basis of Eq. (2). Since β is the maximum deviation from the minimum cavity diameter, the product of β and the random number $R(i,j)$, which takes on a value between 0 and 1, essentially implies that a fraction of that maximum deviation is taken. The product (i.e., $\beta R(i,j)$) is then added to the minimum value, D_m, to get D_c from Eq. (2). It can be easily seen that D_c can vary from 1.77 to 2.76 μm. The deviation β does not have to have a fixed value. The choice of a value for β should be dictated by the information the analyst has about the minimum cavity size on a given surface lattice and the maximum cavity size on the heater surface. Thus, β may vary from one surface lattice to the other.

2.4.2 Thermal Diffusion

2.4.2.1 Governing equation. Since thermal conduction is occurring in the fluid, the following governing equation is applicable as a three-dimensional boiling field is simulated.

$$\frac{\partial T}{\partial t} = \alpha \left(\frac{\partial^2 T}{\partial x^2} + \frac{\partial^2 T}{\partial y^2} + \frac{\partial^2 T}{\partial z^2} \right) \tag{4}$$

The medium is assumed to be isotropic and homogeneous. The fluid may exist in the state of either liquid, liquid and vapor, but each fluid lattice can contain either liquid or vapor at a given time.

2.4.2.2 Boundary conditions. A periodic boundary condition [19] is imposed on four sides of boiling field, $i=1$, $i=l$, $j=1$, and $j=$m because it is assumed that the heater surface is infinite in the x and y directions, respectively, and the boiling scenario is identical in every 3.5 mm $\times$ 3.5 mm section. Thus the theory of Taylor instability can be applied in the present model. The temperature on the top of the field ($k=n$) is fixed at a constant prescribed liquid temperature (saturation temperature in this case). The bottom, $k=1$, is at prescribed heater temperature (T_w).

2.4.2.3 Initial condition. At $t=0$,

$$T_{i,j,k} = T_{\text{sat}} \quad \text{for all } i,j,k \tag{5}$$

$$F_{i,j,k} = 0 \quad \text{for all } i,j,k \tag{6}$$

2.4.2.4 Discretization scheme. An explicit finite difference scheme is used to discretize the governing equation.

2.4.2.5 Finite difference equations. In the present study, $l=30$, $m=30$, and $n=30$. It may be noted that, in the following equations,

$$r_1 = \alpha \Delta t / (\Delta x)^2$$

$$r_2 = \alpha \Delta t / (\Delta y)^2$$

$$r_3 = \alpha \Delta t / (\Delta z)^2$$

At any interior grid point (i,j,k), the following equation is valid:

$$T'_{i,j,k} = T^p_{i,j,k}(1 - 2r_1 - 2r_2 - 2r_3) + r_1(T^p_{i-1,j,k} + T^p_{i+1,j,k})$$
$$+ r_2(T^p_{i,j-1,k} + T^p_{i,j+1,k}) + r_3(T^p_{i,j,k-1} + T^p_{i,j,k+1}) \tag{7}$$

At the left boundary ($i=1$, $j=2$ to $m-1$, $k=2$ to $n-1$), using periodic boundary condition, $T^p_{0,j,k} = T^p_{l,j,k}$ in Eq. (7), gives

$$T'_{1,j,k} = T^p_{1,j,k}(1 - 2r_1 - 2r_2 - 2r_3) + r_1(T^p_{l,j,k} + T^p_{2,j,k})$$
$$+ r_2(T^p_{1,j-1,k} + T^p_{1,j+1,k}) + r_3(T^p_{1,j,k-1} + T^p_{1,j,k+1}) \tag{8}$$

At the right boundary ($i=l$, $j=2$ to $m-1$, $k=2$ to $n-1$), using periodic boundary condition, $T^p_{l+1,j,k} = T^p_{1,j,k}$ in Eq. (7), gives

$$T'_{l,j,k} = T^p_{l,j,k}(1 - 2r_1 - 2r_2 - 2r_3) + r_1(T^p_{l-1,j,k} + T^p_{1,j,k})$$
$$+ r_2(T^p_{l,j-1,k} + T^p_{l,j+1,k}) + r_3(T^p_{l,j,k-1} + T^p_{l,j,k+1}) \tag{9}$$

At the front boundary ($j=l$, $i=2$ to $l-1$, $k=2$ to $n-1$), using the

periodic boundary condition, $T^p_{i,0,\mathrm{k}} = T^p_{i,m,k}$ in Eq. (7), gives

$$T'_{i,1,k} = T^p_{i,1,k}(1 - 2r_1 - 2r_2 - 2r_3) + r_1(T^p_{i-1,1,k} + T^p_{i+1,1,k})$$
$$+ r_2(T^p_{i,m,k} + T^p_{i,2,k}) + r_3(T^p_{i,1,k-1} + T^p_{i,1,k+1}) \tag{10}$$

At the rear boundary ($j=n$, $i=2$ to $l-1$, $k=2$ to $n-1$), using the periodic boundary condition, $T^p_{i,m+1,k} = T^p_{i,1,k}$ in Eq. (7), gives

$$T'_{i,m,k} = T^p_{i,m,k}(1 - 2r_1 - 2r_2 - 2r_3) + r_1(T^p_{i-1,m,k} + T^p_{i+1,m,k})$$
$$+ r_2(T^p_{i,m-1,k} + T^p_{i,1,k}) + r_3(T^p_{i,m,k-1} + T^p_{i,m,k+1}) \tag{11}$$

Note that $(0,j,k)$ and $(l+1,j,k)$ are fictitious points outside the computational domain placed at a distance of Δx from the left and right vertical boundaries and $(i,0,k)$ and $(i,m+1,k)$ are fictitious points outside the computational domain placed at a distance of Δy from the front and rear boundaries, respectively.

At the top boundary ($i=1$ to l, $j=1$ to m, $k=n$),

$$T' = T_{\text{sat}} \tag{12}$$

At the bottom boundary ($i=1$ to l, $j=1$ to l, $k=1$),

$$T' = T_w \tag{13}$$

2.4.2.6 Stability. For the stability of numerical calculations, the following condition should be satisfied:

$$\Delta t \leq \frac{1}{2\alpha[(\Delta x)^{-2} + (\Delta y)^{-2} + (\Delta z)^{-2}]} \tag{14}$$

2.4.2.7 Grid spacing and stability. In the present case, $\Delta x = 0.120$ mm and $\Delta y = 0.120$ mm; $\Delta z = 0.024$ mm, $\Delta t = 10^{-5}$ s is used to ensure numerical stability.

2.4.3 Bubble Rising Motion and Thermal Convection.
The bubble motion due to buoyancy and its effect on temperature may be expressed simply by the following mapping.

$$T''_{i,j,k} = T'_{i,j,k} + \frac{S_{i,j,k}}{2}(\boldsymbol{\rho}_{\mathrm{i,j,k+1}} - \boldsymbol{\rho}_{\mathrm{i,j,k-1}})T'_{i,j,k} \tag{15}$$

where $\boldsymbol{\rho}=1$ for a liquid lattice and $\boldsymbol{\rho}=0$ for a vapor lattice. Note that $\boldsymbol{\rho}$ is dimensionless in this case. The parameter $S_{i,j,k}$ represents the velocity of bubble rising motion and the strength of thermal convection. Equation (15) has been derived from the equations of motion and energy by assuming that the liquid motion is mainly driven by the buoyancy force, and velocities in the x and y directions and viscous force may be negligibly small (see the Appendix).

2.4.4 Phase Change and Effects of Bubble Motion.
It is known that latent heat is consumed when liquid evaporates and is released when vapor condenses. This phase change process is formulated as follows [12]:

If $F_{i,j,k}=0$ and $T''_{i,j,k} > T_{c(i,j,k)}$ then $T^{p+1}_{n(i,j,k)} = T''_{n(i,j,k)} - \eta$

$$\tag{16}$$

If $F_{i,j,k}=1$ and $T''_{i,j,k} < T_{c(i,j,k)}$ then $T^{p+1}_{n(i,j,k)} = T''_{n(i,j,k)} + \eta$

$$\tag{17}$$

The suffix $n(i,j,k)$ represents the nearest neighboring four lattices and $T_{c(i,j,k)}$ is the phase change temperature, which is determined according to the phase change criteria given below. In Eqs. (16) and (17), η is a parameter related to the enthalpy of vaporization and has a unit of $^\circ$C. The aforesaid equations also represent the mixing effect of bulk liquid due to bubble motion.

2.4.4.1 Phase change criteria. The value of $T_{c(i,j,k)}$ for the liquid lattice adjacent to the heater is nucleation superheat, as shown in Figs. 2(a) and 2(b) at $j=1$ to m in the x-z planes. The value for liquid lattices in the bulk is assumed to be the homoge-

neous nucleation temperature of the liquid (which is 300°C for water), but for liquid lattice neighboring the vapor lattice, the saturation temperature of liquid which is 100°C for water.

2.4.5 Taylor Instability. In film boiling, vapor bubbles depart from the vapor film on a heated surface at regular horizontal spacing due to Taylor instability, i.e., the unstable configuration of liquid over vapor. The heavy phase falls down at one node of a wave and the light fluid rises into the other node. In the present model, this effect is included in the dynamic process mentioned earlier (Sec. 2.4.3) by defining $S_{i,j,k}$ in Eq. (15) as follows [12]:

$$S_{i,j,k} = \delta \text{ when } \cos(2\pi i/\lambda^*)(\cos 2\pi j/\lambda^*) \geq \sqrt{2}a \quad (18)$$

$$S_{i,j,k} = -\delta \text{ when } \cos(2\pi i/\lambda^*)(\cos 2\pi j/\lambda^*) \leq \sqrt{2}a \quad (19)$$

where λ^* is the magnitude of λ corresponding to its mm dimension as calculated by

$$\lambda = \frac{2\pi\sqrt{6}}{\sqrt{(\rho_l - \rho_v)g/\sigma}} \quad (20)$$

for two-dimensional waves [20] and a is an appropriate constant; and i and j in the cos function of Eqs. (18) and (19) are the grid point number in the x and y directions, respectively. The idea behind the use of Eq. (19) is to inhibit the bubble rising motion in order to create a situation conducive to transitional boiling. The CHF criterion is Taylor-Helmholtz instability as proposed by Zuber [21].

3 Method of Solution

3.1 Time Advancement. Time is advanced by repeating a set of mapping the dynamic processes (Secs. 2.4.2–2.4.5) in such a manner that

$$T^p \to T' \to T'' \to T^{p+1} \quad (21)$$

where the superscripts p and $p+1$ indicate the present and future time values of the temperature.

3.2 Parameter Values. The present model has four parameters. In the CML method, the parameter values are determined so as to reproduce the phenomena satisfactorily. In the present computations, the parameter values are

$$\delta = 0.015$$

$$\lambda^* = 38.178$$

$$\eta = 1 \quad (k > 2)$$

$$a = 0.85$$

The η value for $k=2$ grid points is employed as shown in Fig. 3 to include the microlayer and macrolayer evaporation. The negative sign before 2 indicates a decrease in temperature. It should be noted that different parameter values might be needed for different boiling systems and conditions.

The value of "δ" is dictated by Eq. (A7) and that of λ^* by Eq. (20). The value of η is determined by taking into consideration the observation of Nukiyama [1] who reported a drop of 0.2–0.5°C in the temperature of bulk water adjacent to steam bubbles. The choice of the value of "a" is arbitrary. It is chosen to make sure that the pool boiling curve is reproduced satisfactorily.

3.3 Overall Solution Algorithm.

1. Specify $T_w = 101°C$ and T^p.
2. Calculate T' by solving the thermal diffusion equation (Eq. (4)).
3. Apply the nucleation criterion (Equation (3)) only if the entire pool is in the liquid state, i.e., $F_{i,j,k}=0$.
4. Determine the phase state of each fluid lattice by using *phase change criteria*.
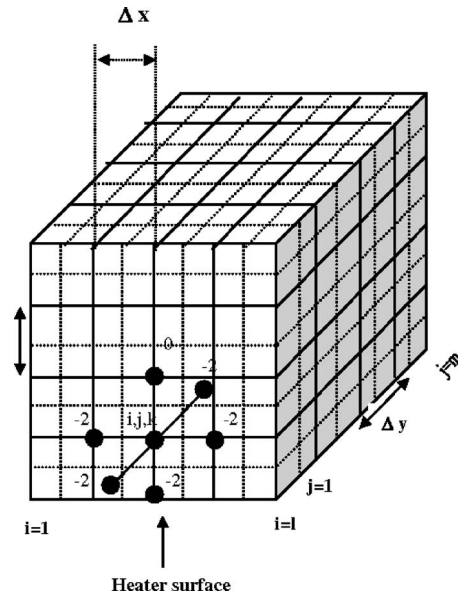
Fig. 3 Values of η for $k=2$ evaporating (i,j,k) lattices

5. Use Eq. (15) to get $T^\parallel$.
6. Check the phase state of each fluid lattice again.
7. Apply Eqs. (16) and (17) to obtain T^{p+1}.
8. Check the phase state of each fluid lattice once more.

Is steady state reached? If yes, go to step 10. If not, calculate the overall vapor fraction, f (by volume), and equivalent density, specific heat, and thermal conductivity and diffusivity of the liquid/vapor mixture using the following equations, enhance the molecular thermal conductivity and diffusivity of the fluid by a suitable factor as described below to include the effect of mixing effect of the bubbles, and go to step 2:

$$k_{eq} = fk_v + (1-f)k_l \quad (22)$$

$$\rho_{eq} = f\rho_v + (1-f)\rho_l \quad (23)$$

$$c_{eq} = fc_v + (1-f)c_l \quad (24)$$

$$\alpha_{eq} = \frac{k_{eq}}{\rho_{eq}c_{eq}} \quad (25)$$

The overall vapor fraction, f, is defined as the ratio of the volume of vapor and the volume of liquid/vapor mixture in the pool:

If $f \leq 0.1$, then k_{eq} and hence α_{eq} is multiplied by a factor of 1.5.
If $f > 0.1$, then the enhancement factor is 2.

The enhancement factor basically takes into account the turbulent mixing in the fluid resulting from the bubble stirring action which enhances the thermal diffusivity of the fluid.

9. Calculate the steady state wall heat flux as follows:

$$q^\parallel = -k_{eq}(1/lm)\sum_{i=1}^{l}\sum_{j=1}^{m}\left(\frac{\partial T}{\partial z}\right)_{i,j,1} \quad (26)$$

where $(\partial T/\partial z)_{i,j,1}$ is calculated by a five-point forward difference scheme [19] and 1=total number of grid points in the x direction (=30 in the present case), m=total number of grid points in the y direction (=30 in the present case).

10. Print the wall superheat, heat flux.

Fig. 4 Flow chart of the overall solution algorithm

11. $T_w = T_w + 1$; respecify T^p.
12. Is $T_w > 145\,^\circ C$? If yes, go to step 13. If no, go to step 2.
13. STOP

A concise flow chart of the solution algorithm is shown in Fig. 4.

4 Result and Discussion

4.1 Saturated Pool Boiling Curve for Water. Figure 5 shows the comparison of pool boiling curve for water at 1 bar
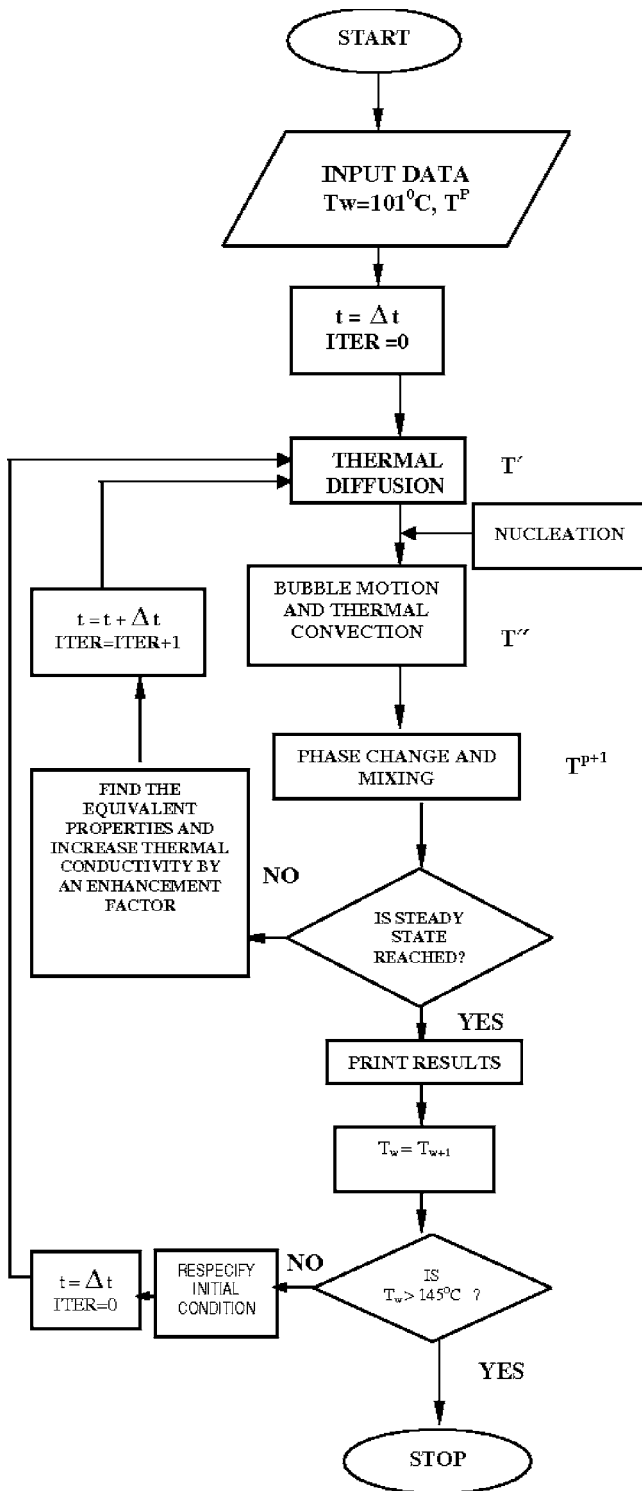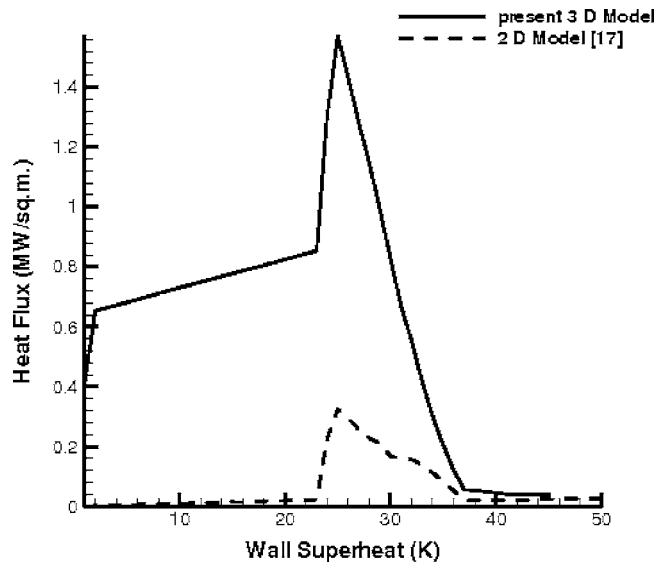

Fig. 5 Comparison of saturated pool boiling curves for water at 1 bar based on 2D and 3D CML models

using 3D and 2D CML (at $t = 1$ s, which is approximately the time required to reach the steady condition). For the prescribed wall temperature mapping is repeated 100,000 times (since $\Delta t = 10^{-5}$ s) until the stationary (steady) state is attained. The steady state here means that the temperature at each grid point shows virtually no time variation. The input data are shown in Table 1.

The sources of the property data for water (liquid and vapor phases) and pure copper are Holman [22], Incropera and Dewitt [23], and van Stralen and Cole [24]. The optimum number of grid points after a grid independent test is carried out is $30 \times 30 \times 30$. On the SUN Enterprise 10,000 computer system approximately 336 h of CPU time were required to produce the pool boiling curve using a step of 1 K wall superheat in 45 such steps. It is evident that the CML model has qualitatively reproduced the classical pool boiling curve. The predicted critical heat flux (CHF) is 1.57 MW/m^2 as compared to the actual value of 1.3 MW/m^2 (obtained from Zuber's correlation [21]) and 0.36 MW/m^2 predicted by the 2D CML model of Ghoshdastidar et al. [17].

It may be noted that in the present 3D model enhancement factor used is only 1.5–2.0 as compared to 10–15 in the model of Ghoshdastidar et al. [17]. Thus, the 3D CML model has been able to capture the physics of pool boiling significantly better than the corresponding 2D model. It is evident that 3D modeling is a natural and necessary step for the simulation of turbulent mixing. Thus bubble stirring action is realistically captured in the case of 3D CML modeling. The capability of the present model in predicting CHF very close to the actual value and producing a realistic pool

Table 1 Properties of water in liquid and vapor phases at 1 bar

Water (liquid phase)

1. Surface tension = 58.8×10^{-3} N/m
2. Saturation temperature = $100\,^\circ C$
3. Homogeneous nucleation temperature = $300\,^\circ C$
4. Latent heat of vaporization = 2257 kJ/kg
5. Thermal conductivity = 0.68 W/mk
6. Specific heat = 4.2 kJ/kg K
7. Density = 960 kg/m^3

Water (vapor phase)

1. Density = 0.5955 kg/m^3
2. Thermal conductivity = 24.6×10^{-3} W/mk
3. Specific heat = 2.06 kJ/kg K
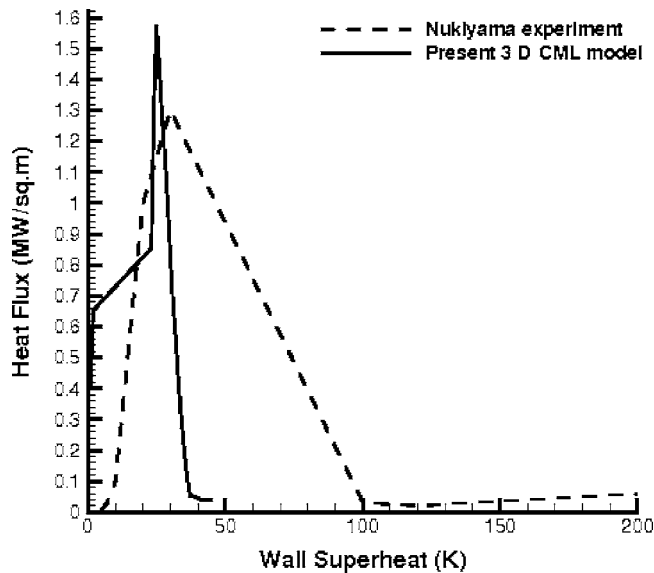
Fig. 6 Comparison of the saturated pool boiling curve for water at 1 bar predicted by the present 3D CML model and that produced in the experiment of Nukiyama [1]

Fig. 7 Variation of vapor fraction in the *x-z* plane at *j*=10 and *j*=15 of the pool

boiling curve is a significant improvement over the earlier works.

Figure 6 shows a comparison of the pool boiling curve predicted by the present 3D CML model and that produced in the experiment of Nukiyama [1]. A careful look at the two graphs reveals that (i) the basic shape of the curve produced by the present CML model matches with that of Nukiyama [1]; (ii) CHF predicted by the numerical model is very close to that obtained in the Nukiyama experiment; (iii) as in Nukiyama curve the sharp increase of heat flux from the natural convection regime to the nucleate boiling regime is clearly reflected in CML results. There is a major difference, however, between the two curves, that is, the transition boiling regime in the CML-generated curve is too narrow. While in the Nukiyama experiment the minimum heat flux occurred at a wall superheat of 120 K, the CML simulation result shows that the corresponding wall superheat is only 40 K. The modeling of transition boiling regime can be made more realistic by making cavity sizes smaller as is evident from Fig. 8.

4.2 Vapor Fractions Versus Wall Superheat Plots. Figure 7 shows the overall vapor fractions versus wall superheat plots for the 3D CML model. The vapor fraction is calculated on the basis of the vapor content in different layers of the pool. In the present case $j=10$ and $j=15$ are considered. The effect of third dimension can be clearly visualized from the plots. In the stable film boiling regime the entire pool is in vapor phase.

5 Sensitivity Study

Several arbitrary parameters have been used in the present CML model. They are minimum cavity diameter (D_m), β in Eq. (2), η (in Eqs. (16) and (17)), a in Eqs. (18) and (19), and enhancement factor used in Eqs. (22)–(25). In the following sensitivity study the effect of the above parameters on the atmospheric saturated pool boiling curve for water is investigated.

5.1 Minimum Cavity Diameter (D_m). Figure 8 shows pool boiling curves for $D_m=1$, 1.77, and 3 μm. Lower D_m gives rise to lower D_c (see Eq. (2)) and hence, larger activation or nucleation superheat (see Eq. (1)). As a result, with decrease in D_m, boiling curve shifts to the right. Furthermore, CHF increases with decrease in the minimum cavity diameter. Furthermore, as the cavity diameter decreases the transition boiling regime becomes broader
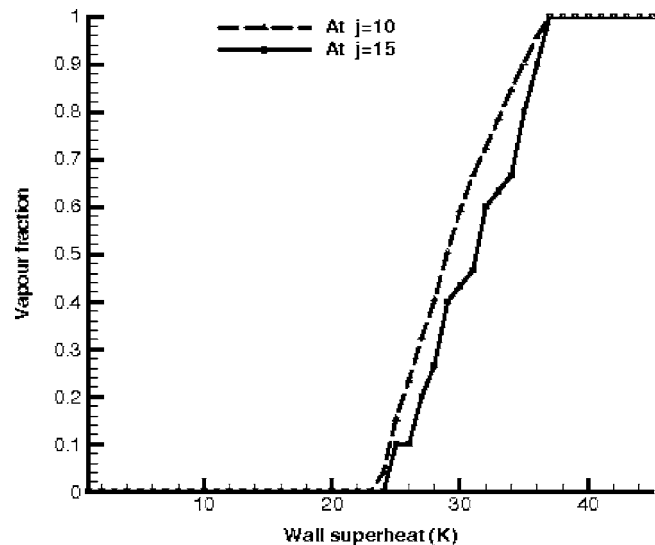
which is more realistic. It may be noted here that for $D_m=1$ μm, full boiling curve could not be reproduced as the computation was carried out up to $\Delta T_w=45$ K.

5.2 Parameter β. "β" appears in Eq. (2). Since β is the maximum deviation from the minimum cavity diameter, larger value of β implies larger cavity diameters. In this study three values of β were taken, that is, 0.7, 0.8, and 0.99. As expected, with increase in the value of β, the boiling curve shifts to the left (Fig. 9). However, CHFs for $\beta=0.8$ and $\beta=0.99$ are more or less the same although for $\beta=0.7$ CHF is showing a lower value.

5.3 Parameter η. "η" appears in Eqs. (16) and (17). η is a parameter related to the enthalpy of vaporization and has a unit of $^\circ$C. It is seen from Fig. 10 that changing η (for $k>2$ grid points)
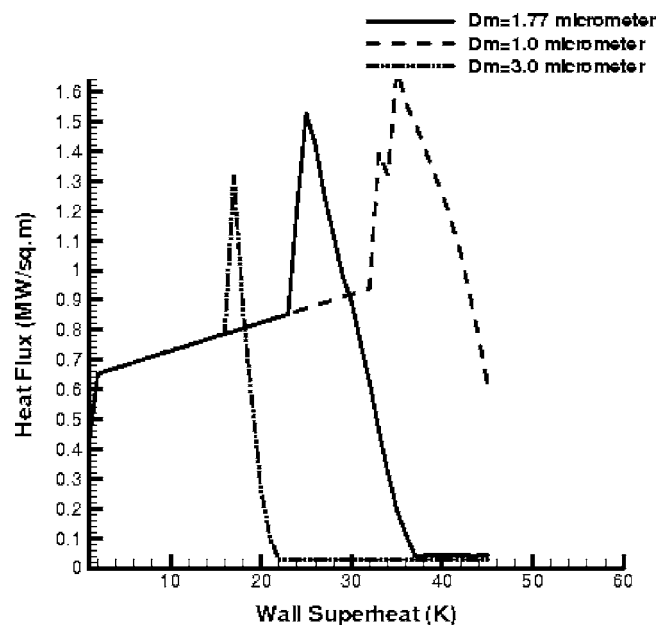
Fig. 8 Effect of minimum cavity diameter (D_m) on the saturated pool boiling curve for water at 1 bar
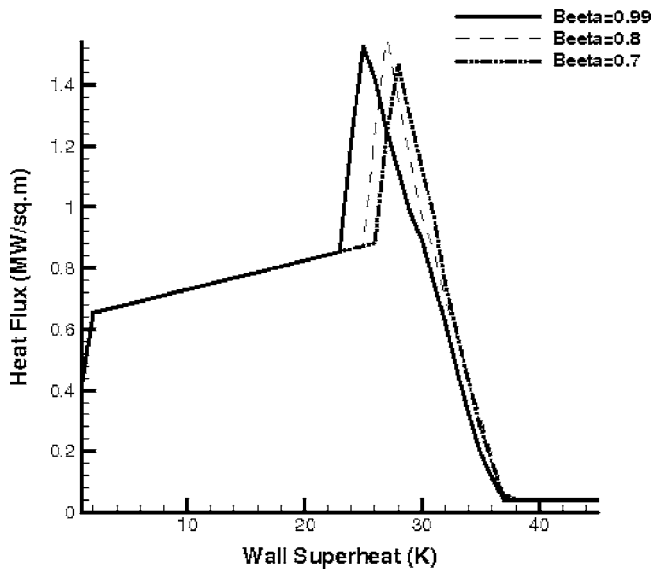
Fig. 9 Effect of the parameter β (in Eq. (2)) on the saturated pool boiling curve for water at 1 bar

Fig. 11 Effect of the parameter a (in Eqs. (18) and (19)) on the saturated pool boiling curve for water at 1 bar

from 1 to 3 (the corresponding value for $k=2$ being 2–4) has little effect on the pool boiling curve except in the transition boiling regime.

5.4 Parameter a. "a" is used in Eqs. (18) and (19). Figure 11 shows that varying a from 0.75 to 0.95 does not change the pool boiling curve significantly.

5.5 Enhancement Factor. The enhancement factor is used to increase k_{eq}, ρ_{eq}, c_{eq}, and α_{eq} in Eqs. (22)–(25), respectively, in order to include mixing effect of bubbles. In the present 3D CML model, if overall vapor fraction f is less than or equal to 0.1, then the factor is taken as 1.5, otherwise it is 2. The CHF predicted is 1.57 MW/m^2 which is very close to the actual value of 1.3 MW/m^2. This clearly shows that in the present model there is little need to artificially increase the thermal diffusivity. The turbulent mixing due to bubble stirring action is automatically taken care of in the 3D CML model as there is now mixing due to evaporation and condensation of vapor lattices in both x-y as well as x-z planes. When the enhancement factors are increased from 1.5 to 10, and 2 to 15 it is observed from Fig. 12 that CHF rises to around 16 MW/m^2 which clearly shows that unlike in the 2D CML model, in the 3D CML model raising the value of thermal diffusivity by an order of magnitude is not required.

Thus, the above sensitivity analysis clearly shows that the present 3D CML model gives physically realistic and stable results.

6 Conclusions

In conclusion it can be said that the present 3D CML model has been able to capture the physics of pool boiling significantly better than the corresponding 2D model. For the first time a coupled map

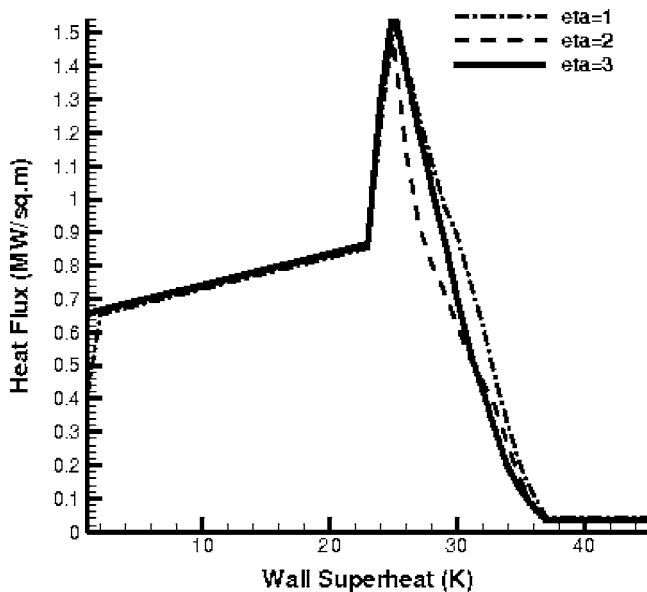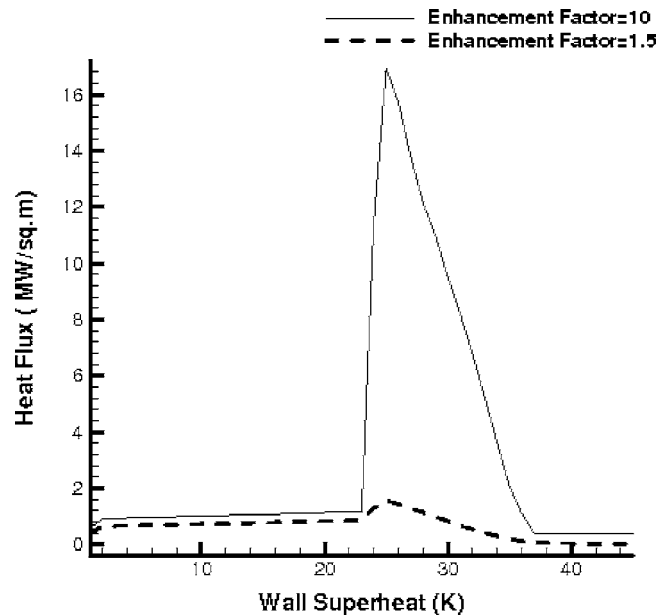**Fig. 10 Effect of the parameter η (in Eqs. (16) and (17)) on the saturated pool boiling curve for water at 1 bar**

Fig. 12 Effect of enhancement factor on the saturated pool boiling curve for water at 1 bar

lattice method which is essentially qualitative in nature has been able to predict the CHF of saturated pool boiling of water at 1 bar very close to the actual value. A sensitivity analysis shows that the model gives physically realistic and stable results. This shows the promise of using a CML model for the quantitative prediction of CHF in future for fluid other than water and pressures other than 1 bar.

Nomenclature

c = specific heat (J/kg K)
D_c = diameter of the largest nucleating cavity on a surface lattice (μm)
D_m = minimum cavity diameter on a surface lattice (μm)
f = overall vapor fraction in the pool
$F_{i,j,k}$ = flag function
g = acceleration due to gravity (m/s^2)
h_{fg} = latent heat of vaporization (J/kg)
i = grid point index in the x direction
j = grid point index in the y direction
k = thermal conductivity (W/mK), grid point index in the z direction
l = number of grid points in the x direction
m = number of grid points in the y direction
n = number of grid points in the z direction
$q^{\parallel}$ = wall heat flux (W/m^2)
R = random number between 0 and 1
$S_{i,j,k}$ = parameter for thermal convection
t = time (s)
Δt = time increment (s)
T = temperature (K)
T_{act} = nucleation wall temperature (K)
T_{sat} = saturation temperature (K)
T_w = wall temperature (K)
ΔT_{act} = nucleation superheat, $T_{\text{act}} - T_{\text{sat}}$ (K)
ΔT_w = wall superheat, $T_w - T_{\text{sat}}$ (K)
x, y, z = Cartesian coordinates

Greek Symbols

α = thermal diffusivity $= (k/\rho c)$ (m^2/s)
β = maximum deviation from D_m (μm)
δ = parameter in Eq. (15)
η = parameter in phase change or mixing (°C)
λ = wave length of Taylor instability (m) (Eq. (20))
λ^* = magnitude of λ corresponding to its mm dimension (Eqs. (16) and (17))
ρ = density (kg/m^3)
ρ = ratio of liquid or vapor density to saturation density of the liquid, Eq. (15)
σ = surface tension (N/m)

Subscripts

eq = equivalent
l = liquid
m = minimum
sat = saturation
v = vapor

Superscripts

$*$ = dimensionless
p = present time
$p+1$ = future time, at the end of overall mapping process in time step, Δt

Abbreviations

CHF = critical heat flux
CML = coupled map lattice

Appendix

Derivation of Eq. (15)

Assumptions.

1. No horizontal component of velocity, i.e., $u=0$, $v=0$, $V = w\hat{k}$
2. Inviscid flow, i.e., $\nu \approx 0$
3. Ideal gas equation is valid for the fluid for which the equation of state is $p = \rho RT$

where "p" is pressure, "ρ" is the density of the fluid, "R" is the particular gas constant, "T" is the temperature of the fluid.

Continuity Equation.

$$\frac{\partial u}{\partial x} + \frac{\partial v}{\partial y} + \frac{\partial w}{\partial z} = 0 \tag{A1}$$

Here, ρ=constant except in the z-momentum equation, using the Boussinesq approximation.

Since, $u=0$, $v=0$, Eq. (A1) reduces to $\partial w/\partial z = 0$.

Hence w=constant in the z direction.

Momentum Equations.
x and y-momentum equations are neglected as $u=0$, $v=0$

z-momentum equation:

$$\rho \frac{\partial w}{\partial t} + u\frac{\partial w}{\partial x} + v\frac{\partial w}{\partial y} + w\frac{\partial w}{\partial z} = Z - \frac{\partial p}{\partial z} + \nu \nabla^2 w \tag{A2}$$

Since $u=0$, $v=0$, $\partial w/\partial z = 0$ and $\nu \approx 0$, Eq. (A2) reduces to

$$\rho \frac{\partial w}{\partial t} = Z - \frac{\partial p}{\partial z} \tag{A3}$$

Energy Equation.
Note that thermal diffusion has already been considered in the first map and hence the diffusion term in the right hand side term is not appearing here.

$$\frac{\partial T}{\partial t} + u\frac{\partial T}{\partial x} + v\frac{\partial T}{\partial y} + w\frac{\partial T}{\partial z} = 0$$

Since $u=0$, $v=0$, energy equation reduces to

$$\frac{\partial T}{\partial t} + w\frac{\partial T}{\partial z} = 0 \tag{A4}$$

Now in equation (A3), $Z = -\rho g$ (here, y is positive upward and "g" is acting downward) where ρ is the density in the thermal boundary layer.

$$\frac{\partial p}{\partial z} = -\rho_\infty g \text{ (hydrostatic)}$$

where ρ_∞ is the bulk density of the fluid.

Substituting "Z" and $\frac{\partial p}{\partial z}$ in Eq. (A3)

$$\rho \frac{\partial w}{\partial t} = -\rho g - (-\rho_\infty g) = -\rho g + \rho_\infty g = g(\rho_\infty - \rho)$$

$$\frac{\partial w}{\partial t} = \frac{g}{\rho}(\rho_\infty - \rho) \tag{A5}$$

Assuming ρ versus T linearly varying in the small temperature range,

$$\frac{\rho_\infty - \rho}{T_\infty - T} = \frac{\partial \rho}{\partial T}$$

$$\rho_\infty - \rho = (T_\infty - T)\frac{\partial \rho}{\partial T}$$

Putting the value of $(\rho_\infty - \rho)$ in Eq. (A5), we get

$$\frac{\partial w}{\partial t} = \frac{g}{\rho}\frac{\partial \rho}{\partial T}(T_\infty - T)$$

Using the explicit finite difference scheme (note that superscript ′ refers to thermal diffusion map and bubble rising velocity is zero at that time)

$$\Rightarrow \frac{w - 0}{\Delta T} = \frac{g}{\rho}\frac{\partial \rho}{\partial T}(T_\infty - T'_{i,j,k})$$

$$\Rightarrow w = \frac{g}{\rho}\frac{\partial \rho}{\partial T}(T_\infty - T'_{i,j,k})\Delta t \tag{A6}$$

From Eq. (A6), $\frac{\partial T}{\partial t} = -w\frac{\partial T}{\partial z}$

Substituting the expression for "w" from Eq. (A6) in the above equation

$$\frac{\partial T}{\partial t} = -\frac{g}{\rho}\frac{\partial \rho}{\partial T}(T_\infty - T'_{i,j,k})\Delta t\frac{\partial T}{\partial z}$$

$$\Rightarrow \frac{\partial T}{\partial t} = -\frac{g}{\rho}(T_\infty - T'_{i,j,k})\Delta t\frac{\partial \rho}{\partial T}\frac{\partial T}{\partial z}$$

$$\Rightarrow \frac{\partial T}{\partial t} = -\frac{g}{\rho}(T_\infty - T'_{i,j,k})\Delta t\frac{\partial \rho}{\partial z}$$

Using the explicit finite difference scheme

$$\frac{T''_{i,j,k} - T'_{i,j,k}}{\Delta t} = -\frac{g}{\rho}(T_\infty - T'_{i,j,k})\Delta t\frac{\partial \rho}{\partial z}$$

$$\Rightarrow T''_{i,j,k} = T'_{i,j,k} - \frac{g}{\rho}(T_\infty - T'_{i,j,k})(\Delta t)^2\frac{\partial \rho}{\partial z}$$

$$= T'_{i,j,k} - \frac{g}{\rho}(T_\infty - T'_{i,j,k})$$

$$\times (\Delta t)^2\left(\frac{\rho_{i,j,k+1} - \rho_{i,j,k-1}}{2\Delta z}\right)$$

$$= T'_{i,j,k} - \frac{1}{2}\left[\frac{g(T_\infty - T'_{i,j,k})(\Delta t)^2}{\Delta z}\right]\frac{1}{\rho}(\rho_{i,j,k+1}$$

$$- \rho_{i,j,k-1})$$

$$= T'_{i,j,k}$$

$$- \frac{1}{2}\left[\frac{g(T_\infty - T'_{i,j,k})(\Delta t)^2}{\Delta z}\right]\frac{RT'_{i,j,k}}{P}(\rho_{i,j,k+1}$$

$$- \rho_{i,j,k-1})\left(\text{since } \rho = \frac{p}{RT}\right)$$

Assuming $p = p_{sat} = \text{constant} = \rho_{sat}RT_{sat}$

$$T''_{i,j,k} = T'_{i,j,k} - \frac{1}{2}\left[\frac{g(T_\infty - T'_{i,j,k})(\Delta t)^2}{\Delta z}\right]$$

$$T'_{i,j,k}\frac{1}{\rho_{sat}T_{sat}}(\rho_{i,j,k+1} - \rho_{i,j,k-1})$$

$$T''_{i,j,k} = T'_{i,j,k} + \frac{1}{2}\left[\frac{-g(T_\infty - T'_{i,j,k})(\Delta t)^2}{\Delta zT_{sat}}\right]T'_{i,j,k}\left(\frac{\rho_{i,j,k+1}}{\rho_{sat}} - \frac{\rho_{i,j,k-1}}{\rho_{sat}}\right)$$

$$T''_{i,j,k} = T'_{i,j,k} + \frac{\delta}{2}T'_{i,j,k}\left(\frac{\rho_{i,j,k+1}}{\rho_{sat}} - \frac{\rho_{i,j,k-1}}{\rho_{sat}}\right)$$

$$\text{where } \delta = \left[\frac{-g(T_\infty - T)(\Delta t)^2}{\Delta zT_{sat}}\right] \tag{A7}$$

When the fluid is in the liquid state,

$$\frac{\rho_{i,j,k+1}}{\rho_{sat}} \quad \text{or} \quad \frac{\rho_{i,j,k-1}}{\rho_{sat}} = \boldsymbol{\rho}_{i,j,k+1} \quad \text{or} \quad \boldsymbol{\rho}_{i,j,k-1} = 1$$

ρ_{sat} is the saturation density of the liquid.

When the fluid is in vapor state,

$$\frac{\rho_{i,j,k+1}}{\rho_{sat}} \quad \text{or} \quad \frac{\rho_{i,j,k-1}}{\rho_{sat}} = \boldsymbol{\rho}_{i,j,k+1} \quad \text{or} \quad \boldsymbol{\rho}_{i,j,k-1} = 0$$

Finally, the convection equation reduces to the following form

$$T''_{i,j,k} = T'_{i,j,k} + \frac{S_{i,j,k}}{2}(\boldsymbol{\rho}_{i,j,k+1} - \boldsymbol{\rho}_{i,j,k-1})T'_{i,j,k} \tag{A8}$$

where $S_{i,j,k} = +\delta = -\delta$ depending upon Taylor instability criteria, that is, Eqs. (18) and (19).

References

[1] Nukiyama, S., 1934, "The Maximum and Minimum Values of the Heat Q Transmitted From Metal to Boiling Water Under Atmospheric Pressure," J. Japan Soc. Mech. Engrs., **37**, pp. 367–374 [Translation: Int. J. Heat Mass Transfer, **9**. pp. 1419–1432 (1966)].

[2] Drew, T. B., and Mueller, C., 1937, "Boiling," Trans. AIChE, **33**, pp. 449–473.

[3] Jakob, M., 1949, *Heat Transfer*, Wiley, New York.

[4] Wang, C. H., and Dhir, V. K., 1993, "Effect of Surface Wettability on Active Nucleation Site Density During Pool Boiling of Water on a Vertical Surface," Trans. ASME, Ser. C: J. Heat Transfer, **115**, pp. 659–669.

[5] Sakashita, H., and Kumada, T., 2001, "Method for Predicting Boiling Curves of Saturated Nucleate Boiling," Int. J. Heat Mass Transfer, **44**, pp. 673–682.

[6] He, Y., Shoji, M., and Maruyama, S., 2001, "Numerical Study of High Heat Flux Pool Boiling Heat Transfer," Int. J. Heat Mass Transfer, **44**, pp. 2357–2373.

[7] Maruyama, S., Shoji, M., and Shimizu, S., 1992, "A Numerical Simulation of Transition Boiling Heat Transfer," *Proc. Second JSME-KSME Thermal Engineering Conference*, Kitakyusyu, Vol. 3, pp. 345–348.

[8] Kaneko, K., 1993, *Theory and Applications of Coupled Map Lattices*, Wiley, Chichester, UK.

[9] Yanagita, T., and Kaneko, K., 1993, "Coupled Map Lattice Model for Convection," Phys. Lett. A, **175**, pp. 415–420.

[10] Sadasivan, P., Unal, C., and Nelson, R. A., 1995, "Nonlinear Aspects of High Heat Flux Nucleate Boiling Heat Transfer," Report No. LA-UR-95-609.

[11] Shoji, M., and Tajima, K., 1997, "Mathematical Simulation Model of Boiling: Modes and Chaos," in *Convective Flow and Pool Boiling Conference*, Kloster Irsee, Germany, May 18–23.

[12] Shoji, M., 1998, "Boiling Simulator—A Simple Theoretical Model of Boiling," in *Third International Conference on Multiphase Flow*, Lyon, France, June 8–12.

[13] Ellepola, J., and Kenning, D., 1996, "Nucleation Site Interactions in Pool Boiling," in *Proceedings of the Second European Thermal Sciences and 14th UK National Heat Transfer Conference*, Rome, Italy, May 29–31.

[14] Nelson, R., Kenning, D., and Shoji, M., 1996, "Nonlinear Dynamics in Boiling Phenomena," J. Heat Transfer Soc. Jpn., **35**, pp. 22–34.

[15] Nelson, R., Kenning, D., and Shoji, M., 1997, "Nonlinear Effects and Behavior in Nucleate Boiling," in *Fourth Experimental Chaos Conference*, Boca Raton, FL, August 6–8.

[16] Yanagita, T., 1992, "Phenomenology for Boiling: A Coupled Map Lattice Model," Chaos, **2**, pp. 343–350.

[17] Ghoshdastidar, P. S., Kabelac, S., and Mohanty, A., 2004, "Numerical Modelling of Atmospheric Pool Boiling by the Coupled Map Lattice Method," J. Mech. Eng. Sci., IMechE Part C, **218**, pp. 195–205.

[18] Kenning, D. B. R., 1977, "Pool Boiling," in *Two-phase Flow and Heat Transfer* (D. Butterworth and G. F. Hewitt, eds.), Oxford University Press, London, Chap. 7.

[19] Tannehill, J. C., Anderson, D. A., and Pletcher, R. H., 1997, *Computational Fluid Mechanics and Heat Transfer*, 2nd ed., Taylor and Francis, London, pp. 69, 94.

[20] Lienhard, J. H., 1981, *A Heat Transfer Textbook*, Prentice–Hall, Englewood Cliffs, NJ, Chap. 10.

[21] Zuber, N., 1959, "Hydrodynamic Aspects of Boiling Heat Transfer," Ph.D. thesis, Research Laboratory, Los Angeles and Ramowoolridge Corporation, University of California, Los Angeles.

[22] Holman, J. P., 1981, *Heat Transfer*, 5th ed., McGraw–Hill, Maidenhead, UK, p. 536.

[23] Incropera, F. P., and Dewitt, D. P., 1990, *Fundamentals of Heat and Mass Transfer*, 3rd ed., Wiley, Chichester, UK.

[24] van Stralen, S., and Cole, R., 1979, *Boiling Phenomena*, Hemisphere, New York, Vol. 1.

Effect of Surface Orientation on Nucleate Boiling of FC-72 on Porous Graphite

Jack L. Parker

Mohamed S. El-Genk[1]
e-mail: mgenk@unm.edu

Institute for Space and Nuclear Power Studies
and Chemical and Nuclear Engineering
Department,
The University of New Mexico,
Albuquerque, NM 87131

Effects of orientations of porous graphite and smooth copper surfaces, measuring $10 \text{ mm} \times 10 \text{ mm}$, *on saturation nucleate boiling and critical heat flux (CHF) of FC-72 dielectric liquid and of liquid subcooling (0, 10, 20, and 30 K) on nucleate boiling in the upward facing orientation are investigated. Inclination angles* (θ) *considered are 0 deg (upward-facing), 60, 90, 120, 150, and 180 deg (downward facing). The values of nucleate boiling heat flux, nucleate boiling heat transfer coefficient (NBHTC), and CHF are compared with those measured on the smooth copper surface of the same dimensions and CHF values on both copper and porous graphite are compared with those reported by other investigators on the smooth surfaces and microporous coatings. Results demonstrated higher NBHTC and CHF on porous graphite, particularly in the downward-facing orientation* ($\theta = 180$ deg). *In the upward-facing orientation, NBHTCs on both surfaces decrease with increased subcooling, but increase with increased surface superheat reaching maxima then decrease with further increase in surface superheat. In saturation boiling on copper and both saturation and subcooled boiling on porous graphite these maxima occur at or near the end of the discrete bubble region, and near CHF in subcooled boiling on copper. Maximum saturation NBHTC on porous graphite increases with decreased surface superheat and inclination angle, while that on copper increases with increased surface superheat and decreased surface inclination. At low surface superheats, saturation nucleate boiling heat flux increases with increased inclination, but decreases with increased inclination at high surface superheats, consistent with previously reported data for dielectric and nondielectric liquids. The fractional decreases in saturation CHF with increased* θ *on smooth copper and microporous coatings are almost identical, but markedly larger than on porous graphite, particularly in the downward-facing orientation. In this orientation, saturation CHF on porous graphite of* 16 W/cm^2 *is much higher than on copper* (4.9 W/cm^2) *and as much as 53% of that in the upward-facing orientation, compared to only* ~18% *on copper.* [DOI: 10.1115/1.2352783]

Introduction

Advanced cooling methods and techniques are being developed for removing anticipated high thermal power dissipation by new generation computer chips. The increases in packing density of transistors and the clock speed of these chips not only increase the total thermal power dissipated and dissipation heat flux but also cause hot spots on the surface. The hot-spot heat flux on the surface of POWER4 chips from IBM exceeds 100 W/cm^2 and is almost twice the average heat flux [1]. The average dissipation heat flux from a single chip package is projected to reach 100 W/cm^2 and the hot-spot local heat flux could be more than two times higher [2]. The thermal gradient and mechanical stresses caused by the developed hot spot could cause the chip or CPU to fail and/or shorten its useful life.

To remove the anticipated high dissipation thermal power and mitigate the effect of the nonuniform surface heat flux, liquid-based, rather than air-based, cooling methods are more effective. These methods include forced convection in microchannels, liquid spray and impinging jets, and immersion pool boiling of dielectric liquids (e.g., [3–10]). In immersion pool boiling of dielectric liquids, such as FC-72 and HFE-7100, the dissipated thermal power by a CPU or a high performance chip, is removed by nucleate boiling at high heat fluxes (e.g., [3–6,11–19]). In addition to the low saturation temperature of the candidate dielectric liquids ($\leq 61\,^{\circ}\text{C}$), nucleate boiling helps make the surface temperatures of the spreader and the computer chip more uniform, effectively decreasing the junction or die temperature. The dissipated thermal power by the chip would also be removed at a relatively small total resistance ($<0.5\,^{\circ}\text{C/W}$), depending on the properties and subcooling of the boiling liquid and the characteristics of the exposed surface of the spreader on which boiling takes place [20–22]. Such a surface could be made of smooth copper or silicon, has microfins or manufactured cavities, or covered by a thin layer of microporous coatings or highly porous materials.

Experimentally determined nucleate boiling heat fluxes and heat transfer coefficients and critical heat flux (CHF) of dielectric liquids on microporous coatings, microfinned surfaces, and porous graphite are significantly higher than those reported on smooth copper and silicon [3,4,12,13,15–18,23–25]. Most reported results are in the upward-facing orientation (inclination angle $\theta = 0$ deg) at different liquids subcoolings and surface sizes ranging in sizes from $10 \text{ mm} \times 10 \text{ mm}$ to $50 \text{ mm} \times 50 \text{ mm}$. In these investigations, the size of the boiling surface had little or no effect on the nucleate boiling heat flux and CHF. Fewer results have been reported on nucleate boiling of saturation and subcooled dielectric liquids at other than the upward-facing orientation [5,6,11,15,19,26–29].

The reported results on the effect of surface orientation are consistent with earlier data for nondielectric liquids such as water, nitrogen, and helium [30–33] showing that at low surface superheats, nucleate boiling heat flux increases as θ increases from 0 deg to 180 deg (downward facing), but at higher surface super-

---

heats it decreases with increased surface inclination. CHF decreases slightly as θ increases to 90 deg then it decreases rapidly with increased inclination to its lowest value at 180 deg. The reported values of saturation boiling CHF for FC-72 and HFE-7100 on smooth copper and microporous coatings in the downward-facing orientation ($\theta=180$ deg) are typically $\sim$7% to 28% of those measured in the upward-facing position ($\theta=0$ deg) [5,6,11,19,26–29]. The fractional decreases in CHF for both FC-72 and HFE-7100 liquids on smooth copper and microporous coatings with increasing θ are very similar, however, the actual CHF values for HFE-7100 are much higher than for FC-72 and those measured on microporous coatings and microfinned surfaces are higher than on smooth copper and silicon [4–6,12,13,25,34]. Microporous and microfinned surfaces significantly decrease temperature excursion at boiling incipience caused by the high wetting property of dielectric liquids. On copper, such temperature excursions could be as much as 35 K, which may cause the junction temperature of the chips to exceed the recommended value of 85°C. Recent experiments have shown no temperature excursion prior to boiling incipience and large increases in the saturation nucleate boiling heat transfer coefficient and CHF for both FC-72 and HFE-7100 liquids on porous graphite in the upward-facing orientation [17,18,23,24].

Compact electronics packing and high thermal power dissipation may require changing the orientation of the boiling surface or using subcooled liquids. This paper investigates the effects of surface orientation on saturation boiling of degassed FC-72 liquid on porous graphite and copper surfaces measuring 10 mm $\times$ 10 mm and of liquid subcooling of 10, 20, and 30 K on the nucleate boiling heat transfer coefficient (NBHTC) on both surfaces in the upward-facing orientation. The results on copper are used herein, as a reference, to quantify the enhancement in the nucleate boiling heat transfer on porous graphite and those reported by other investigators on different surfaces [11,26–28]. Digital photographs of nucleate boiling on porous graphite are recorded to illustrate the processes of vapor bubbles nucleation, growth, coalescence, and release and the induced mixing in the boundary layer in the different orientations. For practical applications, most of the presented results on porous graphite are for an aged surface. In addition, fewer results on unaged porous graphite surface are included for comparison. For consistency of comparing with other surfaces, the present results on smooth copper are all for a newly prepared surface.

Experiments

Descriptions of the experimental facility, test section construction and assembly, and experiment procedures have been detailed elsewhere [5,6,17], and a brief summary is provided below. Figures 1(a) and 1(b), respectively, present the scanning electron microscope (SEM) images of the porous graphite and copper surfaces used in the present pool boiling experiments; both surfaces measure 10 mm $\times$ 10 mm and are 3 mm and 1.6 mm thick, respectively. The graphite is highly porous has randomly interconnected pores and cavities with sizes ranging from $<$1.0 to tens and hundreds of microns and anisotropic thermal conductivity that is lower than that of copper (Fig. 1(a) and Table 1). The reentrant cavities in porous graphite have noncircular openings and ragged nonsmooth interiors and could be several hundred microns deep (Fig. 1(a)). The porous graphite is used in the present experiments without any surface preparation, while the copper surface (Fig. 1(b)) is prepared following consistent procedures. First, it is sanded with emery paper #400 in even strokes to remove deep scratches and dents, then polished with a metal polishing liquid and cleansed with water and alcohol, and finally finished using fine emery paper #1500 by applying equal number of strokes in two perpendicular directions. The induced markings on the copper surface seen in the SEM image in Fig. 1(b) show randomly dis-

(a) SEM Images of Porous Graphite.

(b) SEM Images of Copper Surface.
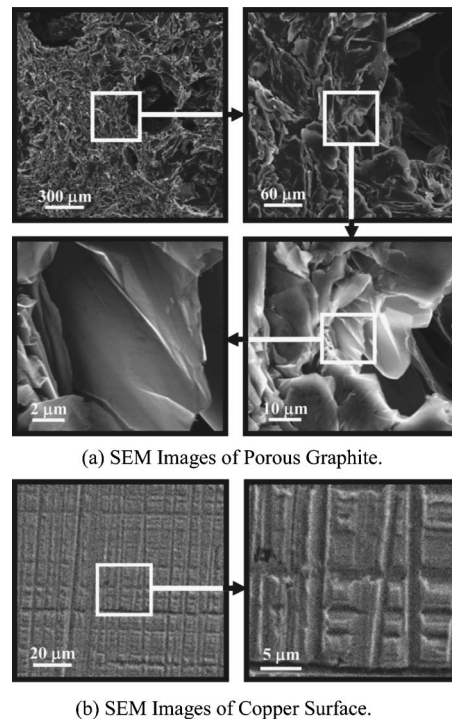
Fig. 1   SEM images of porous graphite

tributed longitudinal and cross groves $<$5 μm wide, 2–3 μm deep, and $\sim$5–1000 μm long. A deeper indent could still be seen in the prepared copper surface.

FC-72 liquid has very high air solubility of as much as 48% by volume at atmospheric pressure and room temperature. Thus, for consistency of results, the present experiments are conducted with degassed FC-72 liquid. It typically took a few hours of continuous boiling in conjunction with using a magnetic stirrer to outgas the FC-72 liquid pool prior to conducting the experiments [35]. At the conclusion of the degassing process and venting of the released air, the test vessel is tightly sealed to prevent liquid leakage and air from entering the test vessel. The monitored degassing process considered complete when the formation of air bubbles in the liquid pool and at selected sites on the wall of the vessel ceases to occur. During degassing, the temperature of the water bath in which the test vessel is immersed is kept a few degrees (5–7 K) above the saturation temperature of FC-72. Studies investigating the effect of dissolved gas on nucleate boiling on plane, microporous, and microfinned surfaces [4,25,34] concluded that dissolved gas reduces incipient boiling temperature and improves nucleate boiling in the low heat flux region. However, there is little or no effect of the dissolved gas on nucleate boiling in the high heat flux region or on CHF. The reported data showed that the boiling curves for gas-dissolved and degassed liquid merge at values between approximately 10% and 30% of CHF [4,25,34].

Table 1   Properties of porous graphite and copper surfaces in the present experiments

Material	Thermal conductivity (W/m K)	Density (kg/m³)	Volume porosity (%)	Open pores (%)
Copper [36]	400	8,950	NA	NA
Porous graphite [37]	70 in plane and $\sim$245 normal to the plane surface	900	$\sim$61	$\sim$95

In the present experiments, the temperature of FC-72 liquid pool is monitored using four submerged K-type thermocouples. The liquid bulk temperature is taken as the average of those indicated by the two thermocouples placed ~5–10 mm from the porous graphite or copper surface to avoid disturbing pool boiling on the surface, while providing accurate measurements of the liquid bulk temperature as close to the surface as possible. In the upward-facing orientation, the height of the liquid above the surface of the test section in the vessel is kept constant at ~8 cm. The test vessel is immersed in a water bath, which has a submerged electrical heater to regulate the subcooling of the FC-72 pool in the experiments and also maintain the pool temperature above saturation during the outgassing procedures. The test vessel is equipped with a water-cooled copper reflux condenser that is fastened to the inside of the top cover.

In subcooled boiling experiments, the two copper cooling coils submerged in the FC-72 liquid pool are used to adjust and maintain the pool temperature to within a fraction of a degree of the desired values. The temperature of the submerged coils is regulated using a liquid bath chiller. To avoid disturbing the boiling process in the experiments the test vessel dimensions are significantly large, allowing at least 5 cm clearance between the assembled test section and any possible obstruction at all orientations. In addition, the volume of the liquid pool in the test vessel (120 mm × 140 mm × 220 mm) is significantly larger than that of the assembled test section (30 mm × 30 mm × 16.9 mm), the actual height of the vessel is 300 mm.

The assembled test section consists of a Teflon block with a square cavity (~1.0 mm deep) at the center of the top surface for placing the heating elements. The porous graphite or copper section is mounted onto the heating element using a thin layer (~0.1 mm) of high thermal conductivity (1.4 W/m K) and high electrical resistivity (10^{15} Ω cm) epoxy. The porous graphite block is 3.0 mm thick and its surface protrudes ~1.4 mm into the liquid, and the copper block is 1.6 mm thick and protrudes ~0.3 mm into the liquid pool. The Nicrome wire-heating element is wound tightly below the porous graphite or copper blocks and the wires are insulated using the high electrical resistivity epoxy. To determine the surface temperature in the experiments, two K-type thermocouples are inserted in two 0.6 mm diameter horizontal holes on one side, ~0.8 mm from the exposed surface, and half way into the graphite or the copper blocks. The exposed tips of the thermocouples are covered with a very thin layer of the same epoxy used for mounting the graphite and copper blocks onto the heating element to ensure good solid-solid contact, and in case of the porous graphite also avoid wetting the thermocouples with liquid from the pool and recording false temperature readings. For constructing the pool boiling curves the average reading of these thermocouples is taken as the surface temperature, after accounting for the temperature drop due to conduction to the surface of the porous graphite or copper block; estimated at ≤2.0 K and 0.5 K, respectively. Due to the high elevation in Albuquerque, NM, the local atmospheric pressure for all the experiments reported in this paper is ~0.085 MPa.

The fully assembled test section (Fig. 2) is encased in a Lexan frame with a closed bottom and measures 30 mm × 30 mm. The shallow cavity on top is filled with translucent two-part epoxy adhesive that also seals the sides of the porous graphite (or copper) block, leaving no tiny grooves that could act as active nucleation sites for vapor bubbles in the experiments, thus skewing the pool boiling curves. Thus, the exposed surface area of the porous graphite and of copper blocks (10 mm × 10 mm) is the effective area for nucleate boiling in the present experiments. In the experiments, no bubble nucleation is observed on the sidewalls of either the copper or the porous graphite blocks. The heat losses through the sides of the assembled test section are calculated using ANSYS finite element software to be negligibly small, thus the dissipated power from the boiling surface is taken the same as that generated by the underlying heating elements. This power is determined
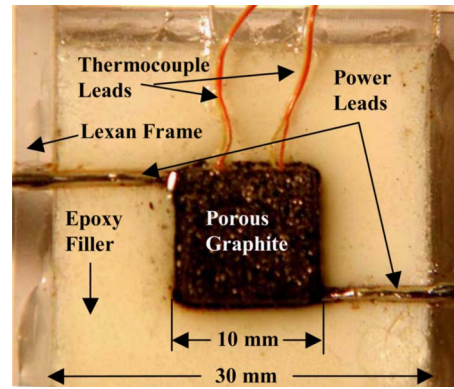

Fig. 2   SEM images of copper surface

from the measured voltage across the heating element and the electric current provided by the power supply.

The estimated uncertainties in the experiments are +0.7 K in the temperature and ±2% in the steady state nucleate boiling heat flux measurements. Implemented in the procedures in the experiments the electrical power to the heating element is incrementally increased by increasing the applied dc voltage to the Nichrome-wire heating element in steps of <0.2 V. As the nucleate boiling heat flux increases, the incremental increase in the applied voltage to the heating element in the test section is adjusted down to ensure that the maximum power increase is no more than 0.5 W (or the increase in the surface heat flux is <0.5 W/cm²). When approaching CHF, the incremental increases in the heater's power are limited to ~0.15 W, to avoid a large temperature surge and burning the test section. The nucleate boiling heat flux and average surface temperature for constructing the boiling curves are recorded after reaching steady state, when the measured change in the average surface temperature in subsequent measurements is <0.2 K. Each of these surface temperatures is the average of ~30 consecutive measurements. Near CHF, the incremental increase in the heating element's power could result in a large increase in the average surface temperature. However, to determine CHF and the corresponding surface superheat while at the same time avoid burning the heating element, when the measured increase in subsequent average surface temperatures exceeds 30 K, it is considered an indication of reaching CHF and the experiment was terminated. A higher increase in the surface temperature criterion could burn the test section, with <2% increase in CHF, as the slope of the boiling curves near CHF is relatively small (Fig. 3). Visual observations, backed up with digital photographs and video confirmed the transition to film boiling when increasing the surface temperature criterion beyond 30 K. With the present procedures, the estimated uncertainty in the CHF values is ~3% however; the uncertainty in the corresponding surface superheat could be as much as 4 K.

Results and Discussion

This section presents the measured saturation pool boiling curves for FC-72 on both porous graphite and on smooth copper at the different surface orientations. The inclination angles investigated are $\theta = 0$ deg (upward facing), 60, 90 (vertical), 120, 150, and 180 deg (downward facing). Photographs of saturation boiling on porous graphite in the different orientations are presented and discussed. In addition, the results on the effect of liquid subcooling of 10, 20, and 30 K on the nucleate boiling heat transfer coefficient (NBHTC) and CHF of FC-72 on both porous graphite and copper in the upward-facing orientation are compared. The present saturation CHF values are compared with those reported by other investigators on smooth and microporous surfaces and correlated as a function of inclination angle. The presented results
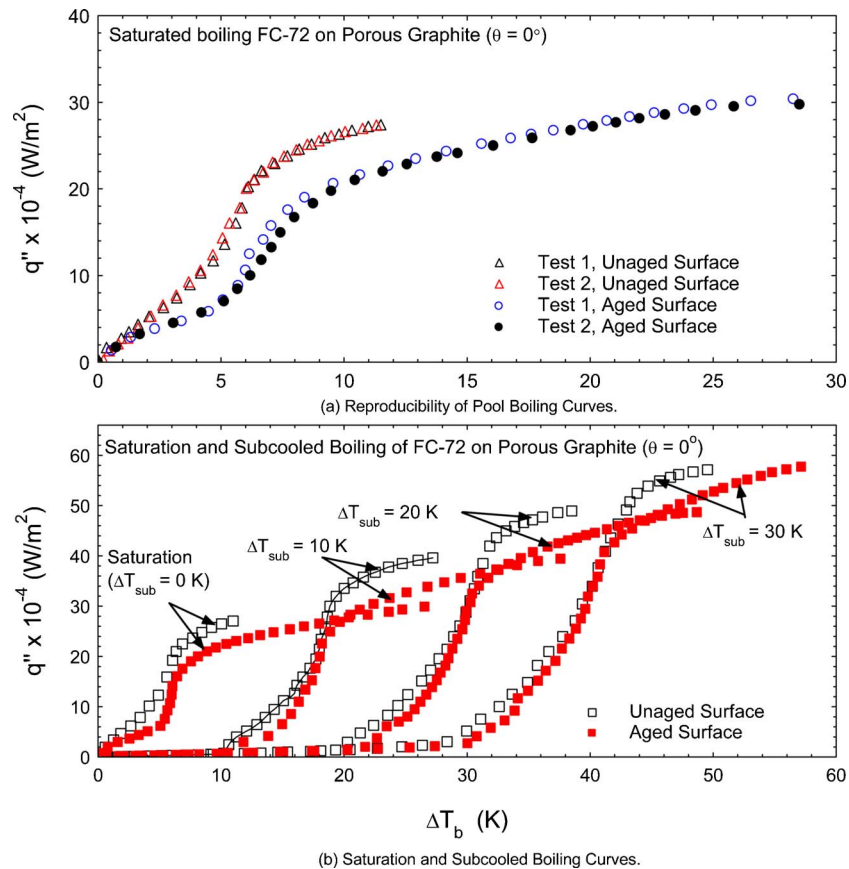
Fig. 3 Effect of aging on pool boiling of FC-72 on porous graphite

on porous graphite are for both aged and new (or unaged) surfaces. The aged surface has been submerged in the FC-72 liquid pool for ~50 days during which more than 165 hours of boiling in 50 tests at different liquid subcoolings are conducted. The unaged surface has been submerged in the FC-72 liquid pool for only tens of hours and used in less than ten boiling tests. For each condition, the presented pool boiling curves are highly reproducible (Fig. 3(a)). As shown in Fig. 3(b), the nucleate boiling heat fluxes on the aged porous graphite surface are lower and the corresponding surface superheats are higher than those on the unaged surface. In addition, the CHF and the corresponding surface superheat are much higher on the aged surface. This difference between the results on the aged and unaged porpous graphite is pronounced at and near CHF, but decreases with decreased nucleate boiling heat flux, becoming insignificant at low surface superheats. Most of the results presented in the following sections on porous graphite are for the aged surface and a fewer results are for the unaged surface. The copper results are all for a recently prepared surface.

The effect of aging on the boiling curves on copper is partially caused by the deposition of the plasticizers leached into the dielectric liquid from the epoxy used in the test section assembly. The increase in the surface tension of the FC-72 liquid due to the increase of the plasticizers in the pool over time in the experiments, may also contribute to the aging effect. However, since graphite is inert, the second cause is solely responsible for the aging effects on the boiling curves. This is confirmed with the experimental measurements showing that using new graphite tests section with both aged and fresh FC-72 liquids give the same aging effects as shown in Figs. 3(a) and 3(b). The increased surface tension of the FC-72 liquid due to the presence of plasticizers decreases the nucleate boiling heat flux and shifts the boiling curve to higher surface superheats, which is consistent with the present results and those of Chang [38]. He reported that the pres-

ence of plasticizers in FC-72 liquid caused the saturation boiling CHF on microporous coatings to increase slightly and occur at a significantly higher superheat.

Effect of Surface Orientation. Figures 4(a) and 4(b) present the measured saturation pool boiling curves of FC-72 on smooth copper and aged porous graphite, respectively, in the upward-facing (θ=0 deg), 60, 90, 120, 150, and 180 deg (downward-facing) orientations. The results in these figures are consistent with those previously published by other investigators of the effect of surface orientation on the nucleate boiling of dielectric liquids [5,6,11,15,19,26–29] and of non-dielectric liquids [30–33]. Excluding the 180 deg orientation, when the surface superheat of copper is <11.5 K, the nucleate boiling heat flux generally increases with increased inclination angle, but decreases with increased inclination angle at higher surface superheats (Fig. 4(a)). Similarly, the nucleate boiling heat flux on porous graphite increases slightly with increased surface inclination at low surface superheats, $\Delta T_{sat} \le \sim 5$ K, but decreases with increased inclination angle at higher surface superheats (Fig. 4(b)).

The solid square symbols at the end of the boiling curves in Figs. 4(a) and 4(b) and 5(a)–5(f) indicate the CHF values determined using the experimental procedures described earlier. CHF of FC-72 on either porous graphite or smooth Cu decreases with increased inclination angle and so does the surface superheat at CHF. The latter shows some variation due to the uncertainties associated with the procedures used in the present experiment for determining CHF. Figures 4(a) and 4(b) show marked enhancement in nucleate boiling and increase in CHF of FC-72 on porous graphite. For the same inclination and surface superheat, the nucleate boiling heat flux of FC-72 on porous graphite is 2–20 times that on copper.

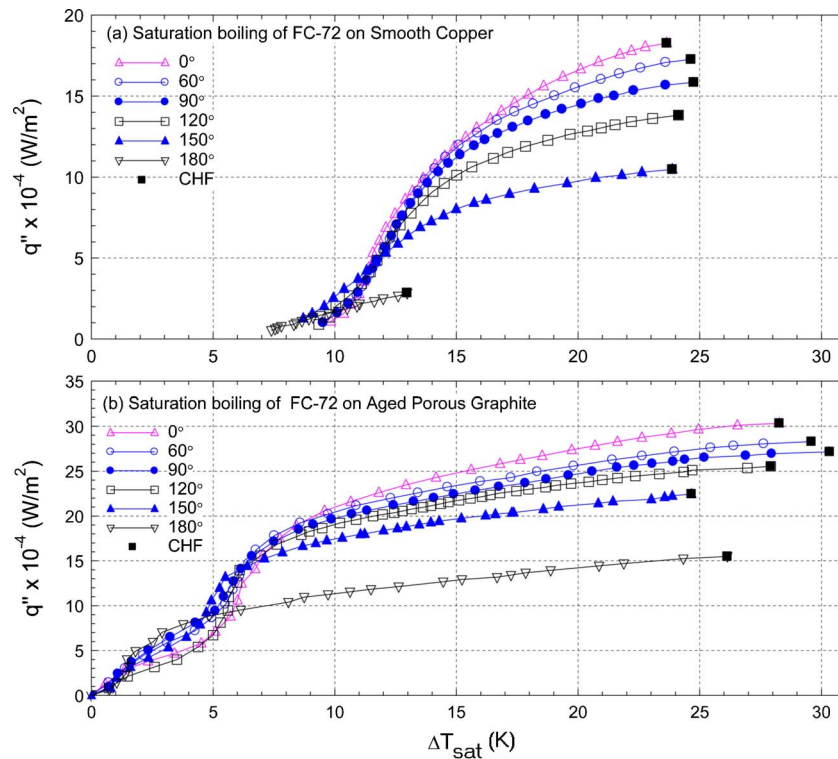The saturation pool boiling curves of FC-72 on copper and

Fig. 4 Comparison of saturation pool boiling curves of FC-72 liquid at different inclinations on smooth copper and aged porous graphite

porous graphite at 0, 60, 90, 120, 150, and 180 deg inclinations are compared in Figs. 5(a)–5(f). These figures show no excursion in the surface temperature of porous graphite prior to boiling incipience; however, on copper temperature excursions of 10.5 K to 19 K are measured. The CHF values of FC-72 on porous graphite are higher than those measured on copper, with the largest difference in the downward-facing orientation (180 deg). In this orientation, CHF of FC-72 on porous graphite is 6.4 times that on copper but at lower inclinations of 150, 90, and 0 deg it is ~4.14, 1.69, and 1.67 times that on copper. The surface superheat at CHF on porous graphite is also higher than on copper, particularly in the downward facing orientation (Fig. 5(f)).

Nucleate Boiling Heat Transfer Coefficient. Figures 6(a) and 6(b) plot the calculated saturation NBHTC of FC-72 versus the measured surface superheat at different orientations of the porous graphite and the copper surface, respectively. The values of NBHTC are calculated from the measured pool boiling curves by dividing the measured nucleate boiling heat flux by the corresponding ΔT_b, the difference between the measured surface temperature T_w, and that of the liquid pool near the boiling surface T_b in the experiments. The solid circle symbols in these figures indicate the maximum NBHTC, whose values and those of the corresponding wall superheat depend not only on the surface orientation but also on the surface material and characteristic (porous graphite or copper). At the same surface superheats, the values of NBHTC of FC-72 on porous graphite are typically 2–3 time those on copper (Figs. 6(a) and 6(b)). On both porous graphite and copper, the nucleate boiling heat flux and NBHTC at higher surface superheats decrease with increased surface inclination (Figs. 4 and 5). On porous graphite, NBHTC increases with decreased surface superheat reaching a maximum then decreases with further decrease in the surface superheat (Fig. 6(a)). Such dependence of NBHTC on surface superheat is also true on copper, but the rate of change in its value with decreasing wall superheat is much milder than on porous graphite (Fig. 6(b)). Figure 6(a)

shows that although NBHTC of FC-72 on porous graphite in the downward facing orientation at high surface superheat (>1.5 K) is the lowest, its maximum value is the highest.

As delineated in Figs. 4(b) and 6(a), at the same surface superheat the saturation nucleate boiling heat flux of FC-72 on porous graphite is higher than on copper, which explains the significantly higher NBHTC of FC-72 on the former. In the upward-facing orientation (θ=0 deg), the maximum NBHTC of FC-72 on porous graphite is ~2.25×10⁴ W/m² K and occurs at a surface superheat of 8 K, compared to only 0.85×10^4 W/m² K and 18 K on copper. Similarly, in the downward-facing orientation (θ =180 deg), the maximum NBHTC of FC-72 on porous graphite is 2.75×10^4 W/m² K and the corresponding wall superheat is only 1.5 K, compared to only 0.19×10^4 W/m² K and as much as 13 K on copper (Figs. 6(a) and 6(b)). The high values of the maximum NBHTC on porous graphite reflect higher nucleate boiling heat fluxes and lower surface superheats, compared to those on copper. The importance to electronic cooling applications is that a porous graphite spreader at the maximum NBHTC not only enhances the cooling processes of the underlying chip but also decreases significantly the junctions' temperature, compared to a copper spreader [20,22]. However, due to the low thermal conductivity of porous graphite in plane (Table 1) but high NBHTCs, a composite spreader composed of a top layer of porous graphite and a copper substrate would dissipate much more thermal power from the underlying chip than a porous graphite or copper spreader. Copper is a good spreader material because of its high and homogeneous thermal conductivity (Table 1), but as delineated in Figs. 4 and 5 it is not as good as porous graphite for nucleate boiling cooling [20,22].

The maximum saturation NBHTC, h_{NB}^*, and the corresponding maximum Nusselt number Nu_{NB}^*, for FC-72 on porous graphite and copper are determined from the calculated values of h_{NB} and Nu_{NB} and are plotted in Figs. 6–8. Figure 7(a) shows that both Nu_{NB}^* and h_{NB}^* on porous graphite increase as the surface super-
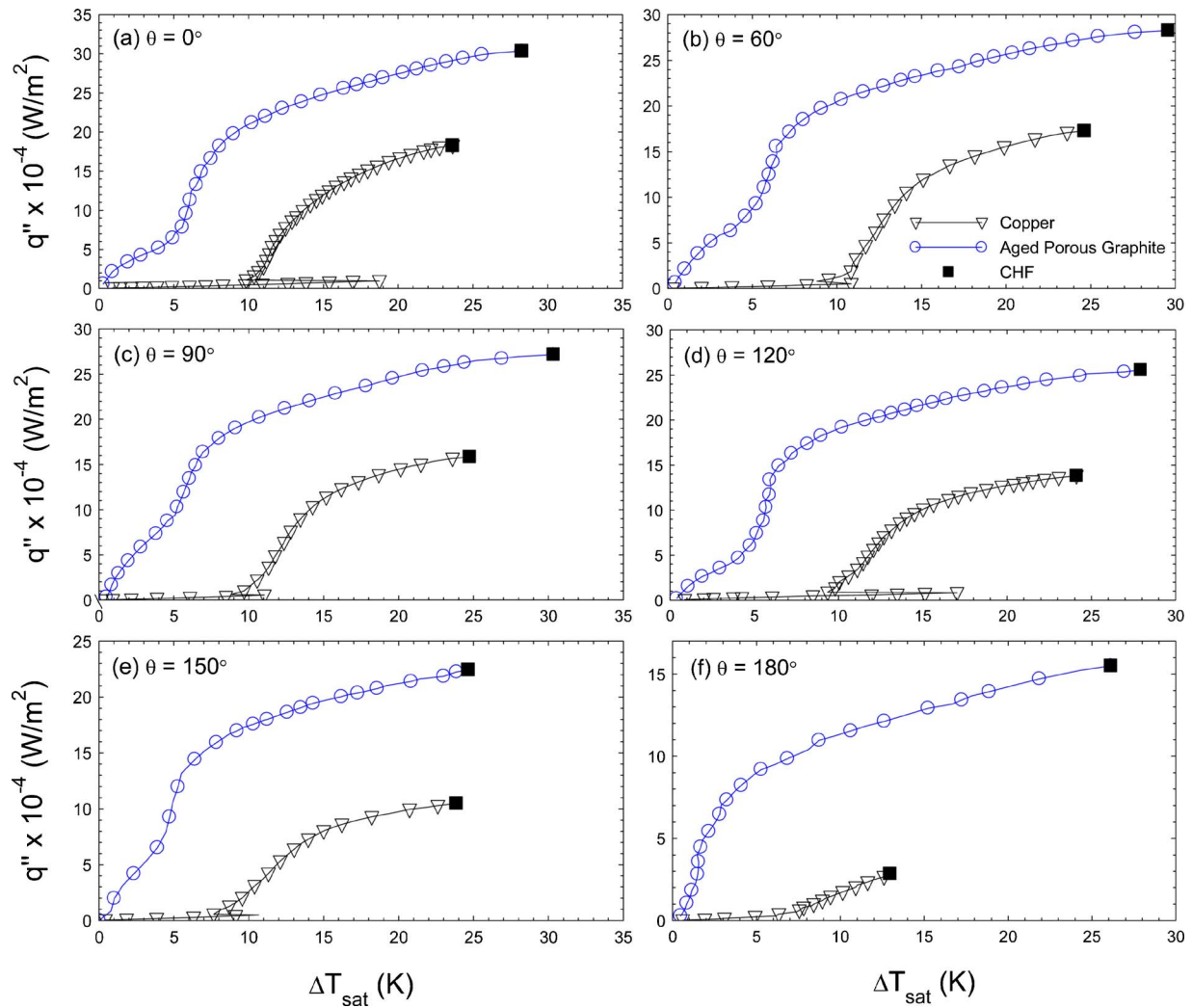
Fig. 5 Saturation boiling curves of FC-72 on porous graphite and copper at different inclinations

heat decreases because of the high nucleate boiling heat flux and the low corresponding surface superheat (Figs. 4(b) and 6(a)). Conversely, Nu_{NB}^* and h_{NB}^* for FC-72 on copper increase as the surface superheat increases because of the low nucleate boiling heat flux and the high corresponding surface superheat (Figs. 4(a) and 6(b)). The effect of inclination angle on Nu_{NB}^* and h_{NB}^* on porous graphite is also opposite to that on copper (Figs. 6(a) and 6(b)). As these figures indicate, both Nu_{NB}^* and h_{NB}^* of FC-72 on porous graphite increase while those on copper decrease as the surface inclination increases. This trend may be attributed to a higher nucleation site density on porous graphite and the intense mixing in the boundary layer by the departing vapor bubbles, confirmed in the video images and photographs taken of the boiling process. As the inclination angle increases the residence time of the sliding bubbles on the surface increases, which together with the high nucleation sites density on porous graphite explain the higher nucleate boiling heat flux and CHF of FC-72, compared to those on copper (Figs. 6(a) and 6(b)); more on that later in the paper. The relatively low nucleation density on copper allows departing bubbles to grow, decreasing mixing, and effectively increasing the heat transfer resistance in the boundary layer with increased surface inclination. The scattering in the data in Fig. 7(a) (±8%) is due to larger uncertainty in the measured small surface superheats (1.5–8.5 K). Conversely, the smaller scattering (±3%) in the values of Nu_{NB}^* and h_{NB}^* on copper is because of the higher values of the corresponding surface superheats of 13–18 K

(Fig. 7(b)). The values of Nu_{NB}^* and h_{NB}^* in Figs. 7(a) and 7(b) are empirically correlated using second-degree polynomials as

1. On porous graphite (Fig. 7(a))

$$Nu_{NB}^* = 4,975 + 114\Delta T_{sat} - 27\Delta T_{sat}^2, \quad \text{and} \quad (1a)$$

$$h_{NB}^* = 2.69 + 0.0616\Delta T_{sat} - 0.0146\Delta T_{sat}^2. \quad (1b)$$

2. On copper (Fig. 7(b))

$$Nu_{NB}^* = 394 + 419(\Delta T_{sat} - 13) - 35.8(\Delta T_{sat} - 13)^2, \quad \text{and}$$
$$(2a)$$

$$h_{NB}^* = 0.249 + 0.226(\Delta T_{sat} - 13) - 0.193(\Delta T_{sat} - 13)^2.$$
$$(2b)$$

Figure 8 plots the values of the saturation Nu_{NB}^* for FC-72 on both copper and porous graphite versus the inclination angle. On porous graphite, Nu_{NB}^* increases with increased inclination angle and its values are much higher than on copper. Also on the latter, Nu_{NB}^* decreases with increased inclination angle. In the upward-facing orientation (θ=0 deg) Nu_{NB}^* on porous graphite is ~2.8 times that on copper, while in the downward-facing position (θ=180 deg) Nu_{NB}^* on porous graphite is 13 times that on copper. Nu_{NB}^* and h_{NB}^* on aged porous graphite increase with increased
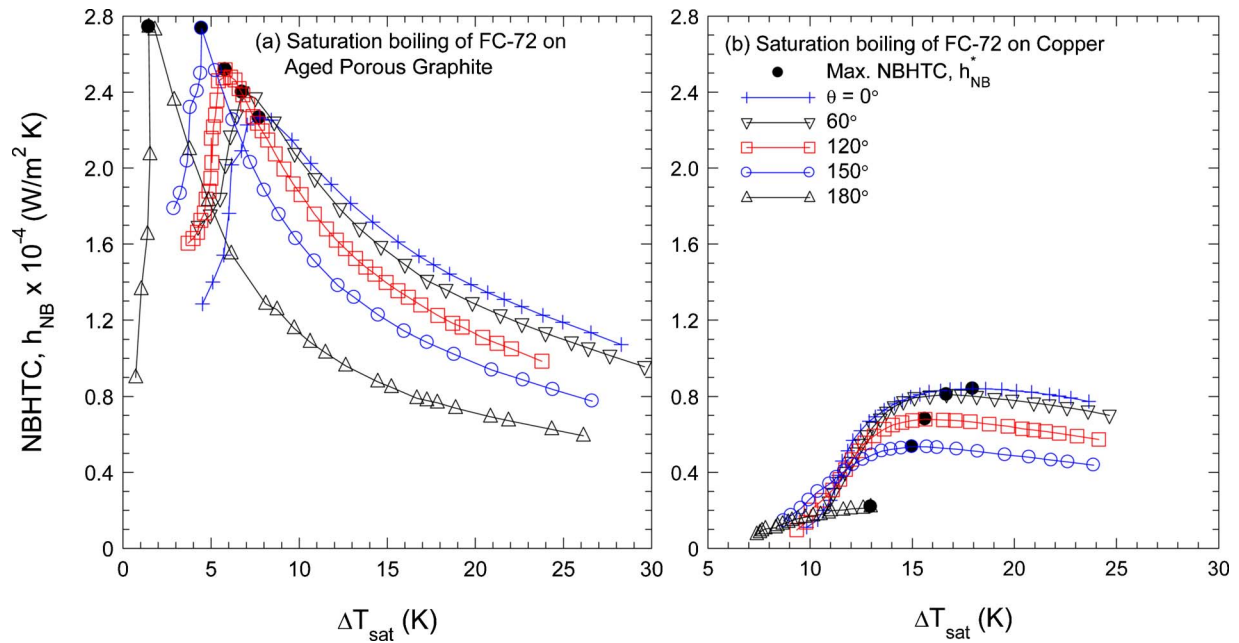
Fig. 6 Effect of surface orientation on saturation NBHTC of FC-72 on aged porous graphite and on copper

inclination because the saturation nucleate boiling heat flux decreases less than the corresponding surface superheat with increased surface inclination (Figs. 6(a)). On the other hand, Nu_{NB}^* and h_{NB}^* on copper decrease with increased surface inclination because the nucleate boiling heat flux decreases more than the corresponding surface superheat with increased inclination (Fig. 6(b)).

Figure 9 plots the ratio of the saturation NBHTC for FC-72 on aged porous graphite and on copper versus the surface superheat for different inclination angles. Except at 180 deg (downward-facing orientation), the ratio of the NBHTC decrease with increased inclination angle at low surface superheats $<\sim 12.5$ K, but increases with increased inclination angle at higher superheats. When $\Delta T_{sat} = 12.5$ K, the ratio of the NBHTC is in excess of ~ 3.5 and as much as 20–24 at lower surface superheats; the highest value occurs at $\theta = 0$ deg (upward-facing orientation).

Conversely, for $\Delta T_{sat} > 12.5$ K the ratio of the NBHTC increases with increased inclination angle, with the lowest value also occurring at 0 deg inclination. At these high surface superheats and $\theta = 0$ deg, the NBHTC ratio approaches ~ 1.67 K at 24 K surface superheat, which is near that corresponding to CHF (Figs. 4 and 5(a)). In the downward facing orientation ($\theta = 180$ deg), the NBHTC ratio decreases from as much as 20 at $\Delta T_{sat} = 7$ K to ~ 4.0 at ~ 13 K, which is close to that at CHF (Figs. 4 and 5(f)).

Photographs of Saturation Nucleate Boiling on Porous Graphite. The fact that at the same surface temperature or superheat, the nucleate boiling heat flux of FC-72 on porous graphite is much higher than on copper (Figs. 4 and 5) is indicative of the higher density of active nucleate sites on the former. Figures 10–12 present saturation pool boiling curves of FC-72 on porous graphite in the upward-facing (0 deg), vertical (90 deg), and
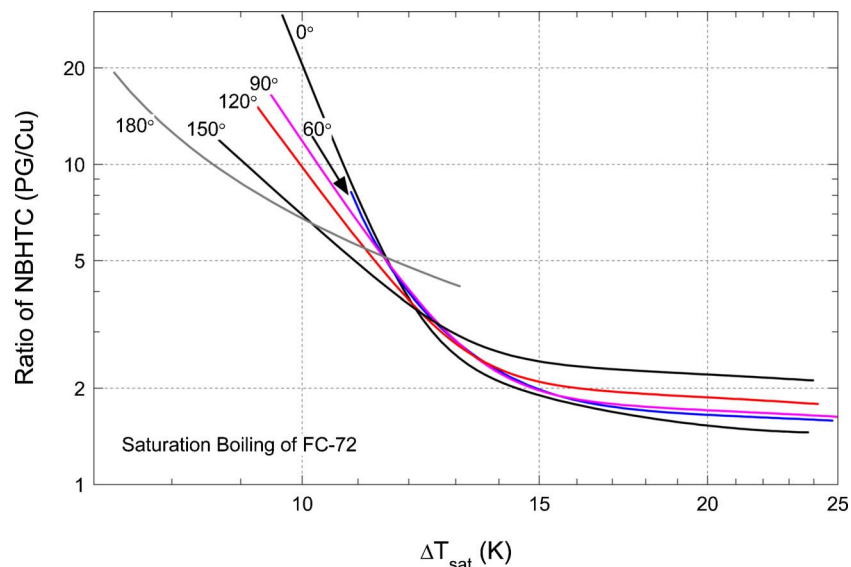
Fig. 9 Ratios of saturation NBHTC of FC-72 on porous graphite and copper
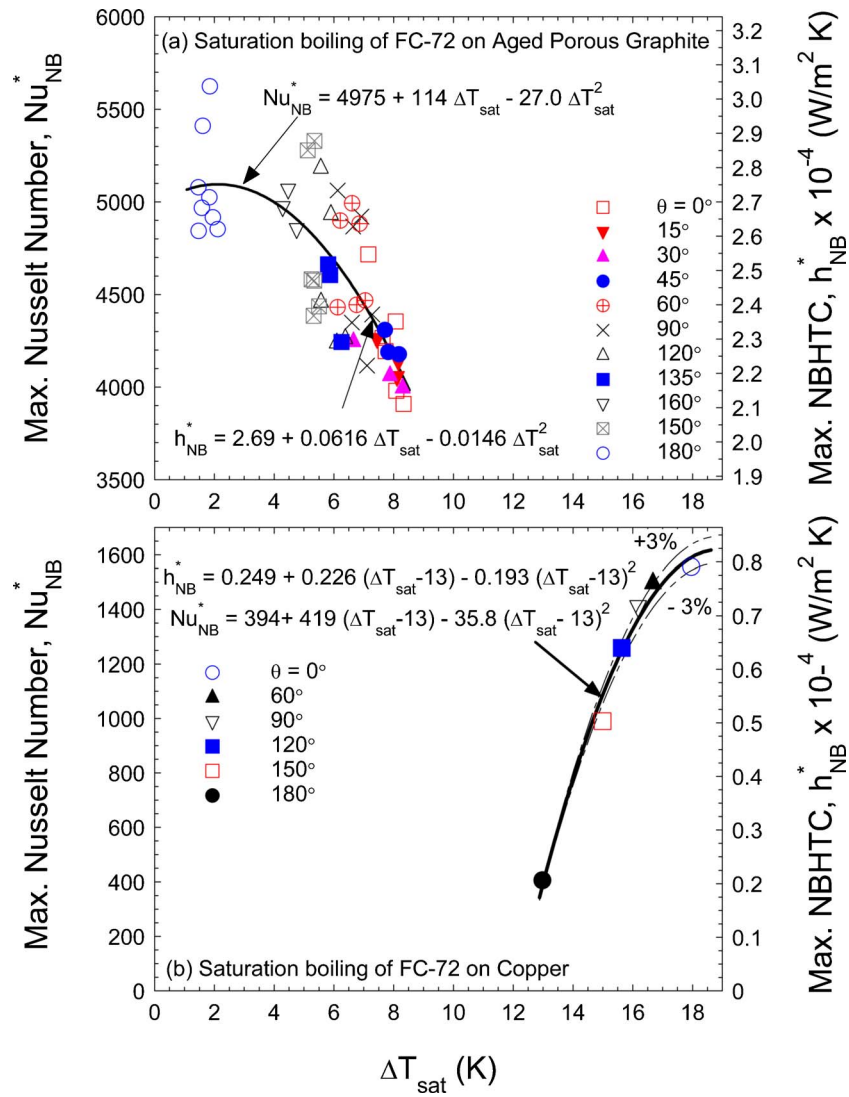
Fig. 7 Effect of surface orientation on maximum NBHTC and Nusselt number of FC-72 on aged porous graphite and on copper
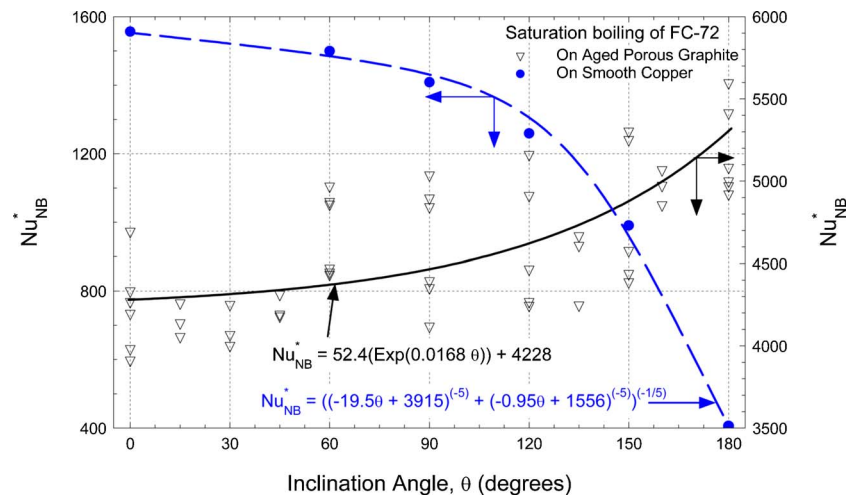
Fig. 8 Dependences of maximum NBHTC and Nusselt number of FC-72 on aged porous graphite and copper on surface orientation
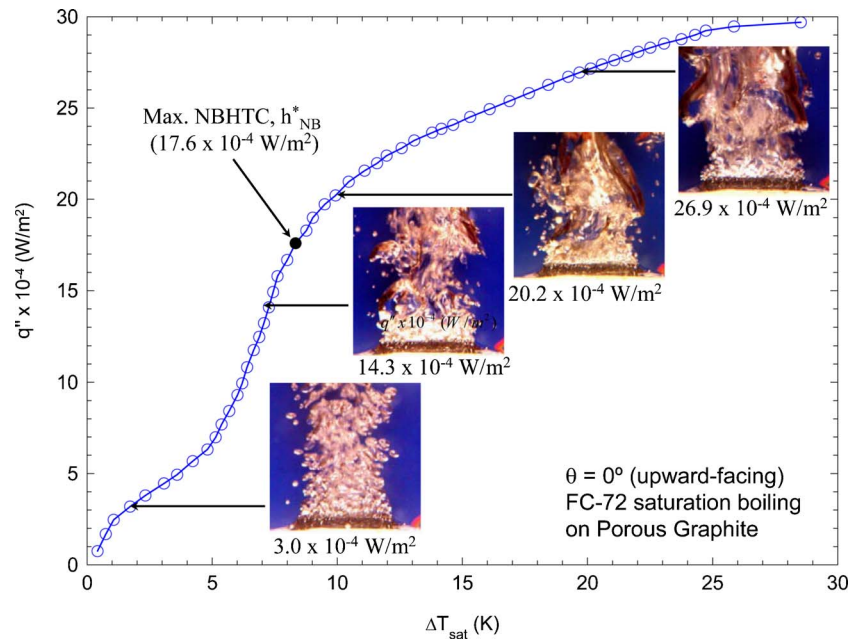
Fig. 10 Saturation boiling curve and photographs on aged porous graphite in upward facing orientation

downward-facing (180 deg) orientations. In these figures, the solid circle symbols indicate the nucleate boiling heat flux and surface superheat at the maximum NBHTC, h_{NB}^*, or Nu_{NB}^*, and the inserted photographs are of the boiling process at the surface superheats and heat fluxes indicated by the arrows. Because of the low surface tension of the dielectric liquids of FC-72 and HFE-7100, the average diameter of a single detaching bubble is in the order of 0.5–0.6 mm [5].

Nucleate boiling of FC-72 on porous graphite at 0 deg and 90 deg inclinations (Figs. 10 and 11) can generally be divided into three distinct regions, with increased surface superheat, or decreased slope of the boiling curve, namely: (I) developing discrete

bubbles; (II) developed discrete bubbles; and (III) bubbles coalescence. In the first region, discrete bubbles nucleate at selective sites on the surface and the density of the active sites increases and hence, the values of the nucleate boiling heat flux and NBHTC increases as the surface superheat increases. Higher active nucleation sites density, with some lateral coalescence, characterize region (II), in which there is a steep rise in the nucleate boiling heat flux with little increase in the surface superheat (Figs. 10 and 11). At the end of this region, indicated by the solid circle symbol, the density of the active nucleation sites peaks, which corresponds to the maximum saturation NBHTC. Further increase in the nucleate boiling heat flux into region (III) increases lateral
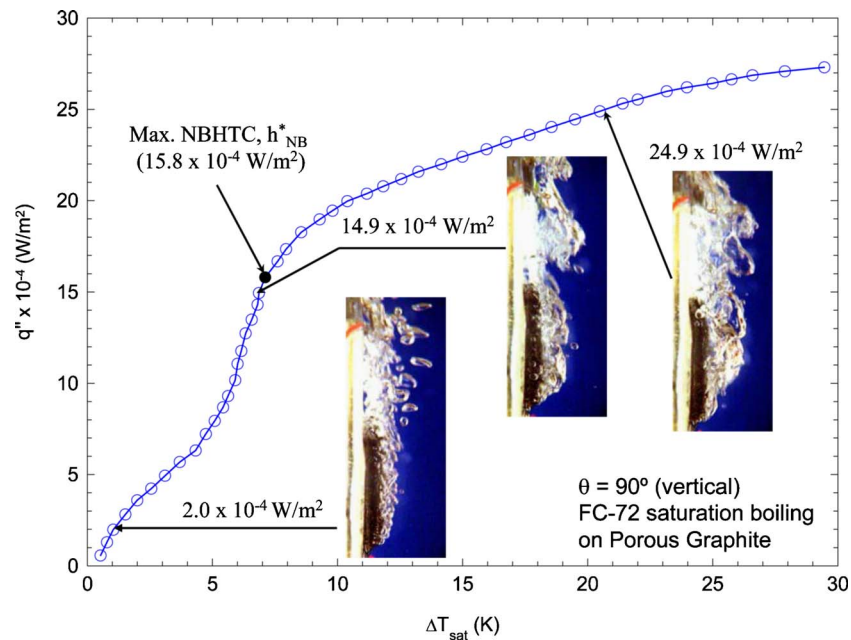
Fig. 11 Saturation boiling curve and photographs on aged porous graphite in vertical orientation
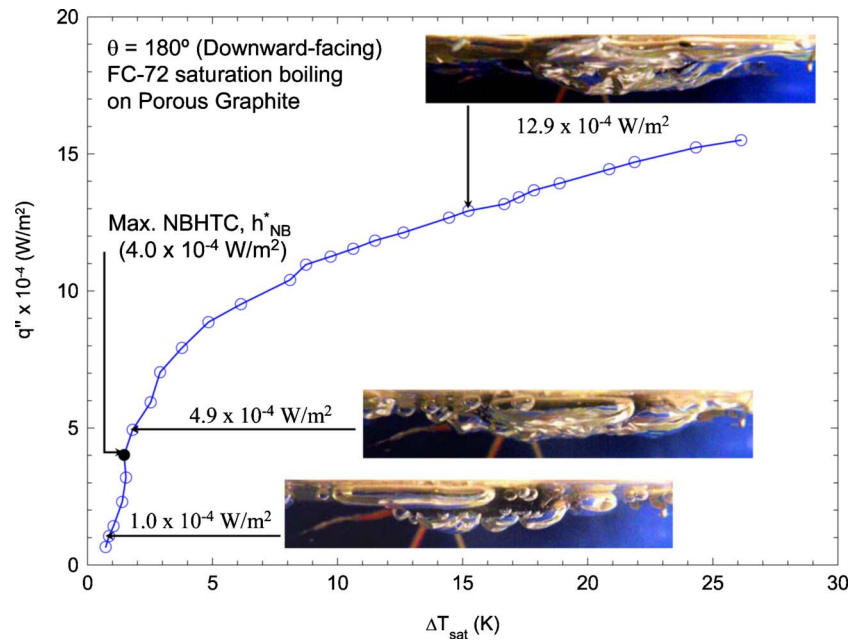
Fig. 12 Saturation boiling curve and photographs on aged porous graphite in downward-facing orientation

coalescence of departing bubbles near the surface, causing NBHTC to decrease as the surface temperature increases. This is indicated by the decrease in the slope of the boiling curves in this region. The increase in bubbles coalescence and the formation of large vapor masses near the surface in region (III) become increasingly detrimental to the heat removal from the surface as indicated by the low slope of the boiling curve, eventually reaching CHF.

The photographs in Fig. 10, starting at the low surface superheat, are of saturation nucleate boiling of FC-72 in regions I, II, and III, respectively, on porous graphite in the upward-facing orientation. In this orientation, gravity plays a pivotal role in the detachment of the vapor bubbles from the surface. As the active nucleation sites density increases, in the presence of a limited lateral coalescence, mixing in the boundary layer above the surface increases, increasing the nucleate boiling heat transfer coefficient (region II). In region III, despite the intense mixing in the boundary layer, the lateral coalescence of detaching bubbles near the surface decreases the rate of increase in the nucleate boiling heat flux and thus, decreases the heat transfer coefficient (Fig. 6(a)) with increased surface superheat. The photographs embedded in Figs. 10 and 11 show the increased intensity of the hydrodynamics mixing in the two-phase boundary layer at and above the porous graphite surface with increased nucleate boiling heat flux.

Regions II and I are indistinguishable in the downward-facing orientation. In this orientation ($\theta=180$ deg), the gravity and the opposing inertia force of the vapor generating at the contact line of the bubbles with the surface prior to detachment influence nucleate boiling. During the initial growth phase, the bubbles are spherical despite the gravity acting in the upward direction because of the high inertia of the generating vapor, which forces the bubbles to detach from the surface. The upward gravity forces the detached bubbles to spread laterally; coalescing with adjacent bubbles and becoming flat with a very thin liquid film separating them from the heated surface. These flattened vapor masses continue to spread laterally and slide across the surface (see embedded photographs in Fig. 12). As they slide laterally across the porous graphite surface, separated by a thin liquid film, the flattened large masses of the vapor cause some mixing in the bound-

ary layer. They also continue to grow due to the vapor generation at the liquid film-vapor interface by the heat transfer across the underlying thin liquid film (approximately several microns thick).

For a 10 μm thick liquid film, the film heat transfer coefficient could be as high as $\sim 5.4 \times 10^4$ W/m^2 K, despite the low thermal conductivity of the FC-72 liquid (~ 0.054 W/m K). Such a heat transfer coefficient is much higher than the maximum NBHTC measured in the present work for FC-72 on porous graphite in the downward-facing orientation (Figs. 6(a) and 7(a)). The processes of bubbles nucleation, detachment, and lateral coalesce and sliding across the surface, and their eventual release from the edge of the test section occurs cyclically within 2–3 video frames (or ~ 70–100 ms). Such a cyclical process has been observed in all orientations, but at slightly higher frequencies. The photographs embedded in Fig. 12 show individual bubbles spreading across the surface, even at low surface superheat. As the heat flux increases, the coalescence of detached and laterally growing bubbles decreases the NBHTC with increased surface temperature or superheat (Fig. 6(a)).

Figure 13 presents a series of photographs of the saturation nucleate boiling of FC-72 on porous graphite in the vertical orientation ($\theta=90$ deg) at increasing heat flux values. Note the increase in the intensity of the hydrodynamic mixing in the boundary layer by growing and coalescing vapor bubbles with increasing the nucleate boiling heat flux. The photograph at a heat flux of 27.1 W/cm^2 shows the boiling process near CHF on the porous graphite. In the vertical orientation, the build up of vapor near the boiling surface and the subsequent release from the upper edge of the test section is also cyclical with an average frequency of ~ 15 Hz, compared to ~ 10 Hz in the downward-facing orientation. Figure 14 presents four photographs of the saturation nucleate boiling of FC-72 liquid on porous graphite in the inclined orientation of 150 deg. These photographs also show increased hydrodynamic and two-phase mixing within the boundary layer by growing and sliding vapor bubbles with increased nucleate boiling heat flux.

Effect of Liquid Subcooling. The results presented in this section on the effect of liquid subcooling on the nucleate boiling heat transfer and CHF of FC-72 liquid on smooth copper (Fig. 15) and
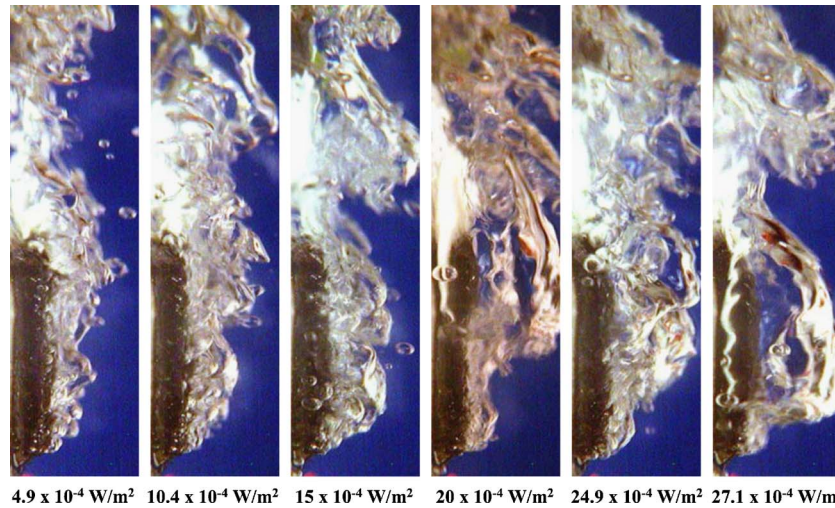
4.9 x 10⁻⁴ W/m²   10.4 x 10⁻⁴ W/m²   15 x 10⁻⁴ W/m²   20 x 10⁻⁴ W/m²   24.9 x 10⁻⁴ W/m²   27.1 x 10⁻⁴ W/m²

Fig. 13 Saturation boiling photographs on aged porous graphite in vertical orientation

porous graphite (Fig. 16) are only in the upward-facing orientation [18]. Investigating the effect of varying the surface orientation on subcooled boiling of both FC-72 and HFE-7100 is ongoing and will be reported in a future paper. The solid circle symbols in Figs. 15 and 16 indicate the maximum NBHTC, which in saturation boiling coincides with the transition from region II to III of the boiling curves on both porous graphite and copper. The maximum NBHTC also coincides with the transition from regions II and III in subcooled boiling on porous graphite (Fig. 16) but close to CHF on copper (Fig. 15). In order to clearly distinguish the various boiling regions, the nucleate boiling heat flux (Figs. 15(a) and 16(a)) and NBHTC (Figs. 15(b) and 16(b)) are plotted versus ΔT_b, which is the temperature drop in the boundary layer, or the difference between the surface and the bulk liquid temperatures ΔT_b. The extents of these boiling regions are determined from the change in the slope of the boiling curves with increasing surface superheat, and thus are approximate.

In region I, the density of the active nucleation sites on the surface increases at an increasing rate with increasing surface temperature. In region II, however, the rate of increase in the nucleate boiling heat flux, or of NBHTC, with increased surface temperature is much higher than in region I due to the higher and continuous increase in the active nucleation sites density. Near the end of region II and in region III, the nucleate boiling heat flux continues to increase, but the coalescence of the vapor bubbles near the surface causes the surface temperature to increase and

NBHTC to decrease. The maximum NBHTC of FC-72 on copper occurs at a much higher surface temperature than on porous graphite, typically at the end of region II in saturation boiling and near CHF in subcooled boiling (Figs. 15 and 16). Figures 15(b) and 16(b) show that NBHTC of FC-72 on porous graphite is not only much higher than on copper but the surface temperature is much lower. For example, in 10 K and 30 K subcooled nucleate boiling the maximum NBHTC on copper is 0.675 $\times 10^4$ W/m² K and 0.546$\times 10^4$ W/m² K and occurs at ΔT_b =31.2 K and 53.41 K, respectively, while those on porous graphite (1.676$\times 10^4$ W/m² K and 1.205$\times 10^4$ W/m² K) are ~2.5 and 2.3 times those on copper and occur at lower ΔT_b of 20.3 K and 44.7 K, respectively. As shown in Figs. 15(a) and 16(a), CHF on both copper and the unaged porous graphite increases linearly with liquid subcooling [18], however, the rate of fractional increase of CHF with increased liquid subcooling on porous graphite of 0.041 K⁻¹ is much higher than that on copper of 0.018 K⁻¹. The results of the effect of surface orientation on saturation boiling CHF of FC-72 on both graphite and copper are present and discussed next.

Critical Heat Flux. Figure 17 compares the present values of saturation CHF of FC-72 on porous graphite and smooth copper as functions of the surface orientation (or inclination angle) with those reported by other investigators on copper and microporous coatings. The CHF values in this figure are for 10 mm $\times$ 10 mm, 12.7 mm $\times$ 12.7 mm, and 30 mm diameter surfaces, showing no clear effect of the size of the surface on CHF. The highest CHF values are those measured in the present work on porous graphite followed by those reported on microporous coatings; the lowest values are those measured in this work and reported earlier by other investigators on copper. In the upward-facing orientation ($\theta = 0$ deg), saturation CHF on porous graphite (29.6–30.3 W/cm²) is ~12% higher than that reported by Chang and You [11] on microporous coatings (26.8 W/cm²), and ~57% higher than the average of the values measured in this work and reported by others on copper (~19.1 W/cm²). On copper, the reported CHF values vary from as low as 16.1 W/cm² to as much as 22.4 W/cm² [11,19,26,27,29], compared to 17.9–18.3 W/cm² in the present work.

There is a relatively large scattering in the reported saturation CHF values of FC-72 on copper by the different investigators at all inclination angles, including 180 deg (downward facing). In this orientation, the reported CHF values vary from 1.6 W/cm² [11] to as much as 4.9 W/cm² [26]; the value determined in the
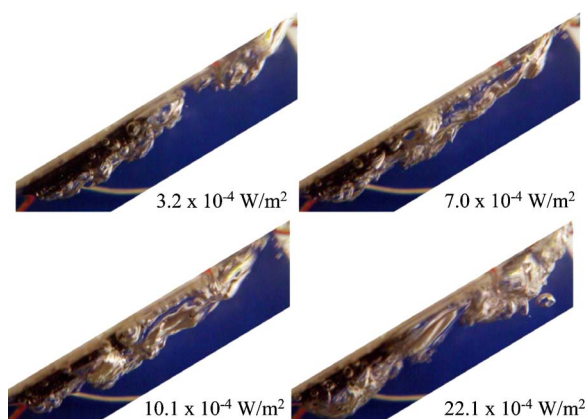

3.2 x 10⁻⁴ W/m²   7.0 x 10⁻⁴ W/m²

10.1 x 10⁻⁴ W/m²   22.1 x 10⁻⁴ W/m²

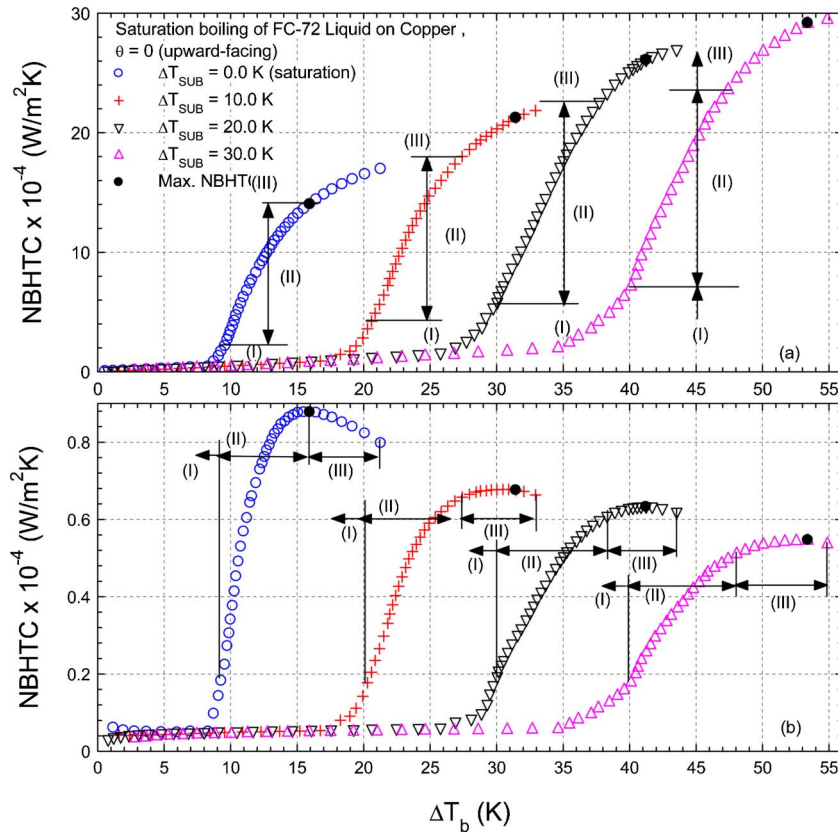**Fig. 14 Saturation boiling photographs on aged porous graphite in 150 deg orientation**

Fig. 15 Effect of subcooling on nucleate boiling of FC-72 on copper in upward-facing orientation

present work is ~2.5 W/cm². Such large variation in CHF values in the 180 deg inclination is attributed to the sensitivity of CHF to the slightest error in adjusting the surface inclination. Such sensitivity also exists, but to a much lesser extent with decreased inclination angle. The decreases in saturation CHF of FC-72 with increased inclination are similar on copper, microporous coatings, and porous graphite, but the actual values are different (Fig. 17).

In general, CHF decreases slowly with increased inclination angle up to 90 deg (vertical) then decreases much faster with increased inclination angle to its lowest value at 180 deg (Fig. 17). The rate of decrease in the saturation CHF of FC-72 with increased inclination angle up to 90 deg is very similar on porous graphite, microporous coatings, and copper. Beyond 90 deg, however, the rate of decrease in the saturation CHF on porous graphite with increased inclination angle is much lower than reported for the same liquid on microporous coatings, measured in this work, and reported by other investigators on copper. The results in Fig. 17 show consistently higher CHF values on porous graphite [17,23,24]. The saturation CHF on porous graphite in the downward-facing orientation (180 deg), 16 W/cm², is ~53% of that measured in the upward-facing orientation (0 deg) and 6.4 times that measured in the present work on copper, while that reported on microporous coatings of 4.9 W/cm² is only 18% of that reported in the upward-facing orientation [11] and 1.96 times the present value on copper.

The present and reported values of the saturation CHF of FC-72 liquid on the various surfaces in Fig. 17 are correlated using the general form suggested by Kutateladze [39]. This form has been employed successfully for correlating CHF data of water, liquid helium, liquid nitrogen, and HFE-7100 as function of inclination angle θ [5,6,31]. The suggested correlation for the saturation CHF of FC-72 liquid can be written as

$$\mathrm{CHF}(\theta) = C_{\mathrm{CHF}}(\theta)\rho_v^{0.5}h_{fg}[\sigma g(\rho_\ell - \rho_v)]^{0.25} \qquad (3)$$

The coefficient in this correlation $C_{\mathrm{CHF}}(\theta)$ depends on the liquid properties, the surface characteristics (e.g., porous or smooth), and θ. It can be expressed as the product of two quantities representing the separate effects of the surface characteristic, $C_{\mathrm{CHF,sat}}$, and the inclination angle $R(\theta)$ as

$$C_{\mathrm{CHF}}(\theta) = C_{\mathrm{CHF,sat}} \cdot R(\theta) \qquad (4)$$

In Fig. 18, the values of $C_{\mathrm{CHF,sat}}$ for CHF of FC-72 liquid on porous graphite and on copper are based on CHF measurements in 9 and 19 sequential tests, respectively [17,23,24]. The least squares fit of these and others based on the reported CHF values by other investigators on copper and silicon surfaces of different dimensions yields $C_{\mathrm{CHF,sat}}=0.166$, which is within +6% and −10% of all the data in Fig. 18 [3,4,18,19,25,27,40–42]. Similarly, the obtained value of $C_{\mathrm{CHF,sat}}$ from the least squares fit of the present CHF data on porous graphite and of the values based on the reported CHF values of FC-72 on micro-porous coatings [3,13,41,43] and on microfined silicon surfaces [34] is 0.263 (Fig. 18). This value is ~58% higher than that on smooth surfaces (0.166) and within ±7% of the entire set of data (Fig. 18).

The empirical CHF orientation coefficient $R(\theta)$ is determined from the CHF data of FC-72 liquid on smooth copper, porous graphite, and microporous coatings. The reported empirical correlations of $R(\theta)$ for saturation boiling of FC-72 and HFE-7100 on copper are almost identical to those on microporous coatings [6]

1. FC-72 on copper; [11] (0 deg $\leq \theta \leq$ 180 deg):

$$R(\theta) = [1 - 0.0012\theta\tan(0.414\theta) - 0.122\sin(0.318\theta)]$$
$$(5a)$$
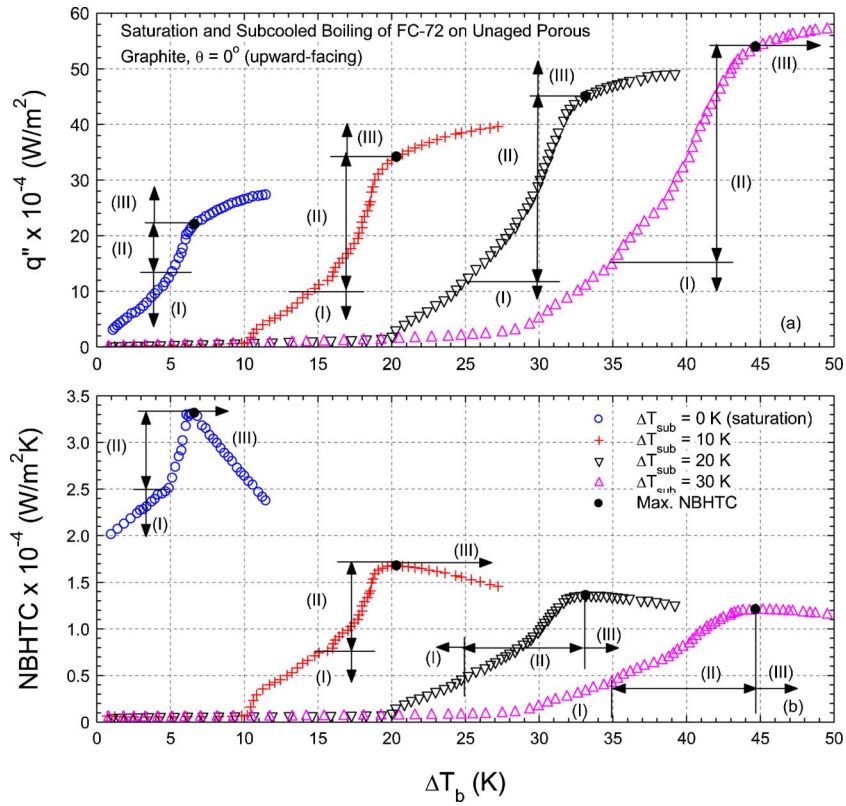
Fig. 16 Effect of subcooling on nucleate boiling of FC-72 on unaged porous graphite in upward facing orientation

2. FC-72 and HFE-7100 on copper; [6] (0 deg $\leq \theta \leq$ 180 deg):

$$R(\theta) = [(1 - 0.00127\theta)^{-4} + (3.03 - 0.016\theta)^{-4}]^{-0.25} \quad (5b)$$

3. FC-72 and HFE-7100 on copper; [19] (0 deg $\leq \theta \leq$ 175 deg):

$$R(\theta) = 1 - 1.1117 \times 10^{-3}\theta + 7.794 \times 10^{-6}\theta^2$$
$$- 1.3768 \times 10^{-7}\theta^3 \quad (5c)$$

As delineated in Figs. 19(a) and 19(b), Eqs. (5a)–(5c) fit most
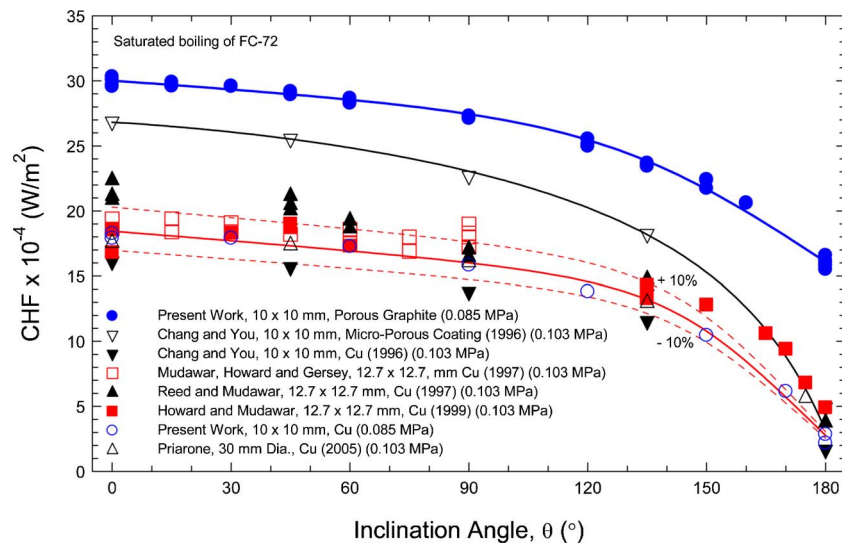
Fig. 17 Effect of inclination angle on saturation CHF of FC-72 on different surfaces
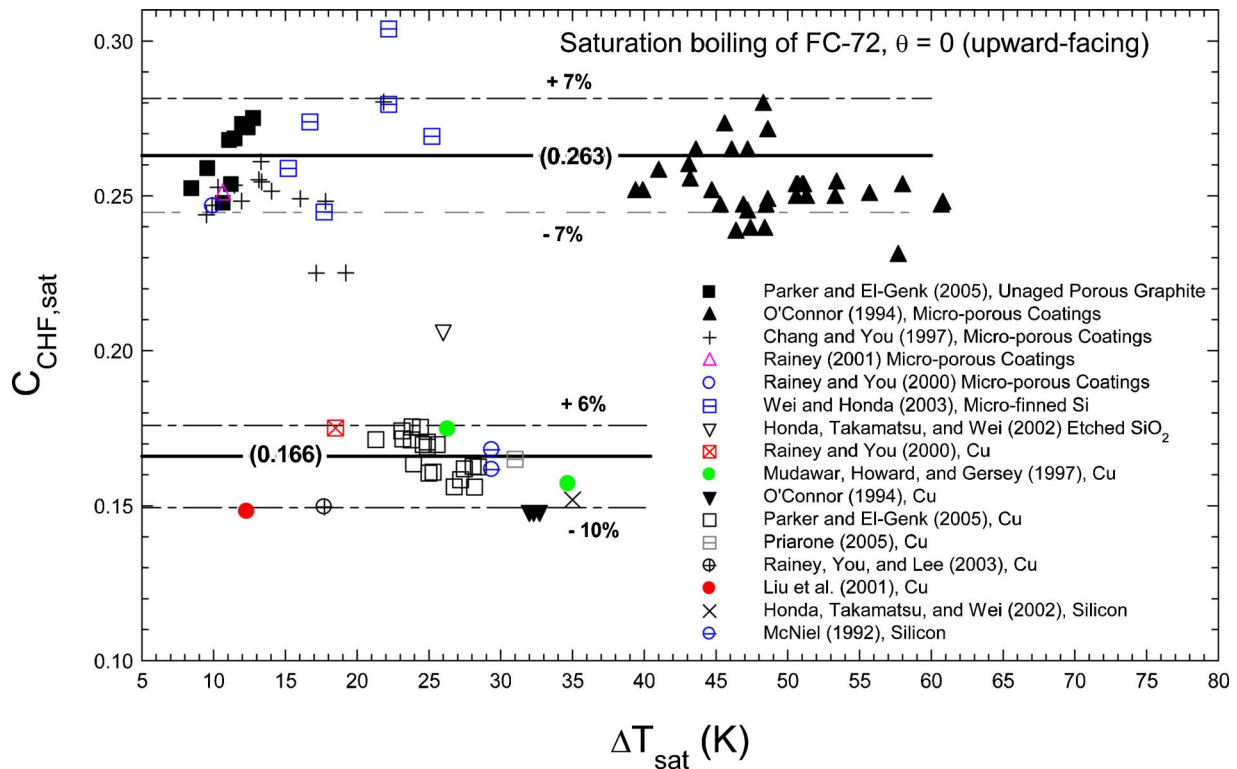
Fig. 18 Saturation CHF coefficients for FC-72 on different surfaces

saturation CHF data of FC-72 and HFE-7100 on copper [6,11,19,26–29,44,45] and microporous coatings [11,28] to within $\pm 10\%$. The values of $R(\theta)$ on porous graphite (Fig. 19(*b*)), are consistently higher than those of FC-72 on copper and microporous coatings and correlated as

$$R(\theta) = [(1 - 0.000796\theta)^{-4} + (1.8 - 0.00703\theta)^{-4}]^{-0.25} \quad (6)$$

Equation (6) fits the present porous graphite CHF data to within $\pm 5\%$. It is worth noting that $R(\theta)$ given by any of the above empirical correlations (Eqs. (5*a*)–(5*c*) and (6)) is a fraction whose value increases as the inclination angle decreases, and becomes unity in the upward-facing orientation ($\theta = 0$ deg). Figure 19(*c*) compares Eqs. (5*a*)–(5*c*) and (6) for R(θ). The values on porous graphite are significantly higher than on copper and microporous coatings, particularly at higher inclinations. For example, $R(180 \text{ deg})$ on porous graphite is 0.54 versus only 0.15 on both Cu and microporous coatings. Similarly, at lower inclinations of 150 deg and 90 deg, $R(\theta)$ on porous graphite is ~0.73 and ~0.9 versus ~0.56 and 0.84, respectively, on both Cu or microporous coatings.

Although $R(\theta)$ for FC-72 on Cu and microporous coatings are similar, the actual CHF values on the latter are significantly higher than on the former (Fig. 17). To illustrate this difference, the reported values of saturation CHF for FC-72 on microporous coatings and the present values on porous graphite are divided by those measured in the present work on smooth copper. The obtained ratios are plotted in Fig. 20 versus the inclination angle. This figure indicates that CHF on porous graphite in the upward-facing orientation is ~1.65 times that on Cu. This ratio increases slightly with increased inclination up to 60 deg, then increase precipitously with a further increase in the inclination angle to its highest value of ~6.4 in the downward-facing orientation ($\theta = 180$ deg). On 20 mm × 20 mm and 50 mm × 50 mm surfaces with microporous coatings, CHF ratios [28] are identical at all inclinations except 180 deg and ~15% higher than those measured on Cu in the present work. In the downward-facing orien-

tation, the reported values of the saturation CHF for FC-72 liquid on microporous coatings is as much as two times those measured in this work on copper (Fig. 17). The ratios of the reported CHF by Chang and You [11] on microporous coatings onto a 10 mm × 10 mm surface are similar, but are ~15%–20% higher than reported by Rainey and You [28] for microporous coatings on larger surfaces (Fig. 20).

Summary and Conclusions

Experiments performed which investigated saturation pool boiling of FC-72 liquid on flat, aged porous graphite, and on smooth newly prepared copper surfaces measuring 10 mm × 10 mm and the effect of surface orientation on NBHTC and CHF. The inclination angles considered are 0 deg (upward facing), 60 deg, 90 deg (vertical), 120, 150, and 180 deg (downward facing). Also investigated are the effects of liquid subcooling of 10, 20, and 30 K on NBHTC of FC-72 liquid on copper and porous graphite in the upward-facing orientation. Results demonstrated significant increases in NBHTC and CHF on aged porous graphite compared to those on copper. At low surface superheats, nucleate boiling heat flux increases with an increasing inclination angle, but decreases with an increased inclination angle at high surface superheats. Photographs and video images of pool boiling on porous graphite at different orientations showed the process to be cyclical with an average frequency of ~15 Hz in the vertical and ~10 Hz in the downward facing orientation.

On both copper and porous graphite, nucleate boiling heat flux and NBHTC at higher surface superheats (>6 K) decrease with increased surface inclination. Saturation NBHTC of FC-72 on porous graphite increases with decreased surface superheat. It reaches a maximum then decreases with further decrease in the surface superheat. Such a trend is also true on copper, but the rate of change in NBHTC with increasing surface superheat is much milder than on porous graphite and the maximum values on the latter are much higher. At high surface superheats (>6 K), although in the downward-facing orientation the NBHTC on porous
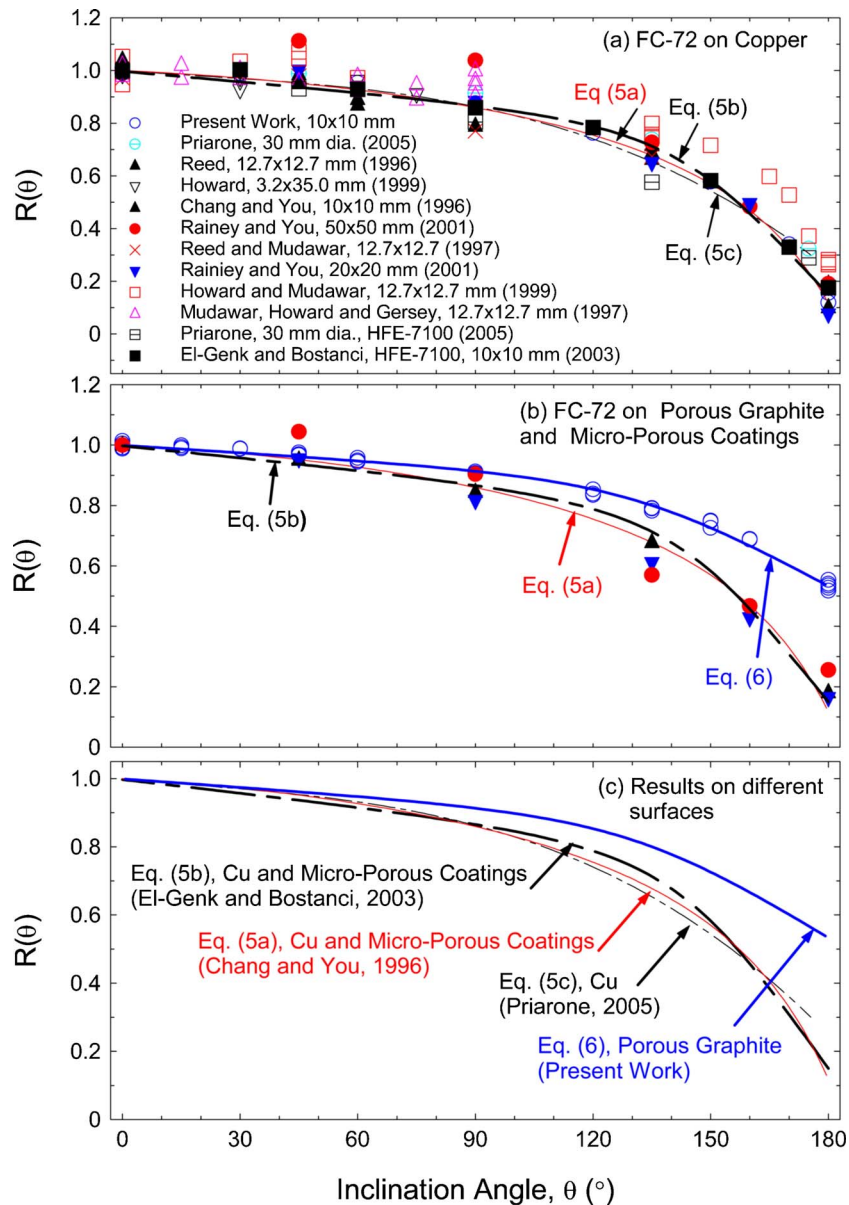
Fig. 19 Inclination coefficients of saturation CHF of FC-72 on different surfaces

graphite is the lowest, its maximum value is the highest. The maximum NBHTC decreases; however, the corresponding surface superheat increases with decreased surface inclination. Conversely, on copper both the maximum NBHTC and the corresponding wall superheat increase with decreased surface inclination.

The CHF on copper and porous graphite decrease slowly with an increased inclination angle up to 90 deg, then faster with increased inclination beyond 90 deg to its lowest values at 180 deg (downward-facing orientation). The rate of decrease in the saturation CHF with increased inclination angle up to 90 deg is similar on porous graphite, microporous coatings, and copper. Beyond 90 deg, the rate of decrease in CHF on porous graphite with an increased inclination angle is smaller than reported by other investigators on copper and microporous coatings and measured in this work on copper. The values of CHF are highest on porous graphite followed closely with those on microporous coatings; but those on copper are significantly lower. CHF on porous graphite in the downward-facing orientation (16×10^4 W/m^2) is ~53% of that in the upward-facing orientation (0 deg) and 6.4 times that

measured in the present work on copper. The reported value in the downward-facing orientation on microporous coatings of 4.9 $\times 10^4$ W/m^2 is 1.96 times the present value on copper and only ~18% of that in the upward-facing orientation. The present CHF values for FC-72 liquid on porous graphite at inclinations of 0, 90, and 150 deg are ~1.67, 1.69, and 4.14 times those on copper.

The general form suggested by Kutateladze [39] is used successfully to correlate the saturation CHF values of FC-72 on porous graphite to within ±5%, and the database of the present and reported CHF values by other investigators on copper to within ±10%. The value of the coefficient in the present CHF correlation depends on both the surface characteristics and orientation. In the upward-facing orientation, the value of this coefficient for porous graphite, microporous coatings, and microfinned silicon surface is the same (0.263), but much larger than that on smooth copper and silicon (0.166). This coefficient decreases with increased inclination, but on porous graphite, its rate of decrease is smaller than on copper and microporous coatings.
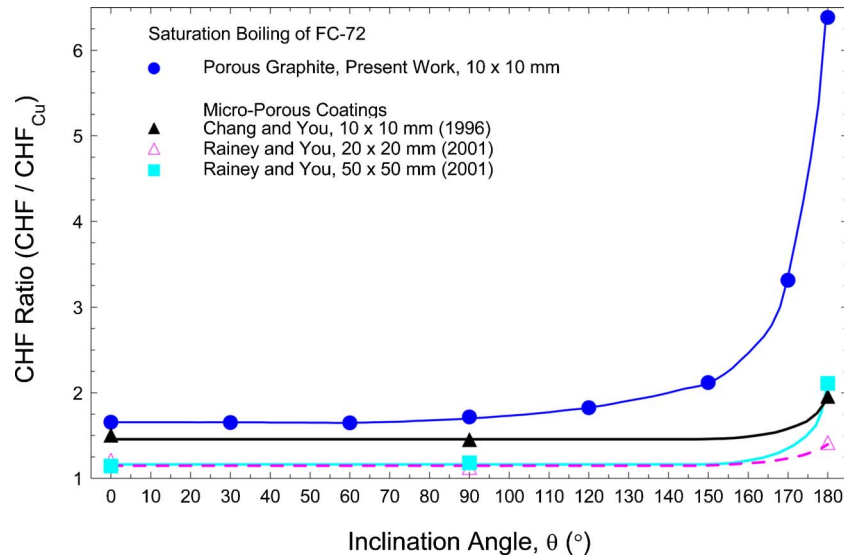
Fig. 20 Ratios of saturation CHF of FC-72 on porous graphite and microporous coatings to that measured on copper

Acknowledgment

Nomenclature

CHF = critical heat flux (W/m^2)
C_{CHF} = CHF coefficient
$C_{CHF,sat}$ = saturation CHF coefficient
g = gravitational acceleration (m/s^2)
h_{fg} = latent heat of vaporization (J/kg)
h_{NB} = NBHTC $(W/m^2 K)$
h_{NB}^* = maximum NBHTC $(W/m^2 K)$
h_{fg} = latent heat of vaporization (J/kg)
k_1 = liquid thermal conductivity (W/m K)
L = characteristic length of boiling surface (10 mm)
NBHTC = nucleate boiling heat transfer coefficient, $q''/\Delta T_b (W/m^2 K)$
Nu_{NB} = Nusselt number, $(q''L)/(\Delta T_b k_l)$
Nu_{NB}^* = maximum Nusselt number
q'' = nucleate boiling heat flux $(W/cm^2$ or $W/m^2)$
R = CHF orientation coefficient
T_b = liquid pool temperature (K)
T_{sat} = liquid saturation temperature (K)
T_w = wall or boiling surface temperature (K)

Greek Symbols

ΔT_b = $(T_w - T_b)$ (K)
ΔT_{sat} = $(T_w - T_{sat})$ (K)
θ = inclination angle (°)
ρ_v = vapor density (kg/m^3)
ρ_l = liquid density (kg/m^3)
σ = surface tension (N/m)

References

[1] Knickerbocker, J. U., et al., 2002, "An Advanced Multichip Module (MCM) for High-Performance UNIX Servers," IBM J. Res. Dev., **46**(6), pp. 779–804.
[2] ITRS, International Technology Roadmap for Semiconductors, 2004.
[3] Rainey, K. N., and You, S. M., 2000, "Pool Boiling Heat Transfer from Plain and Microporous, Square Pin-Finned Surfaces in Saturated FC-72," J. Heat Transfer, **122**, pp. 509–516.
[4] Rainey, K. N., You, S. M., and Lee, S., 2003, "Effect of Pressure, Subcooling, and Dissolved Gas on Pool Boiling from Microporous Surfaces in FC-72," J. Heat Transfer, **125**, pp. 75–83.
[5] El-Genk, M. S., and Bostanci, H., 2003a, "Saturation Boiling of HFE-7100 from a Copper Surface, Simulating a Microelectronic Chip," Int. J. Heat Mass Transfer, **46**, pp. 1841–1854.
[6] El-Genk, M. S., and Bostanci, H., 2003b, "Combined Effects of Subcooling and Surface Orientation on Pool Boiling of HFE-7100 from a Simulated Electronic Chip," Exp. Heat Transfer, **16**, pp. 281–301.
[7] Chen, X. Y., Toh, K. C., Wong, T. N., Chai, J. C., Pinjala, D., Navas, O. K., Ganesh, H. Z., and Kripesh, V., 2004, "Direct Liquid Cooling of a Stacked MCM," *Proceedings 9th Intersociety Conference on Thermal Phenomena*, Las Vegas, NV, June 1–4, IEEE, Piscataway, NJ, Vol. 1, pp. 199–206.
[8] Ravigururajan, T. S., and Drost, M. K., 1999, "Single-Phase Flow Thermal Performance Characteristics of a Parallel Microchannel Heat Exchanger," J. Enhanced Heat Transfer, **6**, pp. 383–393.
[9] Mathews, W. S., Lee, C. F., and Peters, J. E., 2003, "Experimental Investigations of Spray/Wall Impingement," Atomization Sprays, **13**(2,3), pp. 223–242.
[10] Pautsch, G., and Shedd, T. A., 2005, "Spray and Impingement Cooling with Single- and Multiple-Nozzle Arrays. Part I: Heat Transfer Data Using FC-72," Int. J. Heat Mass Transfer, **48**, pp. 3167–3175.
[11] Chang, J. Y., and You, S. M., 1996, "Heater Orientation Effects on Pool Boiling of Microporous Enhanced Surfaces in Saturated FC-72," J. Heat Transfer, **118**, pp. 937–943.
[12] Chang, J. Y., and You, S. M., 1997a, "Boiling Heat Transfer Phenomena from Micro-porous and Porous Surfaces in Saturated FC-72," Int. J. Heat Mass Transfer, **40**, pp. 4437–4447.
[13] Chang, J. Y., and You, S. M., 1997b, "Enhanced Boiling Heat Transfer from Micro-porous Surfaces: Effects of a Coating Composition and Method," Int. J. Heat Mass Transfer, **40**, pp. 4449–4460.
[14] Arik, M., and Bar-Cohen, A., 2001, "Ebullient Cooling of Integrated Circuits by Novec Fluids," Adv. Electron. Circuit Packag., **2**, pp. 627–637.
[15] Honda, H., and Wei, J. J., 2003, "Advances in Enhanced Boiling Heat Transfer From Electronic Components," JSME Int. J., Ser. B, **46**, pp. 479–490.
[16] Wei, J. J., and Honda, H., 2004, "Enhanced Boiling Heat Transfer From Electronic Components by Use of Surface Microstructures," Exp. Therm. Fluid Sci., **28**, pp. 159–169.
[17] El-Genk, M. S., and Parker, J. L., 2005, "Enhanced Boiling of HFE-7100 Dielectric Liquid on a Porous Graphite Surface," Energy Convers. Manage., **46**, pp. 2455–2481.
[18] Parker, J. L., and El-Genk, M. S., 2005, "Enhanced Saturation and Subcooled Boiling of FC-72 Dielectric Liquid," Int. J. Heat Mass Transfer, **48**, pp. 3736–3752.
[19] Priarone, A., 2005, "Efect of Surface Orientation on Nucleate Boiling and Critical heat Flux of Dielectric Fluids," Int. J. Therm. Sci., **44**, pp. 822–831.
[20] El-Genk, M. S., Saber, H. H., and Parker, J. L., 2005, "Thermal Analyses of Composite Copper/Porous Graphite Spreaders for Immersion Cooling Applications," *Proceedings of Conference on Integration and Packaging of MEMS, NEMS, and Electronics (InterPack'05)*, Paper No. IPACK2005-73226, San Francisco, CA, July 17–22, ASME, New York.
[21] Klett, J. W., and Trammell, M., 2004, "Parametric Investigation of a Graphite Foam Evaporator in a Thermosyphon With Fluorinert and a Silicon CMOS Chip," IEEE Trans. Device Mater. Reliab., **4**, pp. 626–637.
[22] Coursey, J. S., Kim, J., and Boudreaux, P. J., 2005, "Performance of Graphite Foam Evaporator for Use the Thermal Management," J. Electron. Packag.,

127, pp. 127–134.

[23] El-Genk, M. S., and Parker, J. L., 2004a, "Pool Boiling in Saturated and Subcooled HFE-7100 Dielectric Fluid From a Porous Graphite Surface," *Proceedings 9th Intersociety Conference on Thermal Phenomena*, Las Vegas, NV, June 1–4, IEEE, Piscataway, NJ, Vol. 1, pp. 655–662.

[24] El-Genk, M. S., and Parker, J. L., 2004b, "Pool Boiling in Saturated and Subcooled FC-72 Dielectric Fluid from a Porous Graphite Surface," *Proceedings, ASME International Mechanical Engineering Congress*, Paper No. IMECE2004-59905, Anaheim, CA, November 13–19, ASME, New York.

[25] Honda, H., Takamastu, H., and Wei, J. J., 2002, "Enhanced Boiling of FC-72 on Silicon Chips With Micro-Pin-Fins and Submicron Scale Roughness," J. Heat Transfer, **124**, pp. 383–390.

[26] Howard, A. H., and Mudawar, I., 1999, "Orientation Effects on Pool Boiling Critical Heat Flux (CHF) and Modeling of CHF for Near-Vertical Surfaces," Int. J. Heat Mass Transfer, **42**, pp. 1665–1688.

[27] Mudawar, I., Howard, A. H., and Gersey, C. O., 1999, "An Analytical Model for Near Saturated Pool Boiling Critical Heat Flux on Vertical Surfaces," Int. J. Heat Mass Transfer, **40**, pp. 2327–2339.

[28] Rainey, K. N., and You, S. M., 2001, "Effects of Heater Size and Orientation on Pool Boiling Heat Transfer from Microporous Coated Surfaces," Int. J. Heat Mass Transfer, **44**, pp. 2589–2599.

[29] Reed, S. J., and Mudawar, I., 1997, "Elimination of Boiling Incipience Temperature Drop in Highly Wetting Fluids using Spherical Contact With a Flat Surface," Int. J. Heat Mass Transfer, **42**, pp. 2439–2454.

[30] Beduz, C., Scurlock, R. G., and Sousa, A. J., 1988, "Angular Dependence on Boiling Heat Transfer Mechanisms in Liquid Nitrogen," *Advances in Cryogenic Engineering*, R. Fast, ed., Vol. 33, Plenum Press, New York, pp. 363–370.

[31] El-Genk, M. S., and Guo, Z., 1993, "Transient Boiling From Inclined and Downward-facing Surfaces in a Saturated Pool," Int. J. Refrig., **16**, pp. 414–422.

[32] Nishikawa, K., Fujita, Y., Uchida, S., and Ohta, H., 1984, "Effect of Surface Configuration on Nucleate Boiling Heat Transfer," Int. J. Heat Mass Transfer, **27**, pp. 1559–1571.

[33] Vishnev, I. P., Filatov, I. A., Vinokur, Ya. G., Gorokhov, V. V., and Svalov, G. G., 1976, "Study of Heat Transfer in Boiling of Helium on Surfaces with Various Orientations," Heat Transfer-Sov. Res., **8**, pp. 104–108.

[34] Wei, J. J., and Honda, H., 2003, "Effects of Fin Geometry on Boiling Heat Transfer from Silicon Chips with Micro-Pin-Fins Immersed in FC-72," Int. J. Heat Mass Transfer, **46**, pp. 4059–4070.

[35] You, S. M., Simon, T. W., and Bar-Cohen, A., 1992, "A Technique for Enhancing Boiling Heat Transfer with Application to Cooling of Electronic Equipment," IEEE Trans. Compon., Hybrids, Manuf. Technol., **15**, pp. 823–831.

[36] *CRC Handbook of Chemistry and Physics*, 66th ed., 1986, R. C. Wheast, ed., CRC Press, Boca Raton, FL.

[37] Poco Graphite Inc., 2005, Poco HTC Product Information.

[38] Chang, J. Y., 1997, "Enhanced Boiling Heat Transfer from Micro-Porous Surfaces," Ph.D. dissertation, University of Texas at Arlington, TX.

[39] Kutateladze, S. S., 1961, "Boiling Heat Transfer," Int. J. Heat Mass Transfer, **4**, pp. 31–45.

[40] McNiel, A. C., 1992, "Pool Boiling Critical Heat Flux in a Highly Wetting Liquid," Masters thesis, University of Minnesota, Minneapolis, MN.

[41] O'Connor, J. P., 1994, "Enhancement of Pool Boiling Heat Transfer in Highly Wetting Dielectric Liquids," Ph.D. dissertation, University of Texas at Arlington, TX.

[42] Liu, Z. W., Lin, W. W., Lee, D. J., and Peng, X. F., 2001, "Pool Boiling of FC-72 and HFE-7100," J. Heat Transfer, **123**, pp. 399–400.

[43] Rainey, K. N., 2001, "Pool and Flow Boiling Heat Transfer from Microporous Flat and Finned Surfaces in FC-72," Ph.D. dissertation, University of Texas at Arlington, TX.

[44] Reed, S. J., 1996, "Elimination of Boiling Incipience Temperature Drop and Enhancement of Boiling Heat Transfer in Highly Wetting Fluids Through Low Contact Force Attachments," Master's thesis, Purdue University, West Lafayette, IN.

[45] Howard, A. H., 1999, "Effects on Orientation and Downward-Facing Convex Curvature on Pool Boiling Critical Heat Flux," Ph.D. dissertation, Purdue University, West Lafayette, IN.

Lattice Boltzmann Method Simulation of Backward-Facing Step Flow With Double Plates Aligned at Angle to Flow Direction

Chao-Kuang Chen[1]
e-mail: ckchen@mail.ncku.edu.tw

Tzu-Shuang Yen

Yue-Tzu Yang

Department of Mechanical Engineering,
National Cheng Kung University,
Tainan, 70101, Taiwan

This study applies the lattice Boltzmann method (LBM) to simulate incompressible steady low Reynolds number backward-facing step flows. In order to restrict the simulations to two-dimensional flows, the investigated Reynolds number range is limited to a maximum value of Re=200. The field synergy principle is applied to demonstrate that the increased interruption within the fluid caused by the introduction of two inclined plates reduces the intersection angle between the velocity vector and the temperature gradient. The present results obtained for the velocity and temperature fields are found to be in good agreement with the published experimental and numerical results. Furthermore, the numerical results confirm the relationship between the velocity and temperature gradient predicted by the field synergy principle. [DOI: 10.1115/1.2352786]

Keywords: lattice Boltzmann method, backward-facing step, heat transfer, field synergy principle

1 Introduction

In recent years, the lattice Boltzmann method (LBM) has emerged as a promising numerical scheme for simulating fluid flows and modeling the physics of fluids [1]. Unlike conventional numerical schemes based on the discretization of macroscopic continuum equations, the LBM is based on microscopic models and mesoscopic kinetic equations. These algorithms attempt to model a fluid by simulating a discretized one-particle phase space distribution function similar to that described by the traditional Boltzmann equation. The fluid is treated on a statistical level and the movements and interactions of a single particle or ensemble-average particle density distribution function are simulated by solving a velocity discrete Boltzmann equation. The fundamental concept of the LBM is to construct simplified kinetic models which incorporate the essential physics of microscopic or mesoscopic processes such that the macroscopic averaged properties obey the desired macroscopic equations.

The use of the lattice Boltzmann equation as a numerical scheme was first proposed by McNamara and Zanetti [2]. This equation neglects the motion of individual particles and results in a smooth macroscopic behavior. Higuera and Jimenez [3] and Succi and Benzi [4] introduced a linearized collision operator to simplify the scheme and eliminate statistical noise. A particularly simple linearized version of the collision operator is the Bhatnagar-Gross-Krook collision operator [5], which uses a single relaxation time parameter. The relaxation term is known as the BGK operator and the corresponding model is referred to as the lattice Boltzmann BGK model. The BGK collision operator greatly accelerates the computation process. Due to its extreme simplicity, the lattice BGK (LBGK) equation [6] has emerged as the most widely employed version of the lattice Boltzmann model.

Since the method typically uses uniform regular Cartesian lattices in space, curved boundaries are generally approximated by a series of stairs. However, this approximation leads to a reduction in the computational accuracy. Accordingly, an approach for curved walls has recently been proposed by Fillipova and Hanel [7] based on an improvement of the bounce-back rule. The numerical stability was further improved by Mei et al. [8] with a revision expression for $\Delta < 1/2$. Guo et al. [9] extended the extrapolation scheme proposed by Chen et al. [10] to develop a new treatment for curved boundaries.

The problem of channel flow over a backward-facing step is often used to evaluate the accuracy of a numerical scheme. The main characteristic of flows of this type is the formation of a recirculation region immediately downstream of the step. The length of the recirculation region is a function of the geometry of the channel (i.e., the expansion ratio), the fluid momentum (i.e., the Reynolds number), and the flow regime (i.e., laminar or turbulent). This flow pattern has a large number of practical engineering applications, including airfoils, electrical devices, diffusers, and combustors. Kondoh [11] used a traditional computational fluid dynamics (CFD) method to simulate laminar heat transfer in a separating and reattaching flow. The numerical results were found to be in good agreement with the experimental data of Aung [12] and Hall and Pletcher [13].

Drawing an analogy between heat convection and heat conduction, Guo et al. [14] and Wang [15] studied the mechanisms of convective heat transfer and proposed a novel approach for enhancing convective heat transfer under a parabolic fluid flow structure. Guo et al. [14] suggested that the convection term can be transformed into a dot product of the velocity vector and the temperature gradient and the energy equation integrated over the thermal boundary layer. This novel approach was aimed at improving the uniformity of the velocity and temperature profiles and reducing the included angle between the velocity vector and the temperature gradient. Guo et al. [14] referred to this approach as the field synergy principle and Tao et al. [16,17] extended the concept from parabolic to elliptic fluid flows and to other transport phenomena.

The objective of this study is to analyze the velocity and tem-

perature fields of incompressible steady low Reynolds number backward-facing step flows. The flow is investigated both with and without the insertion of double plates oriented at various angles to the flow direction downstream from the step. The influence of the angle of inclination of the double plates on the heat transfer performance is verified for different Re numbers (Re <200). The computed results are then compared with the published experimental and numerical results.

2 Lattice Boltzmann Equations

2.1 Lattice Boltzmann Equations for Density and Velocity Fields.
This study simulates the steady backward-facing step flow using the nine-velocity LBM model with a two-dimensional (2D) square lattice, designated the D2Q9 model. In this model, $c = \delta x / \delta t = \delta y / \delta t$ is the lattice streaming speed and δx and δy are the grid spacings in the x and y directions, respectively, and correspond to the distance which a particle moves in each time step of the LBM simulation. The discrete velocities for the D2Q9 model are defined as

$$\vec{e}_\alpha = (0,0), \quad \alpha = 0, \quad \text{rest particle}$$

$$\vec{e}_\alpha = (\pm c, 0), (0, \pm c), \quad \alpha = 1,2,3,4$$

$$\vec{e}_\alpha = (\pm c, \pm c), \quad \alpha = 5,6,7,8 \tag{1}$$

The LBM solves the microscopic kinetic equation for the particle distribution $f(\vec{x}, \vec{V}, t)$, where $\vec{x}$ and $\vec{V}$ are the particle position and velocity vectors, respectively, in phase space $(\vec{x}, \vec{V})$ and time t. The governing equation for the density distribution function is given by

$$f_\alpha(\vec{x} + \vec{e}_\alpha \delta t, t + \delta t) - f_\alpha(\vec{x}, t) = -\frac{1}{\tau_v}[f_\alpha(\vec{x}, t) - f_\alpha^{eq}(\vec{x}, t)] \tag{2}$$

where τ_v characterizes the relaxation time of the density distribution function toward the local equilibrium f_α^{eq}. The equilibrium density distribution is expressed as

$$f_\alpha^{eq} = w_\alpha \rho \left[1 + \frac{3\vec{e}_\alpha \cdot \vec{V}}{c^2} + \frac{9}{2} \frac{(\vec{e}_\alpha \cdot \vec{V})^2}{c^4} - \frac{3}{2} \frac{\vec{V}^2}{c^2} \right] \tag{3}$$

where $w_0 = 4/9$, $w_\alpha = 1/9$ for $\alpha = 1,2,3,4$, $w_\alpha = 1/36$ for $\alpha = 5,6,7,8$.

The macroscopic density and velocity are calculated from

$$\rho = \sum_\alpha f_\alpha \tag{4}$$

$$\rho \vec{V} = \sum_\alpha \vec{e}_\alpha f_\alpha \tag{5}$$

Adopting the same procedure as that employed by Hou et al. [18], the continuity and Navier-Stokes equations can be derived through the Chapman-Enskog expansion of the density distribution function. The details of this derivation are provided in [18]. If only the physics in the long-wavelength and low-frequency limit are of interest, the lattice spacing δx and the time increment δt can be regarded as small parameters of the same order δ. The Navier-Stokes equation and continuity equation are then given by

$$\partial_t \rho + \nabla \cdot (\rho \vec{V}) = 0 + (\delta^2) \tag{6}$$

$$\partial_t(\rho \vec{V}) + \nabla \cdot (\rho \vec{V} \vec{V}) = -\nabla p + v[\nabla^2(\rho \vec{V}) + \nabla(\nabla \cdot (\rho \vec{V}))] + O(\delta^2) \tag{7}$$

where $p = c_s^2 \rho$ is the pressure, derived from the equation of state for an ideal gas, $c_s = c/\sqrt{3}$ is the speed of sound, and the kinematic viscosity is given by

$$v = \frac{(2\tau_v - 1)}{6} \frac{(\delta x)^2}{\delta t} \tag{8}$$

The Mach number is defined as $M = \vec{V}/c_s$. A low Mach number assumption can be invoked as the nearly incompressible limit is approached, i.e., $M \ll 1$. The incompressible Navier-Stokes equation and continuity equation are expressed as

$$\nabla \cdot \vec{V} = 0 + O(\delta^2) \tag{9}$$

$$\partial_t \vec{V} + \vec{V} \cdot \nabla \vec{V} = -\frac{\nabla p}{\rho} + v \nabla^2 \vec{V} + O(\delta^2) \tag{10}$$

2.2 Lattice Boltzmann Equation for Temperature Field.
In general, previous thermal Lattice Boltzmann models fall into three distinct categories: the multispeed approach [19]; the passive scalar temperature distribution approach [20]; and the thermal energy distribution model [21]. The multispeed approach is a straightforward extension of the isothermal model, but suffers severe numerical instability. The temperature variation is limited to a narrow range and a fixed Prandtl number. The passive scalar approach utilizes the fact that the macroscopic temperature satisfies the same evolution equation as a passive scalar. However, it neglects viscous heat dissipation and the compression work done by pressure. Finally, although the thermal energy distribution model is an adequate tool for solving real thermal problems, it suffers a number of shortcomings. For example, it contains a complicated gradient operator term in the evolution equation for the temperature, and hence the simplicity characterizing the LBM is lost. Furthermore, since viscosity is involved not only in the momentum equation, but also in the energy equation, additional variables for the thermal energy distribution function must be introduced in order to ensure that the viscosity remains consistent in the governing equations of the thermal energy distribution model and to avoid implicitness of the schemes [21]. Consequently, the current study employs the simplified thermal model proposed by Peng et al. [22] for simulation purposes. This model considers that the compression work done by the pressure and the viscous heat dissipation can be neglected for incompressible flow, and hence the gradient term used to recover these terms through the Chapman-Enskog expansion can be dropped from the evolution equation.

The governing equation of the simplified thermal energy distribution model is given by

$$g_\alpha(\vec{x} + \vec{e}_\alpha \delta t, t + \delta t) - g_\alpha(\vec{x}, t) = -\frac{1}{\tau_c}[g_\alpha(\vec{x}, t) - g_\alpha^{eq}(\vec{x}, t)] \tag{11}$$

According to He, Chen, and Doolen [21], the equilibrium energy distribution functions g can be written as

$$g_0^{eq} = -\frac{2\rho\varepsilon}{3} \frac{\vec{V}^2}{c^2} \tag{12}$$

$$g_{1,2,3,4}^{eq} = \frac{\rho\varepsilon}{9} \left[\frac{3}{2} + \frac{3}{2} \frac{\vec{e}_\alpha \cdot \vec{V}}{c^2} + \frac{9}{2} \frac{(\vec{e}_\alpha \cdot \vec{V})^2}{c^4} - \frac{3}{2} \frac{\vec{V}^2}{c^2} \right] \tag{13}$$

$$g_{5,6,7,8}^{eq} = \frac{\rho\varepsilon}{36} \left[3 + 6\frac{\vec{e}_\alpha \cdot \vec{V}}{c^2} + \frac{9}{2} \frac{(\vec{e}_\alpha \cdot \vec{V})^2}{c^4} - \frac{3}{2} \frac{\vec{V}^2}{c^2} \right] \tag{14}$$

where $\varepsilon = DRT/2$, in which R is the gas constant and D is the dimension. The macroscopic temperature can then be calculated by

$$\rho\varepsilon = \sum_\alpha g_\alpha \tag{15}$$

Using the procedure presented by Hou et al. [18], the Chapman-Enskog expansion for the new thermal energy distribution func-

tion can be used to recover the macroscopic energy equation. Using $g_\alpha^{(0)}$ rather than g_α^{eq}, and expanding g_α about $g_\alpha^{(0)}$, it can be shown that

$$g_\alpha = g_\alpha^{(0)} + \delta g_\alpha^{(1)} + \delta^2 g_\alpha^{(2)} + O(\delta^3) \qquad (16)$$

where δ is the expansion parameter. To investigate changes in different time scales, t_0 and t_1 are introduced as $t_0 = t, t_1 = \delta t, \ldots$; such that

$$\partial_t = \partial_{t0} + \delta \partial_{t1} + \delta^2 \partial_{t2} + \cdots \qquad (17)$$

The first-order expansion of Eq. (11) is

$$(\partial_{t0} + \vec{e} \cdot \nabla) g_\alpha^{(0)} = -\frac{1}{\tau_c} g_\alpha^{(1)} \qquad (18)$$

The second-order expansion of Eq. (11) is

$$\partial_{t1} g_\alpha^{(0)} + \left(1 - \frac{1}{2\tau_c}\right)(\partial_{to} + \vec{e} \cdot \nabla) g_\alpha^{(1)} = -\frac{1}{\tau_c} g_\alpha^{(2)} \qquad (19)$$

Summing Eqs. (18) and (19) gives

$$\partial_{t0}(\rho \varepsilon) + \nabla \cdot (\rho \vec{V} \varepsilon) = 0 \qquad (20)$$

$$\partial_{t1}(\rho \varepsilon) + \left(1 - \frac{1}{2\tau_c}\right) \prod^{(1)} = 0 \qquad (21)$$

where $\prod^{(1)} = -(2/3)\tau_c \nabla^2(\rho \varepsilon)$. Combining Eqs. (20) and (21), the energy equation can be obtained as

$$\partial_t(\rho \varepsilon) + \nabla \cdot (\rho \vec{V} \varepsilon) = \chi \nabla^2(\rho \varepsilon) + O(M^2 \delta T) \qquad (22)$$

Furthermore, the diffusivity χ is determined by

$$\chi = \frac{2}{3}\left(\tau_c - \frac{1}{2}\right)\delta t \qquad (23)$$

Equations (2) and (11) should both be solved using a two-step procedure, i.e., a collision step followed by a streaming step. The streaming step requires little computational effort since it simply advances the data from the neighboring lattice points, while the collision step is completely localized.

2.3 Boundary Conditions in LBM. The implementation of appropriate boundary conditions is very important when simulating backward-facing step flows. A difficulty inherent in the LBM is that the boundary conditions for the distribution function are not known beforehand. It is therefore necessary to construct suitable conditions for f_α and g_α based on the macroscopic flow variables. The simulations performed in this study consider three specific cases.

- **Case A**: The thermal boundary condition is the same as that presented by Kondoh et al. [11], i.e., the step-side lower wall downstream of the step is maintained at a constant temperature higher than that of the inlet temperature, while the remaining part of the wall is considered adiabatic.
- **Case B**: A constant high inlet temperature with the walls at a constant lower temperature.
- **Case C**: Double plates inserted at different angles of inclination with respect to the direction of flow. The thermal boundary conditions are the same as those of case B. The inserted plates are assumed to be thermally isolated such that they play no role in heat transfer, but serve only to interrupt the flow. As shown in Fig. 1, the double plates are separated by a distance of 1/3 H and are located at a distance of 5/6 H downstream from the step. In the simulations, the distance between the lee side of each plate and the walls is specified as either 1/6, 1/4, or 1/3 H, corresponding to angles of 45, 27, and 0 deg, respectively. The area of the plates remains constant at each angle.
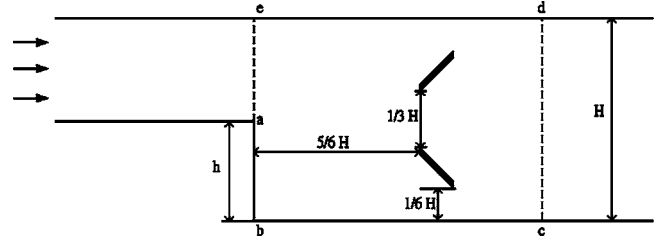
Fig. 1 Geometry of backward-facing step with double plates inclined at angle to flow direction

A uniform grid is used throughout the current numerical simulations. The convergence criteria in each run are as follows:

$$\frac{\sum_{i,j} \|\vec{V}(x_{i,j}, t + \delta t) - \vec{V}(x_{i,j}, t)\|}{\sum_{i,j} \|\vec{V}(x_{i,j}, t)\|} \leq 1.0 \times 10^{-8} \qquad (24)$$

$$\frac{\sum_{i,j} \|T(x_{i,j}, t + \delta t) - T(x_{i,j}, t)\|}{\sum_{i,j} \|T(x_{i,j}, t)\|} \leq 1.0 \times 10^{-8} \qquad (25)$$

where $\|*\|$ is the L_2 norm.

2.3.1 Boundary Conditions of Velocity Field. A constant velocity flow of 0.05 is applied at the inlet. The velocity is specifically chosen to be less than 10% of the speed of sound to avoid generating significant compressibility effects, which are known to increase with the square of the Mach number. Using the bounce-back rule of the nonequilibrium distribution proposed by Zou and He [23], the equilibrium density distribution function is computed from the pressure and the given velocity and imposed at the first lattice column. At the outlet, a fixed pressure is imposed in terms of the equilibrium distribution function. The velocity components are extrapolated upstream.

The bounce-back rule of the nonequilibrium distribution proposed by Zou and He [23] is used for the no-slip boundary condition at the wall. The density distribution function at the boundary must satisfy the following condition:

$$f_\alpha^{\text{neq}} = f_\beta^{\text{neq}} \qquad (26)$$

where e_α and e_β have opposite directions. The velocity at the wall is used when calculating f^{eq} for the boundary nodes in order to enforce the no-slip boundary condition.

2.3.2 Boundary Conditions of Temperature Field. For the thermal problem, the thermal energy distribution function at the boundary satisfies

$$g_\alpha^{\text{neq}} - e_\alpha^2 f_\alpha^{\text{neq}} = -(g_\beta^{\text{neq}} - e_\beta^2 f_\beta^{\text{neq}}) \qquad (27)$$

The temperature of the wall is used when calculating g^{eq} for the boundary nodes in order to satisfy the given temperature. This study imposes Neumann and Dirichlet boundary conditions for the temperature field. For the Dirichlet type condition, the given temperature is applied directly on the boundary. Meanwhile, the Neumann type condition (adiabatic or constant heat flux) is transferred to the Dirichlet type condition through the conventional second-order finite difference approximation in order to obtain the temperature at the boundary [24]. When the temperature gradient is given, the temperature at the boundary can be calculated by

$$\left.\frac{\partial T}{\partial y}\right|_{x,1} = \frac{-3T_{x,1} + 4T_{x,2} - T_{x,3}}{2\Delta y} \qquad (28)$$

Equation (28) yields the corresponding Dirichlet type boundary condition for both the adiabatic and constant heat flux boundary conditions.

Fig. 2 Dimensionless velocity and temperature profiles for porous plate flow

2.4 Validation of Simplified Thermal Energy Distribution Model.

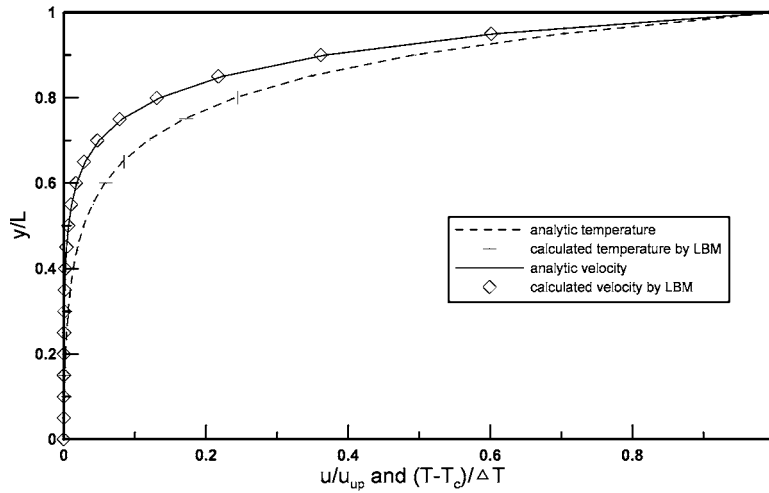To validate the proposed thermal energy distribution model, this study considers the porous plate with a temperature gradient analyzed previously by Peng et al. [22]. The porous plate problem involves a channel flow in which the upper cool plate moves with a constant velocity while a constant normal flow of fluid is injected through the bottom warm plate and withdrawn at the same rate from the upper plate. The analytical solution of the steady state velocity field is given by

$$u = u_{\mathrm{up}} \left(\frac{e^{(\mathrm{Re}\, y/L)} - 1}{e^{\mathrm{Re}} - 1} \right) \quad (29)$$

where u_{up} is the velocity of the upper plate, Re is the Reynolds number corresponding to the injection velocity, and L is the channel width. The temperature profile in the steady state is expressed as

$$T = T_c + \Delta T \left(\frac{e^{(\mathrm{Pr}\, \mathrm{Re}\, y/L)} - 1}{e^{\mathrm{Pr}\, \mathrm{Re}} - 1} \right) \quad (30)$$

where $\Delta T = T_h - T_c$ is the difference between the temperature of the hot bottom plate (i.e., T_h) and that of the cool upper plate (i.e., T_c).

In the current verification simulation, the Prandtl number is set to 0.71 and the Reynolds number is Re=10. The simulated velocity and temperature profiles are presented in Fig. 2. It is apparent that a good agreement exists between the current results and the analytical solutions. Therefore, the verification results confirm that the developed thermal model can be applied to simulate the current backward-facing step flow problem.

2.5 Boundary Condition Treatment of Double Plates Aligned at Angle.

This study applies the boundary treatment proposed by Guo et al. [9] to the double plates inserted in the channel downstream of the backward step. Basically, this boundary treatment decomposes the distribution function f_α at a wall node into equilibrium and nonequilibrium parts. The nonequilibrium part is approximated by that of the neighboring fluid node along the link, while the equilibrium part is determined by an imaginary equilibrium distribution where the boundary condition is enforced. As shown in Fig. 3, the link between the fluid node $\vec{x}_f$ and the wall node $\vec{x}_w$ intersects the physical boundary at $\vec{x}_b$. The fraction of the intersected link in the fluid region is defined as

$$\Delta = (|\vec{x}_f - \vec{x}_b|)/(|\vec{x}_f - \vec{x}_w|) \quad (31)$$

In order to specify $f_\alpha(\vec{x}_w,t)$, it is necessary to decompose $f_\alpha(\vec{x}_w,t)$ into $f_\alpha^{\mathrm{eq}}(\vec{x}_w,t)$ and $f_\alpha^{\mathrm{ne}}(\vec{x}_w,t)$. Rather than using the origi-

nal definition of the equilibrium density distribution given in Eq. (3), the equilibrium part $f_\alpha^{\mathrm{eq}}(\vec{x}_w,t)$ can be defined approximately as

$$f_\alpha^{\mathrm{eq}}(\vec{x}_w,t) = \mathrm{w}_\alpha \rho_w \left[1 + \frac{3\vec{e}_\alpha \cdot \vec{V}_w}{c^2} + \frac{9}{2}\frac{(\vec{e}_\alpha \cdot \vec{V}_w)^2}{c^4} - \frac{3}{2}\frac{\vec{V}_w^2}{c^2} \right] \quad (32)$$

where $\vec{V}_w$ is an approximation of $\vec{V}_w = \vec{V}(\vec{x}_w)$ and $\rho_w \equiv \rho(\vec{x}_f)$ is an approximation of $\rho_w = \rho(\vec{x}_w)$. It is reasonable to determine $\vec{V}_w$ via linear extrapolation using either $\vec{V}_{w1} = (\vec{V}_b + (\Delta-1)\vec{V}_f)/\Delta$ or $\vec{V}_{w2} = (2\vec{V}_b + (\Delta-1)\vec{V}_{ff})/(1+\Delta)$ and $\vec{V}_w = \vec{V}_{w1} = (\vec{V}_b + (\Delta-1)\vec{V}_f)/\Delta$ for $\Delta \geq 0.75$ and $\vec{V}_w = \Delta\vec{V}_{w1} + (1-\Delta)\vec{V}_{w2}$ for $\Delta < 0.75$. Guo et al. [9] proposed the nonequilibrium part as $f_\alpha^{ne}(\vec{x}_w,t) = f_\alpha^{ne}(\vec{x}_f,t)$ for $\Delta \geq 0.75$ and $f_\alpha^{ne}(\vec{x}_w,t) = \Delta f_\alpha^{ne}(\vec{x}_f,t) + (1-\Delta)f_\alpha^{ne}(\vec{x}_{ff},t)$ for $\Delta < 0.75$. Finally, the post-collision distribution function $f_\alpha^+(\vec{x}_w,t)$ can be obtained as

$$f_\alpha^+(\vec{x}_w,t) = f_\alpha^{\mathrm{eq}}(\vec{x}_w,t) + (1 - 1/\tau_v)f_\alpha^{\mathrm{ne}}(\vec{x}_w,t) \quad (33)$$

The thermal boundary condition of the double plates is adiabatic. Based on the fraction of the intersected link in the fluid region Δ, the temperature of $\vec{x}_f$ can be approximated by interpolation of the neighboring points.
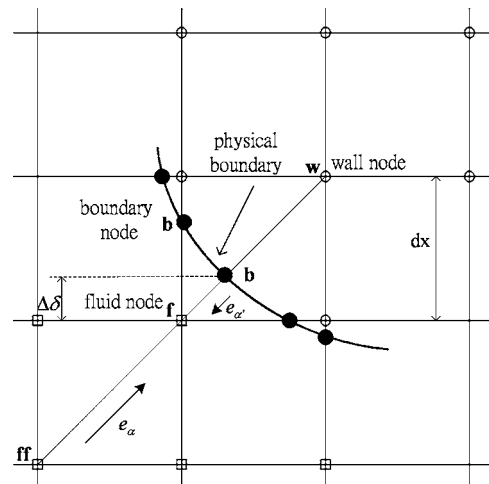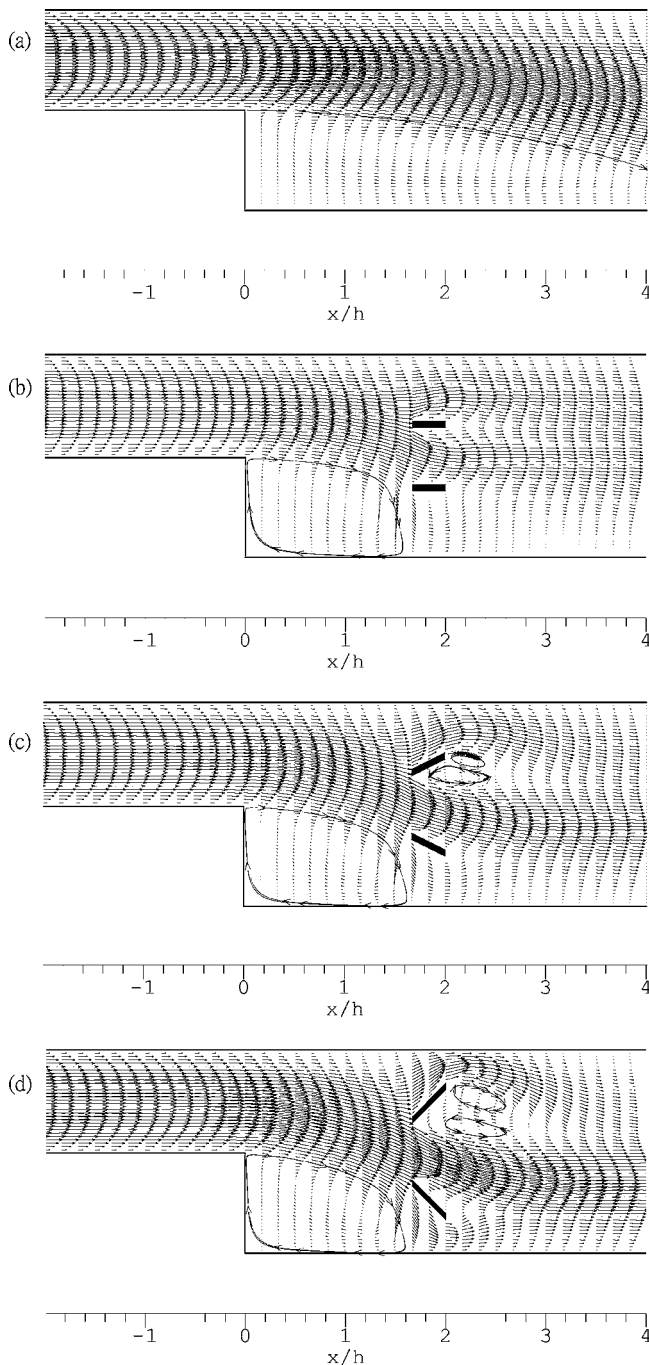

Fig. 3 Curved boundary and lattice nodes

(a)

(b)

(c)

(d)

Fig. 4   Velocity field (ER=2, Re=170) for (*a*) no obstacle, (*b*) plates at 0 deg, (*c*) plates at 27 deg, and (*d*) plates at 45 deg

3   Results and Discussion

3.1   Overview of Velocity Field. The simulations in the current study were performed using a uniform rectangular mesh (801∗61). The channel expansion ratio (ER) was defined as H/h (see Fig. 1) and the Reynolds number (Re) of the flow as $4U(H-h)/3v$, where U is the maximum velocity in the inlet. The velocity vector plots in Fig. 4(*a*), corresponding to the case where the double plates are not present in the flow, provide an overall view of the flow for ER=2 and Re=170. As expected in a backward-facing step flow, a recirculation zone is formed behind the step. The location of the reattachment point is found to be X_R/h=3.18 and 5.5 at Reynolds numbers of Re=100 and 200,
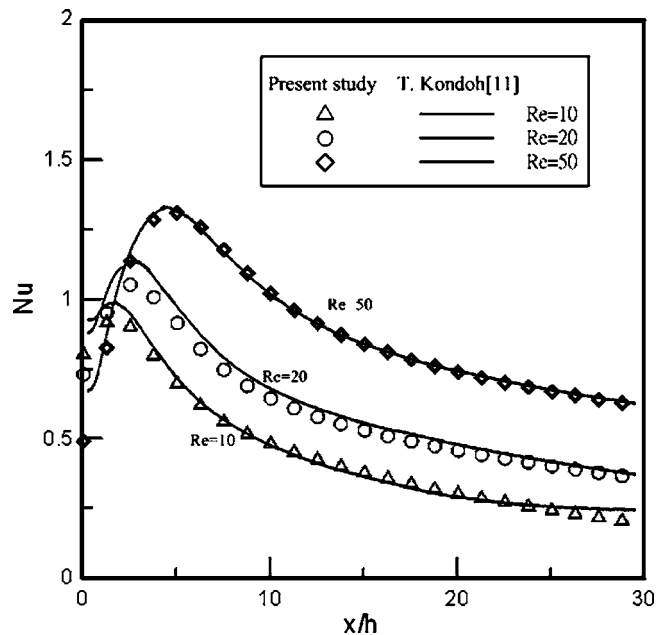
Fig. 5   Comparison of present Nusselt number results with those of Kondoh et al. [11] for Case A (ER=1.5, Pr=0.7)

respectively. These results differ from the experimental findings of Armaly et al. [25], who reported reattachment locations of X_R/h =3.1 and 5.4 at Re=100 and 200, respectively. The discrepancy between the two sets of results can be attributed to the slight difference in the geometric configuration of the flow. However, the present numerical results are similar to those of He and Luo [26], i.e., X_R/h=3.15 at Re=100. As expected, with increasing Reynolds number the length of flow redevelopment downstream of the step increased.

Figures 4(*b*)–4(*d*) show the velocity vector fields when double plates are inserted into the channel and inclined at angles of 0, 27, and 45 deg, respectively, to the flow direction. It is apparent that the introduction of the double plates causes a narrowing of the main recirculation region as a result of the interruption within the flow. The presence of two small recirculation zones behind the upper inclined plate is noted in Figs. 4(*c*) and 4(*d*). As the inclination angle of the double plates increases, the change in the velocity vectors becomes more significant, i.e., the effect of the double plates becomes more pronounced. The overall flow structure is in good agreement with that predicted intuitively.

3.2   Overview of Temperature Field. Case A imposes the same boundary condition as that considered by Kondoh et al. [11]. Figure 5 shows the influence of the Reynolds number on the local heat transfer distribution on the heat transfer surface for conditions of ER=1.5 and Pr=0.7. It can be seen that as the Reynolds number increases, the peak value of Nu not only increases, but also moves downstream. The downstream shift of this peak value is most likely related to a corresponding movement of the flow attachment length. From Fig. 5, it is clear that the present numerical data are in good agreement with the results of Kondoh [11] other than in the vicinity of the step.

Figure 6 shows the influence of the Reynolds number on the local heat transfer distribution on the heat transfer surface for case B (a constant temperature wall boundary condition). Although the results display a broadly similar trend to those shown in Fig. 5, the results obtained for the Nusselt number are somewhat different near the step because of the different thermal boundary conditions applied. Due to the different thermal boundary condition and Rey-
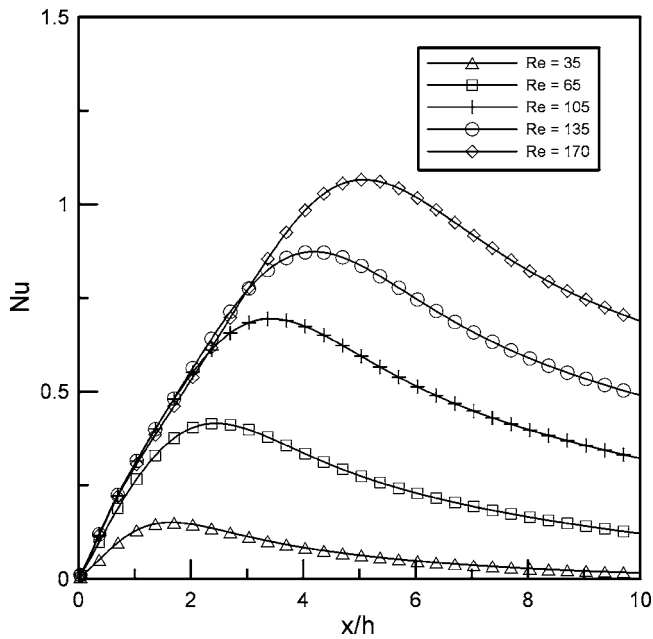
Fig. 6   Effect of Reynolds number on Nusselt number for Case B (ER=2, Pr=0.7)
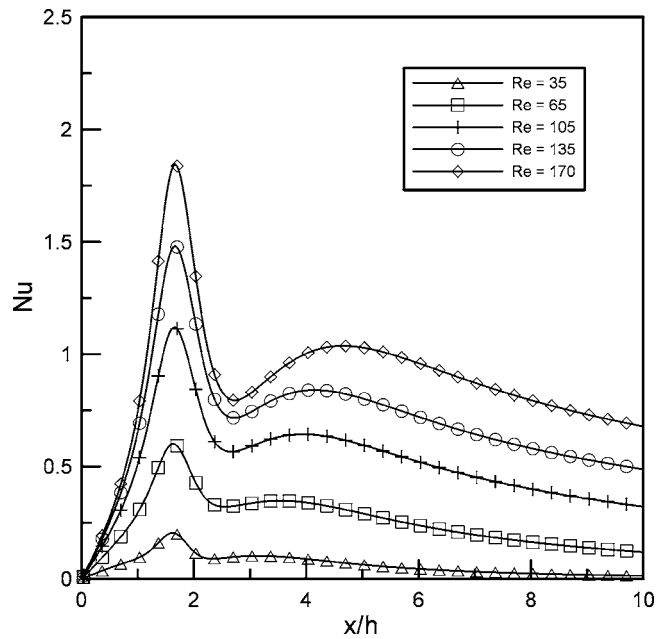
Fig. 8   Effect of Reynolds number on Nusselt number for case C with plates at 27 deg (ER=2, Pr=0.7)

nolds number definition, the corresponding Nusselt number is also different. But the movement of the peak values of the Nusselt number still related to the movement of the flow reattachment length.

Figure 7 shows the influence of the Reynolds number on the local heat transfer distribution for case C, with double plates inserted in the flow and positioned parallel to the flow direction. It can be seen that the local Nu values are higher than in the case when no obstacles are present in the flow. In other words, the convective heat transfer performance is improved. The presence of the double plates in the flow changes the velocity field and compresses the thermal boundary layer, which enhances the heat transfer. Figure 8 shows the influence of the Reynolds number on

the local heat transfer distribution when the double plates are inclined at an angle of 27 deg. Although the convective heat transfer performance is improved compared to the case where the double plates are absent, there is little significant difference between these results and those of Fig. 7. Figure 9 presents the corresponding results when the plates are inclined at an angle of 45 deg. It is apparent that the local Nu distribution is significantly improved compared to the cases where the plates are inclined at angles of either 0 deg or 27 deg to the flow direction. The enhancement effect is particularly evident at higher Reynolds numbers.
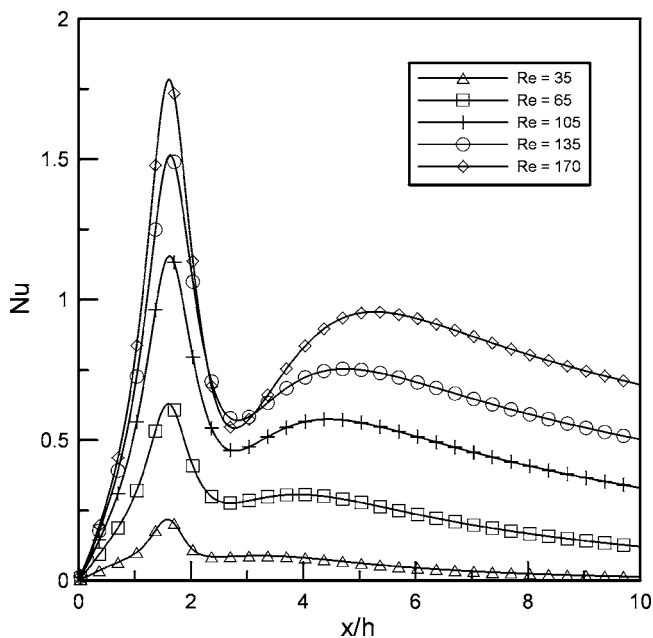

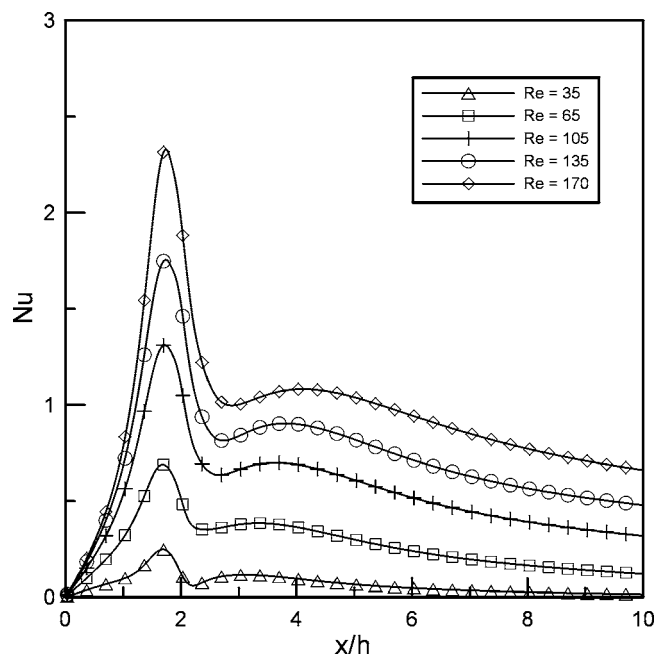Fig. 7   Effect of Reynolds number on Nusselt number for case C with plates at 0 deg (ER=2, Pr=0.7)

Fig. 9   Effect of Reynolds number on Nusselt number for case C with plates at 45 deg (ER=2, Pr=0.7)
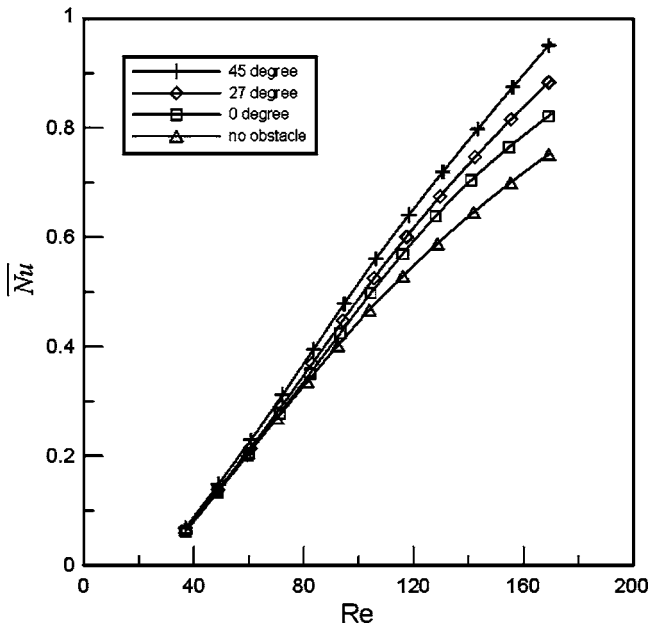
Fig. 10 Effect of Reynolds number on average Nusselt number with and without inclined double plates

Fig. 11 Effect of Reynolds number on dimensionless Int value with and without inclined double plates

3.3 Numerical Verification of Field Synergy Principle. Figure 10 shows the variation of the average Nusselt number with the Reynolds number with and without the insertion of the double plates. It is observed that the double plates enhance the thermal performance, particularly when the Reynolds number is high. From inspection, the thermal performance is found to increase by approximately 33% at Re=170 when plates are inserted in the downstream flow and inclined at an angle of 45 deg. Furthermore, it can be seen that the improvement in the convective heat transfer increases as the angle of inclination of the double plates increases.

Three mechanisms are responsible for enhancing the single-phase convective heat transfer, namely, an increased flow interruption, a reduced thermal boundary layer thickness, and an increased velocity gradient near the solid wall [14]. These three mechanisms lead to a reduction of the intersection angle between the velocity vector and the temperature gradient. This section of the paper compares cases B and C to illustrate the inherent relation between the field synergy principles and to demonstrate that increasing the flow interruption enhances the single phase convective heat transfer.

The steady state 2D incompressible energy equation of fluid flow and heat transfer over the backward-facing step is given by

$$\rho c_P \left(u \frac{\partial T}{\partial x} + v \frac{\partial T}{\partial y} \right) = \frac{\partial}{\partial x} \left(k \frac{\partial T}{\partial x} \right) + \frac{\partial}{\partial y} \left(k \frac{\partial T}{\partial y} \right) \qquad (34)$$

The definition of the Int value is given in Eq. (35) below and represents the energy transferred by convection. Equation (35) implies that the convective heat transfer can be enhanced by increasing the value of the integral of the convection term (i.e., the heat source) over the computation domain. It is also clear that an improved synergy will increase the integration value, i.e., enhance the heat transfer.

$$\text{Int} = \int_\Omega \rho c_P (\vec{V} \cdot \nabla T) dx dy \qquad (35)$$

After integrating both sides of Eq. (34) over the computation domain, Tao et al. [17] applied the Gauss theorem to reduce the integral dimension of the right-hand side (RHS) of Eq. (34). The reduced version of Eq. (34) is equal to the RHS of Eq. (35). Therefore
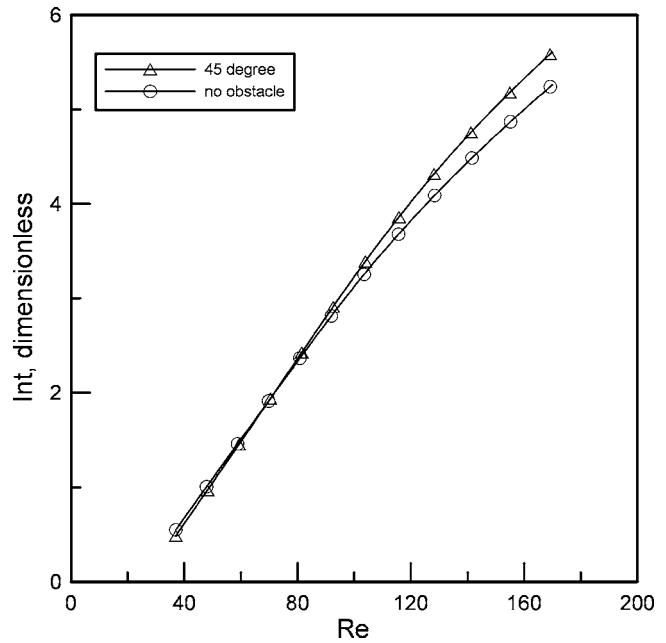
$$\iint_{\Omega=abcdea} \rho c_P (\vec{V} \cdot \nabla T) dx dy = \int_{abc} \vec{n} \cdot k \nabla T dS + \int_{cd} \vec{n} \cdot k \nabla T dS$$
$$+ \int_{de} \vec{n} \cdot k \nabla T dS + \int_{ea} \vec{n} \cdot k \nabla T dS$$

$$(36)$$

where $\vec{n}$ represents the outward normal along each boundary and dS is the length differential of the boundary. From Eq. (36), the Int value over the computation domain can be easily obtained. Figure 11 shows the variation of the nondimensional Int value with the Reynolds number with and without the insertion of double plates inclined at an angle of 45 deg. A higher Int value implies that the integral value of the convection term is higher, and hence the heat transfer is enhanced. The trends of Fig. 11 resemble those of Fig. 10. It can be seen that the Int value rises as Re increases and increases when double plates are inserted downstream of the backward step, particularly at higher Reynolds numbers. Note that the nondimensional Int values for plate inclination angles of 0 deg and 27 deg are deliberately not shown in Fig. 11 since the results are very similar. In general, it is found that the Int values decrease as the angle of inclination decreases, and have a minimum value when the double plates are not present in the flow.

Equation (37) provides a general insight into convective heat transfer. This equation suggests that the heat transfer can be enhanced in one of three ways, namely, increasing the Reynolds and Prandtl numbers, increasing the fullness of the dimensionless velocity and temperature profiles, and increasing the included angle between the dimensionless velocity and temperature gradient vectors.

$$\text{Re Pr} \int (\vec{V} \cdot \nabla T) dy = \text{Nu} \qquad (37)$$

$$\vec{V} \cdot \nabla T = |\vec{V}||\nabla T| \cos \theta \qquad (38)$$

where θ_m is the average intersection angle between the velocity vector and the temperature gradient in the computation domain. If the local value of θ is greater than 90 deg, its value is taken as
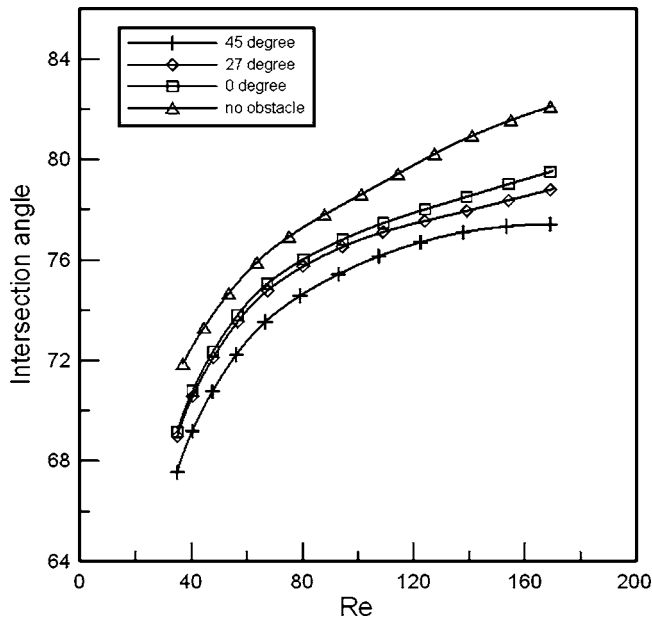
Fig. 12 Effect of Reynolds number on average intersection angle with and without inclined double plates

(180 deg-θ) when added to the summation of the intersection angle [16]. Figure 12 shows the variation of the average intersection angle with Re both with and without the insertion of double plates. An enhanced synergy is obtained by decreasing the intersection angle between the velocity vector and the temperature gradient. From Fig. 12, it is seen that this can be achieved by increasing the interruption within the flow. As the intersection angle reduces by approximately 5 deg, the average Nusselt number increases by approximately 33% for Reynolds numbers below Re=170. In the absence of the field synergy principle, the only indicator of the heat transfer performance is the Nusselt number. However, the synergy principle provides an alternative index for evaluating the heat transfer performance. In theory, the optimal heat transfer is obtained at an intersection angle of 0 deg. In practice, the intersection angle is determined by the geometry of the channel and the boundary conditions imposed. So the field synergy principle is a new direction to assess the heat transfer performance.

4 Conclusions

This study has simulated low Reynolds number backward-facing step flows using a single-relaxation-time model based on the parallel lattice LBM. The numerical results obtained for the velocity and temperature fields are in good agreement with the published experimental and numerical results. The simplified thermal model applied in this study is therefore an appropriate LBM thermal model for performing accurate simulations of incompressible thermal fluid flows. The results have shown that inserting double plates inclined at an angle to the flow direction enhances the convective heat transfer as a result of flow interruption and thermal boundary layer compression effects. The results have indicated that increasing the inclination angle of the double plates is beneficial in enhancing the heat transfer and leads to a reduction in the intersection angle between the velocity vector and the temperature gradient.

Nomenclature

c = lattice streaming speed
c_s = speed of sound
c_p = specific heat capacity
g_α = energy distribution function
g_α^{eq} = equilibrium distribution function for g_α
H = channel width downstream of step
h = step height
Int = integral, Int=$\int_\Omega \rho c_P (\vec{V} \cdot \nabla T) dx dy$
k = thermal conductivity
Nu = Nusselt number
$\overline{\text{Nu}}$ = average Nusselt number
Pr = Prandtl number
p = pressure
Re = Reynolds number
T = temperature
U = maximum velocity in inlet
$\vec{V}$ = velocity vector
X_R = reattachment location
ER = channel expansion ratio, H/h
f_α = density distribution function
f_α^{eq} = equilibrium distribution function for f_α

Subscripts
b = boundary
c = cool
f = fluid
h = hot
up = upper
w = wall
m = mean

Greek symbols
τ_v = relaxation time for f_α
τ_c = relaxation time for g_α
ε = internal energy
χ = diffusivity
Ω = integral area
ρ = density
υ = kinematic viscosity
δ = small parameter
δx = lattice spacing
δt = time step
θ = intersection angle between velocity and temperature gradient

References

[1] Chen, S., and Doolen, G. D., 1998, "Lattice Boltzmann Method for Fluid Flows," Annu. Rev. Fluid Mech., **30**, pp. 329–364.
[2] McNamara, G., and Zanetti, G., 1988, "Use of the Boltzmann Equation to Simulate Lattice-Gas Automata, Phys. Rev. Lett., **61**, pp. 2332–2335.
[3] Higuera, F., and Jimenez, J., 1989, "Boltzmann Approach to Lattice Gas Simulations," Europhys. Lett., **9**, pp. 663–668.
[4] Higuera, F., Succi, S., and Benzi, R., 1989, "Lattics Gas Dynamics With Enhanced Collisions," Europhys. Lett., **9**, pp. 345–349.
[5] Bhatnagar, P. L., Gross, E. P., and Krook, M., 1954, "A Model for Collision Process in Gases. I. Small Amplitude Processes in Charged and Neutral One-Component System," Phys. Rev., **94**, pp. 511–521.
[6] Chen, H., Chen, S., and Matthaeus, W. H., 1992, "Recovery of the Navier-Stokes Equation Using a Lattice Boltzmann Method," Phys. Rev. A, **45**, pp. R5339–R5342.
[7] Filippova, O., and Hanel, D., 1998, "Grid Refinement for Lattice-BGK Models," J. Comput. Phys., **147**, pp. 219–228.
[8] Mei, R., Luo, L.-S., and Shyy, W., 1999, "An Accurate Curved Boundary Treatment in the Lattice Boltzmann Method," J. Comput. Phys., **155**, pp. 307–330.
[9] Guo, Z., Zheng, C., and Shi, B., 2002, "An Extrapolation Method for Boundary Conditions in Lattice Boltzmann Method," Phys. Fluids, **14**, pp. 2007–2010.
[10] Chen, S., Martinez, D., and Mei, R., 1996, "On Boundary Conditions in Lattice Boltzmann Methods," Phys. Fluids, **8**, pp. 2527–2536.
[11] Kondoh, T., Nagano, Y., and Tsuji, T., 1993, "Computational Study of Laminar Heat Transfer Downstream of a Backward-Facing Step," Int. J. Heat Mass Transfer, **36**, pp. 577–591.
[12] Aung, W., 1983, "An Experimental Study of Laminar Heat Transfer Downstream of Backstep," J. Heat Transfer, **105**, pp. 823–829.
[13] Hall, E. J., and Pletcher, R. H., 1985, "An Application of a Viscous-Inviscid Interaction Procedure to Predict Separated Flows With Heat Transfer," J. Heat Transfer, **107**, pp. 557–563.

[14] Guo, Z. Y., Li, D. Y., and Wang, B. X., 1998, "A Novel Concept for Convective Heat Transfer Enhancement," Int. J. Heat Mass Transfer, **41**, pp. 2221–2225.

[15] Wang, S., Li, Z. X., and Guo, Z. Y., 1998, "Novel Concept and Device of Heat Transfer Augmentation," *Proceeding of 11th IHTC*, Korea, Vol. 5, pp. 405–408.

[16] Tao, W. Q., He, Y. L., Wang, Q. W., Qu, Z. G., and Song, F. Q., 2002, "A Unified Analysis on Enhancing Single Phase Convective Heat Transfer With Field Synergy Principle," Int. J. Heat Mass Transfer, **45**, pp. 4871–4879.

[17] Tao, W. Q., Guo, Z. Y., and Wang, B. X., 2002, "Field Synergy Principle for Enhancing Convective Heat Transfer—Its Extension and Numerical Verifications, Int. J. Heat Mass Transfer, **45**, pp. 3849–3856.

[18] Hou, S., Zou, Q., Chen, S., Doolen, G. D., and Cogley, A. C., 1995, "Simulation of Cavity Flow by the Lattice Boltzmann Method," J. Comput. Phys., **118**, pp. 329–347.

[19] Alexander, F. J., Chen, S., and Sterling, J. D., 1993, "Lattice Boltzmann Thermohydrodynamics," Phys. Rev. E, **47**, pp. R2249–R2252.

[20] Shan, X., 1997, "Solution of Rayleigh-Benard Convection Using a Lattice Boltzmann Method, Phys. Rev. E, **55**, pp. 2780–2788.

[21] He, X., Chen, S., and Doolen, G. D., 1998, "A Novel Thermal Model for the Lattice Boltzmann Method in Incompressible Limit, J. Comput. Phys., **146**, pp. 282–300.

[22] Peng, Y., Shu, C., and Chew, Y. T., 2003, "Simplified Thermal Lattice Boltzmann Model for Incompressible Thermal Flows," Phys. Rev. E, **68**, p. 026701.

[23] Zou, Q., and He, X., 1997, "On Pressure and Velocity Boundary Conditions for the Lattice Boltzmann BGK Model," Phys. Fluids, **9**, pp. 1591–1598.

[24] Shu, C., Peng, Y., and Chew, Y. T., 2002, "Simulation of Natural Convection in a Square Cavity by Taylor Series Expansion and Least Square-Based Lattice Boltzmann Method," Int. J. Mod. Phys. C, **13**, pp. 1399–1414.

[25] Armaly, B. F., Durst, F., Pereira, J. C. F., and Schonung, B., 1983, "Experimental and Theoretical Investigation of Backward-Facing Step Flow," J. Fluid Mech., **127**, pp. 473–496.

[26] He, X., and Luo, L.-S., 1997, "A Prior Derivation of the Lattice Boltzmann Equation," Phys. Rev. E, **55**, pp. R6333–R6336.

Thermal Entrance Heat Transfer of an Adiabatically Prepared Fluid With Viscous Dissipation in a Tube With Isothermal Wall

A. Barletta[1]
Mem. ASME
Dipartimento di Ingegneria Energetica,
Nucleare e del Controllo Ambientale (DIENCA),
Università di Bologna,
Via dei Colli 16,
I-40136 Bologna, Italy
e-mail: antonio.barletta@mail.ing.unibo.it

E. Magyari
Chair of Physics of Buildings
Institute of Building Technology,
Swiss Federal Institute of Technology (ETH),
Zürich, CH-8093 Zürich, Switzerland

Forced convection in the thermal entrance region of a circular duct is analyzed. Viscous dissipation effects are taken into account under conditions of laminar hydrodynamically developed flow. The duct wall is assumed to be isothermal in the region downstream of the entrance cross section. The prescription of the initial condition at the entrance cross section is coherent with the assumption of a non-negligible viscous heating in the whole duct. The special case of an adiabatic-wall preparation of the fluid in the upstream region is considered. This adiabatic preparation results in a non-uniform entrance temperature distribution. The governing equations are solved analytically by separation of variables. Important differences are pointed out in the comparison of the solution with those available in the literature, which are based on the assumption of a uniform temperature distribution in the entrance cross section. [DOI: 10.1115/1.2352784]

Keywords: forced convection, duct flow, Graetz problem, viscous dissipation, analytical methods

1 Introduction

The thermal entrance heat transfer in a circular duct with hydrodynamically developed laminar flow has been the subject of several investigations. After the pioneering works by Graetz [1,2] and Nusselt [3], many papers on this subject have been published especially in the second half of the last century. Reviews of the fundamental achievements in this field are available in Refs. [4,5].

The original formulation of the Graetz-Nusselt problem deals with a prescribed uniform wall temperature, under the assumption of negligible effects of viscous dissipation and axial heat conduction in the fluid. Important improvements of the Graetz-Nusselt solution include: the study of prescribed uniform or non-uniform wall heat flux [6–8]; the analysis of non-Newtonian flows [9,10]; the introduction of the effects of viscous dissipation and axial heat conduction in the fluid [9–16]. The latter effects are often neglected in most studies of forced convection in ducts, even if they may result to be important in some technical cases. As is well known, the effect of viscous dissipation becomes non-negligible when fluids with low thermal conductivity and high viscosity flow in a duct with small diameter and low wall heat flux. On the other hand, the effect of axial heat conduction in the fluid becomes important for fluids with high thermal conductivity, e.g., for liquid metals. Technical cases such that both the effects of viscous dissipation and axial heat conduction cannot be neglected are rare. Indeed, by comparing the properties of unused engine oil with those of mercury at a temperature of 300 K, one infers that the ratio between the thermal conductivity k of oil and that of mercury is approximately 0.02, while the ratio between the dynamic viscosity coefficient μ of oil and that of mercury is approximately 300. Since the typical temperature scale of the viscous heating effect is $\mu u_m^2/k$, where u_m is the mean velocity in a duct section,

one can estimate that the ratio between the viscous heating effect of oil and that of mercury, for any prescribed value of u_m, is 1.5 $\times 10^4$.

The aim of the present paper is to show how a physically conceivable assignment of the initial condition for the temperature at the entrance cross section can be important in the evaluation of the temperature field and Nusselt number throughout the downstream thermal entrance region. The importance of a physically coherent prescription of the entrance condition at a given axial station has been pointed out by several authors, when dealing with a non-negligible axial heat conduction effect in the fluid [9]. In that case, the prescription of the entrance temperature and axial heat flux at some axial station must take into account the elliptic nature of the local energy balance equation, which can induce feedback temperature changes also in the upstream region. In the present paper, the effect of axial heat conduction in the fluid will be neglected, while the effect of viscous dissipation will be taken into account. It will be pointed out that also the effect of viscous dissipation poses some restrictions in the assignment of the initial condition at the entrance cross section. Being the local energy balance equation parabolic in this case, these restrictions are not due to some feedback of the temperature field in the upstream region, but to the role played by viscous dissipation in the preparation of the fluid upstream of the entrance region.

In the present paper, the analysis of the thermal entrance region will be performed for a circular duct with a uniform wall temperature. An adiabatic upstream preparation of the fluid which results in a non-uniform temperature distribution in the entrance cross section will be considered. A comparison with the solution that is obtained by employing a uniform entrance temperature distribution will be performed.

2 Governing Equations

Let us consider hydrodynamically developed laminar flow in a circular duct. A sketch of the duct and of the thermal boundary conditions is given in Fig. 1. The hydrodynamically developed velocity field is given by the Poiseuille profile
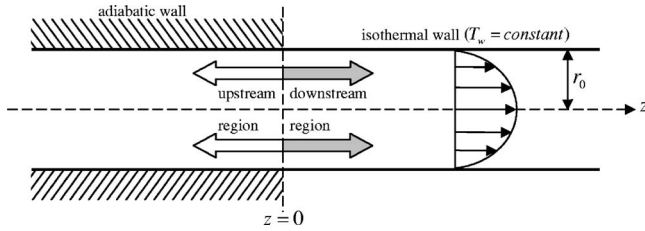

Fig. 1 Circular duct and thermal boundary conditions

$$u(r) = 2u_m\left(1 - \frac{r^2}{r_0^2}\right) \tag{1}$$

Under the assumption of a negligible axial heat conduction in the fluid, the energy balance equation can be written as

$$\rho c_p u \frac{\partial T}{\partial z} = \frac{k}{r}\frac{\partial}{\partial r}\left(r\frac{\partial T}{\partial r}\right) + \mu\left(\frac{du}{dr}\right)^2 \tag{2}$$

The second term on the right hand side of Eq. (2) represents the viscous dissipation term and can be easily evaluated from Eq. (1), so that Eq. (2) can be rewritten as

$$\rho c_p u \frac{\partial T}{\partial z} = \frac{k}{r}\frac{\partial}{\partial r}\left(r\frac{\partial T}{\partial r}\right) + \frac{16\mu u_m^2}{r_0^4}r^2 \tag{3}$$

2.1 Upstream Region ($z<0$). In the region $z<0$, the fluid is prepared for the downstream thermal entrance region ($z>0$). The preparation includes the full development of the velocity field, in order to get the Poiseuille profile, and the thermal adjustment of the temperature field, in order to obtain a given temperature profile in $z=0$. This temperature profile represents the initial condition to be assigned to the parabolic partial differential Eq. (3). Even if, from a mathematical viewpoint, any initial condition can be prescribed in $z=0$, it is not possible, in practice, to adjust a thermal preparation of the fluid that produces an arbitrary temperature profile in the entrance cross section. In fact, the thermal preparation of the fluid can be performed by acting on the wall conditions assigned in the upstream region, since no internal stirring of the fluid can be introduced without perturbing the fully developed velocity field. In this sense, the usual initial condition of a uniform thermal entrance temperature can hardly be prepared in a fluid with non-negligible viscous dissipation. Undoubtedly, the internal generation of heat tends to produce a non-uniform temperature distribution whatever are the wall boundary conditions prescribed.

In this study, a simple thermal preparation of the fluid will be considered: a thermal insulation of the duct wall in the upstream region. By a sufficient length of the tube in the upstream direction, one can obtain a fully developed temperature profile in the vicinity of $z=0$. In the presence of an adiabatic boundary condition, the fully developed temperature profile can be easily obtained by solving Eq. (3) under the assumption of a constant axial change of temperature

$$\frac{\partial T}{\partial z} = \text{constant} \tag{4}$$

Under this assumption, the solution of Eq. (3) which fulfills the boundary condition

$$\left.\frac{\partial T}{\partial r}\right|_{r=r_0} = 0 \tag{5}$$

is

$$T(r,z) = T(r_0,z) - \frac{2\mu u_m^2}{k}\left(\frac{r^4}{r_0^4} - 2\frac{r^2}{r_0^2} + 1\right), \quad z \le 0 \tag{6}$$

In general, the wall temperature $T(r_0,z)$ in the upstream region does not need to match, for $z\to 0^-$, the uniform wall temperature value T_w prescribed in the downstream region. A discontinuity in the wall temperature at $z=0$ is nothing but a rough model of what happens in a real experimental apparatus. Indeed, in a real apparatus neither a perfect thermal insulation nor a perfectly isothermal wall is possible. These imperfections of the real boundary conditions result in a smooth change of the wall temperature when crossing the entrance cross section $z=0$. The characteristics of this smooth change strongly depend on the flow regime and on the thermal properties of the solid wall. The step change in the wall temperature is the simplest way to model the real experimental behavior: it is the same model adopted when viscous dissipation is neglected and the wall temperature is assumed to have an abrupt transition from an initial value T_e to a value T_w. According to this approximation, the prepared initial condition at $z=0$ can be written as

$$T(r,0) = T_e - \frac{2\mu u_m^2}{k}\left(\frac{r^4}{r_0^4} - 2\frac{r^2}{r_0^2} + 1\right) \tag{7}$$

where, in general, $T_e \ne T_w$.

2.2 Downstream Region ($z>0$). In the region $z>0$, the development of the temperature field takes place. The evolution of the temperature profile prescribed at $z=0$ can be studied by solving Eq. (3) with the initial condition expressed by Eq. (7) and the boundary condition

$$T(r_0,z) = T_w, \quad z>0 \tag{8}$$

Equations (3), (7), and (8) will be solved analytically in the next section, by utilizing the standard separation of variables method.

3 Analytical Solution

In the analysis of the thermal entrance region, $z>0$, the temperature field can be expressed as

$$T(r,z) = T_s(r) + \Theta(r,z) \tag{9}$$

where $T_s(r)$ is a particular solution of the equation

$$\frac{1}{r}\frac{d}{dr}\left[r\frac{dT_s(r)}{dr}\right] = -\frac{16\mu u_m^2}{kr_0^4}r^2 \tag{10}$$

and $\Theta(r,z)$ is solution of the homogeneous partial differential equation

$$u(r)\frac{\partial\Theta(r,z)}{\partial z} = \frac{\alpha}{r}\frac{\partial}{\partial r}\left[r\frac{\partial\Theta(r,z)}{\partial r}\right] \tag{11}$$

One can conveniently choose the particular solution $T_s(r)$, so that it matches at $r=r_0$ the wall temperature value T_w,

$$T_s(r) = T_w + \frac{\mu u_m^2}{k}\left(1 - \frac{r^4}{r_0^4}\right) \tag{12}$$

As a consequence, Eq. (9), yields

$$T(r,z) = T_w + \frac{\mu u_m^2}{k}\left(1 - \frac{r^4}{r_0^4}\right) + \Theta(r,z) \tag{13}$$

The boundary and initial conditions for $\Theta(r,z)$ can be easily determined by employing Eqs. (7), (8), and (13),

$$\Theta(r_0,z) = 0 \tag{14}$$

$$\Theta(r,0) = T_e - T_w - \frac{\mu u_m^2}{k}\left(\frac{r^4}{r_0^4} - 4\frac{r^2}{r_0^2} + 3\right) \tag{15}$$

Let us define the dimensionless coordinates

$$\tilde{r} = \frac{r}{D}, \quad \tilde{z} = \frac{z}{PeD} \tag{16}$$

Then, by performing separation of variables in Eq. (11), one obtains

$$\Theta(r,z) = \frac{\mu u_m^2}{k} \sum_{n=0}^{\infty} \Xi_n R_n(\tilde{r}) \exp\left(-\frac{\beta_n^2}{2}\tilde{z}\right) \tag{17}$$

The eigenfunctions $R_n(\tilde{r})$ are solutions of the eigenvalue equation

$$\tilde{r}R_n''(\tilde{r}) + R_n'(\tilde{r}) + \beta_n^2\tilde{r}(1 - 4\tilde{r}^2)R_n(\tilde{r}) = 0 \tag{18}$$

where a prime denotes derivative of a function with respect to its argument. The boundary conditions fulfilled by the eigenfunctions are due to Eq. (14) and to the requirement that no singularity occurs at $\tilde{r}=0$, namely

$$R_n(1/2) = 0 \tag{19}$$

$$R_n'(0) = 0 \tag{20}$$

The eigenvalue problem expressed by Eqs. (18)–(20) is a Sturm-Liouville problem. Therefore, the orthogonality relation

$$\int_0^{1/2} (1 - 4\tilde{r}^2)\tilde{r}R_m(\tilde{r})R_n(\tilde{r})d\tilde{r} = N_n^2\delta_{mn} \tag{21}$$

must hold for any $m, n = 0, 1, 2, \ldots$.

The differential Eq. (18) can be transformed, through a suitable redefinition of the unknown function and of the independent variable, into a confluent hypergeometric equation. More precisely, let us define

$$w = 2\beta_n\tilde{r}^2, \quad B_n(w) = e^{w/2}R_n(\tilde{r}) \tag{22}$$

By substituting the definitions given by Eq. (22) into Eq. (18), one obtains

$$wB_n''(w) + (1 - w)B_n'(w) - \frac{4 - \beta_n}{8}B_n(w) = 0 \tag{23}$$

Equation (23) is a confluent hypergeometric equation. A solution of Eq. (23) regular in $w=0$ and thus in $\tilde{r}=0$ is given by

$$B_n(w) = {}_1F_1\left(\frac{4 - \beta_n}{8}, 1; w\right) \tag{24}$$

where ${}_1F_1$ is the confluent hypergeometric function of first kind [17]. Therefore, from Eq. (22), one obtains

$$R_n(\tilde{r}) = e^{-\beta_n\tilde{r}^2}{}_1F_1\left(\frac{4 - \beta_n}{8}, 1; 2\beta_n\tilde{r}^2\right) \tag{25}$$

which fulfills Eq. (20). The boundary condition expressed by Eq. (19) provides a procedure to determine the eigenvalues β_n. Indeed, one obtains the equation

$$_1F_1\left(\frac{4 - \beta_n}{8}, 1; \frac{\beta_n}{2}\right) = 0 \tag{26}$$

The roots of Eq. (26) can be found numerically. The first 15 eigenvalues β_n are reported in Table 1. The eigenvalues for $n \geq 15$ can be obtained with a high accuracy by adding 8 to the preceding eigenvalue. In Table 1, the normalization factors N_n^2 are also given. These factors have been obtained by a numerical computation of the integral on the left hand side of Eq. (21).

It must be pointed out that all the steps followed up to this point are exactly the same as in the existing treatments of the Graetz-Nusselt problem with viscous dissipation [15,16]. Indeed, the procedure thus far has not been affected by the initial condition, Eq. (7), prescribed at the entrance section. It can be easily checked that the eigenvalues in Table 1 are in full agreement with those reported in Ref. [4].

Table 1 The first 15 values of β_n, N_n^2 and $R_n'(1/2)$

n	β_n	$N_n^2 \times 10^2$	$R_n'(1/2)$
0	5.40872883977	2.34834419813	−2.02860091731
1	13.3580628987	0.937995958063	2.69848324414
2	21.3467590761	0.586053108459	−3.14463867839
3	29.3421569255	0.426177761709	3.49200867010
4	37.3397437289	0.334840234417	−3.78171424793
5	45.3382867177	0.275745214123	4.03293330605
6	53.3373239920	0.234380795973	−4.25632950017
7	61.3366466818	0.203807995114	4.45851083649
8	69.3361476449	0.180290889575	−4.64388667827
9	77.3357666937	0.161639620322	4.81556232937
10	85.3354676111	0.146485592800	−4.97581650936
11	93.3352273956	0.133929475344	5.12637647931
12	101.335030790	0.123355950679	−5.26858629844
13	109.334867305	0.114329802176	5.40351475337
14	117.334729510	0.106534512939	−5.53202735431

The coefficients Ξ_n in Eq. (17) can be determined by using the initial condition (15). Equations (15) and (17) yield

$$\frac{1}{\text{Br}} - 16\left(\tilde{r}^4 - \tilde{r}^2 + \frac{3}{16}\right) = \sum_{n=0}^{\infty} \Xi_n R_n(\tilde{r}) \tag{27}$$

where the definition of Brinkman number

$$\text{Br} = \frac{\mu u_m^2}{k(T_e - T_w)} \tag{28}$$

has been used. Note that $\text{Br} > 0$ corresponds to $T_e > T_w$ (*fluid cooling*), while $\text{Br} < 0$ corresponds to $T_e < T_w$ (*fluid heating*).

By employing Eq. (27) and the orthogonality relation (21), one obtains

$$\Xi_n = -\frac{16}{N_n^2}\int_0^{1/2} (1 - 4\tilde{r}^2)\left(\tilde{r}^4 - \tilde{r}^2 + \frac{3}{16}\right)\tilde{r}R_n(\tilde{r})d\tilde{r}$$
$$+ \frac{1}{\text{Br}N_n^2}\int_0^{1/2} (1 - 4\tilde{r}^2)\tilde{r}R_n(\tilde{r})d\tilde{r}, \quad n = 0, 1, 2, \ldots \tag{29}$$

Both the integrals on the right hand side of Eq. (29) can be easily evaluated on account of Eq. (18),

$$\int_0^{1/2} (1 - 4\tilde{r}^2)\left(\tilde{r}^4 - \tilde{r}^2 + \frac{3}{16}\right)\tilde{r}R_n(\tilde{r})d\tilde{r} = -\frac{2}{\beta_n^4}R_n'(1/2) \tag{30}$$

$$\int_0^{1/2} (1 - 4\tilde{r}^2)\tilde{r}R_n(\tilde{r})d\tilde{r} = -\frac{1}{2\beta_n^2}R_n'(1/2) \tag{31}$$

Therefore, Eq. (29) can be rewritten as

$$\Xi_n = \frac{32R_n'(1/2)}{\beta_n^4 N_n^2}\left(1 - \frac{\beta_n^2}{64\text{Br}}\right) \tag{32}$$

By employing Eqs. (25) and (26) and the properties of the confluent hypergeometric function of first kind [17], one obtains

$$R_n'(1/2) = \frac{1}{4}e^{-\beta_n/4}\beta_n(4 - \beta_n){}_1F_1\left(\frac{12 - \beta_n}{8}, 2; \frac{\beta_n}{2}\right) \tag{33}$$

The first 15 values of the coefficients $R_n'(1/2)$ are reported in Table 1. Therefore, the temperature field can be easily evaluated by employing Eqs. (13), (17), and (32).

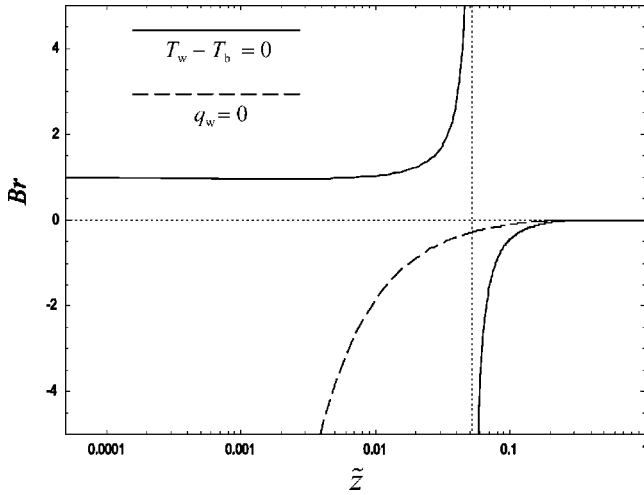Let us introduce the bulk temperature,

Fig. 2 Set of couples (z, Br) corresponding to $T_w - T_b = 0$ (solid line); set of couples (z, Br) corresponding to $q_w = 0$ (dashed line)

$$T_b = 16 \int_0^{1/2} T(1 - 4\tilde{r}^2)\tilde{r}\,d\tilde{r} \qquad (34)$$

Then, by using Eqs. (13) and (17), one can evaluate the difference $T_w - T_b$,

$$T_w - T_b = -\frac{5}{6}\frac{\mu u_m^2}{k} + \frac{8\mu u_m^2}{k}\sum_{n=0}^{\infty}\frac{\Xi_n R_n'(1/2)}{\beta_n^2}\exp\left(-\frac{\beta_n^2}{2}\tilde{z}\right) \quad (35)$$

On account of Eqs. (13) and (17), one can also evaluate the incoming wall heat flux q_w,

$$q_w = k\left.\frac{\partial T}{\partial r}\right|_{r=r_0} = -8\frac{\mu u_m^2}{D} + \frac{\mu u_m^2}{D}\sum_{n=0}^{\infty}\Xi_n R_n'(1/2)\exp\left(-\frac{\beta_n^2}{2}\tilde{z}\right)$$
$$(36)$$

Therefore, the local Nusselt number is given by

$$\mathrm{Nu} = \frac{q_w D}{k(T_w - T_b)} = \frac{48 - 6\sum_{n=0}^{\infty}\Xi_n R_n'(1/2)\exp(-\beta_n^2\tilde{z}/2)}{5 - 48\sum_{n=0}^{\infty}\Xi_n R_n'(1/2)\beta_n^{-2}\exp(-\beta_n^2\tilde{z}/2)}$$
$$(37)$$

4 Discussion of the Results

The expressions of the temperature field and of the local Nusselt number, given by Eqs. (13), (17), (32), and (37), show that the governing parameter in the thermal entrance region is the Brinkman number Br. Two limiting cases can be considered

$$\mathrm{Br} \to 0 \qquad (38)$$

$$\mathrm{Br} \to \pm\infty \qquad (39)$$

The former limit applies when the typical temperature scale of viscous dissipation, $\mu u_m^2/k$, becomes negligible with respect to the wall temperature scale, $|T_e - T_w|$. In this limit, the analytical solution found in Sec. 3 becomes coincident with the classical solution of the Graetz-Nusselt problem, where the viscous dissipation effect is neglected both upstream and downstream of the entrance cross section $\tilde{z} = 0$. Note that, for $\mu u_m^2/k \ll |T_e - T_w|$, the initial condition at $\tilde{z} = 0$ expressed by Eq. (7) becomes a condition of uniform temperature with a value T_e.
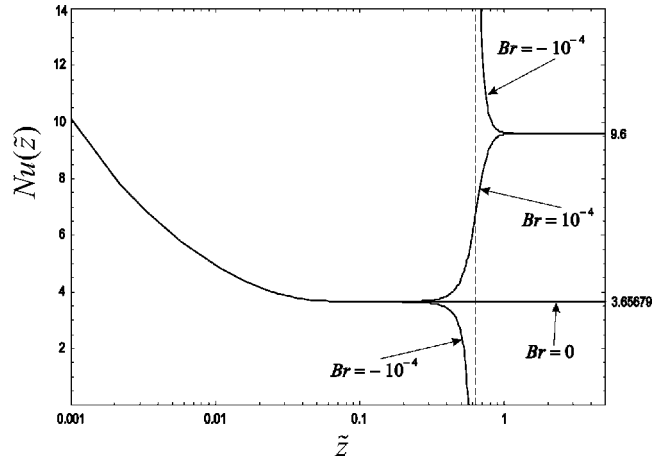
Fig. 3 Local Nusselt number in the thermal entrance region (small values of |Br|)

The limit given by Eq. (39) is reached either if the wall properties are such that no step change of the wall temperature occurs at $z=0$ ($T_e = T_w$) or if the effect of viscous dissipation is so intense that the temperature scale $\mu u_m^2/k$ is much greater than the wall temperature scale $|T_e - T_w|$. Even if the two possibilities are physically different, they can be considered as equivalent from a mathematical viewpoint.

The evaluation of the infinite sums that appear in Eqs. (17) and (37) have been performed by truncating the series to the first 51 terms. As is well known [4], the sums employed in the solution of thermal entrance problems by separation of variables display a very slow convergence for small values of $\tilde{z}$. Let us use the value of Nu for Br=1 and $\tilde{z}=10^{-4}$ as the test quantity and let us define the relative discrepancy

$$\epsilon = \left|\frac{\mathrm{Nu}_N - \mathrm{Nu}_{N-5}}{\mathrm{Nu}_N}\right| \qquad (40)$$

where Nu_N is the value of Nu obtained from Eq. (37) with the sums truncated to $n=N$. Then, it can be shown that, for $N=50$, the relative discrepancy ϵ becomes lower than 0.01%. Note that, for Br=1 and $\tilde{z}=10^{-3}$, almost the same value of ϵ is reached with $N=19$. This increased quality in the convergence of the series at the left hand side of Eq. (37) is an obvious consequence of the exponential term in the infinite sums.

4.1 Zeros and Singularities of Nu. An important feature of the solution found in Sec. 3 is that, for every negative value of Br, there exists an axial station $\tilde{z}=\tilde{z}_0 > 0$ where the wall heat flux evaluated by Eq. (36) becomes zero. A drawing of the set of couples $(\tilde{z}_0, \mathrm{Br})$ is reported in Fig. 2 (dashed line). The physical meaning of this mathematical property of q_w is the following. If Br<0, the initial wall temperature T_e is lower than T_w. This means that, for an axial interval $0 < \tilde{z} < \tilde{z}_0$, the fluid is heated by the external environment ($q_w > 0$). On the other hand, sufficiently far from the entrance cross section ($\tilde{z} > \tilde{z}_0$), the viscous heating effect becomes dominant and the sign of q_w is negative, which means that the fluid heats the external environment. As everyone expects, Fig. 2 shows that the higher is the value of |Br| the smaller is the value of $\tilde{z}_0$. In the limit $|\mathrm{Br}| \to 0$, the value of $\tilde{z}_0$ tends to infinity. Indeed, if the Brinkman number becomes vanishingly small, the viscous dissipation effect can never prevail over the fluid heating due to the higher temperature of the wall.

Figure 2 shows that, for a fixed value of Br, the difference $T_w - T_b$ also becomes zero at some axial station $z=z_1 > 0$. In this case,

Fig. 4 Dimensionless wall heat flux ϕ_w and dimensionless bulk temperature θ_b versus $\tilde{z}$ for Br=0.2 (a), Br=0.4 (b), Br=1 (c), Br=5 (d) and Br$\rightarrow \pm \infty$ (e)

Fig. 5 Dimensionless wall heat flux ϕ_w and dimensionless bulk temperature θ_b versus $\tilde{z}$ for Br=−1 (a), Br=−2 (b), Br=−5 (c) and Br$\rightarrow \pm \infty$ (d)

the values of Br which correspond to a zero of $T_w - T_b$ in the thermal entrance region are all the negative values and all the positive values such that
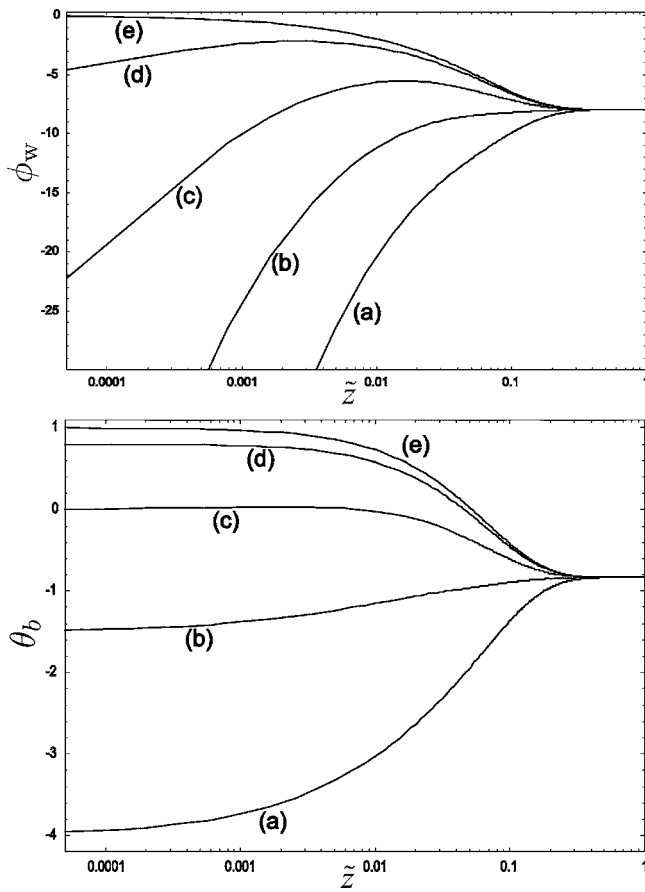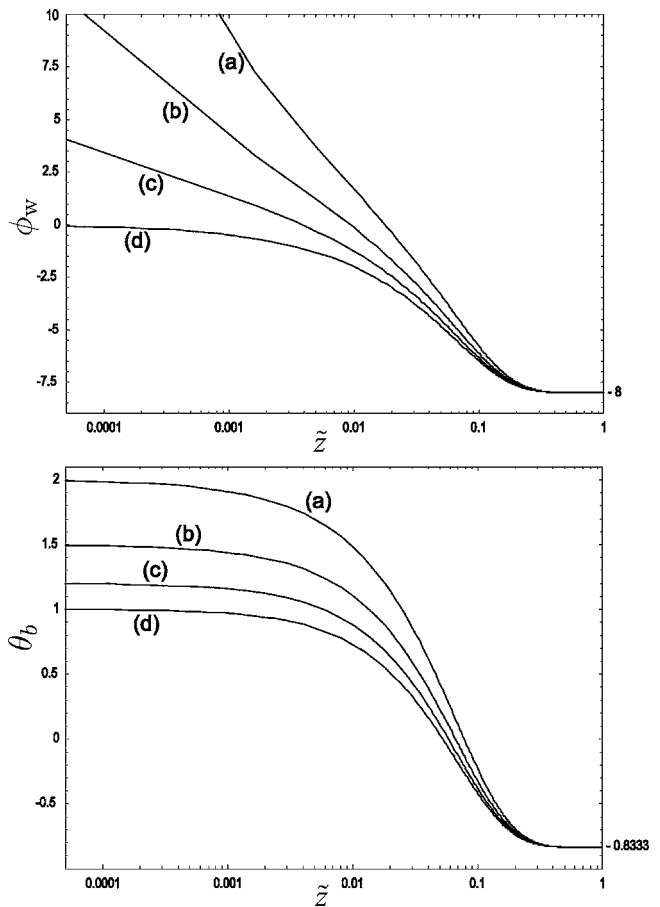
$$\text{Br} > \text{Br}_{\min} = 0.9655185 \tag{41}$$

Figure 2 displays a drawing of the set of couples $(\tilde{z}_1, \text{Br})$ corresponding to a vanishing difference $T_w - T_b$. It can be verified that the set of couples $(\tilde{z}_0, \text{Br})$ which yields $q_w = 0$ is disjoint from the set of couples $(\tilde{z}_1, \text{Br})$. This means that, for a fixed negative value of Br, there exist two distinct axial stations in the thermal entrance region: $\tilde{z} = \tilde{z}_0$ where $q_w = 0$; $\tilde{z} = \tilde{z}_1 > \tilde{z}_0$ where $T_w - T_b = 0$. By considering the definition of local Nusselt number, Eq. (37), it is easily verified that the former axial station ($\tilde{z} = \tilde{z}_0$) corresponds to a vanishing Nusselt number, while the latter ($\tilde{z} = \tilde{z}_1$) corresponds to a singularity of the Nusselt number. Therefore, one may infer that Nu becomes singular at some axial station only for Br<0 and for Br>Br$_{\min}$. Figure 2 shows that, for Br>Br$_{\min}$, the singular point $\tilde{z} = \tilde{z}_1$ of Nu lies in the interval $0 < \tilde{z} < 0.05236552$. On the other hand, for Br<0, the singular point of Nu lies in the range $\tilde{z} > 0.05236552$. The local Nusselt number displays a singularity for $\tilde{z} = 0.05236552$ in the limiting case defined by Eq. (39). This axial position can also be determined very easily and with a fair approximation by considering only the leading term ($n=0$) in the infinite sum on the right hand side of Eq. (35),

$$\tilde{z} \cong \frac{2}{\beta_0^2} \ln\left[\frac{1536 R_0'(1/2)^2}{5 \beta_0^6 N_0^2} \right] = 0.0523 \tag{42}$$

Beyond the mathematical origin of the singularities of Nu, their physical meaning relies on the sign change undergone by the dif-

ference $T_w - T_b$ in the evolution from the initial temperature profile at $\tilde{z} = 0$ to the asymptotic temperature profile reached for $\tilde{z} \rightarrow +\infty$. It is easily checked from Eq. (7) that the initial temperature profile is such that $T_e - T_b > 0$. Moreover, Eq. (35) shows that the asymptotic temperature profile reached for $\tilde{z} \rightarrow +\infty$ is such that $T_w - T_b < 0$. Therefore, if $T_e - T_w < 0$ (Br<0), one has $T_w - T_b > 0$ at $\tilde{z} = 0$ and $T_w - T_b < 0$ for $\tilde{z} \rightarrow +\infty$, so that by continuity there must exist an axial station where $T_w - T_b = 0$ (singularity of Nu). On the other hand, for $T_e - T_w > 0$ (Br>0), one can have $T_w - T_b > 0$ at $\tilde{z} = 0$ only if $T_e - T_w$ is sufficiently small (Br>Br$_{\min}$); thus, only in this case there exists an axial station where $T_w - T_b = 0$ (singularity of Nu). If $T_e - T_w$ is large enough ($0 < \text{Br} < \text{Br}_{\min}$), then the difference $T_w - T_b$ and the wall heat flux q_w remain negative in the whole thermal entrance region and, as a consequence, the local Nusselt number is positive and free of singularities for every $\tilde{z} > 0$.

4.2 Small Values of $|\text{Br}|$. A plot of the behavior of Nu as a function of $\tilde{z}$ for small values of Br is given in Fig. 3. This figure shows that even a very small value of $|\text{Br}|$ can lead to evident discrepancies in the behavior of Nu, with respect to the limiting case of the Graetz-Nusselt solution (Br=0). Indeed, as it is shown in Refs. [15,16], whatever is the nonzero value of Br, the asymptotic value reached by the Nusselt number is $48/5 = 9.6$, as can be easily inferred also from Eq. (37). On the other hand, it is well known [4] that the asymptotic Nusselt number reached in the case Br=0 is approximately 3.6568. The meaning of these apparently contradictory results is illustrated in Fig. 3 where the three cases Br=0, Br=10^{-4} and Br=-10^{-4}, are compared. The figure

Table 2 The first 15 values of Λ_n, in the case of uniform entrance temperature (UET)

n	Λ_n
0	-1.35341083421
1	0.504027201460
2	-0.232180064230
3	0.132358829719
4	-0.0853818516527
5	0.0596293273719
6	-0.0440039382592
7	0.0338137139764
8	-0.0267999316210
9	0.0217663407551
10	-0.0180313003826
11	0.0151832470171
12	-0.0129617290358
13	0.0111953826361
14	-0.00976770328616

shows that the values of the Nusselt number are almost independent of Br for $\tilde{z} \lesssim 0.2$. For higher values of $\tilde{z}$, the effect of viscous dissipation becomes so important that three distinct branches originate from the same curve: one for each value of Br. Note that the branches corresponding to Br$= \pm 10^{-4}$ asymptotically reach the value 9.6, while the branch corresponding to Br$=0$ tends to 3.6568. The curve corresponding to Br$=-10^{-4}$ displays a singularity at $\tilde{z}=0.6285063$. As discussed above, this singularity is due to the existence of an axial station where the denominator, $T_w - T_b$, in the fractional expression of the local Nusselt number becomes zero.

4.3 Large Values of $|\mathrm{Br}|$. The behavior of the temperature field for large values of $|\mathrm{Br}|$ is illustrated in Figs. 4 and 5. These figures refer to positive values of Br and negative values of Br, respectively; they display the axial changes of the dimensionless wall heat flux

$$\phi_w = \frac{q_w D}{\mu u_m^2} = -8 + \sum_{n=0}^{\infty} \Xi_n R_n'(1/2) \exp\left(-\frac{\beta_n^2}{2}\tilde{z}\right) \qquad (43)$$

and of the dimensionless bulk temperature

$$\theta_b = \frac{k(T_w - T_b)}{\mu u_m^2} = -\frac{5}{6} + 8\sum_{n=0}^{\infty} \frac{\Xi_n R_n'(1/2)}{\beta_n^2} \exp\left(-\frac{\beta_n^2}{2}\tilde{z}\right) \qquad (44)$$

As is expected from Eqs. (43) and (44), Figs. 4 and 5 show that the asymptotic values reached by ϕ_w and θ_b are -8 and $-5/6 \cong -0.833333$, respectively. These asymptotic values, as well as the asymptotic value of Nu$= \phi_w / \theta_b$, can be reached either from above or from below depending on the value of the Brinkman number. For large values of $\tilde{z}$, the leading terms in the infinite series which appear in Eqs. (37), (43), and (44) are those corresponding to $n=0$. By inspecting these terms, on account of Eq. (32), one can easily conclude that Nu, ϕ_w and θ_b approach their asymptotic values from below when

$$0 < \mathrm{Br} < \frac{\beta_0^2}{64} = 0.457099 \qquad (45)$$

On the other hand, Nu, ϕ_w and θ_b approach their asymptotic values from above if either Br<0 or Br$>\beta_0^2/64=0.457099$. Illustrations of this feature are given in Figs. 3–5.

The initial condition (7) allows one to deduce that the value of θ_b at $\tilde{z}=0$ is $1-1/\mathrm{Br}$. This feature is clearly shown in Figs. 4 and 5. A check on the convergence of the series employed in Eq. (43) leads to the conclusion that the limit of ϕ_w for $\tilde{z} \to 0^+$ is $\pm\infty$, with the only exception of the special case defined by Eq. (39) where this limit is equal to 0. Indeed, only if Eq. (39) holds, the wall

Fig. 6 Dimensionless wall heat flux ϕ_w and dimensionless bulk temperature θ_b versus $\tilde{z}$ for positive values of Br. Comparison between adiabatic preparation (AP)(solid lines) and uniform entrance temperature (UET)(dashed lines).

temperature does not undergo any step change at $\tilde{z}=0$ and, as a consequence, no singular behavior of q_w takes place for small values of $\tilde{z}$. It must be pointed out that the singular behavior of q_w in the limit $\tilde{z} \to 0^+$ is a well known feature of the classical Graetz-Nusselt solution [4]. Figures 4 and 5, as well as Eqs. (43) and (44), reveal that both ϕ_w and θ_b are monotonic increasing functions of $|\mathrm{Br}|$ for any fixed $\tilde{z}$, if Br>0. On the contrary, they are monotonic decreasing functions of $|\mathrm{Br}|$ for any fixed $\tilde{z}$, if Br<0. The upper frame of Fig. 5 shows that, for any finite negative value of Br, the wall heat flux is positive (incoming) in an initial region of the domain $\tilde{z}>0$. This characteristic has a simple physical meaning: if Br<0, i.e., if $T_w>T_e$, at the beginning of the thermal entrance region, the fluid is heated by the external environment. Sufficiently far from the entrance cross section, the fluid starts to heat the external environment, due to the viscous heating, and the sign of q_w becomes negative (outgoing).

4.4 Comparison With the Uniform Entrance Temperature Case. Several studies of the thermal entrance problem with viscous dissipation in a circular duct with isothermal wall are based on the assumption that the thermal entrance temperature distribution prescribed in $\tilde{z}=0$ is uniform with a value T_e [10,13,16]. If one considers this different initial condition, the application of the separation of variables method is exactly the same as that described in Sec. 3, as far as the eigenvalues and eigenfunctions are determined. On the other hand, the evaluation of the coefficients Ξ_n depends on the initial condition. In the uniform entrance temperature case, Eq. (15) is replaced by
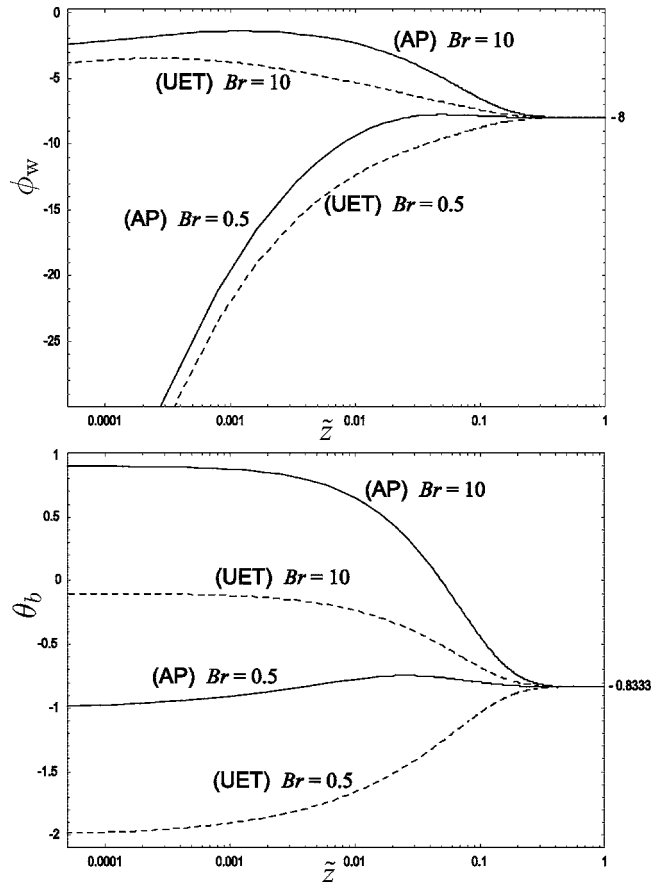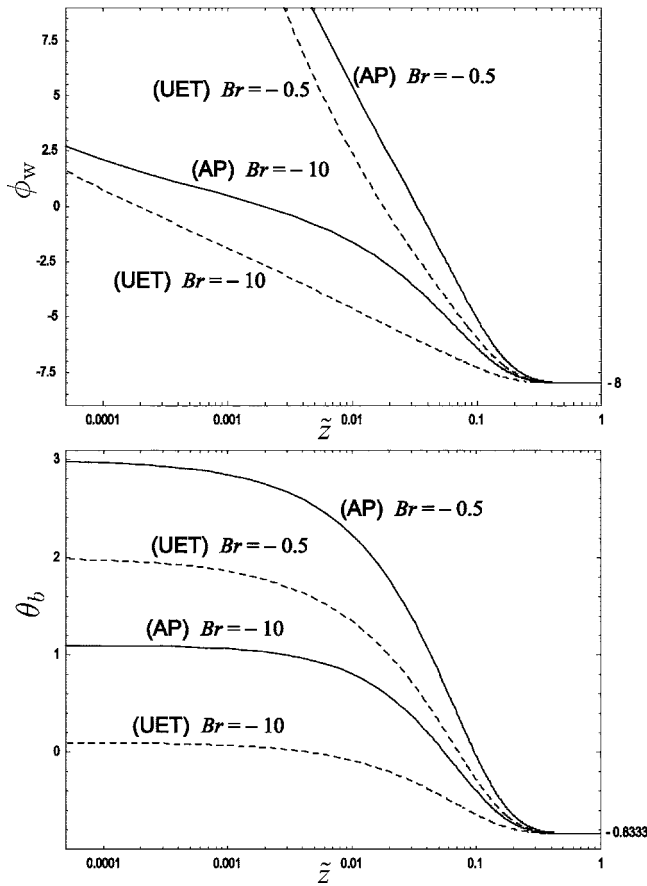
Fig. 7 Dimensionless wall heat flux ϕ_w and dimensionless bulk temperature θ_b versus $\tilde{z}$ for negative values of Br. Comparison between adiabatic preparation (AP)(solid lines) and uniform entrance temperature (UET)(dashed lines).

Fig. 8 Dimensionless temperature $k(T-T_w)/(\mu u_m^2)$ versus $\tilde{r}$ for Br=1 and $\tilde{z}=10^{-3}$ (upper frame) or $\tilde{z}=0.1$ (lower frame). Comparison between adiabatic preparation (AP)(solid line) and uniform entrance temperature (UET)(dashed line).

$$\Theta(r,0) = T_e - T_w - \frac{\mu u_m^2}{k}\left(1 - \frac{r^4}{r_0^4}\right) \qquad (46)$$

Therefore, Eq. (27) is replaced by

$$\frac{1}{\text{Br}} + 16\tilde{r}^4 - 1 = \sum_{n=0}^{\infty} \Xi_n R_n(\tilde{r}) \qquad (47)$$

the coefficients Ξ_n are not expressed anymore by Eq. (32). In the case of uniform entrance temperature, these coefficients are given by

$$\Xi_n = \Lambda_n - \frac{R_n'(1/2)}{2\beta_n^2 N_n^2 \text{Br}} \qquad (48)$$

where

$$\Lambda_n = \frac{1}{N_n^2}\int_0^{1/2}(1 - 4\tilde{r}^2)(16\tilde{r}^4 - 1)\tilde{r}R_n(\tilde{r})d\tilde{r} \qquad (49)$$

As a consequence, Eqs. (13), (17), and (35)–(37), as well as Eqs. (43) and (44), still hold. Moreover, the numerical values reported in Table 1 can still be used. On the other hand, the first 15 values of Λ_n are given in Table 2.

Comparisons between the adiabatic preparation (AP) solution described in the present paper and the uniform entrance temperature (UET) solution proposed in several previous papers on the Graetz problem with viscous dissipation [13,16] are performed in Figs. 6–9. According to Figs. 6 and 7, the comparisons between the values of the dimensionless quantities ϕ_w and θ_b evaluated according to the AP and to the UET solutions reveal strong dif-

ferences. The discrepancies are present throughout the thermal entrance region. As expected from Eqs. (43) and (44), the values of ϕ_w and θ_b evaluated by the two solutions agree in the asymptotic region. Figures 8 and 9 display the radial temperature distributions at the axial stations $\tilde{z}=10^{-3}$ and $\tilde{z}=0.1$ either for Br $=1$ (Fig. 8) or for Br$=-1$ (Fig. 9), according to the AP and to the UET solutions. These figures show that the sensitivity of the temperature field to the prescribed entrance condition is very strong at the earlier axial station $\tilde{z}=10^{-3}$, while it becomes weaker downstream ($\tilde{z}=0.1$). This behavior is specially evident for Br$=1$ (Fig. 8).

In Table 3, values of Nu at different axial positions are reported for Br$=1$ and Br$=10^{-3}$. These values calculated according either to the AP solution or to the classical UET solution are compared with the values of the local Nusselt number obtained in the case of negligible viscous dissipation (Br$=0$) by Cotta and Özişik [18]. An inspection of the data reported in this table shows that strong differences between the UET values and the AP values occur for Br$=1$, while the discrepancies between the two solutions are very small for Br$=10^{-3}$. Moreover, both the AP and the UET values of Nu for Br$=10^{-3}$ are generally in very good agreement with the values obtained in Ref. [18] in the absence of viscous dissipation. In fact, for Br$=10^{-3}$ and $\tilde{z}>0.2$, it becomes apparent that the effect of viscous heating becomes very important and determines the asymptotic value of Nu which, as already pointed out above, is different from that in the case Br$=0$. If Br$=1$, Table 3 shows that, for $\tilde{z}\lesssim0.007$, the value of Nu is negative while, for higher values
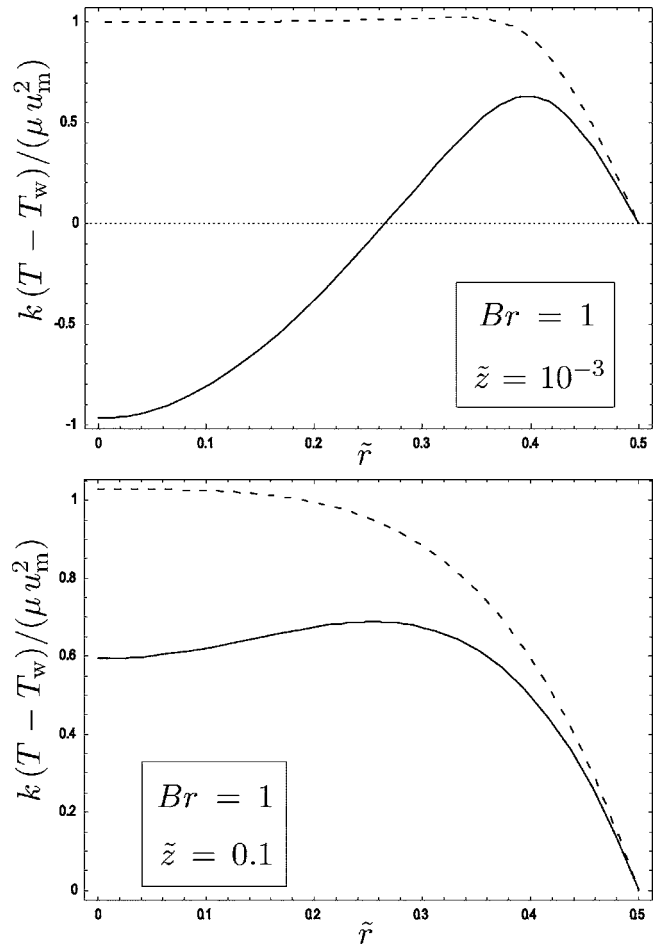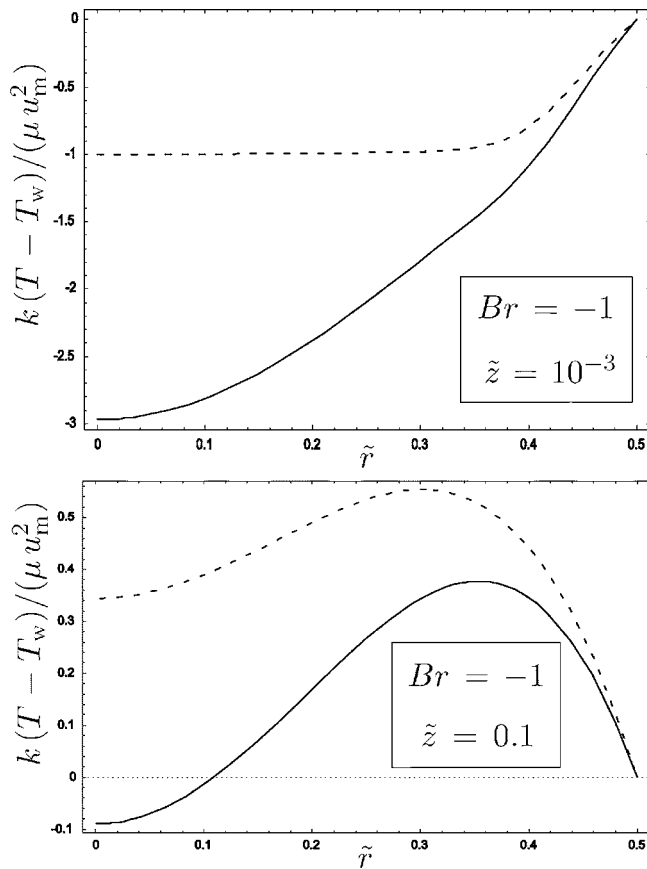
Fig. 9 Dimensionless temperature $k(T-T_w)/(\mu u_m^2)$ versus $\tilde{r}$ for $Br=-1$ and $\tilde{z}=10^{-3}$ (upper frame) or $\tilde{z}=0.1$ (lower frame). Comparison between adiabatic preparation (AP)(solid line) and uniform entrance temperature (UET)(dashed line).

of $\tilde{z}$, it becomes positive. Indeed, as can be easily checked in Fig. 4, the value of q_w for Br=1 is negative throughout the entrance region, while the difference T_w-T_b has small positive values at the beginning of the thermal entrance region ($\tilde{z}<0.00758$) and then becomes negative.

5 Conclusions

The laminar forced convection in a circular duct with isothermal wall has been studied by taking into account the effect of viscous dissipation. An analytic solution of the energy balance equation has been determined in the thermal entrance region. It has been assumed that the initial condition of the thermal entrance region is the result of an adiabatic preparation of the fluid. More precisely, the fluid upstream of the thermal entrance section is supposed to flow through a sufficiently long adiabatic part of the tube where both the velocity profile and the temperature profile become fully developed. The result of this adiabatic preparation is an initial temperature profile which, due to the viscous heating effect, is not uniform.

The solution, obtained by the standard separation of variables method, differs from other solutions based on the assumption of a uniform entrance temperature profile. From a mathematical viewpoint, the differences between the procedures are only in the determination of the coefficients of the infinite series expression of the temperature field, which depend on the initial condition. Considerably dissimilar local values of the wall heat flux, of the difference between the wall temperature and the bulk temperature, of the Nusselt number occur. These discrepancies between solutions corresponding to different entrance section conditions imply a strong sensitivity of the heat transfer process to the initial conditions. The latter feature should be carefully considered in the design of an experiment on thermal entrance heat transfer with important viscous heating effects. The exact solution worked out here is also a useful benchmark against which to test the accuracy of numerical methods for laminar flow and heat transfer in ducts.

It has been shown that the effect of viscous dissipation may produce both positive and negative local values of the Nusselt number. Moreover, singularities of the Nusselt number are shown to exist at the axial station where the difference between the wall temperature and the bulk temperature is zero. These singularities arise for every negative value and for sufficiently high positive values of the Brinkman number.

Table 3 Values of Nu calculated according either to the adiabatic preparation (AP) or to the uniform entrance temperature (UET) solutions

$\tilde{z}$	Nu (AP) $Br=1$	Nu (UET) $Br=1$	Nu (AP) $Br=10^{-3}$	Nu (UET) $Br=10^{-3}$	Nu Ref. [18] $Br=0$
0.0005	−558.75	15.053	12.838	12.826	12.824
0.0010	−346.80	12.827	10.141	10.133	10.130
0.0015	−278.56	11.841	8.8502	8.8435	8.8404
0.0020	−249.01	11.266	8.0454	8.0396	8.0362
0.0030	−235.01	10.613	7.0516	7.0470	7.0432
0.0040	−255.93	10.249	6.4375	6.4337	6.4296
0.0050	−317.70	10.018	6.0092	6.0060	6.0015
0.0060	−478.38	9.8606	5.6887	5.6859	5.6812
0.0070	−1225.9	9.7469	5.4376	5.4351	5.4301
0.0080	1617.2	9.6620	5.2344	5.2321	5.2269
0.0090	461.16	9.5971	5.0658	5.0638	5.0584
0.0100	263.04	9.5464	4.9235	4.9217	4.9161
0.0200	47.396	9.3588	4.1806	4.1798	4.1724
0.0500	17.229	9.3810	3.7225	3.7224	3.7100
0.1000	11.802	9.4894	3.6841	3.6841	3.6581
0.1500	10.489	9.5462	3.7107	3.7106	3.6568
0.2000	9.9970	9.5740	3.7677	3.7675	3.6568
0.5000	9.6046	9.5997	7.2510	7.2492	⋯
1.0000	9.6000	9.6000	9.5974	9.5974	⋯

Nomenclature

Br = Brinkman number, Eq. (28)

Br_{min} = threshold value of Br, Eq. (41)

B_n = function of w, Eq. (22)

c_p = specific heat at constant pressure

D = diameter, $2r_0$

$_1F_1$ = confluent hypergeometric function of the first kind

k = thermal conductivity

N_n^2 = normalization factor, Eq. (21)

Nu = Nusselt number, Eq. (37)

Pe = Peclet number, $\rho c_p u_m D/k$

q_w = wall heat flux, Eq. (36)

T = temperature

T_b = bulk temperature, Eq. (34)

T_e = entrance temperature

$T_s(r)$ = particular solution of Eq. (10)

T_w = wall temperature

u = z-component of velocity

u_m = mean velocity in a duct section

r = radial coordinate

$\tilde{r}$ = dimensionless radial coordinate, r/D

r_0 = radius of the duct

R_n = eigenfunction

w = variable, Eq. (22)

z = axial coordinate

z_0 = axial station where $q_w=0$

z_1 = axial station where $T_w-T_b=0$

$\tilde{z}$ = dimensionless axial coordinate, $z/(\text{Pe}D)$

Greek Symbols

β_n = eigenvalue

ϵ = relative discrepancy, Eq. (40)

δ_{mn} = Kronecker's delta

$\Theta(r,z)$ = solution of Eq. (11)

θ_b = dimensionless bulk temperature, Eq. (44)

Λ_n = coefficients, Eq. (49)

μ = dynamic viscosity

Ξ_n = coefficients, Eqs. (32) and (48)

ρ = mass density

ϕ_w = dimensionless wall heat flux, Eq. (43)

References

[1] Graetz, L., 1883, "Uber die Wärmeleitungsfähigkeit von Flüssigkeiten," Ann. Phys. Chem., **18**, pp. 79–94.

[2] Graetz, L., 1885, "Uber die Wärmeleitungsfähigkeit von Flüssigkeiten," Ann. Phys. Chem., **25**, pp. 337–357.

[3] Nusselt, W., 1910, "Die Abhängigkeit der Wärmeübergangszahl von der Rohrlänge," VDI Z. (1857-1968), **54**, pp. 1154–1158.

[4] Shah, R. K., and London, A. L., 1978, *Laminar Flow Forced Convection in Ducts, Advances in Heat Transfer*, Academic, New York.

[5] Shah, R. K., and Bhatti, M. S., 1987, "Laminar Convective Heat Transfer in Ducts," *Handbook of Single-Phase Convective Heat Transfer*, S. Kakaç et al., eds., Wiley, New York, Chap. 3.

[6] Sellars, J. R., Tribus, M., and Klein, J. S., 1956, "Heat Transfer to Laminar Flow in a Round Tube or Flat Conduit-The Graetz Problem Extended," Trans. ASME, **78**, pp. 441–448.

[7] Siegel, R., Sparrow, E. M., and Hallman, T. M., 1958, "Steady Laminar Heat Transfer in a Circular Tube With Prescribed Wall Heat Flux," Appl. Sci. Res., Sect. A, **7**, pp. 386–392.

[8] Quaresma, J. N. N., and Cotta, R. M., 1994, "Exact Solutions for Thermally Developing Tube Flow With Variable Wall Heat Flux," Int. Commun. Heat Mass Transfer, **21**, pp. 729–742.

[9] Liou, C.-T., and Wang, F.-S., 1990, "Solutions to the Extended Graetz Problem for a Power-Model Fluid With Viscous Dissipation and Different Entrance Boundary Conditions," Numer. Heat Transfer, Part A, **17**, pp. 91–108.

[10] Valkó, P.P., 2005, "Solution of the Graetz-Brinkman Problem With the Laplace Transform Galerkin Method," Int. J. Heat Mass Transfer, **48**, pp. 1874–1882.

[11] Brinkman, H. C., 1951, "Heat Effects in Capillary Flow I," Appl. Sci. Res., Sect. A, **2**, pp. 120–124.

[12] Ou, J. W., and Cheng, K. C., 1973, "Viscous Dissipation Effects on Thermal Entrance Region Heat Transfer in Pipes With Uniform Wall Heat Flux," Appl. Sci. Res., **28**, pp. 289–301.

[13] Ou, J. W., and Cheng, K. C., 1974, "Viscous Dissipation Effects on Thermal Entrance Heat Transfer in Laminar and Turbulent Pipe Flows With Uniform Wall Temperature," *AIAA/ASME 1974 Thermophysics and Heat Transfer Conference*, AIAA Paper No. 74–743, ASME Paper No. 74-HT-50.

[14] Hieber, C. A., 1976, "A Composite Leveque-Graetz Solution to the Brinkman Problem," Lett. Heat Mass Transfer, **3**, pp. 117–124.

[15] Lin, T. F., Hawks, K. H., and Leidenfrost, W., 1983, "Analysis of Viscous Dissipation Effect on Thermal Entrance Heat Transfer in Laminar Pipe Flows With Convective Boundary Conditions," Waerme-Stoffuebertrag., **17**, pp. 97–105.

[16] Basu, T., and Roy, D. N., 1985, "Laminar Heat Transfer in a Tube With Viscous Dissipation," Int. J. Heat Mass Transfer, **28**, pp. 699–701.

[17] Abramowitz, M., and Stegun, I. A., 1972, *Handbook of Mathematical Functions*, National Bureau of Standards, Washington D. C.

[18] Cotta, R. M., and Özişik, M. N., 1986, "Laminar Forced Convection of Power-Law Fluids Inside Ducts," Waerme-Stoffuebertrag., **20**, pp. 211–218.

Self-Consistent Open-Celled Metal Foam Model for Thermal Applications

Eric N. Schmierer

Applied Engineering Technology,
MS J580,
Los Alamos National Laboratory,
Los Alamos, NM 87545
e-mail: schmierer@lanl.gov

Arsalan Razani

Mechanical Engineering Department,
The University of New Mexico,
Albuquerque, NM 87131
e-mail: razani@unm.edu

Many engineering applications require thermal cycling of granular materials. Since these materials generally have poor effective thermal conductivity various techniques have been proposed to improve bed thermal transport. These include insertion of metal foam with the granular material residing in the interstitial space. The use of metal foam introduces a parasitic thermal capacitance, disrupts packing, and reduces the amount of active material. In order to optimize the combined high porosity metal foam-granular material matrix and study local thermal nonequilibrium, multiple energy equations are required. The interfacial conductance coefficients, specific interface area, and the effective thermal conductivities of the individual components, which are required for a multiple energy equation analysis, are functions of the foam geometry. An ideal three-dimensional geometric model of open-celled Duocell® foam is proposed. Computed tomography is used to acquire foam cell and ligament diameter distribution, ligament shape, and specific surface area for a range of foam parameters to address various shortcomings in the literature. These data are used to evaluate the geometric self-consistency of the proposed geometric model with respect to the intensive and extensive geometry parameters. Experimental thermal conductivity data for the same foam samples are acquired and are used to validate finite element analysis results of the proposed geometric model. A simple relation between density and thermal conductivity ratio is derived using the results. The foam samples tested exhibit a higher dependence on relative density and less dependence on interstitial fluid than data in the literature. The proposed metal foam geometric model is shown to be self-consistent with respect to both its geometric and thermal properties. [DOI: 10.1115/1.2352787]

Keywords: open-celled, metal foam, thermal conductivity, geometric model, tomography

1 Introduction

There are many engineering applications where granular materials must be thermally cycled. Materials such as metal hydrides, diatomaceous earth, and molecular sieves are examples. These materials generally have low thermal conductivity due to the poor contact between particles, the tortuous conduction path, and in some cases low thermal conductivity of the parent solid material. Improving the thermal conductivity of these materials has many benefits, especially in applications where thermal cycling must be rapid. In order to improve the thermal conductivity of granular material beds, various techniques have been proposed: insertion of metal foam, integration of copper wire nets, and compaction of a porous metal/metal hydride matrix are examples [1–3].

High porosity metal foam has been used in this way with metal hydride systems for hydrogen storage [4] and for isotope separation [3]. The use of metal foam increases the parasitic heat capacity of the reactor bed, reduces the available active granular material, and disrupts its packing. The geometry of open-celled metal foams, to a certain extent, can be tailored for the particular application. Therefore there is opportunity for optimization of this combined metal foam-granular material matrix.

For the ability to optimize this multi-component matrix and to study local thermal nonequilibrium (LTNE), multiple energy equations are required to represent each component. The interfacial conductance coefficients, specific interface area, and the effective thermal conductivities that couple these equations and govern transport must be determined. The foam thermal conductivity is a function of the tortuous structure of the metal foam. Since solid boundaries disrupt the packing of the granular material, the thermal conductance between the foam and the interstitial material(s) is a function of the metal foam surface area. In order to determine these geometric dependencies and to have a predictive capability, a geometric model based on a full understanding of the metal foam geometry is required. This model should be self-consistent with respect to (1) the intensive geometric properties of the foam: relative density, the specific surface area, and the periodicity of the foam structure, (2) the extensive geometric properties that describe the exact morphology, and (3) its thermal conductance.

Several investigations into the geometry of open-celled metal foam have focused on the geometric parameters in order to determine analytical relations for the effective thermal conductivity. Of these, the ligament diameter, d_f, and pore diameter, d_p, have been key parameters of interest [5,6]. In general, semi-analytical, one-dimensional expressions were developed for thermal conductivity that leave a single free geometric parameter. Data for effective thermal conductivity were used to determine this free parameter [5–7]. Traditional means of measuring d_f and d_p has been microscopy of physical samples, which is a destructive method. A non-destructive method is three-dimensional computed tomography (CT). This technique has been used by several investigations on closed-cell foams. Results have been presented for open-celled metal foam for polymer foam cell morphology [8,9]. Other investigations have focused on the foam geometry for use as a substrate [10]. Scanning electron microscopy (SEM) and nondestructive optical analysis has been used for determining geometric parameters for mechanical analysis as well [11].

A specific surface area, S_v, expression for that of a cubic lattice with cylindrical ligaments has been used in forced convection investigations with coupled energy equations [5,6,12,13]

$$S_v = \frac{3\pi d_f}{d_p^2} \tag{1}$$

Surface area has also been measured using two-dimensional image analysis from CT [14] and preliminary results using three-dimensional CT [15] were presented. Surface area was investigated nondimensionally for cubic and tetrakaidecahedronal lattices numerically [16]. The Brunauer, Emmett, and Teller (BET) technique was used to measure surface area in conjunction with ligament size measurements to determine semi-empirical surface area and density equations for a dodecahedronal unit cell structure [17]. With the exception of the Eq. (1), the authors are unaware of any completely analytical expressions for S_v, and the experimental data have a limited parameter range from two different methods that very greatly in their results.

The heat transfer in the foam/interstitial material matrix consists of conduction through the ligaments of solid metal, radiation, and conduction and convection through the interstitial material. The bulk thermal conductivity of the foam is geometry dependent and application of general amorphous porosity relationships is invalid. A simple representation of the high porosity solid structure was first proposed by Dul'nev [18], who used a cubic lattice structure with a square cross section to analytically calculate the effective thermal conductivity of a fluid-saturated structure. An improvement over this model was introduction of a cubic lump of material at the ligament vertices [19].

Experimental data are presented by several investigations: nickel and aluminum metal foam with water, air, and glycol [20], Al Duocell® foam for air (1 atm) and water combinations [5], Al Duocell® foam for air [21], carbon (RVC)-air (1 atm) and RVC-water combinations [6], and Al Duocell® foam air, water, and oil [16]. These data were fit using a linear combination [6] and a weighted geometric mean [22] of the parallel and series bounding equations for effective thermal conductivity. The later derived the following equation that contains a material dependent coefficient, F

$$k_{\text{eff}} = [\varepsilon k_f + (1-\varepsilon)k_s]^F \left[\frac{k_f k_s}{\varepsilon k_s + (1-\varepsilon)k_f}\right]^{(1-F)} \tag{2}$$

Heat transfer due to radiation is typically neglected. However, results from analytical models and experimental data for radiation are available [23,24]. In a vacuum, if the radiation is neglected, k_{eff} is a function of only the solid thermal conductivity, k_s, the relative density, ρ, and a tortuosity factor that captures the affect of geometry on the conductivity. This effective thermal conductivity, void of interstitial material influence, is the property of interest for application in a multienergy equation analysis or when the ratio of the solid to fluid thermal conductivity, k_s/k_f, is very large (>1000) [16]. Under these circumstances, a simple form can represent k_{eff}

$$k_{\text{eff}} = Ck_s\rho \tag{3}$$

The value of C was derived in closed-cell polymer foam to be 0.33 [25]. Ozmat et al. [17] derive a relation for the foam-only thermal conductivity using the assumption that the electrical and thermal conductance have the same tortuosity factor. Using electrical conductivity measurements, $C=0.345$ was determined. Electrical conductivity was also investigated and related to a tetrakaidecahedronal structure [26]. These data indicated a value of C between 0.40 and 0.46. The foam only contribution was determined by Calmidi and Mahajan [12] by setting $k_f=0$ in their analytical expression of k_{eff}. This method was shown to be in error by Fourie and Du Plessis [27]. They note that for LTNE, the conduction within a phase is also a function of the gradient of the locally
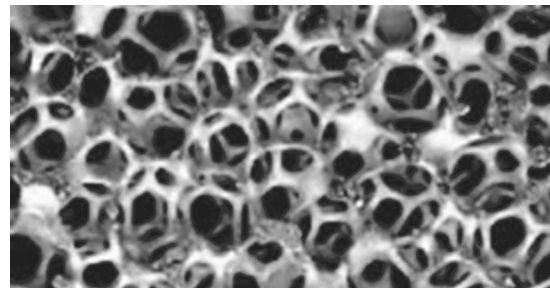
Fig. 1 Photo of real metal foam (see Ref. [27])

mean temperature of the opposing phase. The secondary functions of thermal conductivity were relatively insignificant for large k_s/k_f in this study.

After review of the literature, the authors are not aware of any previous three-dimensional numerical analysis for effective thermal conductivity or report of metal foam in a vacuum. Several geometric models have been proposed in the literature for evaluation of thermal conductivity, however there have been no evaluations of the resulting geometry's self-consistency. Surface area, for example, is a key component in the foam-to-interstitial material heat transfer and is not necessarily represented accurately by a model determined simply by fitting k_{eff} data. The purpose of this study was to evaluate the self-consistency of a proposed three-dimensional geometric model of open-celled Duocell® foam. To accomplish this, thermal conductivity data were obtained experimentally and numerically and the geometry of real metal foam was quantified. The model is shown to be self-consistent with respect to both geometric and thermal properties.

2 Metal Foam Model

In this study, real metal foam (Fig. 1(a)) was represented with a tetrakaidecahedronal lattice that is referred to here as the TetraK model [16]. This geometric shape has been shown experimentally to be less representative than a multicell unit cell in polymer foam [8]; however, it is the most representative single-celled, space-filling, unit cell of the foam [28]. This is shown in Fig. 2 and is similar to the structure proposed by Boomsma and Poulikakos [7] except with spherical nodes, which was deemed more physically accurate than cubes.
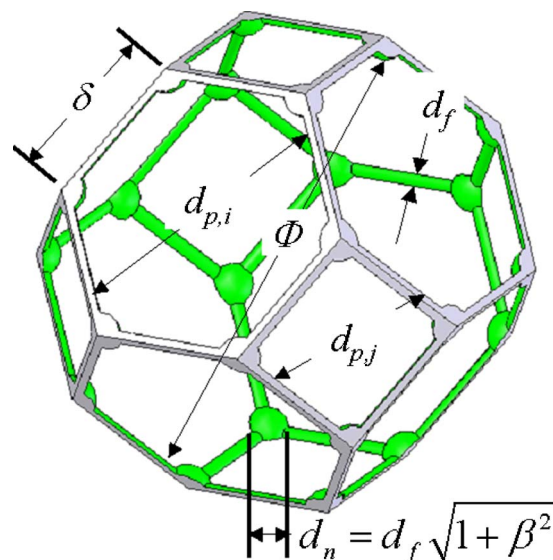
Fig. 2 One cell of the proposed TetraK Model with pertinent geometric parameters indicated

The parameters used to fully describe the TetraK unit cell are the relative density, ρ, specific surface area, S_v, average ligament diameter, d_f, ligament length, δ, and a node size parameter, β. An additional parameter commonly reported by manufacturers of open-celled metal foam is the pore density (pores per unit length (PPI)), which is the inverse of the average pore diameter. In this study, the average pore diameter, $\bar{d}_p$, is defined as the average size of the windows (faces) of the polyhedron. This accounts for the squares, $d_{p,j}$, and the hexagons, $d_{p,i}$. The average size of a pore considering the six squares and the eight hexagons of side length δ is

$$\bar{d}_p = 1.52\delta \qquad (4)$$

The pore diameter is the measure of the periodicity of the structure and is related to the unit cell diameter, Φ, where Φ is defined as the mid-diameter of the polyhedron

$$\Phi = 3\delta \qquad (5)$$

Using the space-filling properties of the tetrakaidecahedron, the following dimensionless relations can be written for the unit cell:

$$\rho = \gamma_1 u^3 + \gamma_2 u^2 \qquad (6)$$

$$S_v \delta = \gamma_3 u^2 + \gamma_4 u \qquad (7)$$

where

$$u = \frac{d_f}{\delta} \qquad (8)$$

and γ_i are functions of the node parameter β [16]

$$\gamma_1 = \pi/8\sqrt{2}[-\sqrt{1+\beta^2} - \beta^2\sqrt{1+\beta^2} + 2\beta^3]$$

$$\gamma_2 = 3\pi/8\sqrt{2}$$

$$\gamma_3 = -3\pi/4\sqrt{2}[(1+\beta)^2 - 2\beta\sqrt{1+\beta^2}]$$

$$\gamma_4 = 3\pi/2\sqrt{2} \qquad (9)$$

It should be pointed out that there are experimental evidences that the cross section of the ligaments vary with porosity [5]. It is also apparent from inspection that the ligaments of real foam are thinner at their midpoints. In this study, the TetraK model ligament cross section is circular and the diameter is constant over its length.

3 Foam Geometric Measurements

No single source of geometric information that covers the necessary parameters from a common set of foam samples exists in the literature. This was desired in order to make a fair evaluation of the TetraK model for predicting geometric and thermal properties. CT, which has the advantage of being nondestructive, was employed to allow geometric and thermal conductivity measurements on the same samples.

CT surface area and volume calculations were performed on samples ranging in pore density and relative density using methods described elsewhere from Hytec Sensors & Imaging Group, Inc. (Los Alamos, NM) [15]. The metal foam samples were Duocell® 6101 aluminum foam (ERG Aerospace, Oakland, CA) whose parameters are listed in Table 1. Each sample has a 10.2 cm diameter, 3.2 cm thickness, and has 6.4 mm thick aluminum plates dip-brazed to each end. The direction of cell elongation was in the direction of the sample axis (z-direction). The CT calculation region was sliced perpendicularly to the z-axis into four equal subsections ($2.5 \times 2.5 \times 0.65$ cm) in which each had surface area and volume analyses conducted. Data were acquired at several magnifications. For the highest magnification, the data had to be reduced to $1/2$ resolution due to memory limitations.

Table 1 Metal foam sample information

Sample ID	Pore density (PPI)[a]	Relative density determined gravimetrically (%)[b]
A	5	8.0
B	10	3.8
C	10	8.7
D	10	11.4
E	20	8.5
F	30[c]	8.7

[a]Provided by manufacturer.
[b]Provided by manufacturer, verified to within 11% uncertainty.
[c]Throughout this paper 30 PPI is the pore density used for this sample, this was indicated as more accurate than the standard value quoted for this material which is 40 PPI (Ref. [29]).

This resulted in voxel (3D pixel) sizes of 115, 84, 73, and 58 μm, which are referred to as $1\times$, $1.3\times$, $1.6\times$, and $2\times$ magnification.

Two-dimensional images were extracted from the CT data for measuring extensive properties. These images corresponded to the center x-y planes of each subsection (e.g., Fig. 3(a)). National Instruments (Austin, TX) IMAQ Vision Builder image analysis software was used for two-dimensional image analysis. For ligament diameter, the objects in Fig. 3(b) were filtered by perimeter to remove the large conglomerations of material leaving only ligament intersections (Fig. 3(c)). Area and perimeter were calculated for each object remaining in the image. The ligament diameter was then determined using the hydraulic diameter definition for each object j

$$d_{f,j} = \frac{4A_j}{P_j} \qquad (10)$$

Cell diameter was measured by manually superimposing ovals onto each cell cross section of the original image (Fig. 3(a) as example). Equivalent diameter was then calculated using the following for each oval consisting of N pixels of size Λ

$$\Phi_i = \sqrt{\frac{4}{\pi} N_{\text{pixels},i} \Lambda^2} \qquad (11)$$

4 Thermal Conductivity Method

The TetraK ideal model has a spherical node; therefore, an analytical solution for the effective thermal conductivity was not readily available due to the complexity of the formulation. The effective thermal conductivity was determined using finite element analysis (FEA) of the unit cell region proposed by Boomsma and Poulikakos [7]. This is $1/16$ of the full tetrakaidecahedron that is shown in Fig 1(b). This region represents the smallest division of the TetraK geometry using its symmetry planes that still contains the TetraK's representative conduction paths. It is comprised of three half-ligaments, two half-nodes, and two quarter-nodes. The overall dimensions of the model were kept constant and the relative ligament and node sizes varied to represent dif-

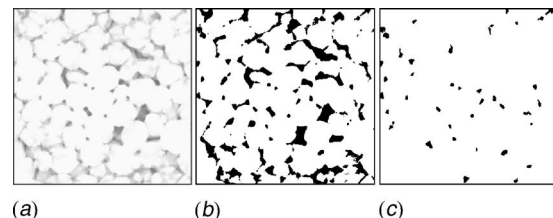
Fig. 3 Image progression to extract ligament cross-sectional information; (a) cropped gray-scale image, (b) binary image with $A_{\text{solid}}/A_{\text{total}}$ matched to relative density, and (c) large perimeter objects filtered out
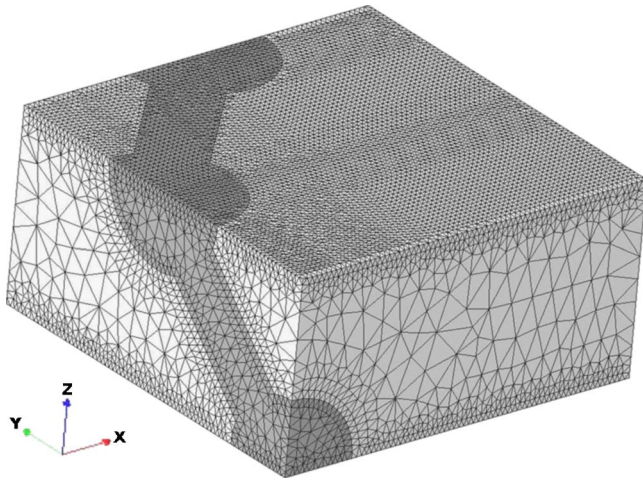
Fig. 4 FEA model of tetrakaidecahedronal (1/16 model) lattice ($\rho=0.07$, $\beta=2$). Mesh was refined at heat flux boundaries and at the dissimilar material interfaces.

spectively. With the foam metal being type 6101 aluminum, the resulting values of k_s/k_f used were 73,000, 12,302, and 1434 representing vacuum, argon, and helium.

The results were determined to be mesh independent by successive refinement at the boundaries and at the solid-fluid interface. The resulting boundary and interface elements were 2.8% and 3.5% of the model's z thickness, respectively. Figure 4 shows the 1/16 model meshed for $\beta=2$ and $\rho=0.07$. The effective thermal conductivity for the x and z directions was calculated using the following:

$$k_{\text{eff},i} = \frac{q_i \Delta x_i}{\Delta T}, \quad i = x, z \tag{12}$$

where q_i is the average heat flux at the boundaries calculated by the FEA software. As a first approximation, the average k_{eff} was calculated from a simple weighting of the separate orthogonal values

$$k_{\text{eff}} = \frac{2k_{\text{eff},x} + k_{\text{eff},z}}{3} \tag{13}$$

Unless otherwise noted, this is the value presented in the results below.

Experimentally, the thermal conductivity of the foam samples listed in Table 1 was measured using the apparatus shown in Fig. 5. This uses a comparative method with a single type 304L stainless steel comparative (standard) material. Thermocouples were located along the axis of the experiment and on the exterior of the acrylic insulation. The temperature gradient in the Al and Cu plates was assumed zero due to their high relative thermal conductivity, and the thermal resistance of the thermal gaskets and foam-to-plate braze joints was neglected. After grouping the radial heat conduction into one term and any mass flow contribution into another, the energy balance about the central portion of the test cell is the following:

ferent foam parameters. Unigraphics solid modeling software (Unigraphics Solutions, Maryland Heights, MO) was used to create solid geometry that was analyzed with DesignSTAR (Structural Research and Analysis Corp., Santa Monica, CA).

Dirichlet type boundary conditions were applied to opposing sides of the model with k_s representing the solid foam and k_f for the interstitial material. The interstitial material was assumed stagnant since this was the assumption in the experimental apparatus discussed later. In order to compare to experimental results, an equivalent thermal conductivity due to radiation was necessary to represent k_f in the case where the foam is under vacuum. This was estimated using methods from Tao et al. [24], which resulted values of $0.001–0.005$ W/m K for low and high density foam, re-
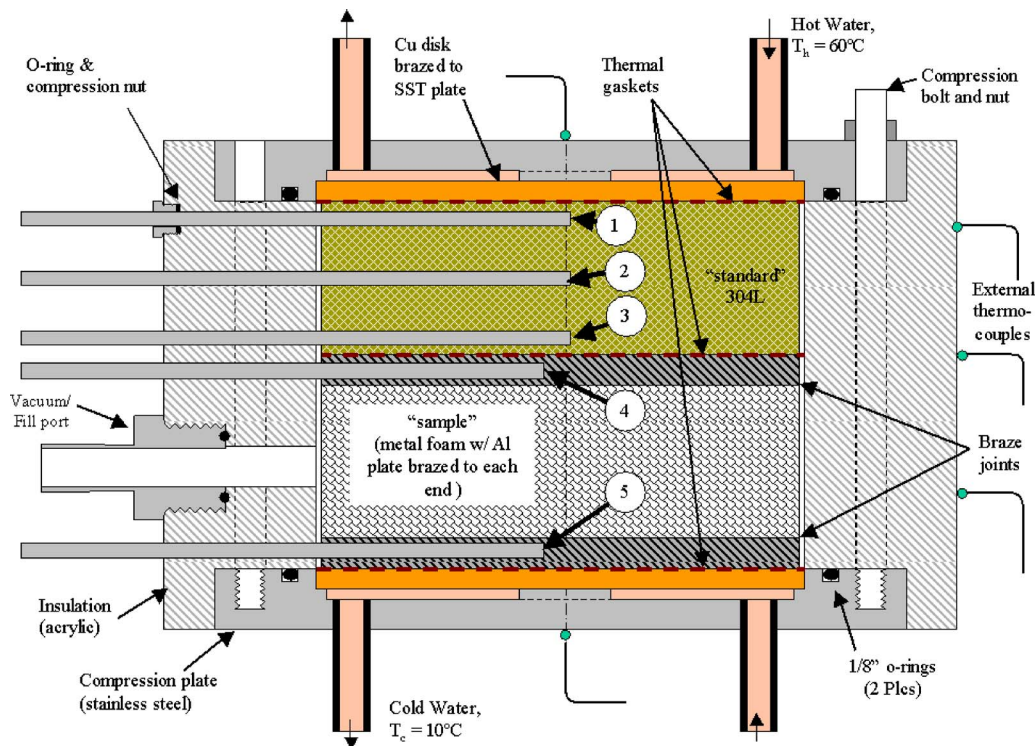

Fig. 5 Cross section of the cylindrical test cell used to measure thermal conductivity showing thermocouple location and numbering

Table 2 K_{eff} experimental setup information

Property	Value
k 6101 Aluminum (W/m K)	218
k Acrylic (W/m K)	0.19
k 304L stainless	Eq. (14)
k argon (W/m K)	0.0269
k helium (W/m K)	0.1450
k radiation (W/m K)	0.001–0.005
Compression bolt torque (N m)	1.8–2.7
L_{12} (mm)	12.7
L_{23} (mm)	12.7
L_{45} (mm) foam only	31.75
T_c (°C)	10
T_h (°C)	60

Fig. 6 Ligament hydraulic diameter histograms at 1×

$$Q_{13} = Q_{45} + Q_{\text{radial}} + Q_{\text{convect}} \qquad (14)$$

where the subscripts refer to the locations shown in Fig. 5. Using Fourier's Law the equation for k_{eff} is

$$k_{\text{eff}} = \left[\frac{k_{\text{st}}}{L_{13}}(T_1 - T_3) - \frac{Q_{\text{radial}}}{A_c} - \frac{Q_{\text{convect}}}{A_c} \right] \frac{L_{45}}{(T_4 - T_5)} \qquad (15)$$

Temperature data were obtained for vacuum ($<10^{-2}$ Pa), helium (101 kPa), and argon (101 kPa). Table 2 includes additional information about the experiment.

5 Results and Discussion

5.1 Geometric Parameters

5.1.1 Ligament Size. The results from the individual foam subsections were compared first for hydraulic diameter. For each sample subsection the modes were within 5% of each other. For each sample the subsection data were then combined and analyzed statistically for each magnification. Versus magnification, all of the sample modes except sample B were within 50 μm. In general the 1.3× results had larger standard deviations. It is believed that there were some braze alloy effects in this data set that shifted the average diameter larger thereby increasing the standard deviation.

The mean, mode, and standard deviation are listed in Table 3 for all the magnifications. Several intervals were analyzed to determine the average mode. The large standard deviations, which averaged 28% of the mean, were likely due to the ligament thinning phenomenon that occurs as δ increases [29]. This is consis-
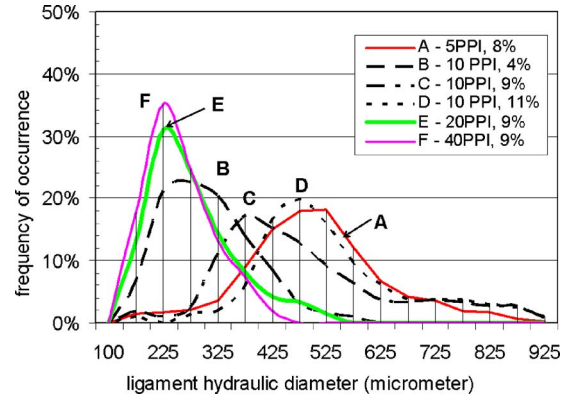
tent with other results [9]. Figure 6 shows the histograms of the samples at 1×. The mean varied directly with density, and both the mean and standard deviation varied indirectly with pore density.

The uncertainty in these measurements was quantified three ways. The hydraulic diameter of each object was calculated from area and perimeter using Eq. (10). The area calculation for Eq. (10) is a simple pixel count, whereas the perimeter calculation is a National Instruments algorithm that tends to smooth the object edges. The results from this algorithm are based to a certain extent on the orientation of the object to the image coordinates. The effect of this was a 3.8–7.3% variation from low to high density, which was based on multiple calculations versus rotation of the image. A second source of error is the uncertainty in the solid material demarcation. The uncertainty of this was assumed equal to Λ for each measurement. Statistically this error is minimal due to the number of objects measured. Finally, the error due to the perimeter algorithm was evaluated by using test images with exact solutions. The error of the National Instruments perimeter algorithm is a strong function of object size. The total uncertainty, U_{df}, was taken as the root of the squared sum of the three contributions.

The arithmetic mean is plotted versus ρ in Fig. 7 as the solid symbols with error bars representing U_{df}. The data from the literature are shown in Fig. 7 also as various other symbols [5,10,11]. The lower pore density samples did not change significantly with the magnification. The 20 and 30 PPI samples in-

Table 3 Ligament results for all foam samples and magnifications

|	Sample	A	B	C	D	E	F
	ρ (%)	8	3.8	8.7	11.4	8.5	8.7
	Pore density (PPI)	5	10	10	10	20	30
1.6×	Mean d_f (mm)	505	366	476	520	366	355
	Mode d_f (mm)	447	336	434	513	328	447
	Stand. dev. d_f (mm)	141	99	132	142	108	97
	$U_{df/df}$ (%) mean	10	14	11	11	15	15
1.3×	Mean d_f (mm)					330	329
	Mode d_f (mm)					241	248
	Stand. dev. d_f (mm)					153	144
	$U_{df/df}$ (%) mean					20	20
1×	Mean d_f (mm)	434	244	359	492	230	230
	Mode d_f (mm)	401	258	350	516	237	203
	Stand. dev. d_f (mm)	130	83	168	154	80	62
	$U_{df/df}$ (%) mean	17	30	18	16	33	35
	Heywood factor	1.21	1.30	1.20	1.18	1.25	1.23
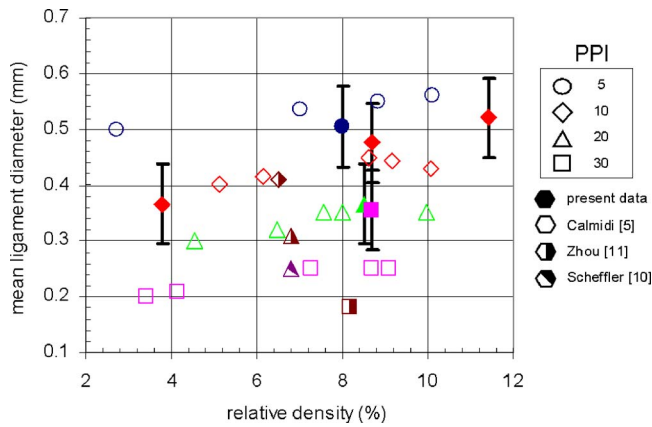
Fig. 7 Mean ligament diameter at 1.6× magnification compared to data in literature (symbol shape indicates PPI and symbol shading indicates source)

creased with magnification indicating final convergence was not obtained for these. Better resolution is necessary to continue a convergence study. Within the uncertainty, the data agree reasonably well with the literature with the exception of the 30 PPI sample, assuming the pore density can be considered a quantitative value.
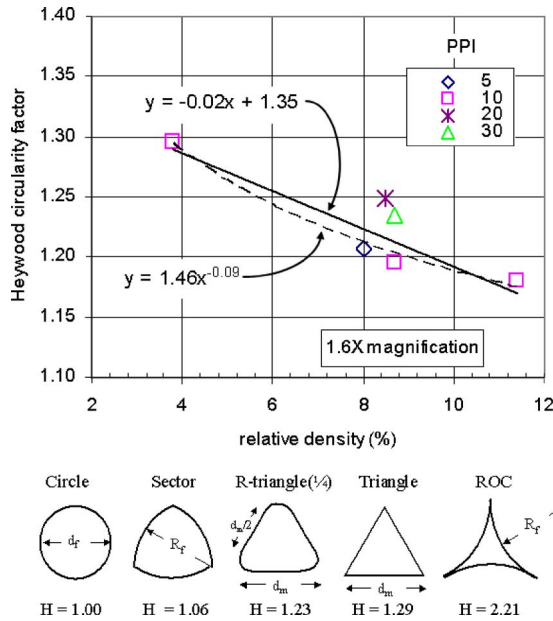

Fig. 8 Average Heywood circularity factor (Eq. (16)) for each sample at 1.6× (above) and for various ideal geometric shapes (below)

5.1.2 Ligament Shape. Ligament cross section is important for convection applications where an empirical heat transfer coefficient based on cross-sectional shape is employed [30]. In order to quantify the ligament cross-section shape, the Heywood circularity factor was used, which is the ratio of the object perimeter to the perimeter of a circle with the same area

$$H = \frac{P_{\text{object}}}{P_{\text{circle},A_i}} = \frac{P_{\text{object}}}{\sqrt{4\pi A_i}} \tag{16}$$

H is equal to one for a circle. This value was averaged over the entire sample data set and is plotted versus density in Fig. 8. The 10 PPI data points are shown with a linear least squares and a power law fit in Fig. 8. The value of H is also shown below for certain ideal shapes. It is unclear which fit function is appropriate without extending the range of density for the other pore densities. In either case, the slopes are negative, which qualitatively agrees with Ref. [5]. It is not clear if the dependence on the pore density is actual or due to random errors. For the high pore density samples at 1.6× the voxel sizes equate to approximately 5 pixels across the diameter of the ligament. If the voxel size was too large to capture the corners of the geometry this would tend to shift H to a lower value (that is, a more circular object), so we believe there is some real dependence on pore density. Measurements should be repeated with a higher magnification over a range of ρ and higher pore density to fully quantify this phenomenon, as there is no other data available for direct comparison. Implicitly, the shape versus density results could be compared to empirical data for Nusselt number correlations from Hwang et al. [31] for example.

5.1.3 Cell Size. Equivalent cell diameter results from Eq. (11) are listed in Table 4. The trend was similar to the ligament diameter results, in that standard deviation decreased with increasing pore density. There was negligible dependence on ρ. The uncertainty was based on two parts: the uncertainty in the image that was created and the uncertainty in the measurement. The image uncertainty was assumed to be the pixel size, which ranged from 2.5% to 4.7%. The measurement uncertainty was determined to be 7.3%, which results in an average total uncertainty of 8.0%.

The standard deviation decreases for smaller cell size and hence for shorter ligament lengths, indicating the propensity for ligament thinning with larger ligament length. The mean of each distribution is plotted in Fig. 9 versus the vendor specified pore density. The error bars represent the 8% uncertainty. The PPI designation is better described as a category of pore size with 30 PPI being more uncertain [29]. Therefore it is not known if the variation in linearity is simply random variation between foam lots or a systemic error in measurement. Also shown are the data from Zhou et al. [11], which were measured from three-dimensional image SEM covering densities of 6.5–8%. The variation in cell diameter with ρ that was shown was not apparent in the present data and was also not apparent in data for another foam production method [32]. The one point (20 PPI, 6.8%) from Scheffler et al. [10] was determined using microCT and image

Table 4 Summary of data from cell size measurements

Sample	A	B	C	D	E	F	Ave.
ρ (%)	8	3.8	8.7	11.4	8.5	8.7	
Pore density (PPI)	5	10	10	10	20	30	
No. samples (cells)	312	312	312	312	312	312	
Mean diam (mm)	4.60	4.20	4.24	4.40	2.80	2.47	3.78
Mode (mm)	4.75	4.55	4.58	4.60	3.00	2.64	
Std. dev. (mm)	0.75	0.71	0.72	0.65	0.46	0.40	
Std. dev. (%)	16	17	17	15	16	16	16.2
U_Φ/Φ (%)	7.7	7.8	7.8	7.8	8.4	8.7	8.0
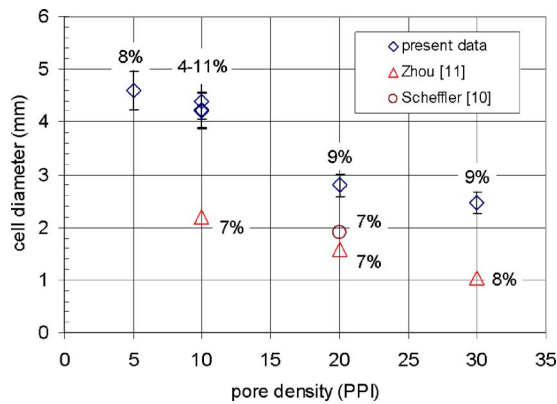
Fig. 9 Comparison of mean cell diameter results to data in the literature

Fig. 10 S_v comparison versus mode of measured cell diameter (8–8.7% density)

analysis without discussion about method or number of samples. The slope of the data is similar, however the present data are higher by 50%.

5.1.4 Surface Area. Both surface area and relative density were calculated for the foam samples using CT. To provide an indication of the accuracy of the CT surface area measurements (presented later), the relative density determined by CT was compared to the gravimetrically determined density of the foam. With the exception of two data points, the results were within the uncertainty of the gravimetric density calculation. For higher pore density, there was less variation with magnification but the error increased to 18% at 30 PPI.

For surface area, each subsection was first compared. The maximum variation of a particular sample was 25% in the sample F. The variation was <12% otherwise, which tended to decrease with magnification. S_v for each sample was calculated by summing the four subsections and then dividing by the total calculation region volume (Table 5). S_v increased with magnification except for the low density, large cell data. In these cases, the 1.6 × data, which were scanned at 3× (38 μm voxel) and then reduced to 1/2 resolution, appears to be a better measurement than the 2× full resolution.

For the 10 PPI sample (B, C, and D) and the constant density samples (ρ=8–8.7%), S_v increased with magnification and appeared to converge. S_v varied directly with relative density and pore density. Data were compared to Eq. (1) with data from Calmidi and Mahajan [5]. The CT values diverged from Eq. (1) with increasing magnification. Equation (1) was 20–25% lower than the high magnification CT values.

Specific surface areas were also measured by Ozmat et al. [17] using the BET method. These were about 40% higher, and there was a common trend with pore density in surface area; however, the trend in density was inverted. The actual surface of the metal foam has smaller scale features that to a certain extent are lost in the x-ray tomography scan producing a larger BET S_v measurement than the CT calculation. Therefore the BET method may be
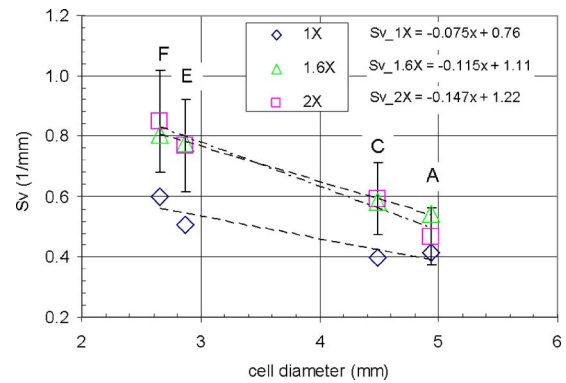
more appropriate depending on the application of the data. It was not clear if the discrepancy is due to loss of the small-scale features. The samples from Ozmat et al. [17] were necessarily compressed by 30% to increase the specific surface area for a given sample size, which may alter the uncompressed surface area. It is also not clear what the uncertainty in the BET measurement is, since this method is typically used for much higher specific surface area materials [33].

Since the PPI designation is better described as a category of pore size for the samples [29], the S_v data were plotted versus the cell diameter measurements from the previous section. This is shown in Fig. 10 with linear least square curve fits for each magnification. The error bars shown correspond to the error between the CT ρ and gravimetrically determined ρ. This shows the same general trend in conversion with increased magnification and a linear relation with cell diameter.

In order to compare the S_v to the TetraK model, a final value as a function of foam parameters was necessary. It is believed that due to the convergence of the S_v data with magnification the calculations are within the error of the density comparison (<18%). We believe this is conservative based on a zeroth order estimate that the error in the volume calculation will be higher due to the higher order dependence on d_f. The slight variations in the results for the 2× and the 1.6× data were believed to be due to random errors in the system and were averaged. These values are shown in Table 5.

5.2 Geometric Property Comparison to 3D Model. With the surface area determined and measurements of cell and ligament size obtained, the TetraK model was evaluated for geometric self-consistency. In dimensional form, the geometric parameters in Fig. 2 create a closed set of parameters (d_f, δ, β, ρ, S_v, Φ), noting that β is really a function of d_n and d_f. These variables are related by the constitutive equations (Eqs. (5)–(8)). Data for d_f and ρ and an assumed β were used to solve Eq. (6) for δ. Then Eq. (7) was used to solve for S_v and subsequently Eq. (5) for Φ. This resulted in calculated values for S_v, δ, d_p, and Φ. The as-

Table 5 S_v for the foam samples versus magnification and voxel size (mm^{-1})

ID	Pore density (PPI)	Relative density (%)	1×	1.3×	1.6×	2×	1.6× and 2× ave.
			0.115	0.084	0.073	0.058	
A	5	8.0	0.41		0.54	0.47	0.51
B	10	3.8	0.32		0.46	0.42	0.44
C	10	8.7	0.40		0.58	0.59	0.59
D	10	11.4	0.47		0.58	0.62	0.60
E	20	8.5	0.51	0.64	0.78	0.77	0.77
F	30	8.7	0.60	0.77	0.80	0.85	0.83

Table 6   Summary of data from TetraK geometric calculations

ID	Pore density (PPI)	Relative density (%)	β	$\Phi_{\text{calculated}}$ (mm)	$\dfrac{\Phi_{\text{calculated}}}{\Phi_{\text{measured}}}$	$d_{p,\text{calc}}$ (mm)	δ (mm)
A	5	0.080	1.5	5.15	1.12	2.61	1.72
B	10	0.038	1.0	5.04	1.20	2.55	1.68
C	10	0.087	1.4	4.55	1.13	2.53	1.52
D	10	0.114	1.9	4.99	1.07	2.30	1.66
E	20	0.085	1.3	3.47	1.24	1.76	1.16
F	30	0.087	1.3	3.25	1.31	1.64	1.08

sumed value for β was iterated until the S_v from Eq. (7) matched the S_v measured with CT. This was successful for each of the six samples, with the exception of sample B ($\rho=3.8\%$), which was not matchable due to a lower limit on β. The resulting geometric parameters are listed in Table 6 and discussed below.

The calculated TetraK cell diameter falls within the standard deviation of the measured values except for smallest cell diameter. Their ratio is listed in Table 6. The measured data are likely lower due to the elongation of the foam cells in the z-direction, which can be as high as 38% [11]. The pore diameter resulting from the TetraK calculation was compared to Calmidi and Mahajan [5]. It was approximately 25% lower than their data. Their data are based on a hexagonal dodecahedron, and it is not clear how a pore diameter was obtained from their data, so we believe that this comparison is qualitative. The average pore diameter of another model, such as the Weaire–Phelan model [28] may compare more favorably since it is a conglomeration of polyhedrons that has a more representative pore shape distribution [8]. The pore diameter was plotted versus the measured cell diameter, which demonstrated a linear relationship. There is limited data for δ, the ligament length. The present calculations have similar slope to the data from the other references [11,17]; however, the values fall between the Ozmat et al. [17] fit to experimental data that used a dodecahedron and Zhou et al. [11] who used optical measurements from three-dimensional SEM images.

The last comparison was for β, ν, and d_n versus ρ and Φ. β varies directly with relative density and cell diameter, which implies material is shifting from the ligaments to the nodes. The sample B ($\rho=3.8\%$) $S_{v,\text{calc}}$, was not matched to the $S_{v,\text{CT}}$, calculation due to a lower limit of 1 for β. A β of less than one is still physical, but the TetraK model does not support this as it was formulated in Eqs. (6) and (7). As $\beta \rightarrow 0$, $d_n \rightarrow d_f$, which is the lower limit on a physically realistic model. This is an indication that in this case the circular ligament cross section is limiting the ability of this model. The S_v will increase as the ligament cross-sectional shape approaches a triangle, which is the case for the small density foam.

The TetraK model was overall a good approximation of the real foam geometry for predicting intensive properties and magnitude of the extensive properties with some exceptions at very low density. Incorporation the shape of the ligament cross section and thinning of the ligaments may improve the geometric model.

5.3 Thermal Conductivity Results. The effective thermal conductivity was first calculated using FEA for a range of densities for $\beta=1$ and $\beta=2$ to understand the effects of this parameter. Using Eq. (12), the maximum variation of k_{eff} for the TetraK model between the x and z directions was determined to be 6% for $\beta=1$ and 4% for $\beta=2$ over the applicable range of relative density. To explore the effects of the unit cell used, FEA results were also obtained for a unit cell with twice the z thickness as Fig. 4. The difference between the k_{eff} results were insignificant between the models. A unit cell that was rotated 45 deg about the z axis in Fig. 4 was modeled as well. Although, the variation between the orthogonal k_{eff} values was greater (13%), the average k_{eff} using

Eq. (13) was nearly identical to the unit cell shown in Fig. 4. Therefore, based on the study of unit cell effects, Eq. (13) with the unit cell shown in Fig. 4 was deemed sufficient to calculate average thermal conductivity for the TetraK structure, and a more elaborate formulation was not pursued.

In general, k_{eff} is a parabolic function of β with a maximum at β equal to approximately 1.4. The FEA results were compared to data in the literature using the correlation in Eq. (2). This indicated that β must increase with increasing density. That is, more material is accumulating at the ligament vertices with increasing density, which is consistent with the findings from the previous geometric comparison results. The k_{eff} was also calculated for each parameter set in Table 1 in order to compare the TetraK ideal model to the real foam. The geometry for each of these later models was determined using the results from the previous geometry section.

The thermal conductivity experiment was characterized in regard to system errors. Ice bath measurements with the thermocouples indicated that the temperature differences, T_1-T_3 and T_4-T_5, had a total error of 0.5% and 0.3%, respectively. Random variations due to assembly alignment variations were investigated by repeated assembly/disassembly and eliminated through various means. The uncertainty in the length measurements was $+/-4.9\%$. For Eq. (15), k_{st} must be known. Data for type 304L stainless steel were gathered from the literature to obtain the following temperature relationship [2,34,35]:

$$k_{\text{st}} = 0.0171T + 14.228 \tag{17}$$

All the 304L data was within $+/-3\%$ of Eq. (17), which was the assumed uncertainty in k_{st}. The Q_{radial} term in Eq. (15) was calculated using the centerline temperature distribution and the temperatures of the outer acrylic insulation. The worst-case radial heat flow was 2% of the axial heat flow and is neglected from here forward. The Q_{conv} term in Eq. (15) was investigated by operating the test cell in multiple orientations with respect to gravity. There were no detectable changes in k_{eff} with respect to orientation therefore this term was assumed negligible. A general uncertainty analysis of the experiment was performed using the remaining terms of Eq. (15) and the following:

$$\frac{U_{k_{\text{eff}}}}{k_{\text{eff}}} = \left[\sum_i \left(\frac{1}{k_{\text{eff}}} \frac{\partial k_{\text{eff}}}{\partial X_i} U_{X_i} \right)^2 \right]^{1/2} \tag{18}$$

where i represents each independent variable of Eq. (15) assuming the uncertainties are independent and Eq. (15) and its derivatives are continuous [36]. This resulted in the following equation for the uncertainty normalized with k_{eff}:

$$\frac{U_{k_{\text{eff}}}}{k_{\text{eff}}} = \left[\left(\frac{U_{k_{\text{st}}}}{k_{\text{st}}} \right)^2 + \left(\frac{U_{L_{45}}}{L_{45}} \right)^2 + \left(\frac{U_{L_{13}}}{L_{13}} \right)^2 + \left(\frac{U_{dT_{13}}}{dT_{13}} \right)^2 \right. $$
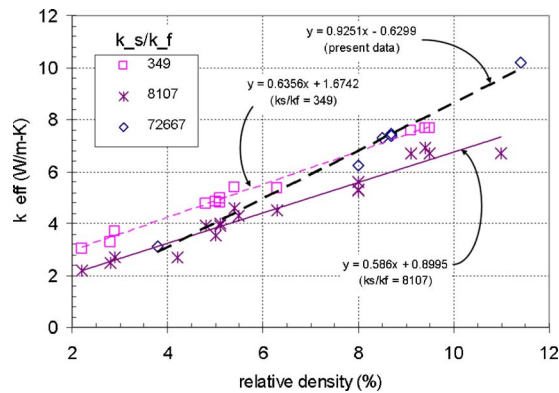$$\left. + \left(\frac{U_{dT_{45}}}{dT_{45}} \right)^2 \right]^{1/2} \tag{19}$$

where

Fig. 11 All k_{eff} data for Duocell® foam in literature (**present data for vacuum**)
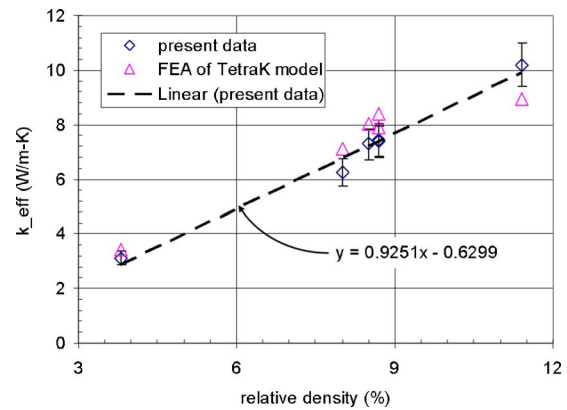

Fig. 12 Comparison of TetraK model numerical k_{eff} and present experimental data for vacuum. Present experimental data has linear least squares curve fit and experimental error from Eq. (19).

$$\left(\frac{U_{dT_{ij}}}{dT_{ij}}\right)^2 = \left(\frac{U_{T_i}}{T_i - T_j}\right)^2 + \left(\frac{U_{T_j}}{T_i - T_j}\right)^2 \qquad (20)$$

The value for Eq. (19) averaged 7.9% for all the data with U_{L13}/L_{13} being the dominant term.

Results from Eq. (15) were normalized by ρ and k_s (218 W/m K) to achieve the form of Eq. (3). This resulted in an average value of $C = 0.39$ with a 6% standard deviation. This falls between values of C from previous investigations [17,25,26], which varied from 0.33 to 0.46. There was insignificant variation with pore density, which was consistent with other investigations [5,20].

The present experimental data were compared with data from the literature [5,16,21] in Fig. 11. Linear least squares curve fits are shown separately for the present data ($k_s/k_f = 72,667$, vacuum), the literature data for $k_s/k_f = 349$ (water), and the literature data for $k_s/k_f = 8107$ (air). The magnitude of the present data's slope is larger compared with data from the literature. Several explanations for the larger slope were investigated. The data from each individual investigation have a characteristic slope with respect to density that appears to be tied to the method by which the foam was joined to the test apparatus. Data from the present investigation, which have the largest slope of all the individual data sets, have the better thermal connection due to the high alloy braze technique used. Braze alloy has wicked itself onto the ligaments near the Al end plates, augmenting k_{eff} in the joint region and has reduced the contact resistance. Data from Calmidi and Mahajan [5] have a smaller slope, which was also obtained with a brazed condition. This may have been a low volume alloy braze however. The slope of the data in the other investigations, Refs. [16,21], is lower yet due to a mechanical joint, which likely results in a larger contact resistance. This contact resistance will be a function of the interstitial fluid thermal conductivity. In the present experiment, brazing the foam to the end plates has minimized this contact resistance and removed the fluid dependence.

Finally, FEA results of the TetraK model and the present experimental values for k_{eff} were compared. As previously indicated, the FEA results for $\beta = 1$ and $\beta = 2$ bound the experimental results. The exact geometries ($1 < \beta < 2$) determined from the previous sections were modeled using FEA and are compared in Fig. 12 for the vacuum case. The linear curve fit is for the experimental data, and the error bars represent the experimental error determined from Eq. (19). The average error between the model and the experimental thermal conductivity data was 11%, and the maximum was 14% for the largest density sample ($\rho = 11.4\%$). The FEA result for this density appears to be anomalistically low in relation to the other densities. We believe this is an indication of a limitation of the TetraK model at large relative density. At large density, β is greatest, therefore the most material is in the nodal region. This region is represented by a sphere, which is not conducting as

efficiently from ligament to ligament as a tetrahedral shape with the same density. After inspection of Fig. 1, it is apparent that a tetrahedral shape is a better representation of the nodal region with respect to thermal conductivity. At lower density the value of β is less significant therefore we do not see this effect. In general, we believe the TetraK model represents the thermal conductivity well with a slight bias to underpredict at high density.

6 Conclusions

A tetrakaidecahedronal three-dimensional model was proposed to simulate the complex structure of high porosity metal foam to evaluate foam geometric and thermal properties. Relations for porosity and specific surface area of the foam were determined in terms of dimensionless parameters convenient for parametric studies. To address limitations in previous investigations, computed tomography at three magnifications was utilized to acquire data for six metal foam samples with varying pores density and porosity. The surface area data trended well with magnification and appeared to converge. An error of less than 18% is attributed to the surface area measurement. The large pore density samples appear to be at the limit of the use of this particular CT apparatus. Cell diameter and ligament diameter were acquired from the samples using two-dimensional image analysis, and the ligament cross-sectional shape was quantified. The proposed three-dimensional geometric model was evaluated with this acquired geometric property data. The node diameter varies directly with cell diameter and relative density, indicating that in real foams extra material accumulates at the vertices at larger densities. Overall, the ideal model was a reasonable approximation of the real foam geometry and is self-consistent with respect to its extensive and intensive geometric properties. The data acquired here allow for future evaluation of other geometric models. The effective thermal conductivities predicted by the proposed model and measured in our experiments were compared with previous investigations. Our data have a larger dependence on relative density compared with others. The method in which the foam is connected in parallel to the experimental apparatus appears to have a significant affect on the results. When using the exact geometric parameters determined from the TetraK model, the thermal conductivity predictions are within the experimental data error with the exception of the high density sample. Therefore, our proposed foam model was shown to be self-consistent with respect to both the geometric and thermal properties with some limitations at the density extremes. We believe this evaluation of a metal foam model for thermal applications is the first of its kind in the literature.

Nomenclature

A_i = area of pixels
A_c = cross-sectional area
BET = Brunauer, Emmett, and Teller surface adsorption technique
C = tortuosity factor used in Eq. (3)
CT = computed tomography determined parameter
F = weighting function used in k_{eff} correlation [22]
FEA = finite element analysis
H = Heywood circularity factor, Eq. (16)
L = length between thermocouple locations (m)
LTNE = local thermal nonequilibrium
N = number of pixels
P = perimeter (m)
PPI = vendor designation for pores density (pores/in.)
R_f = radius of curvature used to describe ideal shapes
Q = heat flow (W)
S_v = specific surface area (m^{-1})
SEM = scanning electron microscopy
T = temperature (°C)
U = measurement uncertainty
X = magnification indication of sample ($1\times = 115$ μm voxel size)
d_f = ligament diameter (m)
d_n = node diameter (m)
d_p = pore diameter (m)
k_{eff} = effective thermal conductivity (W/m K)
$k_{eff,calc}$ = effective thermal conductivity using parallel fluid path (W/m K)
$k_{eff,vac}$ = effective thermal conductivity in vacuum (W/m K)
k_{st} = thermal conductivity of 304 stainless steel (W/m K)
k_s = thermal conductivity of foam parent material (W/m K)
k_{eff} = effective thermal conductivity (W/m K)
k_f = thermal conductivity of interstitial material (W/m K)
q = heat flux (W/m^2)
u = dimensionless ligament diameter to length ratio, d_f/δ
x = spatial dimension in FEA model
β = node size parameter $d_n = d_f\sqrt{1-\beta^2}$
γ_i = geometric function i of β
δ = length of ligament from node center to node center
ε = foam void fraction, $1-\rho$
ρ = relative density (solid fraction), $1-\varepsilon$
Δ = scalar difference
Λ = pixel or voxel size
Φ = foam cell diameter

References

[1] Kim, K. J., Lloyd, G., Razani, A., and Feldman, K. T., 1998, "Development of Lani5/Cu/Sn Metal Hydride Powder Composites," Powder Technol., **99**(1), pp. 40–45.
[2] Lloyd, G., Kim, K. J., Razani, A., and Feldman, K. T., 1998, "Thermal Conductivity Measurements of Metal Hydride Compacts Developed for High-Power Reactors," J. Thermophys. Heat Transfer, **12**(2), pp. 132–137.
[3] Fleming, W. H., Khan, J. A., and Rhodes, C. A., 2001, "Effective Heat Transfer in a Metal-Hydride-Based Hydrogen Separation Process," Int. J. Hydrogen Energy, **26**(7), pp. 711–724.
[4] Heung, L. K., 1998, "On-Board Hydrogen Storage System Using Metal Hydride," *Proceedings of the 2nd International Symposium on Hydrogen Power Theoretical and Engineering Solutions*, August 18–22, 1997, Grimstad, Norway, Kluwer Academic Publishers, Dordrecht, The Netherlands, pp. 251–256.
[5] Calmidi, V. V., and Mahajan, R. L., 1999, "The Effective Thermal Conductivity of High Porosity Fibrous Metal Foams," ASME J. Heat Transfer, **121**(2), pp. 466–471.
[6] Bhattacharya, A., Calmidi, V. V., and Mahajan, R. L., 2002, "Thermophysical Properties of High Porosity Metal Foams," Int. J. Heat Mass Transfer, **45**(5), pp. 1017–1031.
[7] Boomsma, K., and Poulikakos, D., 2001, "On the Effective Thermal Conductivity of a Three-Dimensionally Structured Fluid-Saturated Metal Foam," Int. J. Heat Mass Transfer, **44**(4), pp. 827–836.
[8] Montminy, M., Tannenbaum, A., and Macosko, C., 2004, "The 3-D Structure of Real Polymer Foams," J. Colloid Interface Sci., **37**(6), pp. 501–515.
[9] Montminy, M., Tannenbaum, A., and Macosko, C., 2001, "New Algorithms for 3-D Imaging and Analysis of Open-Celled Foams," J. Cell. Plast., **37**(6), pp. 501–515.
[10] Scheffler, F., Herrmann, R., Schwieger, W., and Scheffler, M., 2004, "Preparation and Properties of an Electrically Heatable Aluminium Foam/Zeolite Composite," Microporous Mesoporous Mater., **67**(1), pp. 53–59.
[11] Zhou, J., Mercer, C., and Soboyejo, W. O., 2002, "An Investigation of the Microstructure and Strength of Open-Cell 6101 Aluminum Foams," Metall. Mater. Trans. A, **33**(5), pp. 1413–1427.
[12] Calmidi, V., and Mahajan, R., 2000, "Forced Convection in High Porosity Metal Foams," ASME J. Heat Transfer, **122**(3), pp. 557–565.
[13] Phanikumar, M., and Mahajan, R., 2002, "Non-Darcy Natural Convection in High Porosity Metal Foams," Int. J. Heat Mass Transfer, **45**(18), pp. 3781–3793.
[14] Tadrist, L., Miscevic, M., Rahli, O., and Topin, F., 2004, "About the Use of Fibrous Materials in Compact Heat Exchangers," Exp. Therm. Fluid Sci., **28**(2–3), pp. 193–199.
[15] Schmierer, E. N., Razani, A., Melton, T., and Keating, S., 2004b, "Characterization of High Porosity Open-Celled Metal Foam Using Computed Tomography," *Proceedings of 2004 ASME International Mechanical Engineering Congress and RD&D Expo*, ASME, New York.
[16] Schmierer, E. N., Razani, A., Paquette, J. W., and Kim, K. J., 2004a, "Effective Thermal Conductivity of Fully Saturated High Porosity Foam," *Proceedings of 2004 ASME Heat Transfer/Fluids Engineering Summer Conference*.
[17] Ozmat, B., Leyda, B., and Benson, B., 2004, "Thermal Applications of Open-Cell Metal Foams," Mater. Manuf. Processes, **19**(5), pp. 839–862.
[18] Dul'nev, G. N., 1965, "Heat Transfer through Solid Disperse Systems," J. Eng. Phys., **9**, pp. 275–278.
[19] Hsu, C. T., Cheng, P., and Wong, K. W., 1995, "A Lumped-Parameter Model for Stagnant Thermal-Conductivity of Spatially Periodic Porous-Media," ASME J. Heat Transfer, **117**(2), pp. 264–269.
[20] Takegoshi, E., Hirasawa, Y., Matsuo, J., and Okui, K.-I., 1992, "A Study on Effective Thermal Conductivity of Porous Metals," Trans. Jpn. Soc. Mech. Eng., Ser. A, **58**(547), pp. 237–242.
[21] Paek, J. W., Kang, B. H., Kim, S. Y., and Hyun, J. M., 2000, "Effective Thermal Conductivity and Permeability of Aluminum Foam Materials," Int. J. Thermophys., **21**(2), pp. 453–464.
[22] Singh, R., and Kasana, H. S., 2004, "Computational Aspects of Effective Thermal Conductivity of Highly Porous Metal Foams," Appl. Therm. Eng., **24**(13), pp. 1841–1849.
[23] Doermann, D., and Sacadura, J. F., 1996, "Heat Transfer in Open Cell Foam Insulation," ASME J. Heat Transfer, **118**, pp. 88–93.
[24] Tao, W. H., Hsu, H. C., Chang, C. C., Hsu, C. L., and Lin, Y. S., 2001, "Measurement and Prediction of Thermal Conductivity of Open Cell Rigid Polyurethane Foam," J. Cell. Plast., **37**(4), pp. 310–332.
[25] Glicksman, L. R., Torpey, M., and Marge, A., 1992, "Means to Improve the Thermal Conductivity of Foam Insulation," J. Cell. Plast., **28**(6), pp. 571–583.
[26] Dharmasena, K., and Wadley, H., 2002, "Electrical Conductivity of Open-Cell Metal Foams," J. Mater. Res., **17**(3), pp. 625–631.
[27] Fourie, J. G., and Du Plessis, J. P., 2004, "Effective and Coupled Thermal Conductivities of Isotropic Open-Cellular Foams," AIChE J., **50**(3), pp. 547–556.
[28] Weaire, D., and Hutzler, S., 1999, *The Physics of Foam*, Clarendon Press, Oxford.
[29] Leyda, B., 2002–2004 (personal communication) (Chief Scientist at ERG Aerospace).
[30] Lu, T. J., Stone, H. A., and Ashby, M. F., 1998, "Heat Transfer in Open-Cell Metal Foams," Acta Mater., **46**(10), pp. 3619–3635.
[31] Hwang, J. J., Hwang, G. J., Yeh, R. H., and Chao, C. H., 2002, "Measurement of Interstitial Convective Heat Transfer and Frictional Drag for Flow Across Metal Foams.," ASME J. Heat Transfer, **124**(1), pp. 120–9.
[32] Zhao, C. Y., Kim, T., Lu, T. J., and Hodson, H. P., 2004, "Thermal Transport in High Porosity Cellular Metal Foams," J. Thermophys. Heat Transfer, **18**(3), pp. 309–317.
[33] Badalyan, A., and Pendleton, P., 2003, "Analysis of Uncertainties in Manometric Gas-Adsorption Measurements. I: Propagation of Uncertainties in Bet Analyses," Langmuir, **19**(19), pp. 7919–7928.
[34] Assael, M. J., Gialou, K., Kakosimos, K., and Metaxa, I., 2004, "Thermal Conductivity of Reference Solid Materials," J. Thermophys. Heat Transfer, **25**(2), pp. 397–408.
[35] ASME, 2003, Part II Materials: Subpart D Properties, in American Society of Mechanical Engineers: Boiler and Pressure Vessel Code.
[36] Coleman, H. W., and Steele, W. G., 1989, *Experimentation and Uncertainty Analysis for Engineers*, Wiley, New York.

Free Convective Heat and Mass Transfer in a Doubly Stratified Non-Darcy Porous Medium

P. A. Lakshmi Narayana

P. V. S. N. Murthy[1]
e-mail: pvsnm@iitkgp.ac.in

Department of Mathematics,
Inidan Institute of Technology, Kharagpur,
Kharagpur, 721 302, W.B., India

Free convective heat and mass transfer from a vertical surface embedded in a doubly stratified non-Darcy porous medium has been analyzed. The wall temperature and concentration are constant and the medium is linearly stratified in the vertical direction with respect to both temperature, and concentration. A series approximation is made for stream function, temperature, and concentration in terms of the stratification parameter. The flow, temperature, and concentration fields are affected by the complex interactions among the diffusion ratio Le, buoyancy ratio N and stratification ratio Sr in addition to the inertia parameter F_c. The effect of double stratification of the medium on nondimensional heat and mass transfer coefficients is discussed.
[DOI: 10.1115/1.2352788]

Keywords: heat transfer, mass transfer, double stratification, boundary layer, porous media, convection, series solution

Introduction

Coupled heat and mass transfer phenomenon in porous media is gaining attention due to its interesting applications. The flow phenomenon in this case is relatively complex than that in pure thermal/solutal convection process. Processes involving heat and mass transfer in porous media are often encountered in the chemical industry, in reservoir engineering in connection with thermal recovery process, in the study of dynamics of hot and salty springs of a sea. Underground spreading of chemical waste and other pollutants, grain storage, evaporation cooling, and solidification are a few other application areas where combined thermosolutal convection in porous media are observed.

Under boundary layer assumptions Bejan and Khair [1] and Lai and Kulacki [2] have analyzed free convection heat and mass

transfer in porous media while Lai [3] studied mixed convection heat and mass transfer from a vertical wall in a Darcian fluid saturated porous medium. Due to the coupling of temperature and concentration, new parameters like buoyancy ratio and Lewis number (diffusion ratio) arise and they influence the convective transport to a greater extent. For moderate flows, the Darcy law is invalid and the effect of inertia and solid boundary are well discussed in Vafai and Tien [4]. Recently, Murthy [5] analyzed the effect of double dispersion on mixed convection heat and mass transfer in a non-Darcy porous medium and discussed the effect of Lewis number, buoyancy ratio on the heat, and mass transfer coefficients in both the aiding and opposing flows. A review of both natural and mixed convection boundary layer flows in Darcy and non-Darcy fluid saturated porous media is given in Nield and Bejan [6].

Although the effect of stratification of the medium on the heat removal process in a porous medium is important, very little work has been reported in the literature. Bejan [7], Singh and Sharma [8], and Kalpana and Singh [9] studied the problem of boundary layer free convection along an isothermal vertical plate immersed in a thermally stratified fluid saturated porous medium using integral and series solution techniques. The case of power law variation of wall temperature with thermal stratification of the medium was discussed at length by Nakayama and Koyama [10], and by Lai et al. [11]. Takhar and Pop [12] investigated the free convective transport from a vertical flat plate in a thermally stratified Darcian medium where the ambient temperature varies as $x^{1/3}$ using the similarity solution technique. In practical situations where the heat and mass transfer mechanisms run parallel it is interesting to analyze the effect of double stratification (stratification of the medium with respect to the thermal and concentration fields) on the convective transport in porous media. Murthy et al. [13] extended the work of Takhar and Pop [12] to uncover the effect of double stratification on free convection heat and mass transfer in a Darcian fluid saturated porous medium using the similarity solution technique. Interesting results for heat and mass transfer in the boundary layers were reported in [13]. The effect of thermal stratification of the medium and thermal dispersion on the mixed convection heat and mass transfer from a vertical wall in a non-Darcy porous medium has been analyzed recently by Chamkha and Khaled [14] using power law variation for the thermal stratification.

In combined heat and mass transfer studies in porous media, Murthy et al. [13] reported that the temperature and concentration became negative in the boundary layer depending on the relative intensity of the thermal and solutal stratification. Similarly, Postelnicu [15] has reported in his study of effect of Dufour and Soret parameters on free convection on combined heat and mass transfer in porous media that both nondimensional heat and mass transfer coefficients become negative for certain combinations of the Lewis number and the buoyancy ratio. These are a few articles to quote from the literature where the temperature/concentration or nondimensional heat/mass transfer coefficients becoming negative. Angirasa et al. [16] presented an analysis of combined heat and mass transfer in a thermally stratified porous enclosure while
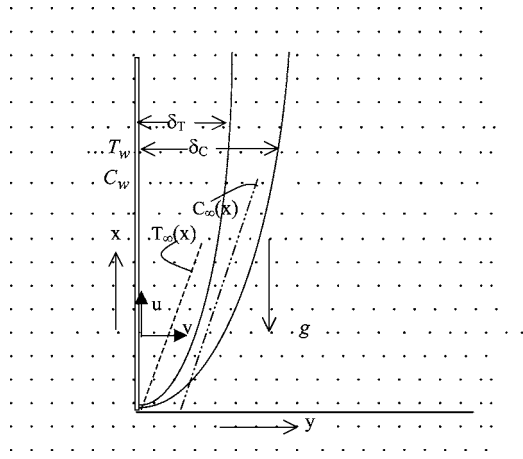
Fig. 1   Free convective heat and mass transfer from a semi-infinite vertical wall in a fluid saturated doubly stratified porous medium

Rathish Kumar and Shalini [17] presented the free convection heat and mass from a vertical wavy surface in a doubly stratified external porous layer.

The results presented in [12,13] have given the impetus for investigating free convection heat and mass transfer characteristics in a non-Darcian fluid saturated doubly stratified porous medium. Unlike in [12] and [13], the medium is assumed to be stratified linearly with the height, which is a more physically realistic case. As a result of this, the mathematical model ceases to have a similar solution. In the light of the results obtained in [13], the present analysis will be more significant as will be clear from the section, "Results and Discussion." This type of investigation is useful in understanding heat and mass transfer characteristics around a hot radioactive subsurface storage site or around a cooling magmatic intrusion where the theory of convection heat and mass transport is involved.

Governing Equations

Consider the flow configuration shown in Fig. 1. The flow is moderate (i.e., order of Reynolds number is greater than one), so pressure drop is proportional to the linear combination of fluid velocity and the square of the velocity (Forchheimer flow model). Viscous resistance due to the solid boundary is neglected under the assumption that the medium is with low permeability. The vertical wall temperature and concentration are assumed to be constant and the porous medium is assumed to be vertically linearly stratified with respect to both heat and concentration as indicated in the Fig. 1. The boundary layer equations along with the equation of continuity may be written as

$$\frac{\partial u}{\partial x} + \frac{\partial v}{\partial y} = 0 \tag{1}$$

$$\frac{\partial u}{\partial y} + \frac{c\sqrt{K}}{\nu}\frac{\partial u^2}{\partial y} = \left(\frac{Kg\beta_T}{\nu}\right)\frac{\partial T}{\partial y} + \left(\frac{Kg\beta_C}{\nu}\right)\frac{\partial C}{\partial y} \tag{2}$$

$$u\frac{\partial T}{\partial x} + v\frac{\partial T}{\partial y} = \alpha\frac{\partial^2 T}{\partial y^2} \tag{3}$$

$$u\frac{\partial C}{\partial x} + v\frac{\partial C}{\partial y} = D\frac{\partial^2 C}{\partial y^2} \tag{4}$$

and the boundary conditions are

$$y = 0: v = 0, T = T_w, C = C_w$$
$$y \to \infty: u \to 0, T = T_{\infty,0} + Ax, C = C_{\infty,0} + Bx \tag{5}$$

Here x and y are the Cartesian coordinates, u and v are the averaged velocity components in x and y directions, respectively, T and C are the dimensional temperature and concentration, respectively, β_T and β_C are the coefficients of thermal and solutal expansion, respectively, c is the Forchheimer constant, ν is the kinematic viscosity of the fluid, K is the permeability, g is the acceleration due to gravity, and α, D are the thermal and solutal diffusivities of the medium. Here, A and B are constants, varied to alter the intensity of stratification in the medium. The thicknesses of thermal and solutal boundary layers (δ_T, δ_c), which are shown in Fig. 1, are depending on the strength of the respective field and for all calculations we have taken the boundary layer thickness as the maximum of these values. The subscripts w, $(\infty,0)$ and ∞ indicate the conditions at the wall, at some reference point in the medium, and at the outer edge of the boundary layer respectively.

Making use of the following transformation which is derived using order magnitudes

$$\eta = \frac{y}{x}\text{Ra}_x^{1/2}, \quad f(x,\eta) = \frac{\psi}{\alpha\text{Ra}_x^{1/2}} \tag{6}$$

$$\theta(x,\eta) = \frac{T - T_{\infty,0}}{T_W - T_{\infty,0}} - \frac{Ax}{T_W - T_{\infty,0}}$$

$$\phi(x,\eta) = \frac{C - C_{\infty,0}}{C_W - C_{\infty,0}} - \frac{Bx}{C_W - C_{\infty,0}} \tag{7}$$

the governing Eqs. (1)–(4) become

$$f'' + 2F_c ff'' = \theta' + N\phi' \tag{8}$$

$$\theta'' + \frac{1}{2}f\theta' = \varepsilon f' + \varepsilon\left(f'\frac{\partial\theta}{\partial\varepsilon} - \theta'\frac{\partial f}{\partial\varepsilon}\right) \tag{9}$$

$$\phi'' + \frac{1}{2}\text{Le}f\phi' = \text{Le Sr}\varepsilon f' + \text{Le }\varepsilon\left(f'\frac{\partial\phi}{\partial\varepsilon} - \phi'\frac{\partial f}{\partial\varepsilon}\right) \tag{10}$$

and the boundary conditions (5) transform into

$$\eta = 0: f(\varepsilon,0) = 0, \quad \theta(\varepsilon,0) = 1, \quad \phi(\varepsilon,0) = 1$$
$$\eta \to \infty: f'(\varepsilon,\infty) = 0, \quad \theta(\varepsilon,\infty) = 0, \quad \phi(\varepsilon,\infty) = 0 \tag{11}$$

The various parameters involved in the present study which influence the system are the Darcy-Rayleigh number $\text{Ra}_x = [Kg\beta_T(T_w - T_{\infty,0})x]/\alpha\nu$ which is defined with reference to the thermal conditions, the inertia parameter F_c which is defined as $[c\sqrt{K}Kg\beta_T(T_w - T_{\infty,0})]/\nu^2$, the diffusivity ratio $\text{Le} = \alpha/D$ and the buoyancy ratio $N = [\beta_C(C_w - C_{\infty,0})]/[\beta_T(T_w - T_{\infty,0})]$. When the Forchheimer coefficient c is zero, F_c will become zero, the inertia effects are absent in the medium, and the study becomes double stratification in the Darcy porous medium. Thermal buoyancy acts always vertically upward, the species buoyancy may act in either direction depending on the relative molecular weights. So $N > 0$ indicates aiding buoyancy where both the thermal and solutal buoyancies are in the same direction and $N < 0$ indicates opposing buoyancy where the solutal buoyancy is in the opposite direction to the thermal buoyancy. When $N = 0$, the flow is driven by thermal buoyancy alone. The thermal stratification parameter is given by $\varepsilon = Ax/(T_w - T_{\infty,0})$. Here we are defining a quantity called the stratification ratio $\text{Sr} = B(T_w - T_{\infty,0})/A(C_w - C_{\infty,0})$ which is a constant, it indicates the relative strengths of solutal and thermal stratification in the medium. As $(T_w - T_{\infty,0})$ and $(C_w - C_{\infty,0})$ are constants, when $\text{Sr} > 1$, solutal stratification is more than the thermal stratification in the medium and vice versa. The product $\text{Sr}.\varepsilon = Bx/(C_w - C_{\infty,0})$ will be the solutal stratification parameter.

Expanding the Stream function, temperature distribution and concentration distribution in terms of perturbation functions f_m, θ_m, ϕ_m as

$$f(\varepsilon, \eta) = \sum_{m=0}^{\infty} (-1)^m \varepsilon^m f_m(\eta)$$

$$\theta(\varepsilon, \eta) = \sum_{m=0}^{\infty} (-1)^m \varepsilon^m \theta_m(\eta) \qquad (12)$$

$$\phi(\varepsilon, \eta) = \sum_{m=0}^{\infty} (-1)^m \varepsilon^m \phi_m(\eta)$$

and substituting Eq. (12) into Eqs. (8)–(11) and equating the co-efficients of various powers of ε to zero, we have the following sets of ordinary differential equations for zeroth, first, and second order in ε as following:

$$f_0'' + 2F_c f_0' f_0'' = \theta_0' + N\phi_0'$$

$$\theta_0'' + \frac{1}{2} f_0 \theta_0' = 0 \qquad (13)$$

$$\phi_0'' + \frac{1}{2} \text{Le} f_0 \phi_0' = 0$$

subject to the boundary conditions

$$f_0(0) = 0, \quad \theta_0(0) = 1, \quad \phi_0(0) = 1$$
$$f_0'(\infty) = 0, \quad \theta_0(\infty) = 0, \quad \phi_0(\infty) = 0 \qquad (14)$$

$$f_1'' + 2F_c(f_0' f_1'' + f_1' f_0'') = \theta_1' + N\phi_1'$$

$$\theta_1'' + \frac{1}{2}(f_1 \theta_0' + f_0 \theta_1') + f_0' + (-f_0' \theta_1 + f_1 \theta_0') = 0 \qquad (15)$$

$$\phi_1'' + \frac{1}{2} \text{Le}(f_1 \phi_0' + f_0 \phi_1') + \text{Le Sr} f_0' + \text{Le}(-f_0' \phi_1 + f_1 \phi_0') = 0$$

subject to the boundary conditions

$$f_1(0) = 0, \theta_1(0) = 0, \quad \phi_1(0) = 0$$
$$f_1'(\infty) = 0, \quad \theta_1(\infty) = 0, \phi_1(\infty) = 0 \qquad (16)$$

and

$$f_2'' + 2F_c(f_0' f_2'' + f_1' f_1'' + f_2' f_0'') = \theta_2' + N\phi_2'$$

$$\theta_2'' + \frac{1}{2} f_0 \theta_2' + \frac{3}{2} f_1 \theta_1' + \frac{5}{2} f_2 \theta_0' - f_1' \theta_1 - 2f_0' \theta_2 + f_1' = 0 \qquad (17)$$

$$\phi_2'' + \frac{1}{2} \text{Le}(f_2 \phi_0' + f_1 \phi_1' + f_0 \phi_2') + \text{Le Sr} f_1'$$
$$- \text{Le}(f_1' \phi_1 + 2f_0' \phi_2 - f_1 \phi_1' - 2f_2 \phi_0') = 0$$

subject to the boundary conditions

$$f_2(0) = 0, \quad \theta_2(0) = 0, \quad \phi_2(0) = 0$$
$$f_2'(\infty) = 0, \quad \theta_2(\infty) = 0, \quad \phi_2(\infty) = 0 \qquad (18)$$

Results and Discussion

The sets of differential Eqs. (13)–(18) are solved successively, by giving appropriate initial guess values for the missing initial conditions $f_i'(0)$, $\theta_i'(0)$, $\phi_i'(0)$, $i = 0, 1, 2$. NAG software (D02HAFE routine) is used for integrating the corresponding first-order system of equations and shooting and matching the initial and boundary conditions. The integration length η_∞ varies with parameter values and it has been suitably chosen at each time such that the boundary conditions at the outer edge of the boundary layer are satisfied. Extensive calculations have been performed to study the effect of double stratification of the porous

medium on flow, temperature, and concentration fields. A wide range of parameter values are considered, the ranges are $-0.5 \leq N \leq 2$, $0.1 \leq \text{Le} \leq 50$, $0.1 \leq \text{Sr} \leq 5$, $0.1 \leq \varepsilon \leq 0.9$, and $0 \leq F_c \leq 1$, and the results obtained in the present study are accurate up to fourth decimal place.

The nondimensional heat and mass transfer coefficients in terms of Nusselt and Sherwood numbers are written, respectively, as

$$\frac{\text{Nu}}{\text{Ra}_x^{1/2}} = \{-\theta_0'(0) + \varepsilon \theta_1'(0) - \varepsilon^2 \theta_2'(0) + \cdots\} \qquad (19)$$

$$\frac{\text{Sh}}{\text{Ra}_x^{1/2}} = \{-\phi_0'(0) + \varepsilon \phi_1'(0) - \varepsilon^2 \phi_2'(0) + \cdots\} \qquad (20)$$

As we have used a series solution for solving the problem and the stream wise derivatives of the dependent variables are also considered in the governing equations, the results obtained here will be much more accurate. The values for $\theta_0'(0)$, $\theta_1'(0)$, $\phi_0'(0)$, and $\phi_1'(0)$ are significant, and the results showed that even if we consider more terms in the series expansion for θ and ϕ (i.e., after the second level of perturbation), the resulting values for $\theta_2'(\eta)$, $\phi_2'(\eta)$, etc., and their contribution (i.e., $+\varepsilon^2 \theta_2' - \varepsilon^3 \theta_3'(\eta) + \varepsilon^4 \theta_4'(\eta) -\cdots$, $\varepsilon^2 \phi_2' - \varepsilon^3 \phi_3'(\eta) + \varepsilon^4 \phi_4'(\eta) - \cdots$) to the heat and mass transfer coefficient will be negligibly small and can be neglected.

Similar to free convection results presented in Murthy et al. [13], it has also been observed in the present study that the non-dimensional temperature and concentration values are becoming negative inside the boundary layer for different values of the stratification parameter depending on the values of stratification ratio and other parameters. It is observed that there exists critical values for η_T, η_C at which both the temperature and concentration profiles become negative and finally they reach their outer edge boundary conditions. Also, η_T shifts toward the wall as the parameter ε becomes large and η_C shifts toward the wall as the parameter Sr. ε becomes large. This can be explained by the way in which the temperature and concentration fields are defined. We have $(T_W - T_{\infty,0})\theta(x, \eta) = (T - T_{\infty,0} - Ax)(= [T - T_\infty(x)])$, and when the temperature in the medium becomes smaller than that of the stratified ambient medium, i.e., $[T - T_\infty(x)] < 0$, then $\theta(x, \eta) < 0$ as $(T_W - T_{\infty,0})$ is always positive quantity. Similarly, $\phi(x, \eta)$ has to be negative when $[C - C_\infty(x)] < 0$, which happens when the solutal stratification parameter is larger. It is quite natural to make an assumption that different strata of the medium are at different stratification levels, to a first-order approximation, we considered linear stratification of the medium for both the temperature and concentration fields. Also, overpowering of thermal stratification over the concentration stratification and vice versa have resulted in a very unusual results for thermal and solutal fields both in the aiding buoyancy and in opposing buoyancy cases, and these results are presented in the following sections for both cases.

Aiding Buoyancy. In Figs. 2 and 3 some of these results are presented for the aiding buoyancy case. From the nondimensional temperature profiles plotted in Fig. 2(a) for varying ε and Sr, it is seen that the nondimensional temperature changes significantly due to both Sr and ε. As the value of thermal stratification parameter ε is increased (here it is varied between 0 and 1 since the series in Eq. (12) converges uniformly in this range), the nondimensional temperature takes negative values up to some value of η inside the boundary layer and finally it attains its outer edge boundary condition i.e., 0 as η increases. It is observed that as the value of Sr increases, the temperature distribution in the medium is further lowered and the magnitude of θ increased with Sr. This is clear from Fig. 2(b). As mentioned earlier, Sr. ε will be the solutal stratification parameter, when Sr. $\varepsilon \geq \varepsilon$, the nondimensional concentration profile takes negative values inside the boundary layer for all values of other parameters. The intensity of
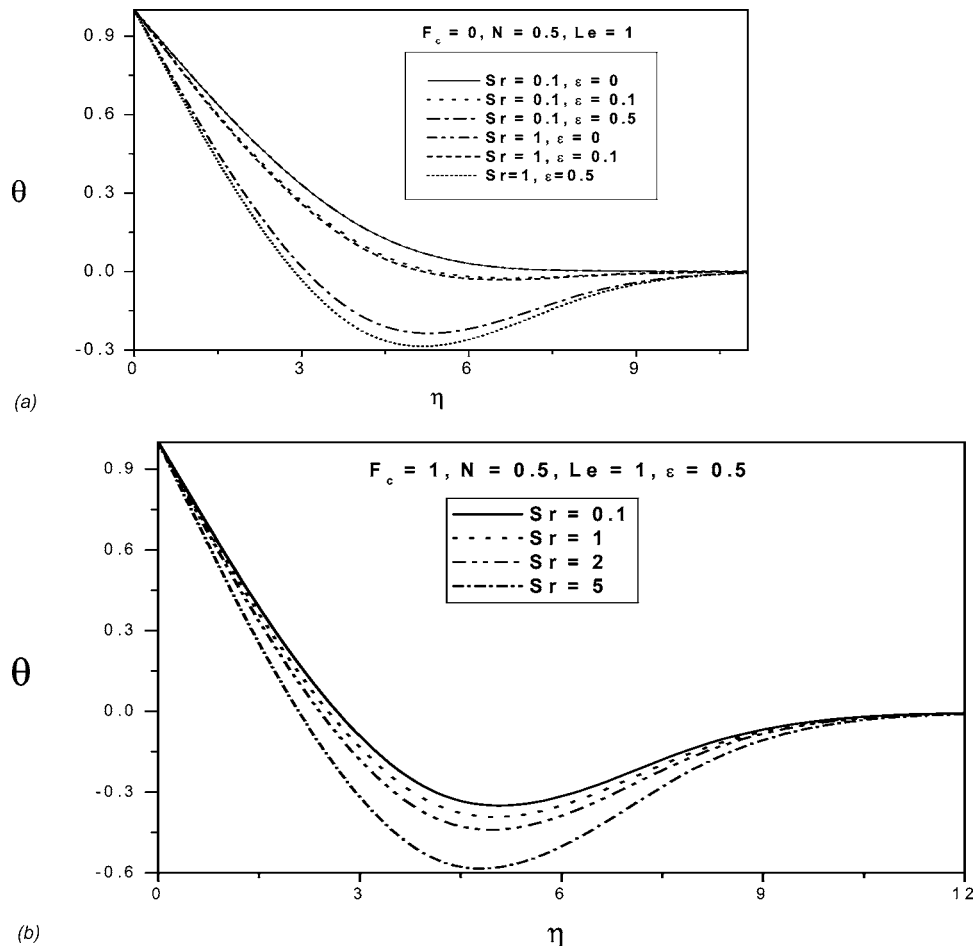
Fig. 2 (*a*) Variation of nondimensional temperature for fixed F_c, *N*, and Le; (*b*) variation of nondimensional temperature for fixed F_c, *N*, Le, and ϵ

these negative values of concentration is observed to increase with increasing values of Sr. Some of these results are shown for both Darcy and non-Darcy media in Figs. 3(*a*) and 3(*b*).

The nondimensional heat transfer coefficient plotted against the stratification parameter in Fig. 4(*a*) for different values of Le and Sr indicates that it increases with the stratification parameter. Also, the results indicated that increases in Sr and Le increases the heat transfer coefficient in aiding buoyancy case. In Fig. 4(*b*) the nondimensional mass transfer coefficient is plotted against the stratification parameter for different Le and Sr. It is evident from this figure that for small values of Lewis numbers the nondimensional mass transfer coefficient becomes negative and decreases with increasing values of ε and increases with increasing value of Sr. But for large values of Lewis numbers it decreases with increasing values of stratification parameter for a small stratification ratio and increases with increasing values of the stratification parameter for large stratification ratio values.

Opposing Buoyancy. Contrary what has been observed in the aiding buoyancy case, the temperature overshoots in the boundary layer for large values of stratification parameter in opposing buoyancy as shown in Fig. 5(*a*). For small values of stratification parameter and stratification ratio, the nondimensional temperature decreases from its maximum to minimum, while $\varepsilon \gg Sr\varepsilon$ the nondimensional temperature exceeds the wall temperature near the wall region and decreases to zero. From Fig. 5(*b*) it is observed that non-dimensional temperature exceeds the wall temperature for small values of Sr inside the boundary layer and attains the outer edge condition as η increases further.

But the nondimensional mass transfer is decreasing with in-

creasing η and increases with increasing values of the stratification parameter as shown in Fig. 6(*a*). From Fig. 6(*b*) it is observed that nondimensional mass transfer takes negative values for large Sr and tend to outer edge condition as η increases further. An interesting result is that for small values of Sr, only nondimensional temperature overshoots the wall temperature inside the boundary layer but this phenomena is not observed for nondimensional concentration.

The nondimensional heat transfer coefficient increases with increasing values of stratification parameter but decreases with increasing values of stratification ratio for small Le as shown in Fig. 7(*a*). But for large Le, the nondimensional heat transfer coefficient becomes negative and decreases as the stratification parameter increases for small stratification ratio values and increases with increasing values of stratification parameter for large stratification ratio. Also the nondimensional mass transfer coefficient is taking negative values and decreases as the stratification parameter increases for small values of stratification ratio and increases for large values of stratification ratio as the shown in Fig. 7(*b*).

In Table 1, typical values of the parameters are given for which the nondimensional temperature and concentration are becoming negative. For instance, in the aiding buoyancy when $\varepsilon \geq 0.1$ for any $Sr > 0$, θ is being negative. But in the opposing buoyancy, this is seen for any ε, when Sr is large. The nondimensional concentration takes negative values when $Sr\varepsilon \geq \varepsilon$ in the aiding buoyancy case whereas in the opposing buoyancy case, the same is observed for sufficiently large Sr. In the aiding buoyancy case the nondimensional heat transfer coefficient is never negative but in the opposing buoyancy case for $0 < Le < 50$, $\varepsilon \geq 0.2$ and for all Sr
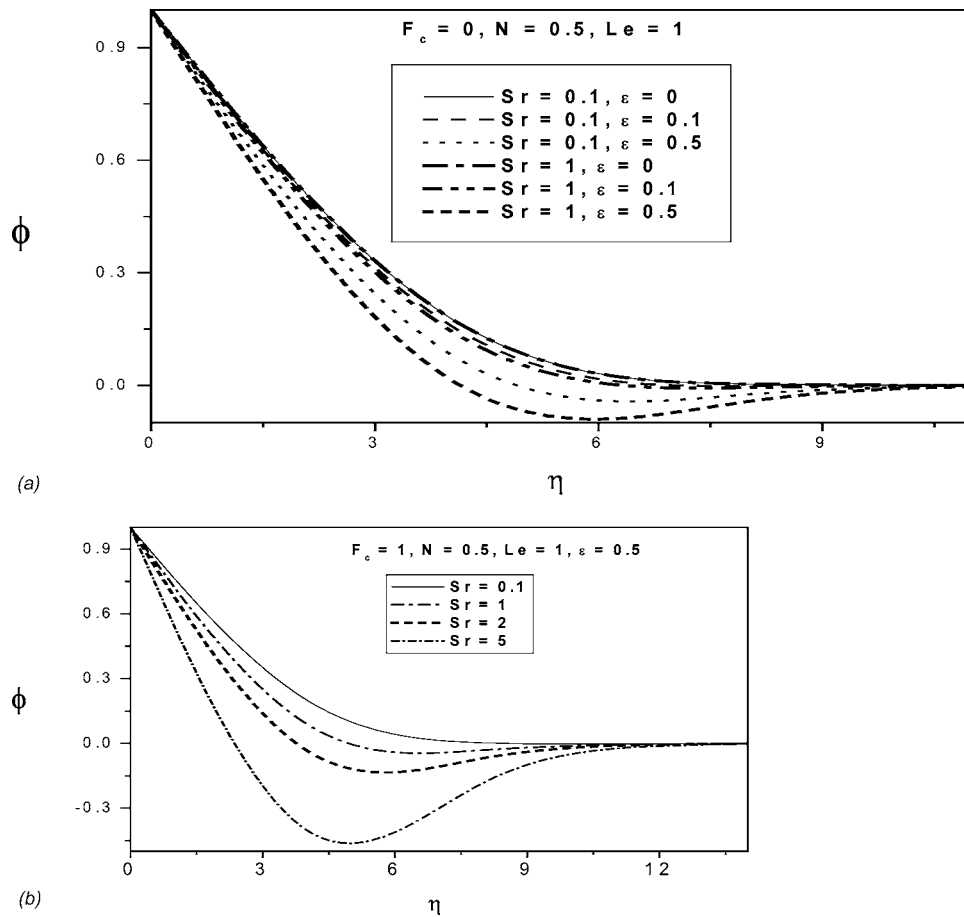
Fig. 3 (*a*) Variation of nondimensional concentration for fixed F_c, *N*, and Le; (*b*) variation of nondimensional concentration for fixed F_c, *N*, Le, and ϵ

≥ 1 heat transfer coefficient becomes negative. Similarly, nondimensional mass transfer coefficient becomes negative in both aiding and opposing buoyancy cases for small values of Le. In aiding buoyancy case, the nondimensional mass transfer coefficient is negative for $\varepsilon > 0$ and for all $Sr < 10$ whereas in the opposing buoyancy case it is negative for $Sr < 5$. These results are shown in Table 2. It is not natural to expect the Sherwood number becoming negative. In the present study, we have limited the ranges of the parameters so that the heat and mass transfer coefficients remain positive, but some typical cases are considered to show how and when the heat and mass transfer coefficients are becoming negative. Only the experimental results can validate the ranges of these parameters for which the nondimensional temperature, concentration, heat, and mass transfer coefficients must be nonnegative.

Effect of Lewis Number

In Fig. 8(*a*) the variation of nondimensional heat transfer coefficient is plotted against the Lewis number in both aiding and opposing buoyancy cases. It is observed that in the opposing buoyancy case the nondimensional heat transfer coefficient attains maximum for small values of Le and up to certain values of Le and then increases with increasing values of Le for an increasing stratification parameter. But in the aiding buoyancy case it is observed that the nondimensional heat transfer coefficient decreases and becomes negative with increasing values of the Lewis number and stratification parameter. In Fig. 8(*b*) variation of the nondimensional mass transfer coefficient is plotted against the Lewis number for both aiding and opposing cases. It has been observed that the nondimensional mass transfer coefficient becomes negative for small values of the Lewis number and further it increases with increasing value of the Lewis number while it decreases with

Table 1 The critical values *N*, Le, ε, and Sr for which nondimensional temperature and concentration are taking negative values

	N	Le	ϵ	Sr
θ	0.5	≥ 1	≥ 0.1	≥ 0.1
	-0.5	≥ 1	≥ 0.5	≥ 5
ϕ	0.5	≥ 1	≥ 0.5	≥ 0.1
	-0.5	≥ 1	≥ 0.5	≥ 2

Table 2 The critical values *N*, Le, ε, and Sr for which nondimensional heat and mass transfer coefficients are taking negative values

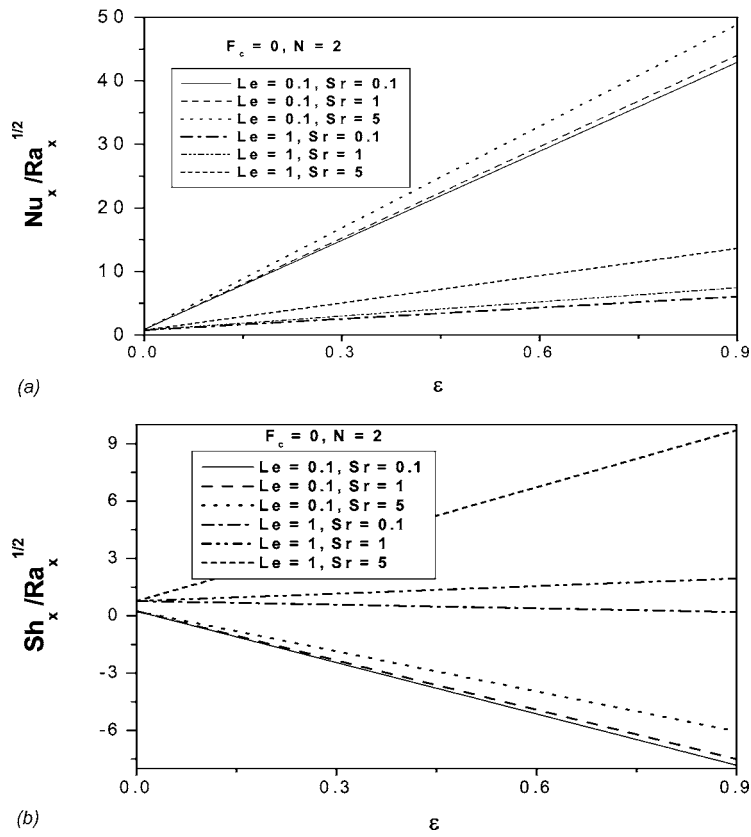|	*N*	Le	ϵ	Sr
$\mathrm{Nu}_x/\mathrm{Ra}_x^{1/2}$	-0.5	≥ 1	≥ 0.2	≥ 1
		≥ 50	≥ 0.1	≥ 1
$\mathrm{Sh}_x/\mathrm{Ra}_x^{1/2}$	2	<1	>0	<10
	-0.5	<1	>0.1	<5

Fig. 4 (*a*) **Variation of nondimensional heat transfer coefficient with ε for fixed F_c, N; (*b*) variation of nondimensional mass transfer coefficient with ε for fixed F_c, N**
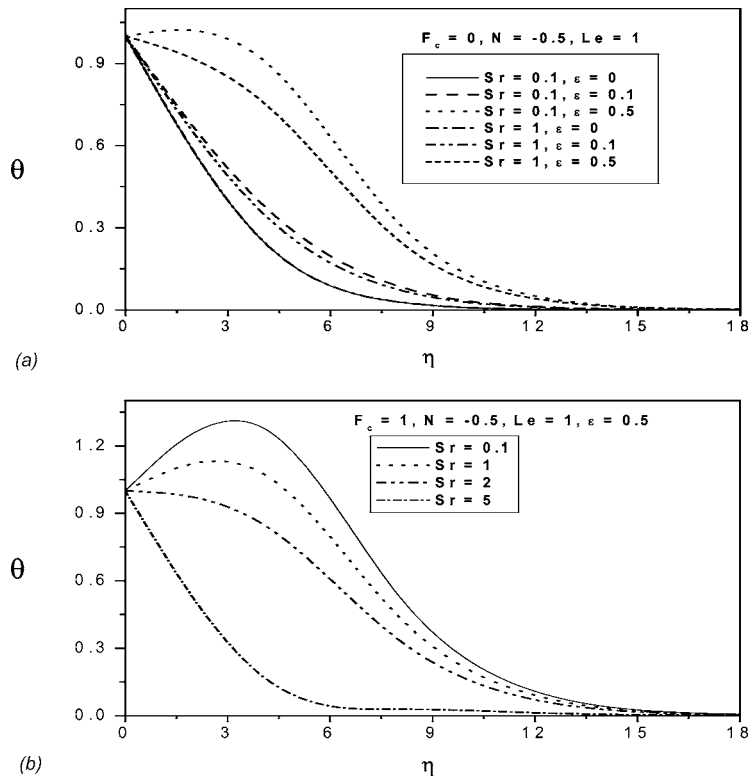

Fig. 5 (*a*) **Variation of nondimensional temperature for fixed F_c, N, and Le; (*b*) variation of nondimensional temperature for fixed F_c, N, Le, and ϵ**
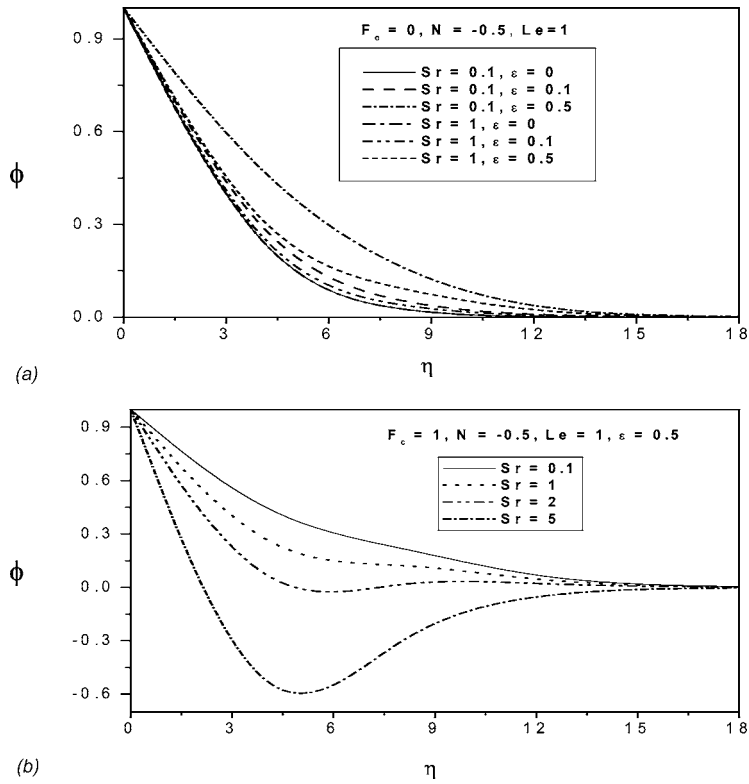
Fig. 6 (*a*) Variation of nondimensional concentration for fixed F_c, *N*, Le; (*b*) variation of nondimensional concentration for fixed F_c, *N*, Le, and ϵ
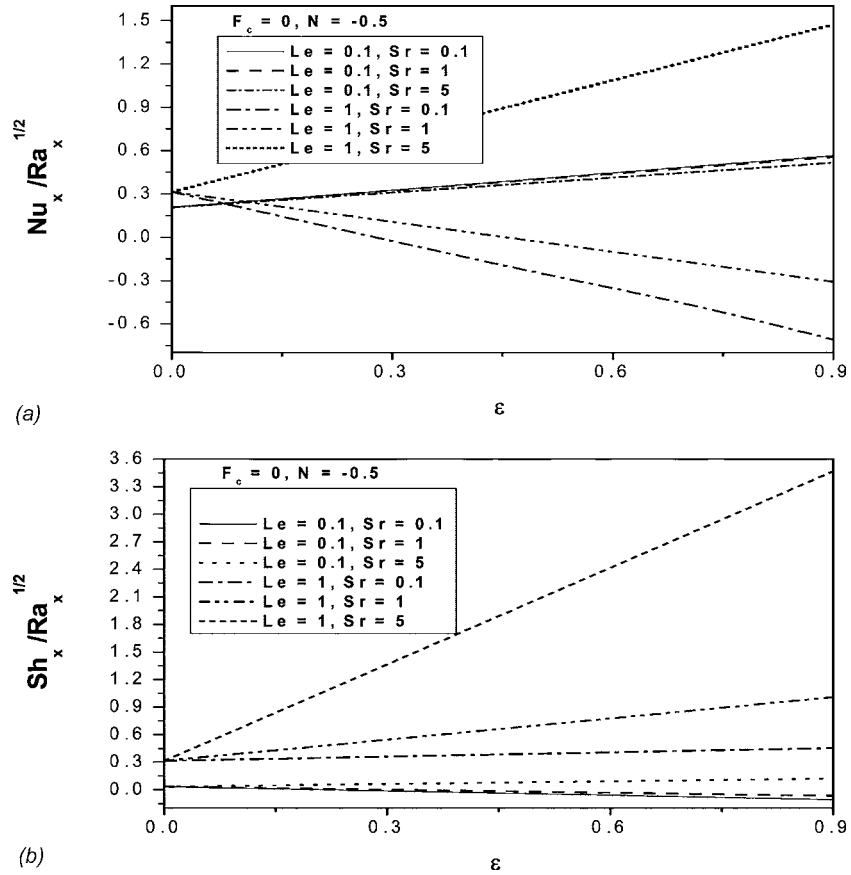

Fig. 7 (*a*) Variation of nondimensional heat transfer coefficient with ε for fixed F_c and *N*; (*b*) variation of nondimensional mass transfer coefficient with ε for fixed F_c and *N*
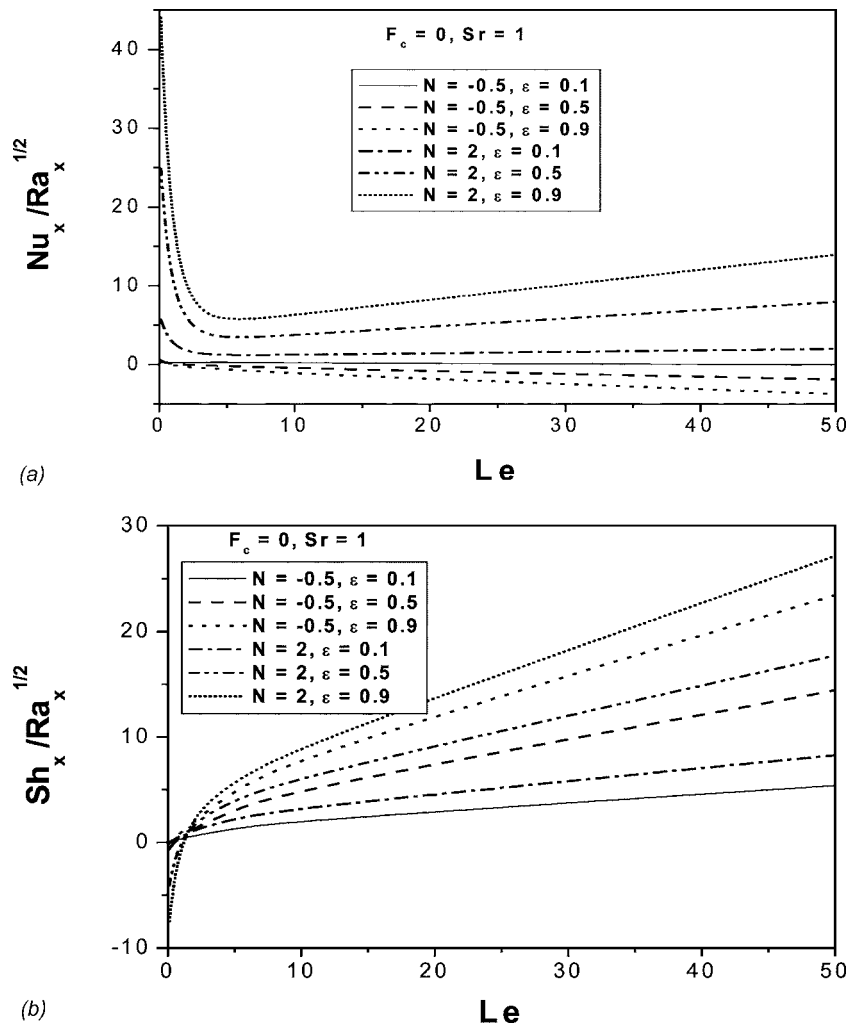
Fig. 8 (*a*) **Variation of nondimensional heat transfer coefficient with Le for fixed** F_c **and Sr;** (*b*) **variation of nondimensional mass transfer coefficient with Le for fixed** F_c **and Sr**

increasing values of the stratification parameter. But in the aiding buoyancy case the nondimensional mass transfer coefficient is increasing with increasing values of the Lewis number and increasing values of the stratification parameter.

Conclusions

Natural convection heat and mass transfer from a vertical surface embedded in a doubly stratified non-Darcy porous medium has been analyzed using series solution technique. The wall temperature and concentration are constant and the medium is linearly stratified with respect to both temperature and concentration in the vertical direction. The flow is moderate, the pressure drop is proportional to the linear combination of fluid velocity and the square of the velocity. Viscous resistance is neglected as the medium is assumed to be with low permeability. In this situation, the flow, temperature, and concentration are governed by the complex interaction among the flow governing parameter, the buoyancy ratio, and diffusion ratio along with the stratification parameters. The evolution of nondimensional heat and mass transfer coefficients as a function of each of these parameters is described in both the aiding and opposing buoyancy. In the aiding buoyancy, it is observed that the heat transfer coefficient is increasing with increasing values of the stratification parameter and for increasing values of the stratification ratio in both Darcy and non-Darcy medium. The nondimensional mass transfer coefficient is positive and de-

creases with increasing values of stratification parameter for sufficiently small stratification ratio and increases with increasing values of stratification parameter for increasing stratification ratio for a large Lewis number. The mass transfer coefficient becomes negative and decreases with increasing values of stratification parameter and increases with increasing values of stratification ratio for small Lewis number. Also, the values of the governing parameters have been tabulated for which the temperature and concentration profiles as well as the nondimensional heat and mass transfer coefficients behave abnormally.

References

[1] Bejan, A., and Khair, K. R., 1985, "Heat and Mass Transfer by Natural Convection in a Porous Medium," Int. J. Heat Mass Transfer, **28**, pp. 909–918.
[2] Lai, F. C., and Kulacki, F. A., 1991, "Coupled Heat and Mass Transfer by Natural Convection From Vertical Surfaces in Porous Media," Int. J. Heat Mass Transfer, **34**, pp. 1189–1194.
[3] Lai, F. C., 1991, "Coupled Heat and Mass Transfer by Mixed Convection From a Vertical Plate in a Saturated Porous Medium," Int. Commun. Heat Mass Transfer, **18**, pp. 93–106.
[4] Vafai, K., and Tien, C. L., 1981, "Boundary and Inertia Effects on Flow and Heat Transfer in Porous Media," Int. J. Heat Mass Transfer, **24**, pp. 195–203.
[5] Murthy, P. V. S. N., 2000, "Effect of Double Dispersion on Mixed Convection Heat and Mass Transfer in Non-Darcy Porous Medium," ASME J. Heat Transfer, **122**, pp. 476–484.
[6] Nield, D. A., and Bejan, A., 1992, *Convection in Porous Media*, Springer-Verlag, New-York.
[7] Bejan, A., 1984, *Convection Heat Transfer*, John Wiley & Sons, New York,

pp. 367–369.

[8] Singh, P., and Sharma, K., 1990, "Integral Method for Free Convection in Thermally Stratified Porous Medium," Acta Mech., **83**, pp. 157–163.

[9] Kalpana, T., and Singh, P., 1992, "Natural Convection in a Thermally Stratified Fluid Saturated Porous Medium," Int. J. Eng. Sci., **30**, pp. 1003–1007.

[10] Nakayama, A., and Koyama, H., 1987, "Effect of Thermal Stratification on Free Convection with a Porous Medium," J. Thermophys. Heat Transfer, **1**, pp. 282–285.

[11] Lai, F. C., Pop, I., and Kulacki, F. A., 1990, "Natural Convection from Isothermal Plates in Thermally Stratified Porous Media," J. Thermophys. Heat Transfer, **4**, pp. 533–535.

[12] Takhar, H. S., and Pop, I., 1987, "Free Convection From a Vertical Flat Plate to a Thermally Stratified Darcian Fluid," Mech. Res. Commun., **14**, pp. 81–86.

[13] Murthy, P. V. S. N., Srinivasacharya, D., and Krishna, P. V. S. S. S. R., 2004, "Effect of Double Stratification on Free Convection in Darcian Porous Me-dium," J. Heat Transfer, **126**, pp. 297–300.

[14] Chamkha, A. J., and Khaled, A.-R. A., 2000, "Hydro-Magnetic Simultaneous Heat and Mass Transfer by Mixed Convection from a Vertical Plate Embedded in a Stratified Porous Medium With Thermal Dispersion Effects," Int. J. Heat Mass Transfer, **36**, pp. 63–70.

[15] Postelnicu, A., 2004, "Influence of Magnetic Field on Heat and Mass Transfer from Vertical Surfaces in Porous Media Considering Soret and Dufour Effects," Int. J. Heat Mass Transfer, **47**, pp. 1467–1472.

[16] Angirasa, D., Peterson, G. P., and Pop, I., 1997, "Combined Heat and Mass Transfer by Natural Convection in a Saturated Thermally Stratified Porous Medium," Numer. Heat Transfer, Part A, **31**, pp. 255–272.

[17] Rathish Kumar, B. V., and Shalini, G., 2005, "Combined Influence of Mass and Thermal Stratification on Double Diffusion non-Darcian Natural Convection from a Wavy Vertical Wall to Porous Media," ASME J. Heat Transfer, **127**, pp. 637–642.

An Experimental Investigation of Heat Transport Capability in a Nanofluid Oscillating Heat Pipe

H. B. Ma
e-mail: mah@missouri.edu

C. Wilson

Q. Yu

K. Park

University of Missouri – Columbia,
Columbia, MO 65211

U. S. Choi
Argonne National Laboratory,
Argonne, IL 60439

Murli Tirumala
Intel Corporation,
Hillsboro, OR 97124

An experimental investigation of a nanofluid oscillating heat pipe (OHP) was conducted to determine the nanofluid effect on the heat transport capability in an OHP. The nanofluid consisted of HPLC grade water and 1.0 vol % diamond nanoparticles of 5–50 nm. These diamond nanoparticles settle down in the motionless base fluid. However, the oscillating motion of the OHP suspends the diamond nanoparticles in the working fluid. Experimental results show that the heat transport capability of the OHP significantly increased when it was charged with the nanofluid at a filling ratio of 50%. It was found that the heat transport capability of the OHP depends on the operating temperature. The investigated OHP could reach a thermal resistance of $0.03\,°C/W$ at a heat input of 336 W. The nanofluid OHP investigated here provides a new approach in designing a highly efficient next generation of heat pipe cooling devices. [DOI: 10.1115/1.2352789]

Keywords: oscillating heat pipe, nanofluid, nanoparticle

Introduction

Effective thermal management has become one of the most serious challenges in many new technologies due to constant demands for faster speeds and continuous reduction of device dimensions. High thermal conductivity of nanofluids produced by adding only a small amount of nanoparticles into the fluid has qualified nanofluids as a most promising candidate for achieving ultra-high-performance cooling [1]. When a small amount (less than 1% volume fraction) of copper nanoparticles or carbon nanotubes were dispersed in ethylene glycol or oil, their thermal conductivity could be increased by 40% and 150%, respectively [2,3]. Since Choi's work [1], outstanding discoveries and seminal achievements have been reported in the emerging field of nanofluids. Das et al. [4] explored the temperature dependence of the thermal conductivity of water-based nanofluids containing Al_2O_3 or CuO nanoparticles and reported the discovery of a two- to

four-fold increase in thermal conductivity enhancement for nanofluids over a temperature range of 21°C to 51°C. Patel et al. [5] have shown a 5–21% increase in thermal conductivity of water at vanishing concentrations (<0.00026 vol %) of monosized gold nanoparticles with citrate stabilization. They suggested that the strong temperature dependence of thermal conductivity is due to the motion of nanoparticles and nanoparticle surface chemistry. Even more interesting behavior was discovered by You et al. [6], Bang and Chang [7], and Vassallo et al. [8], who measured the critical heat flux (CHF) in pool boiling and showed an increase of CHF. These features make nanofluids strong candidates for the next generation of coolants.

Oscillating single-phase fluids significantly enhance heat and mass transfer in a channel, and have been employed in a number of heat transfer devices [9–11]. The oscillating motions generated by a variable-frequency shaker [10,11] could result in a thermal diffusivity of up to 17,900 times higher than those without oscillations in the capillary tubes, but the use of mechanically driven shakers may limit its applications to miniature devices. Akachi [12] invented a new device, called oscillating heat pipe (OHP). It utilizes the pressure change in volume expansion and contraction during phase change to excite the oscillation motion of the liquid plugs and vapor bubbles, which results in four unique features that do not exist in regular heat pipes: (1) OHP is an "active" cooling device, in that it converts intensive heat from the high-power generating device into kinetic energy of fluids in support of the oscillating motion; (2) liquid flow does not interfere with the vapor flow in high-heat removal because both phases flow in the same direction; (3) the thermally driven oscillating flow inside the capillary tube will effectively produce some "blank" surfaces that significantly enhance evaporating and condensing heat transfer; and (4) the oscillating motion in the capillary tube significantly enhances forced convection in addition to the phase-change heat transfer. Because of these features, the OHP has been extensively investigated in the past five years [13–18].

Most recently, Ma et al. [19] charged the nanofluids into an OHP and found that nanofluids significantly enhance the heat transport capability in the OHP. When the nanofluid (high-performance liquid chromatography (HPLC) grade water containing 1.0 vol % 5–50 nm of diamond nanoparticles) was charged to the OHP, the temperature difference between the evaporator and the condenser can be significantly reduced. For example, when the power input added on the evaporator is 100 W, the temperature difference can be reduced from 42°C to 25°C. In the current investigation, an experimental investigation on an OHP charged with nanofluid was conducted to determine the effect of operating temperature on the heat transport capability.

Experimental System and Procedure

For the vapor and liquid regions to remain separate, the diameter of the tube for an OHP must be small enough for capillary forces to dominate over gravitational forces. This diameter can be approximately calculated by the Bond number, i.e., $Bo = D^2 g(\rho_l - \rho_v)/\sigma$. The maximum diameter allowed to create distinct slugs is found by applying a critical Bond number determined experimentally and is defined as $D_{max} = \sqrt{Bo_{crit}\sigma/g(\rho_l - \rho_v)}$. Shafii et al. [20] use a critical Bond number of 1.84 while Khandekar et al. [16] use the value of 2 to determine the minimum tube diameter. In the current investigation, a Bond number of 1.84 and the properties of water are used to determine the inside diameter of the tube. Considering commercial availability, Alloy 122 copper tubing with an inside diameter of 1.65 mm and an outer diameter of 3.18 mm was used for the OHP investigated herein. The heat pipe, as shown in Fig. 1, has 12 turns traversing three sections: evaporator; adiabatic; and condenser section. The evaporator has dimensions of 59.9 mm × 301.5 mm where a uniform heat flux was added on
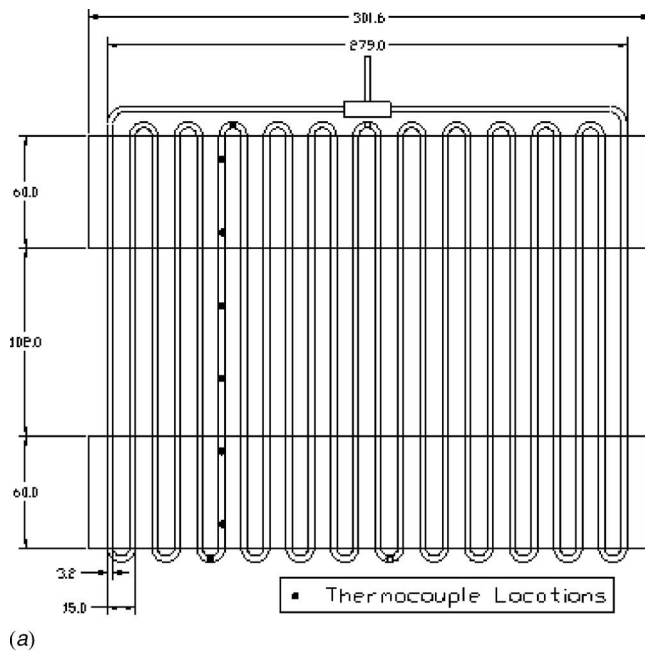
(a)
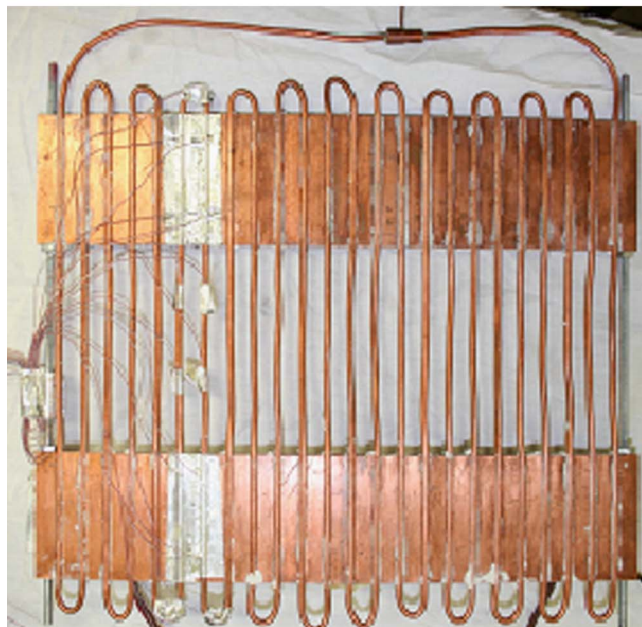
(b)

Fig. 1 Oscillating heat pipe (a) dimensions and thermocouple locations (mm), (b) picture

one side and the condenser has the same dimension where the cooling plate was attached. The distance between the evaporator and the condenser was 101.6 mm.

Nanofluids used in this study were HPLC grade water containing diamond nanoparticles. The nanoparticles with size ranging from 5 nm to 50 nm were fabricated by the 20 kW rf plasma with a high frequency of 13.56 MHz. The nanofluid was produced by adding nanoparticles directly into HPLC grade water. Most of the nanoparticles in the motionless water settle down as shown in Fig. 2. TEM investigation shown in Fig. 3 indicated that only the nanoparticles with size <10 nm can be suspended in the motionless water. In the current investigation, the volume ratio of nanoparticles charged to the heat pipe was 1.0% of the base fluid. Once the OHP was built, it was placed on a scale and the charging tube
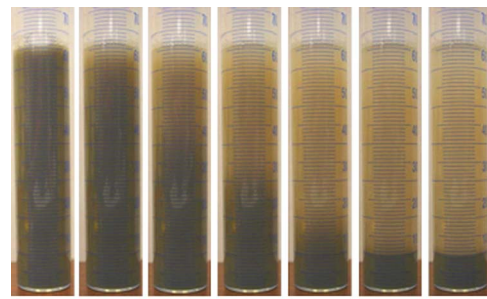
Fig. 2 The sedimentation of untreated diamond nanoparticles at settling times of (a) 0 min, (b) 1 min, (c) 2 min, (d) 3 min, (e) 4 min, (f) 5 min, and (g) 6 min

was connected to a vacuum pump. The air was removed and the working fluid was then introduced into the OHP. Once the correct volume percent was achieved, as indicated by the scale, the charging tube was sealed. Previous experiments [21,22] have shown that the OHP with a working fluid of water can operate at a filling ratio (liquid volume/total volume) of 50%. As a result, a filling ratio of 50% was used for the current study.

Figure 4 illustrates the experimental setup used to test the heat pipe. In order to reduce the contact thermal resistance from the heater to the evaporating section, a copper plate with dimensions 59.9 mm × 301.5 mm × 6.6 mm was used. The semicircular grooves machined on the plate created a good fitting with tubing to further reduce the contact thermal resistance. The condenser was fashioned in the same manner. The OMEGATHERM "201" thermal paste was used between the tubing and the copper plates to reduce contact resistance. The paste was also used to adhere the heater and water cooled blocks onto the evaporator and condenser plates, respectively. The heat input to the evaporator was provided by a strip heater. Two water cooled aluminum blocks were placed on the condenser plate. The temperature controlled water was supplied by a Julabo F34 circulator. Type T thermocouples were placed on the outside surface of OHP in the locations shown in
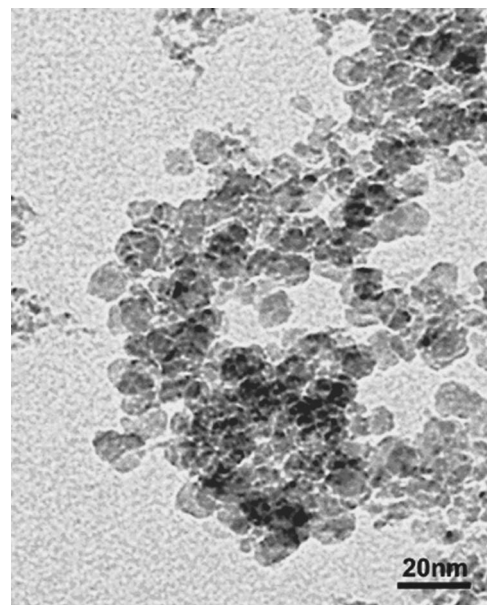

Fig. 3 Transmission electron microscopy image of diamond nanoparticles collected from suspension phases in a motionless nanofluid
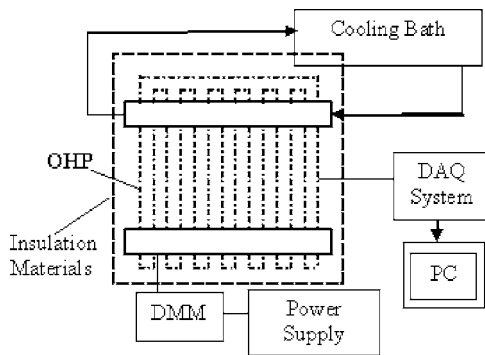
Fig. 4 Experimental setup

Fig. 5 Thermal resistance comparison between a water charged OHP and a nanofluid charged OHP (filling ratio=50%, vertical, T_{op}=20°C)

Fig. 1(b), which could also be used to detect the movement of vapor plugs and liquid slugs by the temperature variation. A NI SCXI-1000 data acquisition system and personal computer provided an uncertainty of 0.1°C of the temperature measurement were used to record the temperatures. Power was supplied by a Staco 3PN501B voltage regulator and the voltage was measured by a Fluke 45 dual display multimeter. The entire OHP was surrounded by insulation material to ensure heat transfer occurs only in the evaporator and condenser regions. At the highest power of 336 W, the temperature on the outer surface of insulation material was 28°C. The heat loss through the insulation to the atmosphere was calculated to be less than 3.0% of the overall heat load. The OHP was tested vertically, i.e., the evaporator on the bottom and condenser on the top.

Prior to the start of the experiment, the system was allowed to equilibrate and reach steady state such that the temperature of the cooling media and the heat pipe were constant at 0±0.5°C over the sample time, which was controlled by the cooling bath. When the desired steady-state condition has been obtained, the input power was increased in small increments. The test indicated that a time of approximately 60 min was necessary to reach steady state at low power levels and 10 min at high power levels. To obtain the data for each successive power level, the power was incremented and the OHP was allowed to reach steady state until the maximum heat power of 336 W which could be provided by the heater. During the tests, the thermal power and the temperature data were simultaneously recorded using the data acquisition system controlled by a personal computer.

Results and Discussion

Using the experimental setup and procedures described above, the effect of operating temperature and power input on the heat transport capability in the OHP was studied. Due to the heater power limit, tests were conducted by varying the heat load between 0 W and 336 W. The operating temperature controlled by the condenser water supply was between 10°C and 70°C. For all tests, the heat pipe was charged with a filling ratio of 50%. In order to demonstrate the nanofluid effect, the same heat pipe charged only with HPLC grade water was tested as well.

Figure 5 shows comparisons of a nanofluid effect on the heat transport capability in an OHP with the one charged only with HPLC grade water. As shown, when the OHP was charged with nanofluids, the thermal resistance significantly reduced. Obviously, this large reduction in thermal resistance is due to the nanoparticles added in the base fluid. However, the detailed information of the nanoparticle effect on the thermal conductivity of nanofluid or/and convection coefficient is not known. When the nanofluids investigated here were motionless, most of the nanoparticles settled down as shown in Fig. 2. For a functional OHP, the thermal energy added on the evaporator produces strong oscillating motions, which suspends the nanoparticles in the base fluid. When the oscillating motion is generated in an OHP, heat is
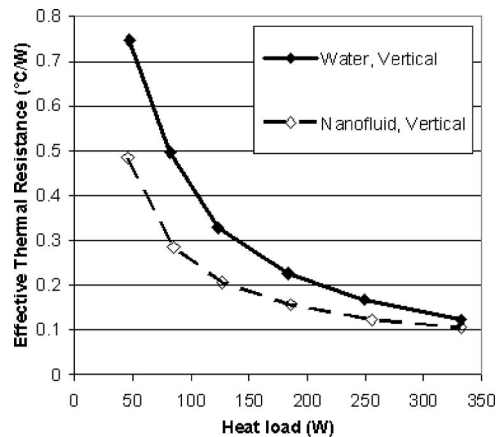
transferred from the evaporator to the condenser through phase-change heat transfer in the evaporator and condenser, and forced convection through the oscillating motions of vapor bubbles and liquid plugs. The oscillating motion excited by the thermal energy in the OHP enhances the forced convection heat transfer, and more importantly it keeps the nanoparticles suspended in the fluid. For both OHPs either charged with pure water or nanofluid, there exists a startup heat input. When the heat input was less than this required startup, no oscillating motions were observed and the temperature difference between the evaporator and condenser increased linearly as the power input increases. Once the oscillating motion started in the OHP, the further increase of power input did not significantly increase the temperature difference. Before the heat input reached the startup, there were no oscillating motions similar to the situation shown in Fig. 2, where most of the nanoparticles settled down. At this situation, the nanoparticles might stay in the evaporating section for a vertical position, i.e., the evaporator on the bottom, and this might be the reason that the heat resistance for the nanofluid OHP is the same as the one with pure water before the heat pipe started to function. Once the oscillating motions started and the nanoparticles were well mixed, the thermal resistance reduced significantly. The nanoparticle suspension excited by the oscillation motion of vapor bubbles and liquid plugs is the primary reason enhancing the heat transport capability in a nanofluid OHP. When the nanoparticle size is reduced, the thermal conductivity of the nanofluid increases [1–3]. However, the nanoparticles may agglomerate, settle, or coalesce to the walls with long-term operation of the nanofluid OHP. Preliminary long-term testing of the prototype device shows that the heat transfer performance remains the same over a period of at least six months, although further research is warranted to establish the longer-term reliability.

Figure 6 shows the operating temperature T_{op} effect on the thermal resistance occurring in the OHP. As shown, when the operating temperature increased, the thermal resistance significantly decreased. When the operating temperature was at 70°C, the thermal resistance occurring in this OHP can reach 0.03°C/W at a total heat input of 336 W. If the heat transfer rate from the evaporator to the condenser is expressed as $Q=UA(T_e-T_c)=(T_e-T_c)/R$, where Q is the heat transfer rate, U is the overall heat transfer coefficient, A is the total cross-sectional area of the OHP, T_e is the average temperature on the evaporator, and T_c is the average temperature on the condenser, the overall heat transfer coefficient (U) increases from 8.13 W/°C at 20°C to 27.8 W/°C at 70°C, which increased 3.4 times when only the operating temperature increased from 20°C to 70°C. When the operating temperature increases, higher thermal conductivity, lower viscosity of
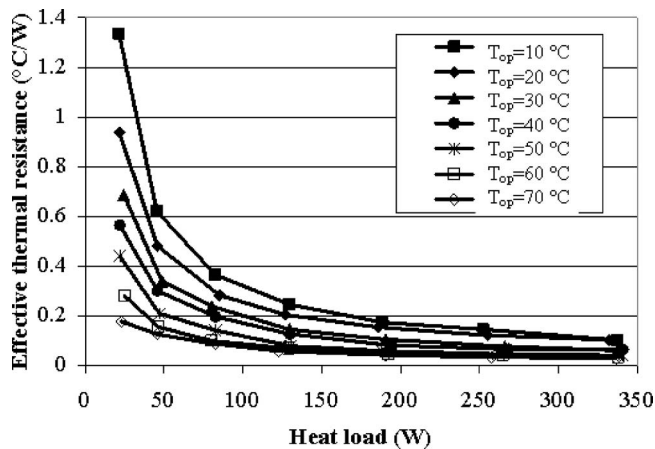
Fig. 6 Thermal resistance at various heat loads and operating temperatures

nanofluid, and stronger oscillating motion might be the primary factors enhancing the heat transport capability in a nanofluid oscillating heat pipe. Further investigation of these aspects is needed for a conclusive determination, and will be addressed in a future work.

Conclusions

An experimental investigation of nanofluid oscillating heat pipe (OHP) was conducted to determine the nanofluid effect on the heat transport capability in an OHP. The nanofluid consisting of HPLC grade water and 1.0 vol % diamond nanoparticles of 5–50 nm can significantly increase the heat transport capability in an OHP. Due to the thermally excited oscillating motion occurring in the OHP, the diamond nanoparticles can be suspended in the base fluid, which can increase the heat transport capability of nanofluid. The operating temperature can significantly affect the heat transport capability in the investigated OHP and when the operating temperature increases, the heat transport capability increases. The investigated OHP charged with nanofluids can reach a thermal resistance of $0.03\,°C/W$ at a power input of 336 W.

Acknowledgment

References

[1] Choi, S. U. S., 1995, "Enhancing Thermal Conductivity of Fluids with Nano-particles," *Developments and Applications of Non-Newtonian Flows*, eds. D. A. Signer and H. P. Wang, The American Society of Mechanical Engineers, New York, FED-Vol. 231/MD-Vol. 66, pp. 99–105.

[2] Choi, S. U. S., Zhang, Z. G., Yu, W., Lockwood, F. E., and Grulke, E. A., 2001, "Anomalous Thermal Conductivity Enhancement in Nano-tube Suspensions," Appl. Phys. Lett., **79**, pp. 2252–2254.

[3] Eastman, J. A., Choi, S. U. S., Li, S., Yu, W., and Thompson, L. J., 2001, "Anomalously Increased Effective Thermal Conductivities of Ethylene Glycol-Based Nano-Fluids Containing Copper Nano-Particles," Appl. Phys. Lett., **78**, pp. 718–720.

[4] Das, S. K., Putra, N., Thiesen, P., and Roetzel, W., 2003, "Temperature Dependence of Thermal Conductivity Enhancement for Nanofluids," J. Heat Transfer, **125**, pp. 567–574.

[5] Patel, H. E., Das, S. K., Sundararajan, T., Nair, A. S., George, B., and Pradeep, T., 2003, "Thermal Conductivities of Naked and Monolayer Protected Metal Nanoparticle Based Nanofluids: Manifestation of Anomalous Enhancement and Chemical Effects," Appl. Phys. Lett., **83**, pp. 2931–2933.

[6] You, S. M., Kim, J. H., and Kim, K. H., 2003, "Effect of Nano-Particles on Critical Heat Flux of Water in Pool Boiling Heat Transfer," Appl. Phys. Lett., **83**, pp. 3374–3376.

[7] Bang, I. C., and Chang, S. H., 2005, "Boiling Heat Transfer Performance and Phenomena of Al2O3-Water Nano-Fluids from a Plain Surface in a Pool," Int. J. Heat Mass Transfer, **48**(12), pp. 2407–2419.

[8] Vassallo, P., Kumar, R., D'Amico, S., 2004, "Pool Boiling Heat Transfer Experiments in Silica-Water Nano-fluids," Int. J. Heat Mass Transfer, **47**(2), pp. 407–411.

[9] Backhaus, S., and Swift, G. W., 1999, "A Thermoacoustic Stirling Heat Engine," Nature (London), **399**, pp. 335–338.

[10] Kurzweg, U. H., 1985, "Enhanced Heat Conduction in Fluids Subjected to Sinusoidal Oscillations," J. Heat Transfer, **107**, pp. 459–462.

[11] Kurzweg, U. H., and Zhao, L. D., 1984, "Heat Transfer by High-Frequency Oscillations: A New Hydrodynamic Technique for Achieving Large Effective Thermal Conductivities," Phys. Fluids, **27**, pp. 2624–2627.

[12] Akachi, H., 1990, "Structure of a Heat Pipe," U.S. Patent 4,921,041.

[13] Zuo, J., North, M. T., and Wert, K. L., 2001, "High Heat Flux Heat Pipe Mechanism for Cooling of Electronics," IEEE Trans. Compon. Packag. Technol., **24**, pp. 220–225.

[14] Ma, H. B., Maschmann, M. R., and Liang, S. B., 2002, "Heat Transport Capability in Pulsating Heat Pipes," Proceedings of the 8th AIAA/ASME Joint Thermophysica and Heat Transfer Conference, St. Louis, MO, June 24–27, ASME, New York.

[15] Khandekar, S., and Groll, M., 2004, "An Insight into Thermo-Hydrodynamic Coupling in Closed-Loop Pulsating Heat Pipes," Int. J. Therm. Sci., **43**, pp. 13–20.

[16] Khandekar, S., Cui, X., and Groll, M., 2002, "Thermal Performance Modeling of Pulsating Heat Pipes by Artificial Neural Network," Heat Pipe Science Technology Application, Proceedings of the 12th International Heat Pipe Conference, Moscow, Russia, May 19–24, Russian Academy of Sciences, pp. 215–219.

[17] Liang, S. B., and Ma, H. B., 2003, "Oscillation Motions in an Oscillating Heat Pipe," Int. Commun. Heat Mass Transfer, **43**(9), pp. 493–500.

[18] Ma, H. B., Hanlon, M. A., and Chen, C. L., 2005, "An Investigation of Oscillating Motions in a Miniature Pulsating Heat Pipe," J. Microfluidics Nanofluidics, **1**(4), pp. 334–342.

[19] Ma, H. B., Wilson, C., Borgmeyer, B., Park, K., Yu, Q., Choi, U. S., and Tirumala, M., 2006, "Nanofluid Effect on the Heat Transport Capability in an Oscillating Heat Pipe," Appl. Phys. Lett., **88**(14), pp. 1161–1163.

[20] Shafii, M., Faghri, A., and Zhang, Y., 2001, "Thermal Modeling of Unlooped and Looped Pulsating Heat Pipes," J. Heat Transfer, **123**, pp. 1159–1172.

[21] Cai, Q., Chen, R., and Chen, C., 2002, "An Investigation of Evaporation, Boiling, and Heat Transport Performance in Pulsating Heat Pipe," Proceedings of IMECE2002 ASME International Mechanical Engineering Congress and Exposition, New Orleans, November 17–22, ASME, New York, pp. 99–104.

[22] Nikkanen, K., Lu, C., and Kawaji, M., 2005, "Effects of Working Fluid, Fill ratio, and Orientation on Looped and Unlooped Pulsating Heat Pipes," 2005 ASME Summer Heat Transfer Conference, San Francisco, CA, July 17–22, ASME, New York.

A Transient Technique for Measuring the Effective Thermal Conductivity of Saturated Porous Media With a Constant Boundary Heat Flux

H. T. Aichlmayr[1]

Mem. ASME
Sandia National Laboratories,
7011 East Avenue,
Livermore, CA 94550
e-mail: htaichl@sandia.gov

F. A. Kulacki

Fellow ASME
Department of Mechanical Engineering,
The University of Minnesota,
Minneapolis, MN 55455
e-mail: kulacki@me.umn.edu

An experimental technique for measuring the effective thermal conductivity of saturated porous media is presented. The experimental method is based on the transient heating of a semi-infinite cylinder by a constant heat flux at the boundary. The data reduction technique is unique because it avoids determining the effective thermal diffusivity and quantifying the boundary heat flux. The technique is used to measure the effective thermal conductivity of glass-water, glass-air, and steel-air systems. These systems yield solid-fluid conductivity ratios of 1.08, 25.7, and 2400, respectively. The solid phases consist of 3.96 mm *glass spheres and* 14 mm *steel ball bearings, which give mean porosities of 0.365 and 0.403. In addition, particular attention is paid to assessing experimental uncertainty. Consequently, this study provides data with a degree of precision not typically found the literature.*
[DOI: 10.1115/1.2352791]

Keywords: porous media, effective thermal conductivity, transient measurement technique

Introduction

The effective thermal conductivity of saturated porous media continues to be an important problem in heat transfer science [1]. In particular, the influence of medium morphology is difficult, if not impossible, to investigate experimentally. Therefore modeling is the only practical approach to explore this dependency. Models however, require reliable effective conductivity measurements for validation. Unfortunately, the accuracy of the existing database is largely unknown. Thus a primary objective of this study is to estimate the experimental uncertainty that can be expected from typical effective conductivity measurements. This is accomplished by measuring the effective conductivity of three representative solid-fluid systems using a recently developed measurement technique.

Measurement Technique

The measurement technique is based on heat conduction in a semi-infinite cylinder following the sudden application of a constant heat flux at the boundary (Fig. 1). Assuming that the solid and fluid phases are in local thermal equilibrium [2,3] and that the fluid phase is stagnant, the temperature field is given by

$$\theta(z,t) = \frac{2q''\sqrt{\alpha_e t}}{\sqrt{\pi}k_e}\exp\left(-\frac{z^2}{4\alpha_e t}\right) - \frac{q''z}{k_e}\text{erfc}\left(\frac{z}{2\sqrt{\alpha_e t}}\right) \quad (1)$$

where $\theta(z,t) = T(z,t) - T_0$ [4]. The effective thermal diffusivity and the effective volumetric heat capacity are defined by

$$\alpha_e = \frac{k_e}{(\rho c_p)_e} \quad (2)$$

and

$$(\rho c_p)_e = \phi(\rho c_p)_f + (1-\phi)(\rho c_p)_s \quad (3)$$

The effective conductivity can be determined by substituting temperature, time, position, and heat flux measurements into Eq. (1) and solving the transcendental equation for the effective thermal diffusivity. The effective conductivity can then be found from Eq. (2) and the effective volumetric heat capacity (Eq. (3)). For instance, Lacroix et al. [5] employ this strategy to determine the effective conductivity of copper wool and duraluminum turnings subjected to a radiative heat flux in a rarefied gas environment.

Although simple, this approach has significant disadvantages from a numerical perspective. For example, if one substitutes typical temperature, time, position, and heat flux measurements into Eq. (1) and determines k_e by iteration, convergence is found to be problematic at best. Iteration fails because $\alpha_e \sim 10^{-7}$ m^2/s and $(\rho c_p)_e \sim 3 \times 10^6$ J/m^{3}K, whereas $k_e \sim 1$ W/mK. Consequently, roundoff can lead to significant errors in k_e. In fact, roundoff may account for the observed variations in the effective conductivity measurements of Lacroix et al. In contrast, Nozad et al. [6] also employ the sudden heating of a semi-infinite domain to measure effective conductivities, but they avoid numerical difficulties by using a constant temperature boundary condition.

Round-off error is minimized by using an alternate form of Eq. (1). This form is obtained by letting θ_0 and ξ represent the boundary temperature and the argument of the complimentary error function. That is

$$\theta_0 = \frac{2q''\sqrt{t}}{\sqrt{\pi}k_e(\rho c_p)_e} \quad (4)$$

and

$$\xi = \frac{z\sqrt{(\rho c_p)_e}}{2\sqrt{k_e t}} \quad (5)$$

Incidentally, it should be noted that

$$\xi = \frac{\text{Fo}^{-1/2}}{2} \quad (6)$$

where

$$\text{Fo} = \frac{\alpha_e t}{z^2} \quad (7)$$

is the Fourier number at location z. Equations (4) and (5) are substituted into Eq. (1), and the result is simplified to give

$$\Theta(\xi) = \exp(-\xi^2) - \sqrt{\pi}\xi\,\text{erfc}(\xi) \quad (8)$$

where

$$\Theta = \frac{\theta(z,t)}{\theta_0} \quad (9)$$

is the temperature ratio. Thus one can measure Θ and solve for ξ. Round-off error is minimized because $\Theta \sim 1$ and $\xi \sim 1$. An addi-
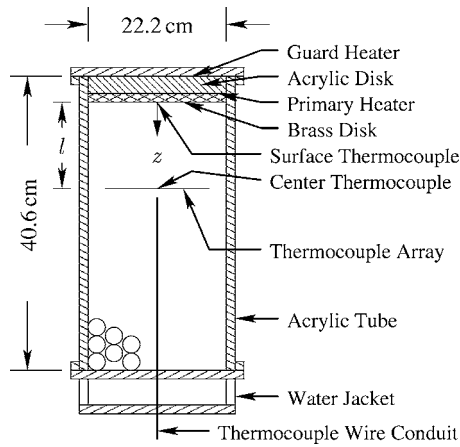
Fig. 1 Effective conductivity measurement apparatus. The cylindrical test chamber is 22.2 cm in diameter and 40.6 cm long (reproduced from Ref. [1]).
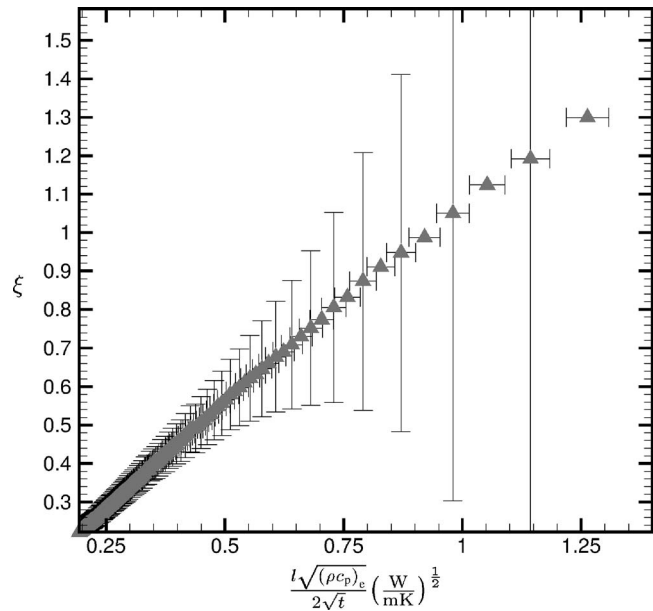

Fig. 2 Typical uncertainty limits encountered when determining k_e (glass-water system, l=30 mm). The effective conductivity is determined by fitting a regression line to the data. Also, time increases from right to left on the ordinate; consequently the uncertainty in ξ decreases with time.

tional benefit of this technique is that heat flux measurements are avoided, with the requirement that the heat flux must be constant.

Therefore to determine the effective conductivity from experimental data and Eq. (8), the following procedure is used: Two axial temperature measurements are recorded while the medium is heated. The first temperature θ_0 is located at the boundary and the second θ_1 is located in the interior at a distance, l from the boundary. Next, the temperature ratio Θ is computed for each pair of measurements and the corresponding value of ξ is obtained from Eq. (8). Finally, the quantity $l/2(\rho c_p)_e^{1/2} t^{-1/2}$ is computed from ancillary experimental data and the effective conductivity is obtained from a plot of ξ versus $l/2(\rho c_p)_e^{1/2} t^{-1/2}$.

Apparatus and Procedure

The test cell consists of a cylinder that is 22.2 cm in diameter and 40.6 cm long (Fig. 1). The chamber is heated from above by a thin foil heater sandwiched between brass and acrylic disks. A guard heater of identical type is located between the acrylic disk and the aluminum cover plate. The power dissipated in the guard heater is adjusted until the temperatures at opposite faces of the acrylic disk are equal, i.e., zero heat flux. This procedure ensures that the heat flux applied to the medium is constant. The boundary temperature is measured by a 30 AWG type E thermocouple mounted in the brass plate that bounds the test cell. The interior temperature of the medium is measured by a thermocouple located at the center of a support that resembles a bicycle wheel. The data acquisition system consists of a computer running Unix System V, and a multichannel multimeter. Thermocouple output is determined to 4.5 digits of precision with an ice bath reference. Further details regarding the experimental apparatus and experimental procedure can be found in Aichlmayr [4] and Aichlmayr and Kulacki [7].

Data Analysis

Thermocouple potentials are acquired sequentially. Consequently the interior temperature θ_1 and the boundary temperature θ_0 are acquired at different times. To incorporate this time lag in the data analysis, a slight modification to Eq. (8) is made. The modified form is obtained by assuming that θ_1 is acquired at time t and that θ_0 is acquired at time $t-\tau$, where τ is the delay time. Equations (1) and (4) are evaluated at these times to give

$$\Theta(\xi,t,\tau) = \exp(-\xi^2) - \sqrt{\pi}\left(\frac{t}{t-\tau}\right)^{1/2} \xi \, \mathrm{erfc}(\xi) \qquad (10)$$

following simplification. One should note that τ is typically 11 s whereas t ranges from hundreds to thousands of seconds. Hence the delay is generally inconsequential.

The effective conductivity is related to the slope of a line fitted to experimental data in ξ versus $l/2(\rho c_p)_e^{1/2} t^{-1/2}$ coordinates. Figure 2 is a representative plot of experimental data in this form. Hence

$$k_e = \frac{1}{b_1'^2} \qquad (11)$$

where b_1' is the slope of a line fitted to the data. One should note however, that the uncertainty in ξ varies greatly during an experiment. Consequently least squares regression, which assumes that the error in the independent variable is zero and that the error in the dependent variable is uniform [8], is not an appropriate method for determining b_1'.

Instead, a technique for estimating the slope of a regression line when both variables have uncertainty is used [8]. This method assumes that the independent and dependent variables have unequal variances. Unfortunately, these variances cannot be determined a priori. To circumvent this problem, variances are approximated by experimental uncertainties [9]. Therefore the uncertainties in ξ and $l/2(\rho c_p)_e^{1/2} t^{-1/2}$ must be estimated before determining the regression equation, which couples the data and uncertainty analyses. One should consult Aichlmayr [4] or Aichlmayr and Kulacki [7] for further details of the uncertainty analysis and an assessment of the constant boundary heat flux assumption.

Results and Discussion

The results of the present study are derived from 19 experiments conducted with three solid-fluid combinations. The solid phases consist of 3 mm glass beads and 14 mm steel ball bearings. Saturating fluids include air and water. Each solid-fluid combination is characterized by two experiments performed at two thermocouple support locations.

Table 1 Summary of effective thermal conductivity measurements

Medium	ϕ	κ	η	k_e (W/mK) at 95%
Glass-Water	0.387	1.08 ± 0.06	1.0 ± 0.2	0.61 ± 0.09
Glass-Air	0.365	26 ± 1	5.6 ± 0.8	0.14 ± 0.02
Steel-Air	0.403	$2.43\text{E} + 03 \pm 70$	14 ± 2	0.37 ± 0.06

The 19 effective conductivity measurements are collapsed into average effective conductivities for each solid-fluid system; the results are presented in Table 1. In addition, these results are compared to the measurements of several investigators [6,10–14] in Fig. 3. One should note that the data are enclosed within the physical bounds delineated by the Maxwell formulas [11] and that the present measurements are consistent with those of previous investigators. The experimental results are also used to estimate overall uncertainties at the 95% confidence level. The relative uncertainties in the overall glass-water, glass-air, and steel-air conductivity measurements are 15, 14, and 16%, respectively.

The present results can be further scrutinized by comparing them to the effective conductivity measurements of Ofuchi and Kunii [13]. Ofuchi and Kunii employ a steady conduction technique to measure the effective conductivities of glass spheres having diameters between 1.15 mm and 12.1 mm and steel balls having diameters between 3.09 mm and 10.9 mm. Saturating fluids include water, helium, carbon dioxide, and air. Hence except for experimental technique, the present study and Ofuchi and Kunii are very similar. The present results are compared to the data of Ofuchi and Kunii in Table 2.

Referring to Table 2, the glass-water result yields the smallest discrepancy between the present study and Ofuchi and Kunii. This difference is 11%, which compares well to the estimated uncertainty of 20% in η (Table 1). Similarly, the glass-air result differs from Ofuchi and Kunii by 17%, which is slightly greater than the experimental uncertainty (14%). The steel-air result however, differs from Ofuchi and Kunii by 25%, which exceeds the experimental uncertainty by 11%. One should note however, that the solid-fluid conductivity ratio of the present study is 45% greater than Ofuchi and Kunii. Consequently the solid materials are different, which diminishes the validity of this comparison.

Conclusion

Effective thermal conductivity measurements of glass-water, glass-air, steel-water, and steel-air media have been obtained using an experimental technique based on a classical transient heat conduction problem. The unique experimental apparatus and procedures facilitate a detailed uncertainty analysis. Moreover, the data reduction procedure is coupled to the uncertainty analysis. The measured effective thermal conductivities of glass-water, glass-air, and steel-water media are 0.61 ± 0.09, 0.14 ± 0.02, and 0.37 ± 0.06 W/mK at 95%, respectively. These measurements are consistent with those of previous investigators.
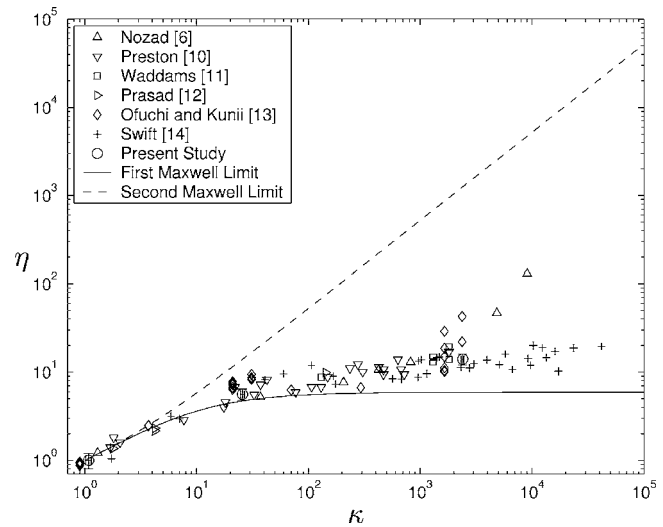
Acknowledgment

Fig. 3 Results of this study compared to previous investigators [6,10-14]. A porosity of 0.38 is assumed when computing the Maxwell limits.

Nomenclature

Roman Symbols

b_1' = estimated slope of the error-free line, Eq. (11)
c_p = constant pressure specific heat (kJ/kgK), Eq. (2)
d_p = particle diameter (mm)
k_e = effective thermal conductivity (W/mK), Eq. (2)
k_f = fluid thermal conductivity (W/mK)
k_s = solid thermal conductivity (W/mK)
l = thermocouple array position (m)
q'' = boundary heat flux (W/m^2), Eq. (1)
T = temperature (°C), Eq. (1)
t = times (s), Eq. (1)
z = axial coordinate (m), Eq. (1)

Greek Symbols

α_e = effective thermal diffusivity (m^2/s), Eq. (2)
η = effective-fluid thermal conductivity ratio, k_e/k_f (unitless)
Θ = temperature ratio (unitless), Eq. (8)
θ_0 = boundary temperature (°C), Eq. (4)
κ = solid-fluid thermal conductivity ratio, k_s/k_f (unitless)
ξ = argument of the complimentary error function (unitless), Eq. (5)
ρ = mass density (kg/m^3), Eq. (2)
τ = temperature measurement delay time (s), Eq. (10)

Table 2 Comparison of the data of Ofuchi and Kunii [13] and the present study

Medium	Ofuchi and Kuinii [13]				Present study				Δ (%)
	d_p (mm)	ϕ	κ	η	d_p (mm)	ϕ	κ	η	
Glass-Water	2.66	0.34	0.90	0.90	2.96	0.376	1.08	1.0	11
Glass-Air	3.69	0.369	21	6.71	2.96	0.376	26	5.6	17
Steel-Air	10.9	0.403	1650	18.6	14	0.403	2400	14	25

References

[1] Aichlmayr, H. T., and Kulacki, F. A., 2006, "The Effective Thermal Conductivity of Saturated Porous Media," *Advances in Heat Transfer*, G. Greene et al., eds., vol. 39, Academic Press, New York, pp. 377–460.

[2] Whitaker, S., 1999, *The Method of Volume Averaging*, Kluwer Academic Publishers, Dordrecht.

[3] Lage, J. L., 1999, "The Implication of the Thermal Equilibrium Assumption for Surrounding-Driven Steady Conduction Within a Saturated Porous Medium Layer," Int. J. Heat Mass Transfer, **42**(3), pp. 447–485.

[4] Aichlmayr, H. T., 1999, "The Effective Thermal Conductivity of Saturated Porous Media," Master's thesis, The University of Minnesota.

[5] Lacroix, C., Bala, P. R., and Feidt, M., 1999, "Evaluation of the Effective Thermal Conductivity in Metallic Porous Media Submitted to Incident Radiative Flux in Transient Conditions," Energy Convers. Manage., **40**(15-16), pp. 1775–1781.

[6] Nozad, I., Carbonell, R. G., and Whitaker, S., 1985, "Heat Conduction in Multiphase Systems II Experimental Method and Results for Three-Phase Systems," Chem. Eng. Sci., **40**(5), pp. 857–863.

[7] Aichlmayr, H. T., and Kulacki, F. A., 2005, "On the effective Thermal Conductivity of Saturated Porous Media," *Proceedings of the ASME Summer Heat Transfer Conference*, San Francisco, CA, July 17–22, ASME, New York.

[8] Guest, P. G., 1961, *Numerical Methods of Curve Fitting*, Cambridge University Press, New York.

[9] Meyer, S. L., 1975, *Data Analysis for Scientists and Engineers*, John Wiley & Sons, Inc., New York.

[10] Preston, F. W., 1957, Mechanism of Heat Transfer in Unconsolidated Porous Media at Low Flow Rates, Ph.D. thesis, Pennsylvania State University.

[11] Waddams, A. L., 1944, "The Flow of Heat Through Granular Material," J. Soc. Chem. Ind., London, London **63**, pp. 336–340.

[12] Prasad, V., Kladias, N., Bandyopadhaya, A., and Tian, Q., 1989, "Evaluation of Correlations for Stagnant Thermal Conductivity of Liquid-Saturated Porous Beds of Spheres," Int. J. Heat Mass Transfer, **32**(9), pp. 1793–1796.

[13] Ofuchi, K., and Kunii, D., 1965, "Heat Transfer Characteristics of Packed Beds With Stagnant Fluids," Int. J. Heat Mass Transfer, **8**(5), pp. 749–757.

[14] Swift, D. L., 1966, "The Thermal Conductivity of Spherical Metal Powders Including the Effect of Oxide Coating," Int. J. Heat Mass Transfer, **9**(10), pp. 1061–1074.

Thermal-Fluid MEMS Devices: A Decade of Progress and Challenges Ahead

I. Hassan

Department of Mechanical and Industrial Engineering,
Concordia University,
Montreal, Quebec, Canada, H3G 1M8
e-mail: IbrahimH@alcor.concordia.ca

Microdevices are becoming more prevalent and important in current and future technologies. Over the past decade, countless studies have been conducted in developing thermal microdevices. This paper focuses on the progress of research made during the last decade regarding heat transfer and fluid flow in microheat sinks, micropumps, microturbines, microengines, micromixers, as well as microsensors. Recent experimental techniques in the thermal microelectromechanical systems (MEMS) field have also been presented. Although some thermal MEMS devices have penetrated the commercial market, the mass implementation of thermal MEMS devices in future technology is still quite far, and is highly desirable. During the next decade, vast amounts of research need to be conducted before other microdevices can infiltrate the mainstream. Possible future directions of research have also been provided. [DOI: 10.1115/1.2352792]

1 Introduction

Microelectromechanical systems (MEMS) are becoming increasingly prevalent in today's technologies. The main advantage of these systems, in addition to their small size, and hence practicality, is that the manufacturing costs are significantly lower when compared to their larger counterparts due to the mass production methods used to fabricate them. Examples include microheat sinks for electronics cooling, and power-plants-on-chips for portable electronics and robotics. An array of micropower-plants-on-chips can also be used as auxiliary or emergency power for flight vehicles. Over the past decade, countless studies have been conducted in this field, which is indicative of the attractiveness of thermal MEMS. The earliest investigations in the field of thermal MEMS focused on single-phase flow in microchannels, and the vast majority of these studies used liquid-phase working fluids.

Papautsky et al. [1] provide a review on single-phase laminar flow in microchannels. Friction factor and surface roughness of liquid flows has been under great investigation by researchers such as Mala and Li [2], Celata et al. [3], Wu and Cheng [4], Lelea et al. [5], and Kim and Darve [6]. Low transition Reynolds numbers ranging from 1600 to 1800 have been reported by Li et al. [7] and Zeighami [8]. Also, in smooth microchannels, the conventional relation of $f \cdot \mathrm{Re} = 64$ for laminar flows in circular channels is acceptable in most of these studies. Figure 1 shows a comparison of experimental data for pressure drop of Peng and Peterson [9] and Xu et al. [10] with conventional theory. It can be seen that more recent studies have less discrepancies with conventional theory than earlier studies. This can be explained by the fact that Xu et al. [10] used silicon micromachined microchannels while Peng and Peterson [9] used machined metal channels. Channel roughness is relatively negligible in silicon microchannels, and thus the actual diameter is much closer to the nominal diameter. Thus, the more recent experimental data show better agreement with conventional theory.

Adiabatic and diabatic two-phase flows in microchannel have also become a topic of interest. Flow regimes in gas-liquid two-phase flow in microchannels of different geometries have been extensively studied in the past decade by numerous research groups (e.g., [11–19]). Regimes of dispersed flow, slug flow, annular flow, and churn flow have been observed in microchannel experiments. Discrepancies were observed when transition lines generated in these studies were compared, as shown in Fig. 2. Two factors explain these discrepancies, the first factor pertains to the scarcity of data related to these transition flow regimes lines and the second is due to inconsistency in the definition of a flow regime. It has been generally accepted that both nucleate boiling and convective boiling mechanisms exist in mini and microchannels, although the dominant mechanism remains inconclusive. The majority of the studies however, suggest that nucleate boiling is the dominant mechanism [20], which has been determined by observing the stronger dependence of heat transfer coefficient with heat flux, and not mass flux. Flow instabilities during boiling have been observed in mini and microchannels (e.g., [21–23]). The length of the period of fluctuations and their large amplitude are unique to the microchannels.

The fundamental knowledge of the underlying physics for heat transfer and fluid flow in microchannels is almost understood and documented in literature. However, the research conducted in the field of thermal-fluid MEMS devices is not as impressive as in microchannels due to many challenges in manufacturing and measurements. In this paper, the author has undertaken the challenging task of reviewing previous work and proposing areas of future research. The paper provides a good overview of the field and can act as a starting point for interested researchers or as a brief summary for experts in the field and industrial decision makers. Only recent references have been given here, and earlier reports may be traced through the reference lists of the papers cited. The reader may need to search further in the cited references in order to fully appreciate the research challenges outlined and motivated in the paper for a particular microdevice. This paper also reviews the
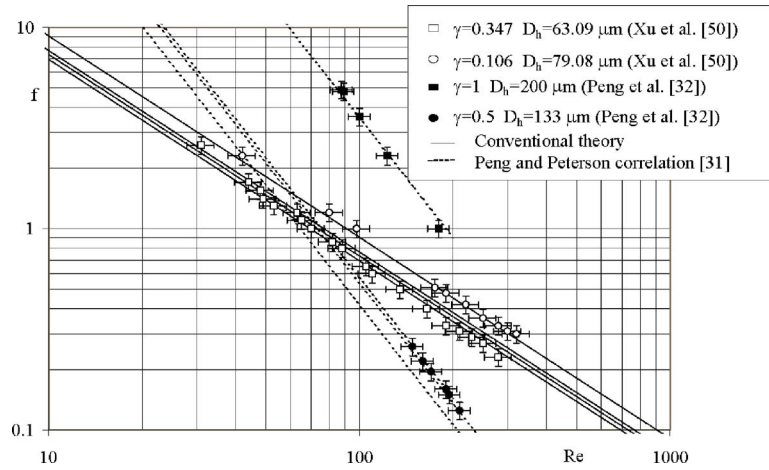
Fig. 1 Comparison of pressure drop data in microchannels from recent and earlier studies [119]

progress of research tools such as heat measurement techniques that have applied at the microscale. Future directions of research and recommendations have been proposed.

2 Microdevices

2.1 Microheat Exchangers. Microheat exchangers, or microheat sinks, are mainly fabricated from a silicon wafer in which parallel grooves are machined. A cover plate is placed on top of the grooves, and the result is a parallel arrangement of microchannels through which a coolant fluid may flow. Tuckerman and Pease [24] introduced the microheat exchangers in 1981. The coolant may be single-phase liquid [25–29] or two-phase [30–32]. Various input parameters have been studied in microchannel heat sinks such as the flow rate or Reynolds number [25,28,31], microchannel size [29,32], and heat flux [26,27,30,33]. For the two-phase heat sinks, the effect of vapor quality was studied as well [30,31].
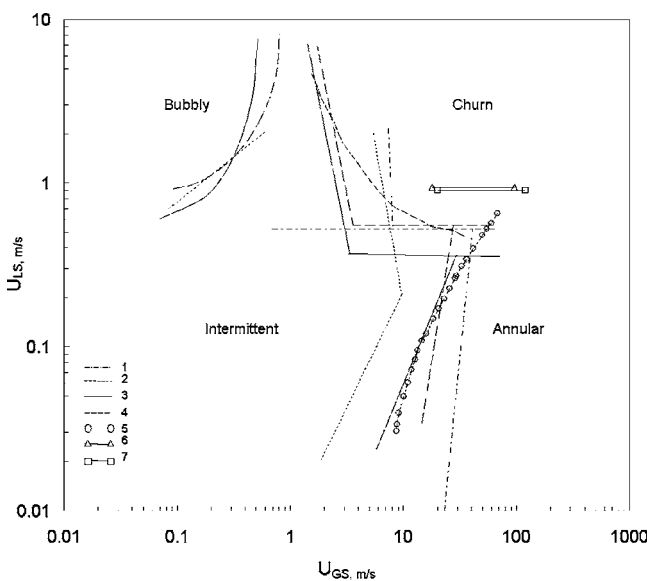
The performance of the microchannel heat sink is dependent on the uniformity of the applied wall heat flux. When a uniform heat flux is applied to the heat sink at a single wall, the heat transfer coefficient was found to be greatest at the entrance since there is minimum convective resistance in that region. In two-phase microchannel heat sinks, it was found that the wall temperature is relatively uniform, rendering it preferable over the single-phase microchannel heat sinks. However, boiling characteristics in mini- and micro-channels are very complex, and are dependent on the vapor quality inside the channel as shown in Fig. 3. In the low quality region, the decreasing heat transfer coefficient with quality is much more significant than for larger channels. Also, as the diameter decreases, dryout occurs at earlier qualities. Koo et al. [32] and Quadir et al. [34] numerically investigated the effect of nonuniform heat flux in microheat sinks, and observed that the thermal resistances of the microchannel increases if the applied nonuniform heat flux distribution is higher at upstream end. In addition, lower pressure drops, lower average wall temperature, and a more uniform temperature field were reported when a hotspot is located near the downstream end.

The critical heat flux (CHF) for an array of microchannels was studied by Bowers and Mudawar [35] and some recent developments have been reviewed by Bergles and Kandlikar [36]. This parameter is of great importance in designing safe microheat ex-

Fig. 2 A comparison of transition lines on a flow regime map plotting the superficial liquid velocity (J_L) versus the superficial gas velocity (J_G) from studies conducted by (1) Damianides and Westwater [11], (2) Fukano et al. [12], (3,4) Triplett et al. [15], (5) Kawahara et al. [18], and (6,7) Hassan et al. [19] in horizontal microchannels [19]
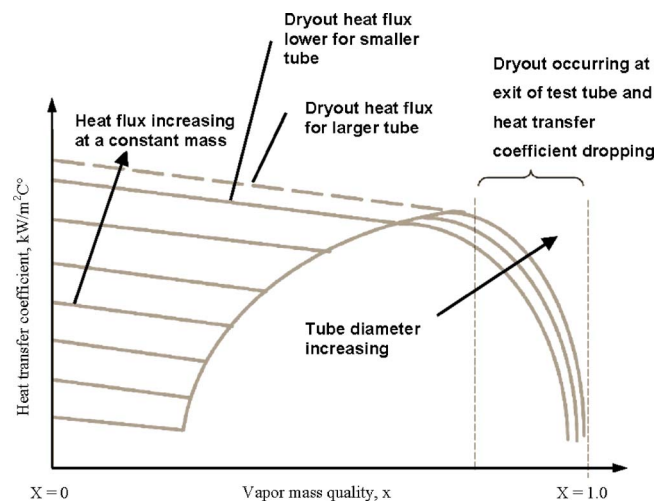

Fig. 3 Boiling characteristics in mini- and micro- channels as a function of vapor mass quality [120]
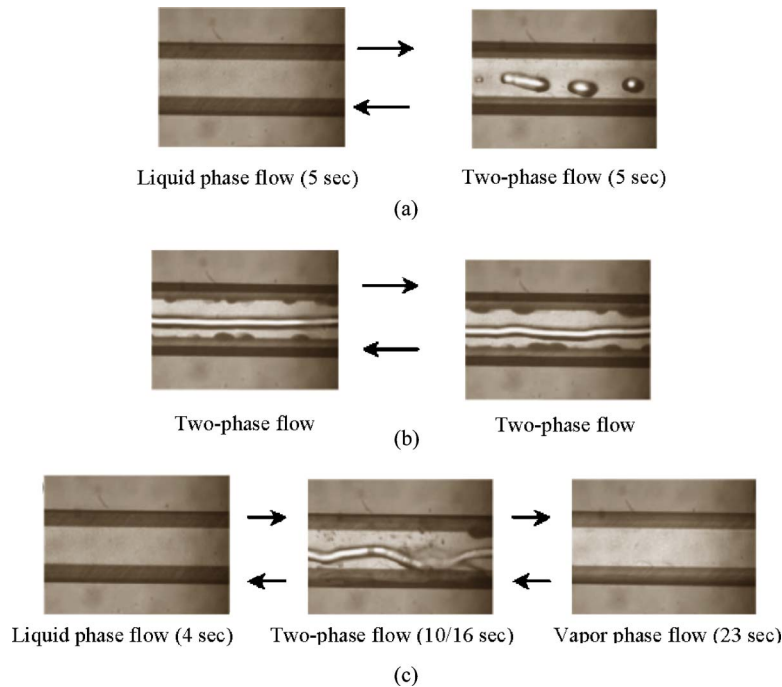
Fig. 4 Unstable boiling modes, (*a*) liquid/two-phase, (*b*) continuous two-phase, (*c*) liquid/two-phase vapour alternating flow [23]

changers. Two limiting cases for failure in microchannel heat sinks induced by CHF are the misdistribution of flow between the channels and the instability between the channels. In a study using a 2.98 mm diameter tube with water as the working fluid, it was found that the CHF occurred at qualities ranging between 0.5 and 1.0, which is higher than that found in larger diameter tubes. In addition, the critical heat flux decreased with decreased mass flux, which is opposite to that occurring in macrosize channels [37].

The boiling incipience has been studied by Hollingsworth [38] and Piasecka and Poniewski [39] among others. There is a sharp transition to boiling in laminar flow, in comparison to turbulent flow. In addition, the transition from incipience boiling to fully developed nucleate boiling takes different paths on the boiling diagram dependant on the states of the wall superheat and/or heat flux. This is contrary to what is observed in standard pool boiling whereby only a single path occurs. Inlet pressure, liquid sub-cooling, and flow velocity have all been found to have an influence on boiling incipience. The functional form for the relation between these parameters and the Nusselt number at boiling incipience is given by

$$\mathrm{Nu}_{\mathrm{BI}} = A \cdot (\mathrm{Re} \cdot \mathrm{Bo})^b \cdot \mathrm{Pr}^c$$

where Nu is the Nusselt number hD_h/k_L, Re is the Reynolds number GD_h/μ_L, Bo is the boiling number $q\rho_L h_{fg}/V$, Pr is Prandtl number $\mu_L C_{pL}/k_L$, and A, b, c are constants corresponding to the dataset. Also, D_h is the hydraulic diameter, h is the heat transfer coefficient, h_{fg} is the latent heat of vaporization, k_L is the thermal conductivity, G is the mass flux, μ_L is the liquid dynamic viscosity, C_{pL} is the liquid specific heat capacity, and q is the heat flux.

Flow instabilities during boiling have been observed in mini- and microchannels [4,21–23]. Three unstable boiling modes were observed by Wu and Cheng [4,23] (a) liquid/two-phase alternating flow occurring at low heat flux and high mass flux; (b) continuous two-phase flow, occurring at medium heat flux and medium mass flux; and (c) liquid/two-phase vapor alternating flow occurring at high heat flux and low mass flux. These different modes are presented in Fig. 4. The instabilities are relatively periodic and cause fluctuations in the temperature, pressure, and mass flux. This was explained by the fact that the onset of boiling increases the pres-

sure drop, which subsequently decreases the mass flux. The reduced mass flux alternatively causes a reduction in pressure drop, and thus initiating the fluctuations. If the heat flux is not sufficient to boil the fluid during an increase in the mass flux period, a single-phase liquid will appear. The length of the period of fluctuations and their large amplitude are unique to the microchannels.

The parallel flow microchannel heat sink has been modified in order to enhance its performance. In one instance, an impinging jet was added to the configuration [27]. It was observed that the thermal resistance decreased and pressure drop increased as the flow rate was increased. The cooling performance of the impinging jet microchannel heat sink was evaluated numerically and its performance compared with that of the parallel flow microchannel heat sink as well as the manifold microchannel heat sink. Results showed that impinging jet microchannel heat sink provides 48.5% better cooling performance than the other two, with 90.5% less pressure drop than the parallel flow microchannel heat sink due to its larger volume flow rate and larger hydraulic diameter. In addition, the recent concept of a two-layered microchannel heat sink with opposite flows in each layer has been proposed [40]. Optimization of the geometric design parameters and the thermal performance was structured on numerical modeling. Simulated results shows lower streamwise temperature and less pressure drop across the two-layered microchannel heat sink when compared to the single-layered heat sink.

Based on the number of parameters that will affect the boiling in microheat exchangers, and the lack of available data, more studies with improved systematic approaches to evaluating the influence of various parameters are recommended. In addition, these studies should follow strict protocol in collecting and presenting their results, as reported by Thome [20]. These guidelines are as follows: (i) validating the test apparatus with single-phase data; (ii) measurement of the surface roughness; (iii) comparison with other works at similar conditions in order to verify the data integrity; and (iv) consistent inlet conditions. The boundary between macro- and micro-channel boiling phenomena is not yet clearly established and so additional data generation and analysis on this subject is required. The critical heat flux (CHF) is critical
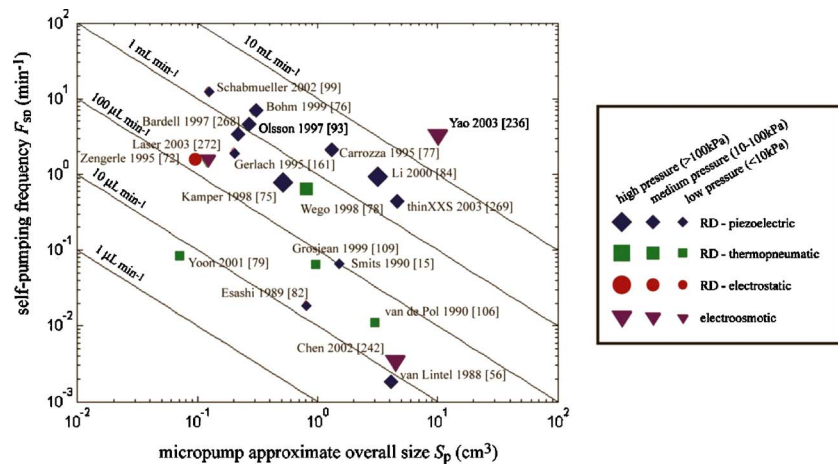
Fig. 5 Comparison of several reported micropumps based on maximum flow rate Q_{max}, maximum pressure Δp_{max}, and package size S_p. Self-pumping frequency is here defined as $f_{sp} = Q_{max} / S_p$ [42]

in rendering future microchannel heat sinks safe for operation, and the amount of work focusing on this phenomenon is limited. Hence, additional research investigating the parameters that influence the CHF, as well as how to control it, are necessary in future studies. Flow instabilities appear to have a unique characteristic in microchannels. Additional studies to complement the work of Wu and Cheng [4,23] are warranted since these fluctuations may shed light on some of the anomalous effects observed due to time-averaged measurements. Future research directions in the field of microchannel heat sinks may include studying the effect of non-uniform heat fluxes in great detail. Different configurations could also be studied, such as the one presented by Jang et al. [27] where an impingement jet is applied to a microchannel. This configuration is more compact and it was shown that the pressure drop is significantly lower, and that the wall temperature distribution is more uniform when compared to that in the parallel flow microchannel heat sink. Novel configurations would also be welcome.

2.2 Micropumps. Micropumps are among the most developed of all microdevices, and have already been implemented into the mainstream. For example, micropumps are used in ink jet printers to inject ink droplets, as well as in fuel injector applications. Micropumps operate as a result of completely different principles than those applied in traditional pumps like the axial or centrifugal pumps. Microdimensions limit the effect of centrifugal forces and inertia forces in general, and the large surface-to-volume ratio amplifies the effect of viscous forces, rendering it the dominant force at the microscale [41]. Laser and Santiago [42] provide an excellent literature review of the progress of research in the field of micropumps over the past 25 years, and which includes 287 references. Figure 5 shows a comparison of several micropumps reported by Laser and Santiago [42]. They identified that though much progress has been made, there is still much future research before micropumps become suitable for important applications.

Positive displacement pumping is the most prevalent method used in micropumps, yet the actuation of the reciprocating diaphragm is achieved by applying different principles. Thermopneumatic, piezoelectrical, and electrostatic actuations are examples of the actuation methods used [43]. The positive displacement micropumps require check valves at the inlet and outlet ports, which add to the complexity of design especially on such a small scale. To simplify the design, Stemme and Stemme [44] suggested the replacing of the check valves with a nozzle at the inlet, and a diffuser at the exit [45]. An oscillating diaphragm can either increase or decrease the chamber's volume. The micropump oper-

ates in supply mode by increasing the chamber volume, where flow is injected at the inlet. In the pump mode, the chamber's volume is decreased and flow subsequently leaves the pump through the outlet. One advantage of this particular micropump is that it is suitable for both gas and liquid working fluids. In addition, the geometry is simple and therefore has low fabrication costs. The valveless micropump was fabricated from silicon by Olsson et al. [46] and CFD simulations were performed by Olsson et al. [47] and Olsson et al. [45]. This type of pump uses channels with small opening angles for redirecting the fluid. While the operation of the pump proved successful, the performance of the pump could still be improved.

Various other pumping ideas were proposed to overcome the valve problem associated with positive displacement pumps. Bart et al. [48] presented the electrohydrodynamic pump, which utilizes dielectric fluids. For this particular pump, a voltage is applied to the electrode array in order to generate an electric field and produce charge at the material interface below. The interaction between the electric field and the induced electric charge generates momentum in the fluid. However, pumping is not possible if one of the materials is a fixed wall. In addition, instabilities that cause mixing can lower the pump's performance. When the micropump was fabricated and tested, it was determined that the performance could be improved by use of induction of the free charge in the fluid volume with the use of temperature-induced conductivity gradients. Electroosmotic pumps, studied by Harrison et al. [49] and by Manz et al. [50], use an electric field to control the flow of an aqueous solvent inside a microchannel. This particular pump incorporates on-chip electrophoretic separation along with electro-osmotic flow. Applying a potential difference across any two inlets of the pump will produce electro-osmotic pumping in the channels connecting the two inlets.

Thermopneumatic micropumps utilize heat transfer in their operation. One form of micropump is the thermopneumatically driven reciprocating displacement pump, and has been widely studied. This micropump consists of a primary pump chamber as well as a second chamber which houses secondary fluid. The secondary fluid is heated using a thin-film resistive heater causing the pump diaphragm to expand, and thus forcing the fluid in the primary chamber through the pump outlet. When the heater is deactivated, the diaphragm relaxes causing the intake stroke to occur. Since the temporal response of the thermal actuator depends on the rate of heat transfer in and out, thus the thermopneumatically driven reciprocating pump tends to operate at low frequencies. Another variant of thermopneumatic micropumps is a "bubble" type pump, where there is no secondary fluid, and the primary

fluid is heated until the phase changes. These thermopneumatic bubble pumps typically operate at higher frequencies than their reciprocating counterparts [42].

All the micropump concepts mentioned above, although applicable, are complex since they involve the use of different auxiliary components in order to make the fluid environment suitable for pumping action to occur. Thus, the viscous micropump was introduced by Sen et al. [41], which incorporates both applicability at the microscale and simplicity in design in a sense that there are less components required. The viscous micropump is simply a cylinder placed eccentrically inside a channel with its axis perpendicular to the channel axis. When the cylinder rotates, a net force is transferred to the fluid due to the unequal shear rates on the upper and lower surfaces of the cylinder, thus forcing the fluid to displace. Its operation depends mainly on viscous forces, and can operate in any situation where viscous forces are dominant. Numerical studies of the viscous micropump has been conducted by Sharatchandra et al. [51,52], Decourtye et al. [53], Abdelgawad et al. [54], and Phutthavong and Hassan [55]. These studied focused on the effect of the channel height, rotor geometries and eccentricity, and pump load. Imperfections in microfabricating the rotor may lead to noncircular rotors. The efficiency of the viscous micropump with noncircular rotors is much lower than that with circular rotors. The sharp corners of the rotor inhibit the flow from attaining higher values since the velocity continually fluctuates. However, it is necessary to study such a configuration since it may not always be possible to implement perfectly circular rotors.

Viscous micropumps with grooves machined on the surface of rotating disks have recently become a subject of interest in the research community, and shall be called henceforth spiral viscous micropumps. There are currently two forms of spiral viscous micropumps under investigation. One is the spiral groove viscous micropump studied by Frechette et al. [56] which has a polar array of radial grooves inclined at a constant spiral angle. This viscous micropump was chosen for a microsteam turbine engine since low liquid flow rates will be used in this device, and also because of the simplicity of the design. Models for the macroscale spiral groove viscous pump were used to determine the effect of channel geometry, rotational speed and flow rate on the pressure rise, torque, and power consumption. Design optimization was conducted over a large range of pressure ratios, and maximum efficiencies between 4% and 5% were obtained. The groove depths considered in their design were 3.1 μm and 4.6 μm, and the clearance was 0.5 μm and 0.6 μm, for the low and high pressure pumps, respectively.

The second spiral channel viscous micropump has been developed by Kilani et al. [57] using Sandia's Ultraplanar Multilevel MEMS Technology (SUMMiT). The spiral channel micropump consists of a rotating disk with a spiral groove machined on one surface with the inlet and outlet located at either end of the spiral groove. The rotating disk rotates over a stationary disk, which creates a spiral microchannel between the two disks measuring 4459 μm in length, 54.4 μm in width, and 10 μm in height. The clearance measures 0.5 μm in height. An analytical model of the spiral channel viscous micropump was generated by Kilani et al. [57] by approximating the spiral channel to a straight channel with identical dimensions and boundary conditions. A linear relation for volumetric flow rate and pressure head was generated, and experimental results from a scaled-up spiral pump were used for comparison. The flow rates obtained experimentally generally agreed well with the predicted flow rates from the analytical model. It was observed that at lower rotating speeds, the analytical results over predicted the experimental data. This was attributed to the existence of cross flow, which occurs through the clearance gap between the spiral wall and stationary disk. The cross flow becomes more significant at higher pressure loads. When the rotational speed of the top disk is increased, centrifugal effects compensate for the losses due to the cross flow. Therefore, it was
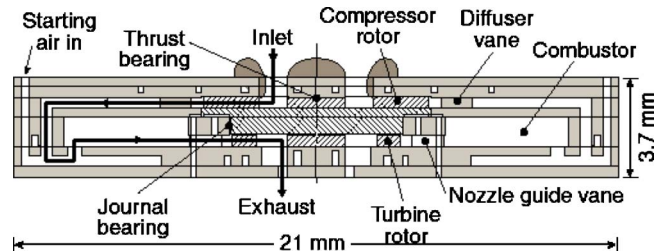

Fig. 6 Six-wafer microgas turbine engine [60]

concluded that the clearance height must be carefully considered in order to minimize the amount of cross flow as well as the amount of power consumed by the micropump.

2.3 Microengines. Microengines are being developed in order to produce electric power for small and portable electronic devices, and they include the micro gas turbine engine, the P^3 microheat engine, the microreciprocating engine, the micro-Wankel engine, and the microsteam engine. All these engines, with the exception of the microsteam engine, rely on the combustion of gases for their operation. The microsteam engine utilizes water as the working fluid. Thermodynamic cycles, such as the Brayton cycle for micro-gas turbine engines, the Rankine cycle for the steam engine, and the Otto cycle for the micro-Wankel engine have been included in the design of these microdevices. Higher power range engines have an output of 1–100 W, which include the microgas turbine engine, the micro-Wankel engine, and the microsteam engine. The purpose of the engines is expected to be for portable power. On the other hand, lower power range engines have outputs in the order of milliwatts or even microwatts, such as the viscous microturbine (mentioned in the previous section), microheat engine, and the Sugiyama and Toriyama [58] microreciprocating engine. These particular microengines could be used in sensor or actuator applications [59].

The millimeter scale microgas turbine engine has been the one of the focii of study of Epstein [60] at the Massachusetts Institute of Technology shown in Fig. 6, and it is still under development. This microturbine engine consists of six silicon wafers, and is equipped with a compressor, diffuser, combustor, nozzle guide vane, and turbine rotor. Thermodynamics of this engine is identical to that used in conventional-sized gas turbine engines. Jacobson and Epstein [59] report that electric and magnetic generators are currently being developed to convert shaft work into electrical power. Isomura et al. [61] are currently developing a microgas turbine engine with Ti-6Al-4V as the primary material instead of ceramic material.

The main component of the microgas turbine engine that has been studied in great detail is the microcombustor [61–63]. Various configurations were studied in order to improve the performance of the microcombustor. Mehra et al. [62] and Spadaccini et al. [63] developed a silicon microcombustor which consists of a recirculation jacket in order to improve efficiency by preventing heat loss to the ambient. Also, different inlets to the microcombustor were tested. The slotted inlet device consists of multiple slots through which the fluid may enter. This configuration generated higher exit temperatures and efficiencies due to the presence of multiple recirculation zones. However, the performance of the microcombustor declined rapidly since the ignition zones were rapidly dispelled. The annular inlet device did not have the multiple slots and so there was a single and large recirculation zone. This allowed longer ignition time but generated lower efficiency. The microcombustor was further modified by adding an array of holes in order to connect the upper recirculation or cooling jacket to the combustion chamber, thus bleeding air into the chamber. By bleeding air into the chamber, the hot combustion gases are cooled to the desired turbine inlet temperature. As a result, there are two zones inside the chamber, and so is called the dual-zone micro-
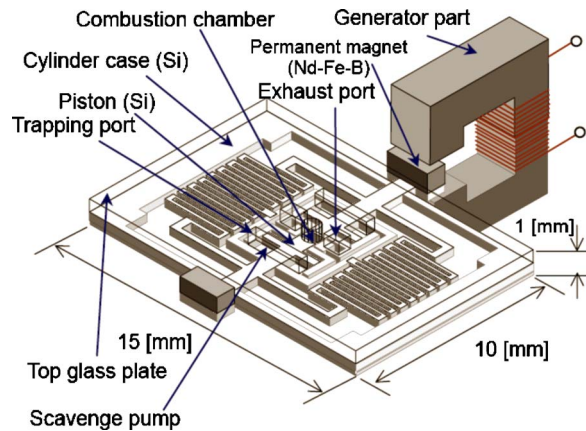
Fig. 7 Microreciprocation engine proposed by Sugiyama and Toriyama [58]

combustor. Isomura et al. [61], on the other hand, developed a cannister type microcombustor, similar to that found on large scale gas turbine engines and compared it to the donut-shaped microcombustor developed by Mehra et al. [62] and Spadaccini et al. [63]. The cannister-type combustor experienced much lower heat loss, and so was chosen for the design of another microgas turbine engine.

The P^3 microheat engine has been developed and tested by Whalen et al. [64,65]. The microheat engine is essentially a cavity containing a saturated two-phase fluid, and is bounded on top by the thin film piezoelectric membrane generator, and at the bottom by a membrane with an integrated heater. Heat is transferred to the two-phase working fluid, causing its quality and volume to increase. Heat then leaves the fluid, causing the quality and volume to decrease. As a result, the piezoelectric membrane flexes in and out acting like a piston, and electrical power is produced as the membrane expands. A reliable power source may be constructed by arranging the individual microheat engines together. In parallel, each cell would operate with the same temperature difference across them. Alternatively, the cells could be arranged in series where an individual cell would operate with only a fraction of the total temperature difference applied across the entire cascade of cells. The main challenge in the design of the microheat engine is the fact that there is a significant amount of heat loss to the device through conduction. As a result, heat transfer cannot occur through phase change processes, and so the vapor cannot recondense. This was attributed to the absence of active cooling of the system, and so heat rejection is slower than heat addition. Therefore, in order to solve this problem, a thermal switch is being developed in order to cool the engine during heat rejection.

Sugiyama and Toriyama [58] and Park et al. [66] have developed micro-reciprocating engines, equipped with pistons and combustion chambers. Sugiyama and Toriyama [58] use voltage and magnetic forces to maintain the oscillatory motion of the pistons, and their engine as shown in Fig. 7. Voltage is generated through changes in magnetic fluxes, using permanent magnets, which are placed at the terminals of the pistons. Springs support the opposite pistons, and are forced into oscillation by the forces produced during combustion. The magnet at the piston's terminal oscillates through a gap inside an induction coil, located outside the engine. The work output is in the order of milliwatts. First, the fuel is injected into the fuel chamber, and proceeds to the combustion chamber where spark plugs ignite it. At this point, the piston is moving toward the combustion chamber thus compressing the fuel. An explosion occurs and the pressure from the explosion causes the piston to move back in the other direction, compressing the fuel being injected in the other side. The burnt fuel is pushed through the exhaust hole by the new fuel being injected on the opposite side. The main problems associated with

the microreciprocating engine is the fact that the combustion chambers are susceptible to a large amount of heat loss due to their miniature sizes, and so must be insulated in the future. Leakage between moving and static parts is also a problem and will reduce the performance of the micro engine. Microseals should be implemented in order to avoid this.

Kirtas et al. [67] developed a high aspect ratio microreciprocating engine used to generate electric power. The free piston is fitted with permanent magnets, and is forced to move as the microengine is placed inside a permanent magnet coil. The aspect ratio of the microengine is high, thus standard design techniques for lower aspect ratio engines could not be applied in the microcombustor's design. Thus, the authors performed large eddy simulations (LES) in order to understand the microcombustor's combustion dynamics. Using the results from the simulations, the microengine was developed, and experiments were conducted in order to determine the accuracy of the simulation results. It was found that the numerical model overpredicted many results, including the work generated by the microdevice. Thus, it was concluded that the numerical model needed to be improved in order to obtain more realistic results. Some of the key factors that have a significant effect on the microcombustor's performance are ignition, flame propogation, heat losses, and quenching.

Aichlmayr et al. [68] presented a complete study of a homogeneous charge compression ignition (HCCI) free-piston-compressor capable of generating 10 W. In HCCI, a fuel-air mixture is compressed until an explosion occurs, and is characterized by simultaneous ignition at various locations within the combustion chamber and rapid consumption of charge. In addition, there is an absence of flame propagation and of an external ignition system, rendering HCCI highly suitable for microengine applications. In addition, quenching is minimized in the HCCI engine. Heat transfer was shown to have a significant effect on the engine, which limits the size of the microengine. Even though the fuel conversion efficiency increases, with decreasing aspect ratio, the specific heat transfer rate increases drastically as the engine size or aspect ratio are decreased. As a result, the region of operation is reduced along with the fuel conversion efficiency. Future work aims to model HCCI by coupling HCCI and free-piston motion using a multizonal formulation.

The microrotary internal combustion Wankel engine has been investigated by Fu et al. [69], Heppner et al. [70], and Lee et al. [71], and is intended to replace common alkaline and lithium-ion batteries. The rotary engine design consists of a triangular-rotor placed eccentrically inside the epitrochoidal-shaped housing. As the rotor rotates, the three apexes of the rotor are constantly in contact with the walls, forming three separately sealed chambers. The microrotary engine operates on four strokes. During the intake stroke, fresh fuel/air mixture enters through the intake port, and as the rotor's apex passes over the port, the volume of the mixture increases. During the compression stroke, the following apex closes the intake port, and the rotation of the rotor causes the working fluid to compress. During the power stroke, the fuel/air mixture is ignited using either a spark plug, glow plug, or compression ignition. The sharp increase in pressure causes a net torque on the rotor axis from which power may be extracted. The exhaust gases are released during the exhaust stroke, where the apex reveals the exhaust port as it continues to rotate. The cycle is repeated as the rotating apex reveals the intake port once again. Leakage and heat loss from the combustor are the main concerns in this particular microengine. Seals were developed in order to solve the problem of leakage. Heppner et al. [70] designed a small slit machined extremely close to the lateral surface of the rotor near each apex. The result is a thin cantilever beam hovering over each apex, and so was named the cantilever flexure apex seal. Meanwhile, Lee et al. [71] developed seals bearing springs, which ensured that the rotor remains in contact with the housing at all times, except in a modified section. The modified section was fabricated in order to eliminate the compression stroke of the Otto
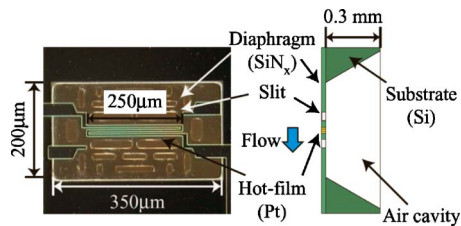
Fig. 8 Microsensor for measuring wall shear stress proposed by Yoshino et al. [74,75]

Fig. 9 Microsensor for measuring heat flux proposed by Oh et al. [78]

cycle. Due to the small surface-to-volume ratio, there is an excessive amount of heat loss through the rather large surface of the engine. This leaves insufficient heat in the engine to sustain combustion. To solve this problem, recesses were implemented along the sidewalls of the rotor in order to increase the combustion chamber's volume by Lee et al. [71].

Frechette et al. [56] proposed a plant-on-a-chip, or microsteam engine, that used water as a working fluid and is based on a closed Rankine cycle. This microengine consists of microheat exchangers (an evaporator as well as a condensor), a viscous micropump, and a generator, which is powered by a microsteam turbine. Two-phase heat exchangers are implemented instead of a combustion chamber, which renders the device more versatile in terms of heat addition purposes. Frechette et al. [56] identified the importance of the condensor's ability to reject the high heat fluxes from the device, whose magnitude would be approximately 50–100 W/cm^2. At the microscale, it is very difficult to isolate hot components from cold ones, and so heat leakage by conduction becomes an extremely important issue. Due to the low thermal resistance between the evaporator and condensor, significant heat loss through direct conduction is a huge issue since the heat would not contribute to any power generation. Another important issue is the fact that, at the microscale, viscous forces dominate, resulting in higher viscous losses and lower adiabatic efficiency, when compared to their larger turbomachinery counterparts.

2.4 Microsensors. Many commercial microsensors are available in the market from companies such as Sensirion and Redwood Microsystems. Sensirion uses CMOSens® technology, which basically integrates a sensor on a CMOS (complementary metal oxide semiconductor) chip. The sensors available from Sensirion are able to detect gas and liquid mass flow rates as well as humidity [72]. Redwood Microsystems have developed a MEMS based pressure sensor, which will be described below. Since the focus of this paper is thermal-fluid microdevices, the following sensors described below are those that may be implemented into thermal microfluidic applications. These microsensors are used to detect various phenomena such as flow rates [73] wall shear stress [74,75], humidity [76], pressure [77], and heat flux [78].

Heat was used to calculate and obtain values for the flow rates, wall stress, and heat flux. The main component of the sensor developed by Wu et al. [73] is a microchannel, with a boron-doped polysilicon thin film resistor embedded inside the wall. A heated polysilicon thin-film sensing element, the heater, is built onto the channel wall, and is placed near the channel exit in order to minimize deflection of the wall. The microconvective heat transfer from the heater to the channel flow is used to determine the temperature of the heater, which is used to calculate the liquid flow rate. Yoshino et al. [74,75] developed a microhot-film shear stress sensor capable of measuring wall shear stress inside a channel with turbulent flow. The microflow sensor is composed of a platinum thin-film heater placed on a diaphragm made of Si_3N_4 with an air cavity fabricated below the diaphragm, and is shown in Fig. 8. There are two hot-films placed perpendicular to one another so that the streamwise and spanwise wall stress components may be measured. It was noted that heat conduction in the fluid
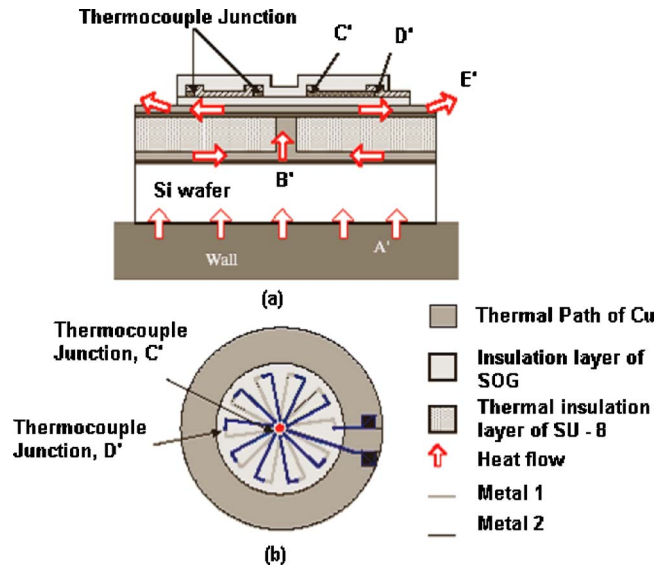
and indirect convective heat transfer has a significant effect in reducing the accuracy of the measurements. The length of the diaphragm was optimized in order to improve the sensor response.

Oh et al. [78] developed a microheat flux sensor, which is circular in shape and capable of measuring convective heat transfer at small heat fluxes. Heat flux from a wall travels to the sensor through a contact layer of copper. The heat then flows through a thermal path made of copper, which runs through the center of a connecting cylinder made of SU-8 serving as insulation, as shown in Fig. 9. The temperature difference is measured between two points in the thermal path, and this measurement is used to determine the wall heat flux. Since the sensor has a thermal resistance itself, heat flux lines are distorted in this area. Future research will aim to further improve the design of the micro heat flux sensor.

Some microsensors use the deformation of certain microstructures to quantify the variation of properties such as humidity and pressure. Lee and Lee [76] developed a microhumidity sensor capable of detecting the humidity, which comprises of a suspended microcantilever over a glass substrate. The suspended microcantilever was coated on one side with a vapor-absorbent film, and when water is absorbed, a tensile stress was developed due to the expansion of the cantilever. The bending of the micro-cantilever changes the measured capacitance between it and the substrate. A definite correlation relates the measured capacitance to the actual relative humidity. The sensitivity of this humidity microsensor is very high, and is capable of compensating for temperature drift. In addition, the microsensor is very stable with low hysteresis and rapid response time. Henning et al. [77] have presented the micropressure sensor developed by Redwood Microsystems. The microsensor is composed of two capacitor plates, where the bottom plate is mechanically fixed, while the top plate is a flexible silicon membrane. The pressure in the sealed cavity is set at a fixed reference value, and as external pressures greater than that of the reference pressure are exerted on the sensor, the membrane deflects toward the fixed plate. The deformation of the membrane can then be correlated to obtain the applied pressure. This pressure microsensor was shown to have high sensitivity, excellent repeatability, is capable to function over a wide range of pressures, and is compatible with most gases and liquids used in semiconductor applications.

Future research in the field of microsensors should focus in improving the accuracy of the measurements. Insulation can be implemented in order to reduce heat transfer leakage, which is the main source in measurement error. Calibration of these devices
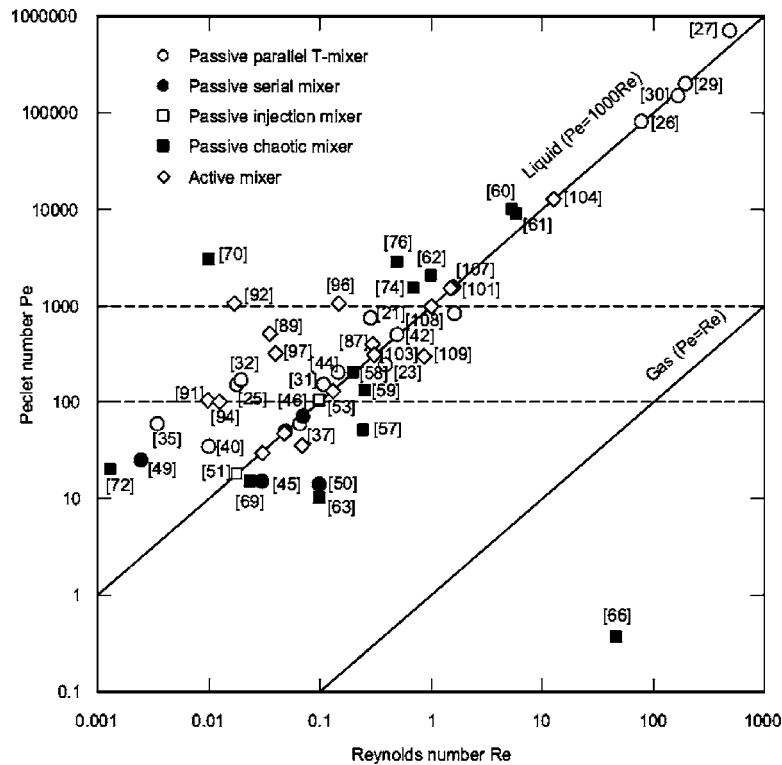
Fig. 10 Typical operating ranges of passive and active micromixers [81]

should also be another issue in future studies. Different fluid types should also be tested in order to ensure that these microsensors yield appropriate measurements for all kinds of fluids.

2.5 Micromixers. Micromixers are typically used in integrated microfluidic devices for mixing reagents prior to chemical or biological reactions in chemical analyses. Complete mixing is necessary in reaction kinetics studies of chemical and biological substances as well as in protein folding investigations. In such cases, mixing times on the order of sub-milliseconds are required, thus the main goal of micromixers is to achieve the shortest mixing time possible. Due to the low Reynolds numbers associated with microdevices, micromixers do not apply turbulent mixing in their operation. Instead, diffusion processes are implemented, and increasing the contact area of the samples has been established as an efficient means of encouraging diffusion [79,80].

Micromixers can be classified as either active or passive, and Fig. 10 from Ngyen and Wu [81] compares the operation ranges of passive and active micromixers from numerous studies. Active micromixers rely on some form of power source, while passive micromixers operate by applying pressure in order to generate mixing through fluid motion. Some active micromixers utilize magnetic forces. The Bau et al. [82] micromixer utilized a series of electrodes to generate magnetic and electric fields in an electrolyte solution, thus producing Lorentz forces in the fluid. The different arrangements of the electrodes can generate various flow fields for mixing purposes. Lu et al. [83] fabricated a complex micromixer that included magnetic microstirrers set into motion by a rotating magnetic field. Rong et al. [84] used magnetic beads inside the fluid set into motion by pairs of integrated electromagnets. Other active micromixers generate acoustic waves by applying ultrasonic frequencies to the samples. Vivek et al. [85] used annular rings of half wave band sources to produce acoustic waves, while Rife et al. [86] used ultrasonic piezoelectric transducers. Yang et al. [87] generated acoustic waves by exciting a piezoelectric lead-zirconate-titanate (PZT) ceramic with a square wave voltage. The main problems associated with these active

micromixers are that these types of mixers are not capable of providing sufficient mixing rates for some biological analyses. Also, in acoustic micromixers, the vibrations of the acoustic waves may generate heat, which can be problematic [79,80].

Typical passive micromixers use microchannels in order to feed samples, although some mixers utilize holes [88] or cantilever plate valves [89]. Various arrangements of microchannels in passive micromixers have been investigated. He et al. [90] fabricated a micromixer with intersecting channels of various lengths and widths, while Knight et al. [91] and Wong et al. [92] investigated the cross-shaped micromixer. Perhaps the most studied configuration is the T-form micromixer. Although turbulence mixing is not typical in micromixers, Bökenkamp et al. [93] achieved a turbulence mixing time of 110 μs by using larger channels 500 μm wide. Gobby et al. [94] numerically studied gaseous flows in a T micromixer in which they showed that the mixing length increases with flow velocity, while the mixing length decreases when the flow is throttled. Engler et al. [95] provide an in-depth study of fluid mechanics in the T micromixer, in which three different flow regimes, laminar flow, vortex flow, and engulfment flow, were identified. At high flow velocities, the symmetry of the flow field breaks down and this is called engulfment flow. Superior mixing is associated with engulfment flow. The T mixer developed by Wong et al. [79], with a 67 μm hydraulic mixing channel, completed mixing in less than a millisecond when 5.5 bar of pressure was applied. Lin et al. [80] developed a T-form mixer which generated electroosmotic flow and flow instabilities simultaneous through the application of a switching dc field. A maximum mixing efficiency of 97% was attained for this particular micromixer [79,80].

3 Advances in Measurements and Simulations

This paper also reviews the progress of research tools such as heat measurement techniques that have applied at the microscale. Cahill et al. [96] reviewed three different techniques for temperature measurement at the micro- and nano-level, and they are ther-

mal microscopy, picosecond reflectance thermometry, and scanning optical thermometry. In scanning thermal microscopy, a sharp tip is placed on the surface, and the surface temperature may be derived from the localized heat transfer between the surface to the tip. Most common setups utilize a cantilevered tip on an atomic force microscope. Spatial resolutions in the range of 30–50 nm have been obtained. Applicable areas in need of improvement are acquiring fundamental understanding of the tip-sample heat transfer, as well as designing and fabricating integrated multifunctional probes. Additional information on the scanning thermal microscope may also be found in Gu et al. [97]. The second method is picosecond reflectance thermometry, which is similar to reflectance thermometry but is extended to picosecond time scales. This method involves generating laser pulses and directing them at the surface of interest. Mode-locked lasers are used to produce a series of less than 1 ps pulses repeating at a rate of 76 MHz. One likely reason for the limited use of picosecond thermoreflectance is the expense of the mode-locked lasers. These pulses diffuse heat into the surface, and the decay of the reflected light is used to obtain measurements. The third technique is scanning optical thermometry where, through the use of solid immersion lens (SIL) technology, spatial resolution of optical measurements can be increased past the diffraction limit. The main problem with scanning optical thermometry is the reduction in transmissivity with a reduced aperture which limits the sensitivity to temperature. The use of solid immersion lens (SIL) technology in principle may possibly be used to mitigate this drawback. The first micromachined lens was recently produced by Fletcher et al. [98], yet this approach is still in its infancy.

Liquid crystal thermometry, and in particular through unencapsulated thermochromic liquid crystals (TLCs), has been demonstrated for microgeometries [99,100]. The liquid crystal material is an anisotropic mesophase formed between the crystalline solid and isotropic liquid phase of some materials. When illuminated with white light, it will reflect light of wavelength proportional to the temperature it is experiencing. Their use has been restricted to the heated coating measurement technique using a thin foil, whereby a voltage is placed across a foil to produce a uniform heat flux surface. The outer wall temperature is usually assumed to be the same as that of the inner wall. In the case of Hohmann and Stephan [100] spatial resolutions of 0.83 μm/pixel were demonstrated. The liquid crystal in its encapsulated form (capsules of 5–50 μm) is favored for macroapplications since it is more resilient and easier to handle, however spatial resolutions such as the above are not possible due to its capsule size. The liquid crystal material has been applied with a paintbrush, yet significant difficulty was noted in obtaining a continuous uniform layer necessary for effective temperature interpretation. Liquid crystals have been utilized by Hollingsworth [38], Piasecka and Poniewski [39], Muwanga and Hassan [101], and Lakshminarasimhan et al. [102] for use in mini- and microchannels.

Infrared thermography has been investigated for measurements in microgeometries by Hapke et al. [103], Hetsroni et al. [104], Narayanan [105], and Diaz et al. [106]. When measuring the temperature of a micro-object with the infrared technique, the background will introduce significant noise if it is at a different temperature than the object being measured. This causes the uncertainty in temperature to be relative to the background. This problem is not immediately solved by adding a microscope lens. Hetsroni et al. [104] compensated for this through the control of the background temperature during measurement of a capillary surface temperature. For the studies incorporating heat transfer measurements, the inner wall temperature was estimated using a one-dimensional (1D) heat conduction approximation.

Kim et al. [107] investigated the applicability of the ratiometric laser induced fluorescence (LIF) thermometry technique at the microscale. They noted that the fluorescing intensity of the dyed fluid is proportional to the illuminating light intensity, the dye concentration, and the optical constant of the dye. For a constant illuminating light intensity and dye concentration, the intensity may be related to temperature. However, since it was difficult to maintain a constant light intensity, the ratiometric technique was introduced. Here, the temperature-dependant dye intensity was normalized with a temperature-independent dye intensity. The dye fluorescence degraded with repeated excitations and it was suggested that the best accuracy and repeatability was obtained with mixtures no older than 2–3 days. This measurement technique was evaluated in a channel 1 mm wide by 45 mm long. Temperature uncertainties of 2.0°C for a 150 μm $\times$ 100 μm area and 0.4°C for a 1200 $\times$ 800 interrogated area were obtained. The accuracy of the LIF technique will be dependant upon the interrogation region considered. This technique should be developed further for use when full surface temperature measurement is required.

Thermocouples are still a standard choice for many researchers while investigating heat transfer due to their relatively low cost. Many studies of microchannel heat transfer have used thermocouples by placing them a distance from the surface of interest and estimating the internal wall temperature through a 1D heat conduction approximation or used them for bulk fluid measurements (e.g., [22,31,37,108,109]). Current fine gage wire thermocouples on the market have diameters as small as 0.0127 mm for K and E Type and 0.0760 mm for D and C Type [110]. Thermocouple diameters for specialized hypodermic probes are as small as 0.2000 mm, while standard small size probes have diameters as small as 1.5875 mm [110]. Although thermocouple probes are available with diameters close to the limiting resolution of TLC and IR, their drawback remains the need for an array when spatial variation is of interest.

An overview of the various kinds of micromachined thermal sensors may be found in Kovacs [111]. Many of the macrosize thermal sensing concepts have been fabricated as a microtransducer. These include thermomechanical sensors which rely on thermal bimorph of two dissimilar metals, thermoresistive transducers where temperature is related to change in resistance, and thermocouple type sensors which rely on the Seebeck and Peltier effect. Self-heating becomes a significant problem as the size gets smaller for resistive sensors due to the excitation required. If the thermal time constants are known for the system, pulsed measurements may be incorporated to minimize this self-heating and increase accuracy. A recent example of the fabrication of an integrated resistive sensor may be found in Liu et al. [112]. It is attractive to manufacture thermocouple type sensors from semiconductor materials which are already readily available, since the Seebeck coefficient is generally larger ($\sim$10^{-3} V/K as opposed to 10^{-8} V/K), and hence is more sensitive. Junction-based sensors utilizing diodes or transistors are also common for micromachined thermal sensors.

Overall, these methods allow for measurements with length scales on the order of the mean free path and times scales on the order of the relaxation times of the electrons and phonons at room temperature. However, the combination of these two is very difficult and further advances are required. Whilst these techniques are being developed to study microscale heat transfer, to further advance these techniques, a better understanding of microscale heat transfer is equivalently required [96]. The main challenge with micromachined thermal sensors lies in the fabrication methodology and application.

Rapid development in measuring techniques also allowed capturing velocity of the flow field in a fraction of second using nonintrusive optical measurements techniques, such as particle image velocimetry (PIV) systems. Currently, micro-PIV systems have mainly been used in liquid microsystems because it is simple to set up and uniform seeding is usually easily attained [113–115]. Micro-PIV tests for gas and two-phase flow in microsystems need to be investigated more in the near future. Micro-PIV presents a number of challenges including visualizing tracer particles that are smaller than the wavelength of light, minimizing errors due to the Brownian motion of tracer particles, and illuminating flow volume

instead of illuminating the light sheet. Accurate PIV measurements in microchannels with spatial resolutions on the order of several microns requires that the diameter of tracer particles d_p must be on the order of 100 nm to 300 nm along with visible light ($\lambda = 532$ nm) to illuminate the particles so that the scattered light should be in Rayleigh scattering range ($d_p \ll \lambda$). Due to the random Brownian motion of fluid molecules in the microchannel, the effect of single collision of seed particles increases with decreasing particle size. Brownian motion creates an unbiased error that can be reduced by averaging over groups of particles. Today, commercially available micro-PIV systems are available from companies such as Dantec Dynamics [116]. However, the micro-PIV system is under continuous development and several improvements are expected in the near future.

A flow imaging process called "microbubble lensing induced photo bleaching" (μ-BLIP) is introduced by Sinton et al. [117] in order to measure local fluid velocity in microgeometries. The process works by injecting a negative scalar flow marker in an aqueous buffer solution inside the microchannel with a 100 μm inner diameter, and with a 200 μm long stationary bubble at the center of the channel. The path of the marker helps in determining the velocity of liquid, while the bubble aids in the photoinjection of the marker. The motion of the marker is governed by electrokinetic transport, thus numerical simulations were produced in order to study the electrical potential and flow field. The region near the bubble was photobleached and a 2600 V potential was applied to the fluid. The electric field lines were found to be concentrated in the thin film region around the bubble. The velocity profiles were obtained at distances 0.1, 0.4, and 1.0 capillary diameters from the bubble's edge. The velocity adjacent to the wall was found to be slightly higher than that at the centerline of the capillary. The velocity rapidly changed into a profile typical of that for traditional plug flows. The disadvantage of this technique was the requirement of a bubble for the photoinjection of the marker. However, it is possible to obtain information on the bubble geometry, bubble velocity, and local fluid velocity in two-phase flow concurrently, which renders it a promising technique in flow imaging.

4 Conclusion

The present paper provides a comprehensive review on the progress of research made during the last decade in the area of heat transfer and fluid flow in microchannels, micropumps, microturbines, microengines, micromixers, as well as microsensors. Recent experimental techniques in the thermal microdevices field have also been presented. During the next decade, vast amounts of research need to be conducted before microdevices infiltrate the mainstream. The following are possible future directions of research.

Microscale internal flows have received much attention over the past two decades. However, there still remain certain microflow conditions for which the pressure drop and heat transfer have not yet been clearly defined and understood. The study of developing flows in the entrance regions of microchannels is limited and should be focused on in the future, since the effect on the subsequent flow field and heat transfer may be quite significant. The development of the hydrodynamic and thermal boundary layers, and location of the entrance regions are all associated with different flow and heat transfer mechanisms, which may dictate the manner in which devices such as microchannel heat exchangers be designed. However, it is still quite difficult to obtain local flow measurements, especially local heat measurements at the microlevel. As microscale measurement techniques improve, flow and heat transfer readings in this very small region may be obtainable. In addition, the effects of varying wall temperature or varying heat flux on internal microflows should be studied in greater depth in the future since they are more realistic boundary conditions.

Both single-phase and two-phase microchannel heat exchangers have been studied in the open literature. In two-phase microchannel heat exchangers, the wall temperature has been found to be relatively uniform, rendering it preferable over the single-phase microchannel heat exchanger. Understanding the fundamental characteristics of two-phase flow boiling heat transfer in mini- and micro-channels is very important in the development of high heat flux miniature cooling devices. Based on the studies to date, the dominant boiling mechanism in such channels remains inconclusive. Although, very high heat transfer rates have been achieved with the two-phase microheat exchangers, stable operation in superheated conditions has rarely been reported. Typically, dry-out, bubbles, unsteady flow phenomena, and the critical heat flux prevent stable superheated operation. There is also a significant lack of data pertaining to boiling two-phase flow regimes inside microchannels, particularly in ranges less than 500 μm. The two-phase boiling study of different fluid types/regimes is also important when considering appropriate nondimensional groupings for boiling in microheat exchangers. Also of main interest are the pressure drop and area required to evaporate and fully superheat a constant water stream. Finally, numerical modeling of two-phase flow studies could greatly contribute to the study of two-phase microchannel heat exchangers by capturing the complex flow field, and should be a future goal in research.

There are still some issues that still need to be resolved concerning micropumps. The first is the complexity of some positive-displacement micropumps. The use of valves may render the pump difficult to maintain and to repair should any problems arise. In order for micropumps to be applicable in the commerical market, they should be as universal as possible. In other words, they should be able to adapt to various situations and applications. Most valveless micropumps are very restricted since they require additional components such as a heater or electrodes. The viscous micropump is simple in design, however requires that the rotor be rotated by some external source. This may be difficult through mechanical means, so investigating biological rotors should be considered in the future, which one research group has already successfully implemented in the cellular motor based micropump [118]. Improving the efficiency of the cellular motor based micropump could be achieved by using the symmetrical dual vertical rotor.

Future research directions for the spiral viscous micropump may include analyzing the effect of spiral curvature, microchannel height, clearance gap height, as well as of cross flow on the pump's performance at both high and low Reynolds numbers [57]. Heat transfer effects should also be investigated, especially if the micropump is to be integrated onto a plant-on-a-chip device that produces heat, such as the microsteam turbine engine. At small scales, heat conduction through the structure of the device could occur causing the viscosity of the working fluid inside the micropump to decrease. This may affect the performance of the pump since it relies heavily on viscous forces for its operation. Applying a constant heat flux to the stationary plate could simulate this situation and provide insight should conduction heat transfer occur.

Most, if not all the engines reviewed here are still in their early stages of development. The two main concerns for microengines are the large amounts of losses and heat transfer. Heat transfer through conduction tends to be a problem since the dimensions within the structure are so small. Microstructures and materials that control heat conduction paths should be developed in future studies. Also, the implementation of seals and cooling mechanisms should be the focus of future research. Detailed numerical studies of microengines should be conducted in order to investigate the effects of different parameters such as geometry and flow conditions on the overall fluid and heat transfer behavior within these devices. Besides the microsteam turbine engine, all microengines use single-phase gas as the working fluid. It may be of interest to develop more microengines that use liquid-phase work-

ing fluids so that micropumps, instead of compressors, are used. This could be advantageous since micropumps are among the most developed microdevices to date.

Most microthermal-fluid experiments still rely on large-scale external apparatus for their operation. Thus, in order to achieve complete portability, the reliance on larger infrastructure must be reduced. Progress in microsensors design, for measurements and control, would lead to the development of future microsystems on chips.

Acknowledgment

References

[1] Papautsky, I., Ameel, T., and Frazier, A. B., 2001, A Review of Laminar Single-Phase Flow in Microchannels, *Proc. ASME International Mechanical Engineering Congress and Exposition*, Nov. 11–16, New York, NY, Micro-Electromechanical Systems Division Publication (MEMS), Vol. 3, Micro-Electro-Mechanical Systems (MEMS), IMECE2001, pp. 495–503.

[2] Mala, G. M., and Li, D., 1999, "Flow Characteristics of Water in Microtubes," Int. J. Heat Fluid Flow, **20**, pp. 142–148.

[3] Celata, G. P., Cumo, M., Gulielmi, M., and Zummo, G., 2000, "Experimental Investigation of Hydraulic and Single-Phase Heat Transfer in 0.130 mm Capillary Tube," *Proceedings of the International Conference on Heat Transfer and Transport Phenomena in Microscale*, Oct. 15–20, Banff, Canada, G. P. Celata, ed., Begell House, New York, NY, pp. 108–113.

[4] Wu, H. Y., and Cheng, P., 2003, "An Experimental Study of Convective Heat Transfer in Silicon Microchannels With Different Surface Conditions," Int. J. Heat Mass Transfer, **46**, pp. 2547–2556.

[5] Lelea, D., Nishio, S., and Takano, K., 2004, "The Experimental Research on Micro Tube Heat Transfer and Fluid Flow of Distilled Water," Int. J. Heat Mass Transfer, **47**, pp. 2817–2830.

[6] Kim, D., and Darve, E., 2005, "Interactions of Wall Roughness and Electroosmotic Flows Inside Nanochannels," *Proceedings of the Third International Conference on Microchannels and Minichannels*, June 13–15, Toronto, Canada, PART B, ICMM2005-75237, ASME, New York, NY, pp. 641–645.

[7] Li, Z. X., Du, D. X., and Guo, Z. Y., 2000, "Experimental Study on Flow Characteristics of Liquid in Circular Microtubes," *Proceedings of the International Conference on Heat Transfer and Transport Phenomena in Microscale*, Oct. 15–20, Banff, Canada, G. P. Celata, ed., Begell House, New York, NY, pp. 162–167.

[8] Zeighami, R., Laser, D., Zhou, P., Asheghi, M., Devasenathipathy, S., Kenny, T., Santiago, J., and Goodson, K., 2000, "Experimental Investigation of Flow Transition in Microchannels Using Micron-Resolution Particle Image Velocimetry," *Proc. IEEE 7th Intersociety Conference on Thermomechanical Phenomena in Electronic Systems*, May 23–26, Las Vegas, NV, IEEE, Vol. 2, ITHERM.2000.866184, pp. 148–153.

[9] Peng, X. F., and Peterson, G. P., 1996, "Convective Heat Transfer and Flow Friction for Water Flow in Microchannel Structures," Int. J. Heat Mass Transfer, **39**(12), pp. 2599–2608.

[10] Xu, B., Ooi, K. T., Wong, N. T., and Choi, W. K., 2000, "Experimental Investigation of Flow Friction for Liquid Flow in Microchannels," Int. Commun. Heat Mass Transfer, **27**(8), pp. 1165–1176.

[11] Damianides, C. A., and Westwater, J. W., 1988, "Two-Phase Patterns in a Compact Heat Exchanger and in Small Tubes," *Proc. IMechE 2nd UK National Conference on Heat Transfer*, Sept. 14–16, Glasgow, U.K., Mech. Engng. Publications Ltd., Bury St. Edmunds, U.K., Vol. 2, pp. 1257–1268.

[12] Fukano, T., Kariyasaki, A., and Kagawa, M., 1989, "Flow Patterns and Pressure Drop in Isothermal Gas-Liquid Cocurrent Flow in a Horizontal Capillary Tube," *Proc. ANS 1989 National Heat Transfer Conference: Technical Sessions*, American Nuclear Society, La Grange Park, IL, Vol. 4, pp. 153–161.

[13] Mishima, K., Hibiki, T., and Nishihara, H., 1993, "Some Characteristics of Gas-Liquid Flow in Narrow Rectangular Ducts," Int. J. Multiphase Flow, **19**, pp. 115–124.

[14] Xu, J., Cheng, P., and Zhao, T. S., 1999, "Gas-Liquid Two-Phase Flow Regimes in Rectangular Channels With Mini/Micro Gaps," Int. J. Multiphase Flow, **25**, pp. 411–432.

[15] Triplett, K. A., Ghiaasiaan, S. M., Abdel-Khalik, S. I., and Sadowski, D. L., 1999, "Gas-Liquid Two-Phase Flow in Microchannels, Part I: Two-Phase Flow Patterns," Int. J. Multiphase Flow, **25**, pp. 377–394.

[16] Zhao, T. S., and Bi, Q. C., 2001, "Co-Current Air-Water Two-Phase Flow Patterns in Vertical Triangular Microchannels," Int. J. Multiphase Flow, **27**,

[17] Feng, Z., and Serizawa, A., 2000, *Two-Phase Flow Patterns in an Ultra-Small-Scale Flowing Passage*, Department of Nuclear Engineering, Kyoto University, Japan.

[18] Kawahara, A. P., Chung, M. Y., Kawaji, M., 2002, "Investigation of Two-Phase Flow Patterns, Void Fraction and Pressure Drop in a Microchannel," Int. J. Multiphase Flow, **28**, pp. 1411–1435.

[19] Hassan, I., Vaillancourt, M., and Pehlivan, K., 2005, "Two-Phase Flow Regime Transitions in Microchannels: A Comparative Experimental Study," Microscale Thermophys. Eng., **9**(2), pp. 165–182.

[20] Thome, J. R., 2004, "Boiling in Microchannels: A Review of Experiment and Theory," Int. J. Heat Fluid Flow, **25**, pp. 128–139.

[21] Kandlikar, S. G., 2002, "Fundamental Issues Related to Flow Boiling in Minichannels and Microchannels," Exp. Therm. Fluid Sci., **26**, pp. 389–407.

[22] Brutin, D., Topin, F., and Tadrist, L., 2003, "Experimental Study of Unsteady Convective Boiling in Heated Minichannels," Int. J. Heat Mass Transfer, **46**, pp. 2957–2965.

[23] Wu, H. Y., and Cheng, P., 2004, "Boiling Instability in Parallel Silicon Microchannels at Different Heat Flux," Int. J. Heat Mass Transfer, **47**, pp. 3631–3641.

[24] Tuckerman, D. B., and Pease, R. F. W., 1981, "High Performance Heat Sinking for VLSI," IEEE Electron Device Lett., **EDL-2**(5), pp. 126–129.

[25] Rahman, M. M., 2000, "Measurements of Heat Transfer in Microchannel Heat Sinks," Int. Commun. Heat Mass Transfer, **27**(4), pp. 495–506.

[26] Fedorov, A. G., and Viskanta, R., 2000, "Three-Dimensional Conjugate Heat Transfer in the Microchannel Heat Sink for Electronic Packaging," Int. J. Heat Mass Transfer, **43**(3), pp. 399–415.

[27] Jang, S. P., Kim, S. J., and Paik, K. W., 2003, "Experimental Investigation of Thermal Characteristics for a Micro Channel Heat Sink Subject to an Impinging Jet, Using a Micro-Thermal Sensor Array," Sens. Actuators, A, **105**, pp. 211–224.

[28] Kawano, K., Sekimura, M., Minakami, K., Iwasaki, H., and Ishizuka, M., 2001, "Development of Micro Channel Heat Exchanging," JSME Int. J., Ser. B, **44**(4), pp. 592–598.

[29] Jiang, P.-X., Fan, M.-H., Si, G.-S., and Ren, Z.-P., 2001, "Thermal Hydraulic Performance of Small Scale Micro Channel and Porous Media Heat Exchangers," Int. J. Heat Mass Transfer, **44**, pp. 1039–1051.

[30] Hestroni, G., Mosyak, A., Segal, Z., and Ziskind, G., 2002, "A Uniform Temperature Heat Sink for Cooling of Electronic Devices," Int. J. Heat Mass Transfer, **45**, pp. 3275–3286.

[31] Qu, W., and Mudawar, I., 2003, "Flow Boiling Heat Transfer in Two-Phase Micro-Channel Heat Sinks: Part I: Experimental Investigation and Assessment of Correlation Methods. Part II: Annular Two-Phase Flow Model," Int. J. Heat Mass Transfer, **46**, pp. 2755–2784.

[32] Koo, J., Jiang, L., Bari, A., Zhang, L., and Wang, E., 2002, "Convective Boiling in Microchannel Heat Sinks With Spatially-Varying Heat Generation," *Proc. IEEE 8th Intersociety Conference on Thermomechanical Phenomena in Electronic Systems*, May 30–June 1, San Diego, CA, IEEE, ITHERM. 2002.1012477, pp. 341–346.

[33] Jiang, L., Wong, M., and Zohar, Y., 2001, "Forced Convection Boiling in a Microchannel Heat Sink," J. Microelectromech. Syst., **10**(1), pp. 80–87.

[34] Quadir, G. A., Mydin, A., and Seetharamu, K. N., 2001, "Analysis of Micro Channel Heat Exchanger Using FEM," Int. J. Numer. Methods Heat Fluid Flow, **11**(1), pp. 59–75.

[35] Bowers, M. B., and Mudawar, I., 1994, "High Flux Boiling in Low Flow Rate, Low Pressure Drop Mini-Channel and Micro-Channel Heat Sinks," Int. J. Heat Mass Transfer, **37**, pp. 321–332.

[36] Bergles, A. E., and Kandlikar, S. G., 2003, "Critical Heat Flux in Microchannels: Experimental Issues and Guidelines for Measurement," *Proc. ASME 1st International Conference on Microchannels and Minichannels*, April 24–25, Rochester, NY, S. Kandlikar, ed., ASME, ICMM2003-1016, pp. 141–147.

[37] Yu, W., France, D. M., Wambsganss, M. W., and Hull, J. R., 2002, "Two-Phase Pressure Drop, Boiling Heat Transfer, and Critical Heat Flux to Water in a Small-Diameter Horizontal Tube," Int. J. Multiphase Flow, **28**, pp. 927–941.

[38] Hollingsworth, K., 2004, "Liquid Crystal Imaging of Flow Boiling in Minichannels," *Proc. ASME 2nd International Conference on Microchannels and Minichannels*, June 17–19, Rochester, NY, S. Kandlikar, ed., ASME, ICMM2004-2320, pp. 57–66.

[39] Piasecka, M., and Poniewski, M. E., 2004, "Influence of Selected Parameters on Boiling Heat Transfer in Minichannels," *Proc. ASME 2nd International Conference on Microchannels and Minichannels*, June 17–19, Rochester, NY, S. Kandlikar, ed., ASME, ICMM2004-2376, pp. 515–521.

[40] Vafai, K., and Zhu, L., 1999, "Analysis of Two Layered Micro Channel Heat Sink Concept in Electronic Cooling," Int. J. Heat Mass Transfer, **42**(12), pp. 2287–2297.

[41] Sen, M., Wajerski, D., and Gad-el-Hak, M., 1996, "A Novel Pump for MEMS Applications," ASME J. Fluids Eng., **118**, pp. 624–627.

[42] Laser, D. J., and Santiago, J. G., 2004, "A Review of Micropumps," J. Micromech. Microeng., **14**(6), pp. R35–R64.

[43] Gravesen, P., Branebjerg, J., and Jensen, O. S., 1993, "Microfluidics – A Review," J. Micromech. Microeng., **3**(4), pp. 168–182.

[44] Stemme, E., and Stemme, G., 1993, "Valveless Diffuser/Nozzle-Based Fluid Pump," Sens. Actuators, A, **39**(2), pp. 159–167.

[45] Olsson, A., Stemme, G., and Stemme, E., 2000, "Numerical and Experimental Studies of Flat-Walled Diffuser Elements for Valve-Less Micropumps," Sens. Actuators, A, **84**(1), pp. 165–175.

[46] Olsson, A., Stemme, G., and Stemme, E., 1996, "Micromachined Diffuser/

Nozzle Elements for Valve-Less Pumps," *Proc. IEEE 9th International Workshop on Micro Electro Mechanical Systems (MEMS '96)*, Feb. 11–15, San Diego, CA, IEEE, MEMSYS.1996.494011, pp. 378–383.

[47] Olsson, A., Stemme, G., and Stemme, E., 1997, "Simulation Studies of Diffuser and Nozzle Elements for Valve-Less Micropumps," *Proc. IEEE 9th International Conference on Solid-State Sensors and Actuators (Transducers '97)*, June 16–19, Chicago, IL, IEEE, Vol. 2, SENSOR.1997.635363, pp. 1039–1042.

[48] Bart, S. F., Tavrow, L. S., Mehregany, M., and Lang, J. H., 1990, "Microfabricated Electrohydrodynamic Pumps," Sens. Actuators, A, **21**(1–3), pp. 193–197.

[49] Harrison, D. J., Manz, A., and Glavina, P. G., 1991, "Electrosmotic Pumping Within a Chemical Sensor System Integrated on Silicon," *Proc. IEEE 6th International Conference on Solid-State Sensors and Actuators (Transducers '91)*, June 24–27, San Francisco, CA, IEEE, SENSOR.1991.149002, pp. 792–795.

[50] Manz, A., Effenhauser, C. S., Burggraf, N., Harrsion, D. J., Seiler, K., and Fluri, K., 1994, "Electroosmotic Pumping and Electrophoretic Separations for Miniaturized Chemical Analysis Systems," J. Micromech. Microeng., **4**(4), pp. 257–265.

[51] Sharatchandra, M. C., Sen, M., and Gad-el-Hak, M., 1997, "Navier-Stokes Simulation of a Novel Viscous Pump," ASME J. Fluids Eng., **119**, pp. 372–382.

[52] Sharatchandra, M. C., Sen, M., and Gad-el-Hak, M., 1998, "Thermal Aspects of a Novel Viscous Pump," J. Heat Transfer, **120**, pp. 99–107.

[53] Decourtye, D., Sen, M., and Gad-el-Hak, M., 1998, "Analysis of Viscous Micropumps and Microturbines," Int. J. Comput. Fluid Dyn., **10**, pp. 13–25.

[54] Abdelgawad, M., Hassan, I., and Esmail, N., 2004, "Transient Behavior of the Viscous Micropump," Microscale Thermophys. Eng., **8**(4), pp. 361–381.

[55] Phutthavong, P., and Hassan, I., 2004, "Transient Performance of Flow Over a Rotating Object Placed Eccentrically Inside a Microchannel—Numerical Study," Microfluidics and Nanofluidics, **1**(1), pp. 71–85.

[56] Frechette, L. G., Lee, C., Arslan, S., and Liu, Y.-C., 2003, "Design of a Microfabricated Rankine Cycle Steam Turbine for Power Generation," *Proc. ASME International Mechanical Engineering Congress*, Nov. 15–21, Washington, DC, Micro–Electromechanical Systems Division Publication (MEMS), Vol. 5, Micro-Electro-Mechanical Systems (MEMS), IMECE2003-42082, pp. 335–344.

[57] Kilani, M. I., Galambos, P. C., Haik, Y. S., and Chen, C.-J., 2003, "Design and Analysis of a Surface Micromachined Spiral-Channel Viscous Pump," ASME J. Fluids Eng., **125**(2), pp. 339–344.

[58] Sugiyama, S., and Toriyama, T., 2003, "Design of a Micro Reciprocating Engine for Power Generataion," IEE J. Trans. Sensors and Micromachines, **123**(9), pp. 351–356.

[59] Jacobson, S. A., and Epstein, A. H., 2003, "An Informal Survey of Power MEMS," *Proc. JSME International Symposium on Micro-Mechanical Engineering*, Dec. 1–3, Tsuchiura and Tsukuba, Japan, ISMME2003-K18.

[60] Epstein, A. H., 2003, "Millimeter-Scale, MEMS Gas Turbine Engines," *Proc. ASME 2003 Turbo Expo: Power for Land, Sea, and Air*, June 16–19, Atlanta, GA, ASME/IGTI Publication, Vol. 4, Scholar Lecture, GT2003-38866, pp. 669–696.

[61] Isomura, K., Murayama, M., Yamaguchi, H., Ijichi, N., Saji, N., Shiga, O., Takahashi, K., Tanaka, S., Genda, T., and Esashi, M., 2002, "Development of Microturbocharger and Microcombustor for a Three-Dimensional Gas Turbine at Microscale," *Proc. ASME 2002 Turbo Expo: Power for Land, Sea, and Air*, June 3–6, Amsterdam, Netherlands, ASME/IGTI Publication, Vol. 1, GT2002-30580, pp. 1127–1134.

[62] Mehra, A., Zhang, X., Ayon, A. A., Waitz, I. A., Schmidt, M. A., and Spadaccini, C. M., 2000, "A Six-Wafer Combustion System for A Silicon Micro Gas Turbine Engine," J. Microelectromech. Syst., **9**(4), pp. 517–527.

[63] Spadaccini, C. M., Lee, J., Lukachko, S., Waitz, I. A., Mehra, A., and Zhang, X., 2002, "High Power Density Silicon Combustion Systems for Micro Gas Turbine Engines," *Proc. ASME 2002 Turbo Expo: Power for Land, Sea, and Air*, June 3–6, Amsterdam, Netherlands, ASME/IGTI Publication, Vol. 1, GT2002-30082, pp. 469–481.

[64] Whalen, S. A., Weiss, L. W., Richards, C. D., Bahr, D. F., and Richards, R. F., 2003, "Characterization of the Thermodynamic Working Cycle in a MEMS-Based Micro Heat Engine," *Proc. ASME International Mechanical Engineering Congress and Exposition*, Nov. 15–21, Washington, DC, Micro-Electromechanical Systems Division Publication (MEMS), Vol. 5, Micro-Electro-Mechanical Systems (MEMS), IMECE2003-41426, pp. 701–707.

[65] Whalen, S., Thompson, M., Bahr, D., Richards, C., and Richards, R., 2003, "Design, Fabrication and Testing of the P³ Micro Heat Engine," Sens. Actuators, A, **104**, pp. 290–298.

[66] Park, D.-E., Lee, D.-H., Yoon, J.-B., Kwon, S., and Yoon, E., 2002, "Design and Fabrication of Micromachined Internal Combustion Engine as a Power Source for Microsystems," *Proc. IEEE 15th International Conference on Micro Electro Mechanical Systems (MEMS)*, June 20–24, Las Vegas, NV, IEEE, MEMSYS.2002.984255, pp. 272–275.

[67] Kirtas, M., Disseau, M., Scarborough, D., Jaqoda, T., and Menon, S., 2002, "Combustion Dynamics in a High Aspect Ratio Engine," Proc. Combust. Inst., **29**(1), pp. 917–923.

[68] Aichlmayr, H. T., Kittelson, D. B., and Zachariah, M. R., 2002, "Miniature Free-Piston Homogeneous Charge Compression Ignition Engine-Compressor Concept – Part I: Performance Estimation and Design Considerations Unique to Small Dimensions; Part II – Modeling HCCI Combustion in Small Scales With Detailed Homogeneous Gas Phase Chemical Kinetics," Chem. Eng. J.,

[69] Fu, K., Knobloch, A. J., Martinez, F. C., Walther, D. C., Fernandez-Pello, C., Pisano, A. P., and Liepmann, D., 2001, "Design and Experimental Results of Small-Scale Rotary Engines," *Proc. ASME International Mechanical Engineering Congress and Exposition*, Nov. 11–16, New York, NY, ASME Advanced Energy Systems Division Publication, IMECE2001, Vol. 41, pp. 295–301.

[70] Heppner, J. D., Walther, D. C., and Pisano, A. P., 2003, "Leakage Flow Analysis for a MEMS Rotary Engine," *Proc. ASME International Mechanical Engineering Congress and Exposition*, Nov. 15–21, Washington, DC, Micro-Electromechanical Systems Division Publication (MEMS), Vol. 5, Micro-Electro-Mechanical Systems (MEMS), IMECE2003-41868, pp. 327–334.

[71] Lee, C. H., Jiang, K. C., Jin, P., and Prewett, P. D., 2004, "Design and Fabrication of a Micro Wankel Engine Using MEMS Technology," Microelectron. Eng., **73–74**, pp. 529–534.

[72] Sensirion: The Sensor Company, www.sensirion.com, current February 2005.

[73] Wu, S., Lin, Q., Yuen, Y., and Tai, Y.-C., 2001, "MEMS Flow Sensors for Nano-Fluidic Applications," Sens. Actuators, A, **89**, pp. 152–158.

[74] Yoshino, T., Suzuki, Y., Kasagi, N., and Kamjunten, S., 2001, "Assessment of the Wall Shear Stress Measurement With Arrayed Micro Hot-Film Sensors in a Turbulent Channel Flow," *Proc. 2nd International Symposium on Turbulence and Shear Flow Phenomena*, June 27–29, Stockholm, Sweden, TSFP-2, Vol. 2, pp. 153–158.

[75] Yoshino, T., Suzuki, Y., Kasagi, N., and Kamiunten, S., 2003, "Optimum Design of Micro Thermal Flow Sensor and Its Evaluation in Wall Shear Stress Measurement," *Proc. IEEE 6th International Conference on Micro Electro Mechanical Systems (MEMS)*, Jan. 19–23, Kyoto, Japan, IEEE, MEMSYS.2003.1189719, pp. 193–196.

[76] Lee, C.-Y., and Lee, G.-B., 2003, "MEMS-Based Humidity Sensors With Integrated Temperature Sensors for Signal Drift Compensation," *Proc. IEEE 2nd Conference on Sensors: IEEE Sensors 2003*, Oct. 22–24, Toronto, Canada, IEEE, Vol. 1, ICSENS.2003.1278963, pp. 384–388.

[77] Henning, A. K., Mourlas, N., Metz, S., and Zias, A., 2002, "A MEMS-Based, High-Sensitivity Pressure Sensor for Ultraclean Semiconductor Applications," *Proc. IEEE/SEMI Conference and Workshop of Advanced Semiconductor Manufacturing*, April 30–May 2, Boston, MA, IEEE, ASMC.2002.1001596, pp. 165–168.

[78] Oh, S. H., Lee, K.-C., Chun, J., Kim, M., and Lee, S. S., 2001, "Micro Heat Flux Sensor Using Copper Electroplating in Su-8 Microstructures," J. Micromech. Microeng., **11**, pp. 221–225.

[79] Wong, S. H., Ward, M. C. L., and Wharton, C. W., 2004, "Micro T-Mixer as a Rapid Mixing Micromixer," Sens. Actuators B, **100**, pp. 359–379.

[80] Lin, C.-H., Fu, L.-M., and Chien, Y.-S., 2004, "Microfluidic T-Form Mixer Utilizing Switching Electroosmotic Flow," Anal. Chem., **76**, pp. 5265–5272.

[81] Nguyen, N. T., and Wu, Z., 2005, "Micromixers – A Review," J. Micromech. Microeng., **15**, pp. R1–R16.

[82] Bau, H. H., Zhong, J., and Yi, M., 2001, "A Minute Magneto Hydro Dynamic (MHD) Mixer," Sens. Actuators B, **79**(2–3), pp. 207–215.

[83] Lu, L. H., Ryu, K. S., and Liu, C. J., 2002, "A Magnetic Microstirrer and Array for Microfluidic Mixing," J. Microelectromech. Syst., **11**(5), pp. 462–469.

[84] Rong, R., Choi, J. W., and Ahn, C. H., 2003, "A Functional Magnetic Bead/Biocell Sorter Using Fully Integrated Magnetic Micro/Nano Tips," *Proc. IEEE 16th Micro Electro Mechanical Systems (MEMS)*, Jan. 19–23, Kyoto, Japan, IEEE, MEMSYS.2003.1189803, pp. 530–533.

[85] Vivek, V., Zeng, Y., and Kim, E. S., 2000, "Novel Acoustic-Wave Micromixer," *Proc. IEEE 13th International Conference on Micro Electro Mechanical Systems (MEMS)*, Jan. 23–27, Miyazaki, Japan, IEEE, MEMSYS.2000.838598, pp. 668–673.

[86] Rife, J. C., Bell, M. I., Horwitz, J. S., Kabler, M. N., Auyueng, R. C. Y., and Kim, W. J., 2000, "Miniature Valveless Ultrasonic Pumps and Mixers," Sens. Actuators, A **86**(1–2), pp. 135–140.

[87] Yang, Z., Matsumoto, S., Goto, H., Matsumoto, M., and Maeda, R., 2001, "Ultrasonic Micromixer for Microfluidic Systems," Sens. Actuators, A, **93**(3), pp. 266–272.

[88] Miyake, R., Lammerink, T. S. J., Elwenspoek, M., and Fluitman, J. H. J., 1993, "Micro Mixer With Fast Diffusion," *Proc. IEEE 6th International Conference on Micro Electro Mechanical Systems*, Feb 7–10, Fort Lauderdale, FL, IEEE, MEMSYS.1993.296914, pp. 248–253.

[89] Voldman, J., Gray, M. L., and Schmidt, M. A., 2000, "Integrated Liquid Mixer/Valve," J. Microelectromech. Syst., **9**(3), pp. 295–302.

[90] He, B., Burke, B. J., Zhang, X., Zhang, R., and Regnier, R. E., 2001, "A Picoliter-Volume Mixer for Microfluidic Analytical Systems," Anal. Chem., **73**(9), pp. 1942–1947.

[91] Knight, J. B., Vishwanath, A., Brody, J. P., and Austin, R. H., 1998, "Hydrodynamic Focusing on a Silicon Chip: Mixing Nanoliters in Microseconds," Phys. Rev. Lett., **80**(17), pp. 3863–3866.

[92] Wong, S. H., Bryant, P., Ward, M., and Wharton, C., 2003, "Investigation of Mixing in a Cross-Shaped Micromixer With Static Mixing Elements for Reaction Kinetics Studies," Sens. Actuators B, **95**(1–3), pp. 414–424.

[93] Bökenkamp, D., Desai, A., Yang, X., Tai, Y. C., Marzluff, E. M., and Mayo, S. L., 1998, "Microfabricated Silicon Mixers for Submillisecond Quenching Flow Analysis," Anal. Chem., **70**, pp. 232–236.

[94] Gobby, D., Angeli, P., and Gavriilidis, A., 2001, "Mixing Chacteristics of T-Type Microfluidic Mixers," J. Micromech. Microeng., **11**(2), pp. 126–132.

[95] Engler, M., Kockmann, N., Kiefer, T., and Woias, P., 2000, "Numerical and Experimental Investigations on Liquid Mixing in Static Micromixers," Chem. Eng. J., **101**(1–3), pp. 315–322.

[96] Cahill, D. G., Goodson, K., and Majumdar, A., 2002, "Thermometry and Thermal Transport in Micro/Nanoscale Solid-State Devices and Structures," J. Heat Transfer, **124**, pp. 223–241.

[97] Gu, Y. Q., Ruan, X. L., Han, L., Zhu, D. Z., and Sun, X. Y., 2002, "Imaging of Thermal Conductivity With Sub-Micrometer Resolution Using Scanning Thermal Microscopy," Int. J. Thermophys., **23**(4), pp. 1115–1123.

[98] Fletcher, D. A., Crozier, K. B., Quate, C. F., Kino, G. S., Goodson, K. E., Simanovskii, D., and Palanker, D. V., 2000, "Near-Field Infrared Imaging With a Microfabricated Solid Immersion Lens," Appl. Phys. Lett., **77**, pp. 2109–2111.

[99] Aligoodarz, M. R., Yan, Y., and Kenning, D. B. R., 1998, "Wall Temperature and Pressure Variation During Flow Boiling in Narrow Channels," *Proc. 11th International Heat Transfer Conference (IHTC)*, Aug. 23–28, Kyongju, Korea, Taylor and Francis Corp., Vol. 2, pp. 225–230.

[100] Hohmann, C., and Stephan, P., 2002, "Microscale Temperature Measurement at an Evaporating Liquid Meniscus," Exp. Therm. Fluid Sci., **26**, pp. 157–162.

[101] Muwanga, R. S., and Hassan, I., 2005, "Local Heat Transfer Measurements in Micro Geometries Using Liquid Crystal Thermography," *Proc. ASME 3rd International Conference on Microchannels and Minichannels*, June 13–15, Toronto, CA, ASME, PART A, ICNMM2005-75019, pp. 217–224.

[102] Lakshminarasimhan, M. S., Hollingsworth, D. K., and Witte, L. C., 2000, "Boiling Incipience in Narrow Channels," *Proc. ASME International Mechanical Engineering Congress and Exposition*, Nov. 5–10, Orlando, FL, ASME Heat Transfer Division Publication, HTD-366-4 (IMECE2000, Vol. 4), pp. 55–63.

[103] Hapke, I., Boye, H., and Schmidt, J., 2000, "Onset of Nucleate Boiling in Minichannels," Int. J. Therm. Sci., **39**, pp. 505–513.

[104] Hetsroni, G., Gurevich, M., Mosyak, A., and Rozenblit, R., 2003, "Surface Temperature Measurement of a Heated Capillary Tube By Means of a Infrared Technique," Meas. Sci. Technol., **14**, pp. 807–814.

[105] Narayanan, V., 2003, "Temperature Measurements and Surface Visualization in Microchannel Flows Using Infrared Thermography," *Proc. ASME 1st International Conference on Microchannels and Minichannels*, April 24–25, Rochester, NY, S. Kandlikar, ed., ASME, ICMM2003-1117, pp. 879–886.

[106] Diaz, M. D., Boye, H., Hapke, I., Schmidt, J., Staate, Y., and Zhekov, Z., 2004, "Flow Boiling in Mini and Microchannels," *Proc. ASME 2nd International Conference on Microchannels and Minichannels*, June 17–19, Rochester, NY, S. Kandlikar, ed., ASME, ICMM2004-2367, pp. 445–451.

[107] Kim, H. J., Kihm, K. D., and Allen, J. S., 2003, "Examination of Ratiometric Laser Induced Fluorescence Thermometry for Microscale Spatial Measurement Resolution," Int. J. Heat Mass Transfer, **46**, pp. 3967–3974.

[108] Bonjour, J., and Lallemand, M., 1998, "Flow Patterns During Boiling in a Narrow Space Between Two Vertical Surfaces," Int. J. Multiphase Flow, **24**, pp. 947–960.

[109] Owhaib, W., and Palm, B., 2004, "Experimental Investigation of Single-Phase Convective Heat Transfer in Circular Microchannnels," Exp. Therm. Fluid Sci., **28**, pp. 105–110.

[110] OMEGA Engineering, 2002, *The OMEGA Made in the USA Handbook*, Vol. I, Omega Engineering, Stamford, CT.

[111] Kovacs, G. T. A., 1998, *Micromachined Transducers Sourcebook*, McGraw-Hill, New York.

[112] Liu, C. W., Gau, C., and Dai, B. T., 2004, "Design and Fabrication Development of a Micro Flow Heated Channel With Measurements of the Inside Micro-Scale Flow and Heat Transfer Process," Biosens. Bioelectron., **20**, pp. 91–101.

[113] Koutsiaris, A. G., Mathioulakis, D. S., and Tsangaris, S., 1999, "Microscope PIV for Velocity-Field Measurement of Particle Suspensions Flowing Inside Glass Capillaries," Meas. Sci. Technol., **10**(11), pp. 1037–1046.

[114] Meinhart, C. D., Werely, S. T., and Santiago, J. G., 1999, "PIV Measurements of Micro Channel Flow," Exp. Fluids, **27**, pp. 414–419.

[115] Kinoshita, H., Oshima, M., Hong, J.-W., Fujii, T., Saga, T., and Kobayashi, T., 2003, "PIV Measurement of Pressure and Electro Kinetically Driven Flow in Micro Channels," Proc. SPIE, **5058**, pp. 113–118.

[116] Dantec Dynamics, 2005, www.dantecdynamics.com

[117] Sinton, D., Erickson, D., and Li, D., 2003, "Micro Bubble Lensing Induced Photo-Bleaching (μ-BLIP) With Application to Micro Flow Visualization," Exp. Fluids, **35**, pp. 178–187.

[118] Pooran, R., Kim, J.-W., Tung, S., Malshe, A., and Lee, C. C., 2003, *A Cellular Motor Based Micro Pump – Integration of Cellular Motors With Micro Channels*, *Proc. ASME International Mechanical Engineering Congress and Exposition*, Nov. 15–21, Washington, DC, Micro-Electromechanical Systems Division Publication (MEMS), Vol. 5, Micro-Electro-Mechanical Systems (MEMS), IMECE2003-41545, pp. 495–499.

[119] Morini, G. L., 2004, "Single-Phase Convective Heat Transfer in Microchannels: A Review of Experimental Results," Int. J. Therm. Sci., **43**(7), pp. 613–651.

[120] Lin, S., Kew, P. A., and Cornwell, K., 2001, "Flow Boiling of Refrigerant R141B in Small Tubes," Chem. Eng. Res. Des., **79**(4), pp. 417–424.